UNIVERSITÀ DEGLI STUDI DELL'INSUBRIA
Facoltà di Scienze, Como
Dipartimento di Fisica e Matematica

APPLICATION OF DOPED SEMICONDUCTOR DEVICES TO THE DEVELOPMENT OF BOLOMETRIC DETECTORS TO BE USED IN EXPERIMENTS FOR THE MEASUREMENT OF THE ν MASS

A doctoral Dissertation
in Partial Fulfillment of the Requirements of the Degree of
Doctor Philosophiae in Physics

Thesis submetted by Erica Andreotti

Dottorato di Ricerca in Fisica ed Astrofisica
XXI CICLO

Supervisor
Prof. Andrea Giuliani

To my family,
who gave me the wings of life

Do not be too timid and squeamish about
your actions. All life is an experiment.
The more experiments you make the better.

It was a high counsel that I once heard given
to a young person:
"always do what you are afraid to do"

(R.W. Emerson)

CONTENTS

INTRODUCTION

The main subject of this PhD thesis consists in the study of the fundamental operating mechanisms of doped semiconductor devices, at low and very low temperatures. The aim of such devices will be their integration in calorimetric detectors to be used in neutrino mass experiments.
This work is developed over two main fronts:

- the characterization of thermal sensors operating in *Variable Range Hopping* regime, based on semiconductors doped slightly below the Metal-to-insulator transition;
- the characterization of highly doped semiconductor devices, so called *heaters*, used for bolometers stabilization.

These activities are connected to the MARE and CUORE experiments, devoted to the search for the neutrino mass, using the bolometric technique. In particular, the MARE project aims at measuring directly the neutrino mass thorugh the study of the Kurie-Plot at the end-point energy of ^{187}Re, contained in silver perrhenate crystals. The experiment will be performed at cryogenic temperatures ($\sim$ 100 mK) in a very low radioactive environment. One of the main tasks involved in the realization of such an experiment will be the developement of microcalorimeters, matching all the high standard technological requirements predicted for the achievement of its main goals.

The final aim of the MARE experiment will be to reach a 0.2 eV sensitivity on neutrino mass and this task will be pursued through a gradual approach. Actually the experiment will be developed in two phases, the first one devoted to improve the understanding about all possible systematic uncertainties and to gather further experience on Rhenium based microcalorimeters. In the meantime a parallel R&D activity for the second phase will be sustained. During the first phase two experiments, directly discending from the two precursors MIBETA and MANU, will be run separately. It is in the context of the MIBETA2 collaboration that one of the main subjects of this thesis is developed, dealing with the characterization of Si-implanted thermistors produced by the MEMS group at ITC-irst (chapter 5). These devices, being based on semiconductor thermistors operating in VRH regime (chapter 1), have been realized as one of the possible candidates to be used as thermal sensors in the 300 channels structure of MIBETA2. Given the technological requests, both in terms of practical reasons (dealing with the production of a large number of homogeneous devices) and good detector performances (dealing with energy resolution and time response) as discussed in chapter 2, an accurate characterization of such devices is necessary, in order to match all the detector prerogatives (chapter 3).

The second subject of this thesis deals with the study of the behaviour of highly doped semiconductor devices, still produced by the MEMS group at ITC-irst, to be used as heating devices for the stabilization of CUORE bolometers. Such elements, able to dissipate a known joule power into the bolometer, will be directly glued on to the TeO_2 crystals, which constitutes the absorbing part of the detectors. The role of heaters consists not only in the stabilization of response which can change with the temperature fluctuations of the heat sink, but also in the determination of the *optimum point* or *working point*, in terms of bias current and voltage applied, corresponding to the maximum detector response (chapter 2 and 3). Even in this case an accurate characterization in conditions very close to the final operating ones is necessary: hence a large part of this thesis is devoted to the accomplishement of this task (chapter 4).

Before entering into the experimental details, involved in the achievement of the above discussed arguments, a wide description of the transport mechanisms taking place in semiconductor materials at low temperatures is presented in the first chapter. This will be useful to understand the physical phenomenons which are at the basis of the functioning of the devices studied in this thesis.

CHAPTER 1

TRANSPORT MECHANISMS IN DOPED SEMICONDUCTORS

The main subject of this thesis is the experimental study of the low temperature behaviour of doped semiconductor devices, fabricated from a silicon substrate doped with phosphorus by ion implantation (Si:P system). Depending on the implanted dopants concentration, these devices can be used as thermal sensors or as heating elements in the developement of bolometric detectors.

Thermal sensors based on lightly doped semiconductor materials operates in the *Variable Range Hopping* or VRH regime. This particular transport mechanism takes place at very low temperatures in semiconductors doped below a critical concentration, which marks the metal-to-insulator transition (MIT). In VRH regime the conductivity has an exponential temperature dependence, thus allowing the developement of very sensitive thermistors. On the other hand heating elements used for the stabilization of bolometers needs to be very stable in terms of electrical conductivity, but at the same time they must possess a sufficiently high resistance. These characteristics can be obtained by doping a semiconductor material well above the MIT, where the transport of charge is of metallic type and thus weakly dependent from temperature.

The first chapter of this thesis is dedicated to review the transport mechanisms in semiconductor materials. Particular care will be given to the description of the "metal-to-insulator" transition and to the physical phenomenons which governs charge transport in doped semiconductors at very low temperatures, as this is the regime of interest for the discussed devices (see also [1–3] for a general overview on semiconductor physics and [4] for a more detailed description on low temperature properties of doped semiconductors). A section is also devoted to the description of the temperature dependence of the heat capacity in doped semiconductors, which represents a further important parameter for the realization of semiconductor devices to be integrated in bolometric detectors.

1.1 GENERAL PROPERTIES OF DOPED SEMICONDUCTORS

1.1.1 Charge transport in intrinsic semiconductors

Intrinsic semiconductors at zero temperature behaves as perfect insulators, since a forbidden energy gap (the width of which depends over the material type) separates the highest occupied band from the lowest empty band. At higher temperatures there is a nonvanishing probability for some electrons to be thermally excited across the gap into the lowest unoccupied energy levels, belonging to the so called *conduction band*. These electrons leave in the highest occupied band, the *valence band*, a corresponding number of unoccupied levels or *holes*. Both electrons in the conduction band and holes in the valence band are almost free to move through-out the semiconductor crystal, thus giving rise to an *intrinsic conductivity*.

At temperature T the *intrinsic carrier concentration*, meaning the fraction of excited electrons in the conduction band n and the equivalent holes concentration in the valence band p, are given by:

$$n = p = \frac{(2\pi\sqrt{m_e m_h}KT)^{3/2}}{4\pi^3\hbar^3} e^{-E_g/2k_BT} \tag{1.1}$$

where m_e and m_h are the masses of electrons and holes, respectivly, and E_g is the width of the forbidden gap. From 1.1 it can be seen that the intrinsic carrier density depends critically on the value of the ratio $-E_g/2k_BT$, so that, when this quantity is small enough, thermal excitation leads to observable conductivity. At room temperature, where $k_BT \sim 0.025$ eV, observable conduction can occur for E_g as high as 0.25 eV, for the factor $e^{-E_g/2k_BT}$ is of order $\sim 10^{-2}$. These facts are at the basis for the distinction between insulators and semiconductors: solids that are insulators at $T = 0$ K, but whose energy gaps are such a size that a non vanishing conductivity is manifested at higher temperatures (below the melting point), are known as semiconductors.

Silicon and germanium are the two most important elemental semiconductors, having the diamond crystal structure and belonging to Group IV of the periodic table.

Energy gaps have a slight temperature dependence, varying by about 10 percent between 0 K and 300 K. The values of the energy gaps for some type of semiconductors, at room and zero temperature, are given in Table 1.1.

Material	E_g (eV) $T = 300$ K	E_g (eV) $T = 0$ K
Si	1.12	1.17
Ge	0.67	0.75
PbS	0.37	0.29
InAs	0.35	0.43
GaAs	1.42	1.52
C	5.47	5.48

Table 1.1: Energy gap for some semiconductors

Typical room temperature resistivities of semiconductors are between 10^{-3} and 10^{9} $\Omega\cdot$ cm, in contrast to metals, with $\rho \sim 10^{-6}$ $\Omega\cdot$ cm and good insulators, with $\rho \sim 10^{22}$ $\Omega\cdot$ cm. The electrical conductivity of semiconductors is a very rapidly increasing function of temperature, given the exponential dependence from $1/T$ of thermally excited electrons. Thus, in striking contrast to metals, semiconductors have a *negative coefficient of resistance*.

In the case of metals conductivity is a weakly dipendent function of temperature and it is given by the Ohm law:

$$\sigma = \frac{ne^2\tau}{m} \tag{1.2}$$

where n is the density of carriers, indipendent of temperature; τ is the *relaxation time* (the time elapsed between two consecutive collisions); m is the electron mass. The temperature dependence in this case fully arises from the relaxation time, which generally decreases with increasing temperature, because of the increase of the electron-phonon scattering. For semiconductor materials the relaxation time dependence from temperature is overwhelmed by the more rapid increase in the density of carriers with increasing temperature.

1.1.2 The role of impurities

Even the most pure material obtainable with modern production processes contains a certain amount of impurity atoms, which unavoidably modify the conduction mechanisms of semiconductors. When impurities contribute a significant fraction of the conduction band electrons and/or valence band holes, one speaks of an *extrinsic semiconductor*. In this case the density of conduction band electrons no longer corresponds to the density of valence band holes at thermal equilibrium. Furthermore, at sufficiently low temperatures, the intrinsic carrier concentration becomes less than the concentration contributed by impurities, which thus starts to dominate most of electronic properties of doped semiconductors.

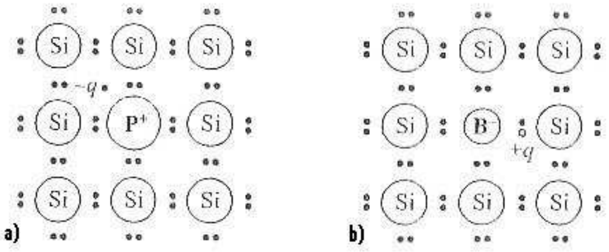

Figure 1.1: Impurities added to the lattice system: a) a donor impurity (phosphorus) in silicon; b) an acceptor impurity (boron) in silicon

In many cases of interest impurities are added by hand by means of well-defined *doping processes*, in order to determine the conduction properties of the materials. An impurity can be of either donor or acceptor type. A donor impurity can be easily ionized in the crystal medium by donating an electron to the conduction band. These electrons can then partecipate in transport processes, while the impurity centers become positively charged. On the other hand an acceptor impurity can capture one electron from the crystal: the impurity center becomes negatively charged while a hole appears in the valence band. Donor impurities are responsible for conductivity by electrons, or *n-type* conductivity. Acceptor impurities are responsible for conductivity by holes, or *p-type* conductivity.

Whether an impurity is a donor or acceptor is determined by the chemical valence of the impurity itself and that of the host material. For example, in the case of semiconductors of Group IV (Si and Ge), impurities which belong to Group V (P, Sb, As) are generally donors. Each atom of the host crystal forms four covalent chemical bonds with its four nearest neighbours, given the tetrahedral lattice structure of Group IV. Elements of Group V have five valence electrons thus, when placed in a tetrahedral host structure, they easily lose the excess electron, becoming donors. On the other hand, elements from Group III (B, Al, Ga, In) lack one valence electron, which they can easily capture from the host crystal, giving rise to a mobile hole in the valence band. Figure 1.1 shows the behaviour of donor and acceptor impurities when placed in the silicon lattice system.

The most important characteristic of an impurity is its ionization energy. For donors this corresponds to the energy necessary to move one electron from the donor level to the bottom of the conduction band; while for acceptors it corresponds to the energy required to produce a hole at the top of the valence band. Donor and acceptor levels are located in the forbidden gap (figure 1.2).

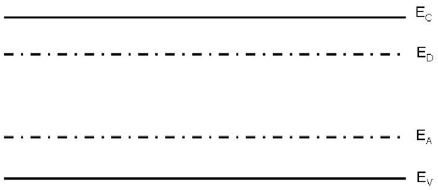

Figure 1.2: Band diagram of a semiconductor. E_C and E_V represents the edges of the conduction and valence bands; E_D and E_A represents the energy levels of donor and acceptor impurities

Impurities are called shallow if their ionization energy is small compared to the whidth of the energy gap. When a donor level is close to the bottom of the conduction band, it happens that an excess electron is weakly bound to the donor center, thus being located far from it on the average. A similar argument can be applied to acceptors, given the right substitutions. The values of the ionization energies at room temperature for some impurity atoms in Si and Ge are reported in table 1.2. Furthermore, since these ionization energies are comparable to $k_B T$ at ~ 300 K, ionization is usually complete at room temperature.

When the impurity concentration is not too large, electrons are captured by donors at sufficiently low temperatures, giving origin to the "freezing-out" of conduction electrons. The same phenomenon can happen to holes which, at low temperatures, are localized near an acceptor. In the following sections the case of donor impurities (which includes the Si:P system case) will be considered, in order to be specific, bearing in mind that for acceptors the argument is similar.

1.2 METAL-TO-INSULATOR TRANSITION

The behaviour of the electrical conductivity in doped semiconductors strongly depends over the dopant concentration. The main steps towards the comprehension of the low temperature charge transport in such materials were done, in the context of the localization theory, by *Anderson* and *Mott*. They stated the existence of a critical doping density which marks the transition from an insulator type behaviour to a metallic type one. This is the MIT ("metal-to-insulator transition") which was at first described by Mott in an ideal model, where the dopants or impurity centers are considered to form a regular sublattice, hosted by the primary crystal [5]. In this picture the MIT is considered as a consequence only of the electron-electron interactions.

1.2.1 Mott transition

In the theory of localization of electronic states the extra electron, located in the proximity of the bottom of the conduction band, is considered to be bound to the donor center only because of its positive charge. Thus the impurity center exerts over the electron a central potential of the form:

$$U(r) = \frac{e^2}{\kappa r} \tag{1.3}$$

where r is the distance to the center and κ the dielectric permittivity of the lattice. The introduction of this kind of potential allows to evaluate the structure of the electronic states and the form of the electronic wave function in the vicinity of a single impurity center. A finite concentration of similar impurities gives origin to an *impurity band* of finite width in energy, which does not possess the same properties of a crystal band, since an electron localized near one of the impurity sites does not spread over

	B	Al	Ga	In
Si	46	57	65	16
Ge	10.4	10.2	10.8	11.2
	P	**As**	**Sb**	**Bi**
Si	44	49	39	69
Ge	12	12.7	9.6	

Table 1.2: Ionization energies (meV) for some donors and acceptors in Si and Ge at room temperature

other centers constituting the band: the wave function of such an electron is defined in the whole lattice but has a probability peak over a single reticular site. The probability density of such an electron will be non negligible only on the nearest neighbours and the wave function remains localized.

Considering the case of regularly distributed impurities the allowed band width results to be linked to the separation between nearest neighbours and hence to the dopant concentration: as the separation increases the allowed band gets narrower. Bands formed by impurities are no more than half filled, since each impurity contributes one electron and the band is twofold spin degenerate. Thus it appears that the conductivity by impurities would be of metallic type, however small the impurity concentration. This is incorrect since the single-electron approximation, considered above, breaks down in the case of the narrow bands of lightly doped materials.

The interaction energy U_0 of two electrons of opposite spin located on the same site is of order:

$$U_0 \approx \frac{e^2}{a} \tag{1.4}$$

where a represents the wave function extension or the effective Bohr radius of the impurity. When the magnitude of U_0 is small compared to the allowed band width, as in the case of good metals, the wave function is only little perturbed by the electron-electron interaction. On the other hand the band width comes to be less than U_0 as the sublattice constant b_0 increases: in this case two electronic states appears on each site, due to the mutual electron interaction.

In the case of b_0 infinitely large the electron energy equals either a value E_0 or $E_0 + U_0$, depending on whether or not there is another electron on the site, as illustrated in figure 1.3. At a finite value of b_0 both levels spread into bands, whose width is of order $\sim exp(-b_0/a)$. The number of positions in each band equals the number of lattice sites, as by definition the bottom band cannot contain a site occupied by two electrons. So the lower band will become filled while the upper band empty: thus when the band width is less then U_0 the material is a dielectric.

As b_0 decreases the width of the forbidden gap will become smaller and finally vanishes at a certain point A: the system goes then into a metallic state. This is the *Mott transition*, whose nature is not yet entirely clear.

The two bands, whose appearence is due to the electrostatic repulsion between electrons, are called the *Hubbard bands*. In practice it happens that in a semiconductor with a single type of impurities, for example donors, the Fermi level E_F (the highest occupied energy level) is settled in the middle of the forbidden gap. When acceptors

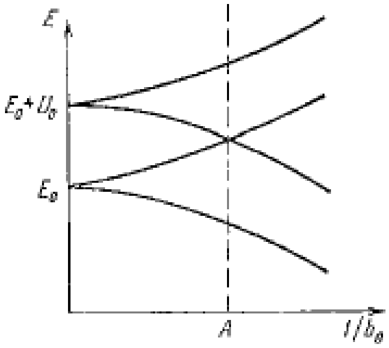

Figure 1.3: Dependence of electron bands on sublattice period and Mott transition

are added the Fermi level moves into the lower band, while, when the donors concentration increases, it arises an overlap of the two bands, giving origin to a conductivity of metallic type.

1.2.2 Anderson transition

In real situations impurities does not form regular lattices, so that, for a real understanding of conduction mechanisms, it is necessary to assume a random distribution of impurity centers. A simplified model for disordered systems has been developed by *Anderson*. He showed that when the number of impurity centers is sufficiently small the electrons are localized and the disorder is high. By increasing the dopants concentration the disorder is reduced, while the overlap of electron wave functions begins to increase, till finally electrons become completely delocalized.

Both the Anderson and the Mott transition are variations of the metal-to-insulator transition. Anderson's transition differs from Mott's transition as it deals with disordered systems and it is developed in a single-electron picture. In practice in this case the impurity band already contains both localized and delocalized states separated by a sharp boundary, the so called *mobility-edge* E_C. By varying the number of electrons in the band the Fermi level will move so that it may cross the boundary of the localized-state region.

In both Anderson and Mott transition, by increasing the impurity density, the *mobility-edge* get closer to the Fermi level: so the MIT can be seen as the entering of the Fermi level into the delocalized region. As long as $E_C > E_F$ (Fermi level in the localized region) the charge transport occurs by thermal activation of carriers into the delocalized region or by activated hopping between localized states. Both mechanisms lead to an exponential temperature dependence of the electrical conductivity at low temperature.

The transition from localized to delocalized states occurs when $E_F = E_C$. This happens for a critical value of the impurity concentration N_C given by the Mott-Anderson criterion (figure 1.4):

$$N_C^{1/3} a = 0.25 \tag{1.5}$$

The value of N_C depends on both the semiconductor material and the dopant. For the Si:P system $N_C = 3.74 \times 10^{18}$ donors/cm^3.

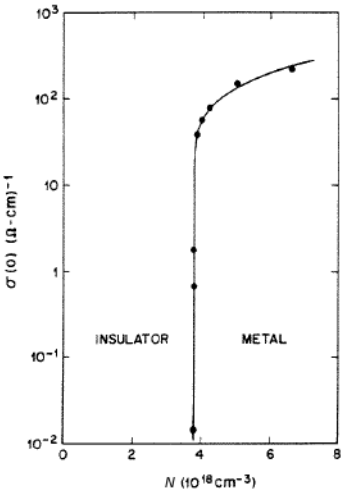

Figure 1.4: Dipendence of the zero-temperature conductivity on the Phosphorus concentration in Silicon

Experimentally, the MIT manifests itself in the fact that the exponential temperature dependence of conductivity, typical of materials doped below the critical concentration, is replaced by a weaker temperature dependence of metallic type, as the impurity concentration exceeds the critical value (highly doped semiconductors). In the case of materials doped above the critical concentration the conductivity does not vanish as $T \longrightarrow 0$, but it tends to a finite limit. It is still important to notice that the conductivity of highly doped semiconductors is much lower than that of ordinary metals and the term "metallic" reflects only the finit limit of conductivity as $T \longrightarrow 0$.

1.3 HOPPING CONDUCTION IN LIGHTLY DOPED SEMICONDUCTORS

Given the above considerations a semiconductor can be defined as lightly doped if there is only a small overlap between the electronic states belonging to different impurities. Hence the average separation between impurities much exceeds the characteristic wave function size a:

$$Na^3 << 1 \tag{1.6}$$

where N is the impurity concentration. As already stated there exists a critical concentration, depending on both the semiconductor material and the impurities, which clearly marks the boundary between metallic and insulator behaviour at low temperatures. This consideration clearly defines the distinction between heavy and light doping: in heavily doped semiconductors the conductivity is of metallic type (it depends weakly on temperature), whereas in lightly doped semiconductors it is of activated type.

The mechanism of interest for the development of thermal sensors based on lightly doped semiconductor materials is that of *hopping conduction*, which takes place at low temperatures due to the presence of *compensating impurities*.

1.3.1 Compensated materials

In real situations semiconductors usually contains both acceptor and donor impurities. The degree of compensation K is defined as the ratio of the minority to the majority impurities. For the system Si:P, where donors represent the main dopants, K is given by:

$$K = \frac{N_A}{N_D} \tag{1.7}$$

where N_D and N_A are respectively the donors and acceptors concentrations. In the case of a compensated n-type semiconductor, at low temperature each acceptor captures an electron, which than is no more available for conduction, from a donor and becomes negatively charged: thus, in addition to neutral donors there exist a certain quantity of positively charged donors which equals the number of negatively charged acceptors. This random distribution of charges gives origin to a fluctuating Coulomb potential and a dispersion of levels, which contributes to localization of electronic states. The electronic states in the impurity band of a lightly doped semiconductor with compensating dopants result then to be strictly localized. Thanks to the existence of charged impurities, electrons can move from one donor to another, giving rise to hopping conduction.

Experimentally it has been observed that it is possible to cross the MIT by simply varying the degree of compensation, while keeping N_D unchanged. This fact has been explained by Fritzsche [6] as due to the dipendence of the position of E_F and E_C over K. In fact, by increasing the degree of compensation, the net charge $n = N_D - N_A$ (the electrons available for conduction) is reduced, and the Fermi level moves into the lower Hubbard band. At the same time E_C grows up due to the increasing disorder, caused by the presence of acceptors. Thus, for compensated materials, the critical concentration of donors (for which $E_F = E_C$) will be higher than that extabilished by the Mott-Anderson criterion. In particular, when $K = 1$ the semiconductor will be an insulator, with no regard to the value of N_D.

1.3.2 General description of hopping conduction

As stated at the beginning of this chapter, semiconductors at high temperatures exhibit an intrinsic electrical conductivity due to the thermal activation of carriers, which decreases very rapidly with decreasing temperature, till the intrinsic carrier concentration becomes less than the concentration contributed by impurities. Thus, at sufficiently low temperatures, the electrical conductivity is entirely determined by impurities and it is called extrinsic.

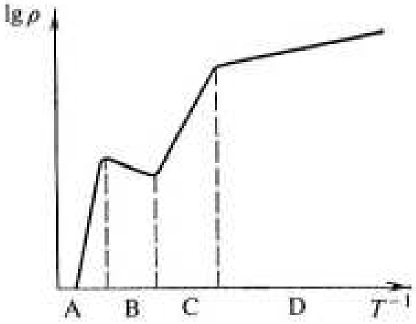

Figure 1.5: Temperature dependence of resistivity for a lightly doped semiconductor: (A) intrinsic conduction range, (B) saturation range, (C) freezing-out range, (D) hopping conduction range

A further decrease in temperature (below 50 K) leads, in lightly doped semiconductors, to the freezing-out of impurity electrons (or holes): the electrical conductivity is thus reduced due to the rapid decrease in the free carriers concentration. Finally, below about 10 K, the main contribution to the electrical conductivity results to be due to the electrons hopping between *nearest neighbouring* impurities, without any excursion to the conduction band: for this reason one talks about "phonon-assisted tunneling" between impurity sites. This is the hopping conduction mechanism, originated by electrons jumping from occupied donors to empty ones: the presence of empty positions on donors is a necessary condition, which at low temperatures can be fulfilled only by compensation. The fluctuating Coulomb potential in compensated semiconductors contributes to the dispersion of the impurity energy levels and the energy difference required in a given tunneling or "hop" is contributed by absorption or emission of a phonon.

Figure 1.5 shows the temperature dependence of resistivity in a lightly doped semiconductor: the temperature range A corresponds to intrinsic conduction, while the ranges B, C and D correspond to extrinsic conduction. Range B is also known as the *saturation range*, which arises when the ionization energy of impurities is much lower than the width of the energy gap E_g. In this range all the impurities are ionized and thus the carrier concentration in the band is independent from temperature. The weakly dependence from temperature is determined by that of the mobility, which is associated with the lowering of the phonon scattering with decreasing temperature.

In range C the gradual freezing-out of impurity carriers leads to a temperature dependence of resistivity given by:

$$\rho(T) = \rho_1 e^{(\varepsilon_1/k_B T)} \tag{1.8}$$

where ε_1 is the *activation energy*, whose value is very close to the ionization energy of an isolated donor.

Range D corresponds to the hopping conduction regime, characterized by a very low mobility, due to the strong carriers localization. In this region the temperature dipendence of the resistivity, as deduced from experimental results, is well approximated by the following expression:

$$\rho^{-1}(T) = \rho_1^{-1} e^{(-\varepsilon_1/k_B T)} + \rho_3^{-1} e^{(-\varepsilon_3/k_B T)} \tag{1.9}$$

The first term is contributed by free carriers in the conduction band and coincides with 1.8, while the second term corresponds to hopping conduction. The activation energy ε_3 is at first enhanced by an increase of the impurity concentration, due to the increasing random Coulomb potential. A further increase in concentration enhances the wave-function overlap, thus leading to a smaller ε_3, which finally vanishes as the impurity concentration equals N_C.

The value of ρ_3 strongly depends on the impurity concentration and it is given by [7]:

$$\rho_3 = \rho_{03} \exp\left(\frac{\alpha}{N^{1/3}a}\right) \tag{1.10}$$

Here N stands for the majority carriers concentration, α is a numerical constant and ρ_{03} is a power-law function of the impurity concentration. The physical reason for the exponential dependence given by 1.10 is linked to the increased wave-function overlap with increasing impurity concentration, which leads to an enhanced hopping probability.

A third activated mechanism contributes to conduction in semiconductors with a low degree of compensation ($K < 0.2$). Thus a further term, of the form $\rho_2^{-1}e^{(-\varepsilon_2/KT)}$, must be added in 1.9. Since $\rho_1 \ll \rho_2 \ll \rho_3$ and $\varepsilon_1 > \varepsilon_2 > \varepsilon_3$, this mechanism works in the intermediate temperature range between the band (range C) and the hopping (range D) conductivity regime. This type of conduction has been extensively studied in literature (see for example [8, 9]). It results to be less probable than hopping between nearest neighbours, while the associated mobility is bigger, as linked to delocalized carriers, able to cross the gap of energy $\varepsilon_2 = E_C - E_F > \varepsilon_3$ thanks to thermal excitation.

Due to the low value of the mobility, it is clear that hopping conduction cannot be interpreted on the basis of a picture of randomly scattered quasi-free electrons. A complete theory should be based on different concepts, first of all that of localized electron states: interaction with phonons and overlap of the wave functions of localized states give rise to infrequent jumps from one state to another. Different approaches have been proposed to develope a theory of hopping conduction (see as reference [7,10,11]).

1.4 VARIABLE RANGE HOPPING REGIME

At temperatures lower than those of the region interested by nearest neighbours hopping, high energy phonons begins to be scarcely available, since $\langle E_{ph} \rangle \sim k_B T$. This favours longer hops, as necessary to find unoccupied sites with energy sufficiently close to that of the original one and for which phonons, with the needed energy value, are available. Due to the increase of the characteristic hopping length with decreasing temperature, this transport mechanism is called *variable range hopping* (VRH) regime.

The VRH regime is of great interest for the developement of thermal sensors, which are usually fabricated by doping a semiconductor substrate just below the MIT. In these conditions it is possible to take advantage of the strong dependence of activated conductivity over temperature which characterizes the VRH regime, making it possible to produce very sensitive devices, while keeping a not too high value of the resistivity.

VRH conduction regime mainly involves impurity sites with energy concentrated in a narrow band near the Fermi level, also called the *optimal band*, whose width ε_0 decreases with decreasing temperature. Mott showed that, provided the density of states does not vanish at the Fermi level ($g(E_F) \neq 0$), it may be considered constant in the narrow band involved in the hopping process. In these conditions the following expression is valid for the temperature dependence of resistivity in VRH [12]:

$$\rho(T) = \rho_0 \exp\left(\frac{T_0}{T}\right)^{1/4} \tag{1.11}$$

with T_0 given by:

$$T_0 = \frac{\beta}{k_B a^3 g(E_F)} \tag{1.12}$$

where $g(E_F)$ is the density of states at the Fermi level, a the localization radius of states near the Fermi level, β a numerical coefficient. Equation 1.11 is known as the *Mott's law*. A peculiarity of the hopping conduction is the temperature dependence of the average hopping lenght, given by:

$$\lambda = a\left(\frac{T_0}{T}\right)^{1/4} \tag{1.13}$$

Mott gave only a qualitative derivation of equation 1.11, while a rigorous one, based on the *percolation theory*, was given by Ambegaokar [13].

Mott's law can be generalized to the case of a spatial dimensionality d, obtaining the following expression for $\rho(T)$:

$$\rho(T) = \rho_0 \exp\left(\frac{T_0}{T}\right)^{p} \tag{1.14}$$

with

$$p = (d+1)^{-1} \tag{1.15}$$

Mott's law is further modified in the case of an energy dependent density of states. Pollak [11] and Hamilton [14] considered the case when the density of states decreases as:

$$g(E) \propto (|E - E_F|)^m \tag{1.16}$$

Than the law 1.14 is valid with p:

$$p = \frac{m+1}{m+1+d} \tag{1.17}$$

Setting $d = 3$ and $m = 0$, corresponding to $g(E) \sim constant$, we get $p = 1/4$, as expected.

Furthermore, for a density of states concentrated in a finite energy range near the Fermi level, it turns out the existence of a critical temperature T_C above which the system undergoes a gradual transition from Mott's law to a dependence of the form given by 1.9.

In experimental studies over crystallic semiconductors it has been observed a value of p equal to 0.5, more than 0.25. This fact can be explained by introducing the theory of the *Coulomb Gap*, which modifies the form of the density of states near the Fermi level.

1.4.1 Coulomb gap

Due to Coulomb interaction between charge carriers contributing to hopping conduction, the density of states diminishes in the immediate vicinity of the Fermi level, by following the law 1.16 wih $m = 2$. For a three-dimensional system Mott's law 1.11 is then modified to:

$$\rho(T) = \rho_0 \exp\left(\frac{T_0}{T}\right)^{1/2} \tag{1.18}$$

The risultant minimum in the density of states is called the *Coulomb gap*, since it gives origin to an energy gap Δ separating the filled and empty states, as shown by Pollak and Knotek [15, 16]. However, untill the temperature is sufficiently high so that the width of the optimal band ε_0 is higher than Δ, the Coulomb gap does not affect the conductivity, and equation 1.11 remains valid. As the temperature decreases, ε_0 also decreses, till it becomes comparable to the gap width: in this circumstance the exponent p in equation 1.14 is modified by the presence of the Coulomb gap.

Shklovskii and Efros [4] proposed the following expression for the density of states near the Fermi level in the presence of the Coulomb gap:

$$g(E - E_F) = \frac{d\kappa^d}{e^{2d}} |E - E_F|^{d-1} \tag{1.19}$$

Taking into account this expression and experimental results, performed with various doping concentrations and compensating degrees, the following expresson for T_0 is obtained:

$$T_0 = 2.8\frac{e^2}{\kappa a}\left(1 - \frac{N}{N_C}\right)^{1.7} \tag{1.20}$$

Here N stands for the concentration of the majority impurity. The above expression clearly shows how the temperature dependence of the resistivity can be modified by varying the impurity concentration. This fact is of great interest for the fabrication of sensitive thermistors operating in VRH regime.

1.4.2 Non-Ohmic behaviours

A doped semiconductor, with resistivity described by equation 1.18, is characterized by a linear current-voltage relationship, given by the Ohm law. However, as the current flow through the semiconductor increases, non ohmic behaviours do appear, which have been observed and reported in literature [17–19]. Several models have been proposed in order to find an explanation to these non-linearities. They differ in details, but they basicly rely on two main effects: the first one is based on the *electric field effect*, the second one is based on a thermal model, the *hot electron model*.

Theoretical models for hopping conduction forsee the existence of an electric field effect, due to the energy acquired by electrons, while jumping from one site to another, when an electric field E is applied. An approximated expression for resistivity in this condition is given by:

$$\rho(T,E) = \rho(T,0)\exp\left(-C\frac{eE\lambda}{k_B T}\right) \tag{1.21}$$

where C is a constant of order unity and λ represents the characteristic hopping length.

The standard electric field form given in 1.21 does not always give a complete description of the observed behaviours. The introduction of an analog to the well known hot electron model in metals (see for example [20]) often allows better explanations for the experimental results. In this model electrons are supposed to form a subsystem with its own temperature T_e, thermally coupled to the phonon subsystem, with temperature T_p, through a finite thermal conductance G_{ep}. As a consequence, the VRH theory is modified, so that the resistivity of the system depents no more over T_p but over T_e, since the bias power injected to measure resistance is totally deposited in the electron subsystem. Mott's law 1.18 becomes then:

$$\rho(T_e) = \rho_0 \exp\left(\frac{T_0}{T_e}\right)^{1/2} \tag{1.22}$$

Furthermore, in the hot electron model it is assumed that the power P_e, transfered to the system as a consequence of its polarization, flows from the electrons to the lattice through a conductance given by:

$$G_{ep}(T_e) \equiv \frac{dP_e}{dT_e} = \alpha g_{ep} T_e^{\alpha-1} \tag{1.23}$$

where α and g_{ep} are constants and G_{ep} is proportional to the volume of the semiconductor device. In the case of metals a dipendance of the form $G_{ep} \propto T^4$ has been found, while for semiconductors a value of $\alpha \sim 5-6$ is generally observed. For a fixed temperature of the phonon system it is possible to calculate the electron temperature as:

$$T_e = \left(T_p^{\alpha} + \frac{P_e}{g_{ep}}\right)^{\frac{1}{\alpha}} \tag{1.24}$$

The difficulty with the hot electron model consists in the fact that it has no basis in the current VRH theory, as in this context electrons should be strongly localized. In VRH regime electrons can change their energy distribution by tunneling from site to site, with emission or absorption of phonons, while in order to allow electrons to set up a thermal distribution by their own, their energy should be somehow delocalized.

1.5 METALLIC BEHAVIOUR IN HEAVILY DOPED SEMICONDUCTORS

Section 1.2 describes how the impurity concentration can affect the transport mechanisms which take place in a doped semiconductor, giving rise to the metal-to-insulator transition. In the subsequent sections the phenomenons which characterize the behaviour of lightly doped semiconductors at low temperature were presented. In particular it was stated the existence of a critical concentration of dopant atoms below which the energy states are strictly localized and conduction is of activated type. This fact was explained by observing that at low impurity concentrations the overlap between electronic wave functions is negligible.

At higher impurity concentrations the interaction between impurity atoms increases, since their reciprocal distances get lower. Thus the electronic wave functions of neighbouring centers do overlap and the local energy levels broaden above and below their original positions, forming impurity bands. The result is a decrease in the ionization energy which, at very high impurity concentrations, becomes negligible. In this case a single allowed band is formed in such a *heavily doped semiconductor*, so that electronic states are delocalized and charge carriers are relatively free.

A semiconductor is called heavily doped (HDS) if its impurity concentration N satisfies the inequality:

$$Na^3 \gg 1 \tag{1.25}$$

where a represents the Bohr radius of the impurity state.

As already mentioned in the previous sections, delocalization of electronic states in HDS gives rise to a conductivity of metallic nature and thus weakly dependant over temperature. However it is worth to remember that conductivity values in HDS are much lower than in ordinary metals. These peculiarities make HDS very useful in the developement of bolometric detectors, as they are good candidate materials for the fabrication of heating devices for bolometers stabilization. These elements must in fact satisfy some requirements, among which the following:

- their resistivity must be reasonably indipendent from temperature;
- their resistance must be much higher than that of the wires used for the electrical connections.

A theory of charge transport and electronic states in HDS is extensively exposed in [4]. It basicly starts from a free-electron picture, thus treating the carriers as an ideal Fermi gas.

In such a picture the behaviour of this type of materials can be interpreted in analogy to that of ordinary metals. Considering the carriers as completely free to move, with no interaction with ions in the lattice, conductivity should be a constant at any temperature. Actually, even in metals, resistivity results to be a weakly increasing function of temperature. This is due to the contribution of two temperature dependant factors: the first one is provided by phonons or lattice vibrations, the second one is due to impurity ions. The contribution due to lattice vibrations decreases with lowering temperature as:

$$\rho_L \sim T \tag{1.26}$$

as long as $T \gg \Theta_D$, where Θ_D is the characteristic *Debye temperature* of the material. While for $T \ll \Theta_D$ the dipendance is given by:

$$\rho_L \sim T^5 \tag{1.27}$$

Both dependences are related to the number of available phonons at a given temperature.

The contribution due to impurity ions ρ_i is indipendent from temperature in the case of relatively low impurity concentrations. As temperature decreases ρ_L comes close to 0, and resistivity is complitely determined by ρ_i. It is this quantity then which dominates at low temperatures, even more in the case of HDS where the impurity concentration is high, giving origin to a finite limit of resistivity as $T \longrightarrow 0$.

1.6 HEAT CAPACITY

A further important parameter for the realization of both thermal sensors and heating devices to be integrated in bolometric detectors, is their heat capacity, due to its contribution to the shape of the thermal pulse (as better explained in chapter 2 and 3). In the case of a pure semiconductor the heat capacity is that of the lattice and it is given by the Debye law:

$$C \propto \left(\frac{T}{\Theta_D}\right)^3 \tag{1.28}$$

For silicon Θ_D corresponds to ~ 645 K. In the case of a doped semiconductor other contributions must be added, which depends over the impurity concentration:

- when delocalized electrons are present they contribute to the heat capacity by a term of metallic type: $C_e \propto N_D^{1/3} T$;
- when the impurity concentration is close to the critical one, experimental results require the introduction of a term due to localized electrons: $\Delta C_e \propto T^{\alpha}$, with α varying between -0.2 and 0.2 as N_D varies between 0.89×10^{18} and 7.3×10^{18} ions/cm^3 for the Si:P system.

At about 100 mK the term ΔC_e is approximately constant and for $N_D = 3.3 \times 10^{18}$ ions/cm^3, close to the impurity concentration of the thermal sensors studied in this thesis, its value is about 0.25 μJ/g/K. Finally it is important to notice that the lattice contribution decreases very rapidly with decreasing temperature, till it becomes negligible. In the case of heavily doped semiconductors, at very low temperatures, the heat capacity results to be dominated by the electronic term, proportional to the temperature T.

CHAPTER 2

DETERMINATION OF THE NEUTRINO MASS AND BOLOMETRIC TECHNIQUE

Neutrinos represent the most common form of matter in the universe, being at the same time elusive, since they are weakly interacting particles. In the Standard Model of electroweak interactions neutrinos are described as massless particles with spin $1/2$ which can assume one of the three leptonic flavors: ν_e, ν_μ, ν_τ.

In recent years experimental results proved that neutrino flavours oscillate, thus providing evidence for the existence of a finite neutrino mass [21–25]. In the hypothesis of a non-zero neutrino mass flavor states $|\nu_l\rangle$ can be written as coherent superpositions of mass eigenvalues $|\nu_i\rangle$:

$$|\nu_l\rangle = \sum_i U_{li} |\nu_i\rangle \qquad l = e, \mu, \tau \qquad i = 1, 2, 3 \tag{2.1}$$

where U_{li} is the Pontecorvo-Maki-Nakagawa-Sakata mixing matrix [26].

From oscillations the neutrino mixing matrix can be evaluated, as well as the mass square differences Δm^2_{ij}, but not the absolute mass values m_1, m_2, m_3 [27, 28]. According to oscillation experimental results the three following possible scenarios arise for neutrino mass hierarchies, as also illustrated in figure 2.1:

- normal hierarchy:
  $\Delta m^2_{23} > 0 \qquad m_1 < m_2 \ll m_3$
  $\Delta m^2_{12} \simeq \Delta m^2_{sol} \simeq m^2_2 \qquad \Delta m^2_{23} \simeq |\Delta m^2_{atm}| \simeq m^2_3$

- inverted hierarchy:
  $\Delta m^2_{23} < 0 \qquad m_3 \ll m_1 < m_2$
  $\Delta m^2_{12} \simeq \Delta m^2_{sol} \qquad \Delta m^2_{23} \simeq -|\Delta m^2_{atm}| \simeq -m^2_1$

- quasi-degenerate hierarchy:
  $\Delta m^2_{ij} \ll m^2_1 \simeq m^2_2 \simeq m^2_3$

The parameters Δm^2_{sol} and Δm^2_{atm} identify the experimental mass square differences inferred respectively from solar and atmospheric neutrino oscillation measurements. Though it is not possible to calculate absolute mass values, ranges for the effective Majorana electron neutrino mass $|\langle m_{\nu_e}\rangle|$ can be inferred, with the help of some further assumpions, in the three different hierarchy schemes.

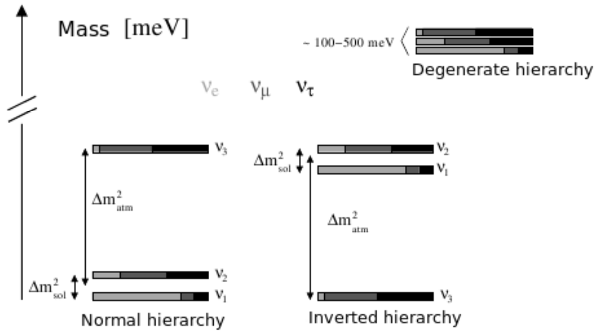

Figure 2.1: Neutrino mass hierarchies schemes

The results of the analysis done by Pascoli et al. [27] is reported in table 2.1. This analysis is useful to predict the discovery potential of the experiments involved in the search for neutrino mass.

$sin^2\theta$	$\lvert\langle m_{\nu_e}\rangle\rvert^{max}_{NH}$ (meV)	$\lvert\langle m_{\nu_e}\rangle\rvert^{min}_{IH}$ (meV)	$\lvert\langle m_{\nu_e}\rangle\rvert^{max}_{IH}$ (meV)	$\lvert\langle m_{\nu_e}\rangle\rvert^{min}_{QD}$ (meV)
0.0	3.7	8.7	50.6	47.9
0.02	4.6	8.6	49.6	42.8
0.04	5.3	9.9	48.6	45.4

Table 2.1: Present constrains on $|\langle m_{\nu_e}\rangle|$ in meV, for the 90% C.L. allowed values of Δm_{sol}, Δm_{atm} and θ_{sol} mixing angle: maximal values for the normal (NH) and inverted (IH) hierarchies; minimal values for inverted (IH) and quasi degenerate (QD) hierarchies [27]

The discovery that neutrino have a finite mass represents the first serious crack in the Standard Model. Efforts to unify the strong and electroweak interactions led to the developement of Grand Unified Theories (GUTs) which forsee the possibility for neutrinos to have a non-vanishing mass. In the context of GUTs it is possible to develop predictive models for fermion and in particular neutrino masses. The experimental determination of neutrino mass scale and properties is then a crucial test for predictive GUTs.

Furthermore the existence of a massive neutrino have a crucial role also in cosmology, as neutrinos may represent a component of dark matter, given their mass is sufficiently small [29]. According to oscillation experimental results the heaviest neutrino mass is in the range $0.04 - 0.6$ eV, and hence much smaller than charged lepton masses. This fact finds an explanation by means of the seesaw mechanism, often incorporated in the GUTs.

In parallel to the discovery of neutrino mass scale some other open questions should be answered by means of experimental observations, such as the nature of neutrino mass, i.e. if neutrino is a Dirac or a Majorana particle (i.e. neutrino corresponds to its own antiparticle). It is clear then that a complete understanding of neutrino properties is crucial for the comprehension of elementary particle physics as well as for the solution of some hot astroparticle problems.

Up to now only upper limits on neutrino mass can be deduced from the so far obtained experimental results. Only one controversial case does exist in which the observation of a Majorana neutrino mass of ~ 0.4 eV has been claimed by a part of the Heidelberg-Moscow collaboration [30], in the context of neutrinoless double beta decay experiments.

Three main approaches involved in neutrino mass investigation are presently available, which are respectively based on cosmological bounds, β decay experiments and neutrinoless double beta decay experiments.

Cosmological bounds are based on kinematical effects and depend on the delicate interplay between CMB and galaxy power spectra, being thus less robust then laboratory measurements. Neutrinoless double beta ($0\nu\beta\beta$) decay experiments will be essential to disentangle the nature of neutrino mass, as $0\nu\beta\beta$ needs to assume neutrino is a Majorana particle. β decay experiments are the only model-indipendent method of investigation, nevertheless it is very hard to get sensitivities much lower than ~ 1 eV. It is worth to notice that all these methodologies are required in order to investigate the different aspects concerning neutrino physics.

In the context of the search for neutrino mass the calorimetric technique is a very promising method, applied to both 0νββ and β decay experiments as described in the following sections.

2.1 BOLOMETRIC DETECTORS OF PARTICLES

A thermal detector generally identifies a sensitive *calorimeter* able to measure the heat released by an impinging particle through the corresponding temperature rise. When thermal detectors are operated at low temperatures they can provide an excellent energy resolution, low energy treshold and wide material choice. Furthermore they have the unique feature to be sensitive to non-ionizing events. For all these reasons they are suitable candidates to be used in the investigation on neutrino mass through the study of 0νββ and β decay.

A typical calorimeter is made up of an energy absorber, in which particles interact, and a thermal sensor, which converts the temperature rise into an electrical signal. These two elements are coupled each other and to the heat sink through a thermal link. The thermal sensor can be either a semiconductor thermistor operating in the VRH regime and more in general a resistive element with a strongly dependence of resistence over temperature, or a any other device able to convert a small temperature change into an electrical pulse.

The energy deposeted in the absorber is at first converted into high energy phonons, thus modifying the system thermal equilibrium (non thermal phonons). When time enough is elapsed ($\sim 1\mu$s) the phonon system relaxes on a new equilibrium distribution, corresponding to an higher temperature (thermal phonons). The detector works as a true calorimeter only when it is not too fast in response, so that a complete thermalization of the deposited energy is guaranteed. There are situations in which the sensor response is so fast that excess non-equilibrium phonons are detected: in this case the thermometer is better defined as a *phonon-sensor*.

Since semiconductor thermistors are relatively slow in response, they are usually operated, as far as possible, as true calorimeters.

Thermal detectors are sometimes called phonon mediated particle detectors (PMDs) due to the physical processes involved in the production of the thermal signal. PMDs were originally proposed as ideal calorimeters, with heat capacity C, able to complitely thermalize all the energy E released by a single particle, thus giving rise to a temperature increase $\Delta T = E/C$. In order to inhance sensitivity the heat capacity must therefore be minimized. This can be done by operating calorimetric detectors at low temperatures. PMDs operated at low temperatures are also known as *bolometers*.

When the detector total mass does not exceed 1 mg and the linear dimensions are a few hundreds of μm maximum, one speaks about a *microcalorimeter*.

One of the prerogatives of calorimetric detectors is the achievable intrinsic energy resolution, much higher in comparison to that of conventional detectors, which are only sensitive to the fraction of energy deposited through ionization ($\sim 30\%$). Energy resolution is intrinsecally limited by the fluctuations in the number of excitations since its value is given by:

$$\Delta E_{FWHM} = 2.35F\sqrt{\varepsilon E} \tag{2.2}$$

where ε is the energy required on the average to produce a single excitation, E represents the total energy deposited in the detector and F is the Fano factor [31]. In conventional semiconductor detectors the energy required to produce an electron-hole pair is of order 1 eV and in other ordinary detectors the excitation energy is even higher. On the other hand the typical energy of a phonon in a calorimeter operating at ~ 100 mK is of order $k_B T \sim 10$ μeV. In this case intrinsic resolution is thus improved by a factor $1-2$. Intrinsic resolution in calorimetric detectors will be thoroughly discussed in section 2.1.1.

Another prerogative of calorimetric detectors, particularly attractive in applications where a coincidence between source and detector may be convenient, is the wide choice of materials available for the fabrication of the absorbing element, which must essentially submit to the fundamental requirement of having a low enough heat capacity in order not to suppress sensitivity. Two classes of material do exist which are suitable for the production of the energy absorber, as they meet the requirements previously exposed: diamagnetic dielectric materials and superconductors. In both cases in fact the heat capacity behaves as a very rapidly decreasing function of temperature, as will be better described in 2.1.1.

A powerful method for the determination of neutrino mass through the study of $0\nu\beta\beta$ and β decay, consists in embedding the source of the decay events under investigation in a bolometric detector, thus making a calorimetric measurement of the decay energy. This allows to maximize the efficiency, as the source is complitely sourrounded by the detector. At the same time all the deposited energy can be measured by means of a temperature rise.

A further important accomplishment, necessary to correctly operate calorimetric detectors of particles, consists in the stabilization of response which can change with the temperature fluctuations of the heat sink. This task can be pursued by means of a fixed resistence (*heater*), directly glued onto the absorber, able to dissipate a known joule power into the bolometer. Another task which can be accomplished by heaters is the determination of the *optimum point* in the $I-V_b$ curve, corresponding to the maximum detector response, as better described in 2.3.1 and 3.2.1. Actually there exist some more methods for response stabilization, as described in 2.3.1, where also the role of heaters will be discussed in details.

2.1.1 Absorber and thermalization process

In principle any kind of material with sufficiently small heat capacity at the operating temperature can be used as energy absorber in the fabrication of bolometric detectors. Usually a dielectric diamagnetic material is used in order to avoid dangerous contributions to the specific heat due to the electronic term, as it happens in metals. In fact in the case of insulators and semiconductors the heat capacity is completely determined by the lattice contribution and given by the Debye law (see also section 1.6):

$$C_p(T_p)\left[\frac{\mathrm{J}}{\mathrm{K}}\right] \propto n\left(\frac{T_p}{\Theta_D}\right)^3 \tag{2.3}$$

Here C_p and T_p represent the lattice heat capacity and temperature respectively, while n is the number of moles in the considered material. Due to the rapid decrease of their heat capacity with decreasing temperature, given by equation 2.3, dielectric materials are good candidates as absorbers in the realization of bolometric detectors. In such devices the energy resolution can be very high and close to the so-called *thermodynamical limit*, corresponding to the statistical fluctuation of the internal energy of the calorimeter, in the hypothesis of a weak thermal link to the heat bath (see section 3.2.1):

$$\Delta E_{FWHM} = \sqrt{k_B T^2 C} \tag{2.4}$$

A crucial parameter of the energy absorber is therfore Θ_D, which should be as high as possible in order to reduce the specific heat.

Heat capacity is a quickly decreasing function of temperature also in superconductors. In this case the fraction of the electrons joined to form Cooper pairs, which do not contribute to the specific heat, gradually increases below the critical temperature T_c. The remaining single electrons contribute with the following term, as given by the BCS theory:

$$C_e(T_e)\left[\frac{\mathrm{J}}{\mathrm{K}}\right] \propto T_c\left(1.76\frac{T_c}{T_e}\right)^{3/2} \exp\left(-1.76\frac{T_c}{T_e}\right) \tag{2.5}$$

Here T_e stands for the temperature of the "free" electrons.

The interaction of an elementary particle with a solid medium produces excitations of its elastic field, so that the energy spectrum of the target phonon system is modified and the starting equilibrium condition is broken. It was previously pointed out that only when the phonon system relax on a new equilibrium condition the detector works as a true calorimeter. As a consequence, in view of the characterization described in chapter 3 and in order to give a correct interpretation of the behaviour of calorimeters, it is necessary to give a description in terms of thermodinamic systems with a well defined temperature while operated. This is only possible if, after the particle interaction, the equilibrium condition is restored before the complete formation of the thermal signal (which typically requires a time of order 100 μs). The processes involved in the restoration of the thermal equilibrium condition are very complex and depends on the material type.

The energy E released by a ionizing particle interecting in a dielectric material is mostly spent in the production of a number of electron-hole pairs given by:

$$N_{eh} = E/\varepsilon_{eh} \tag{2.6}$$

where ε_{eh} is the average energy of the electron-hole pairs, linked to the energy gap E_g. These pairs release their energy excess by emitting high energy *optic* phonons: this process takes a time of order ps. Optic phonons subsequently decay in a few ns into *longitudinal acoustic* phonons, with frequency about half the Debye frequency ν_D. The effect of the interaction of a ionizing particle into the absorber is, in the end, the production of acoustic phonons with energy $\sim h\nu_D$ after a few ns. At the typical operating temperatures ($\sim$ 100 mK) the condition $h\nu_D >> k_B T_p$ is valid, where $k_B T_p$ corresponds to the energy carried by the reticular thermal phonons: this situation does not yet correspond to an equilibrium condition. In order to obtain a temperature increase of the whole system, or better, to get to the new thermal equilibrium, the acoustic phonons must degrade their energy through two different thermalization processes:

- decay of longitudinal acoustic phonons, thanks to the anarmonic terms of the lattice potential;
- isotopic scattering of phonons, which allows also the conversion between longitudinal and transversal acoustic phonons.

Even other mechanisms can give a contribution to the thermalization process, as the interaction of phonons with adsorbing atoms at the surface or with defects in the absorber.

One factor which can be very dangerous for the energy resolution is the presence of electron-hole pairs with energy $\sim E_g$ which can be involved in trapping and radiative recombination processes. This is even more probable in the case of dielectric materials, where impurities and defects lying inside the forbidden band-gap can act as traps. These processes prevent from the full conversion of the deposited energy into heat, since electron-hole pairs get trapped before their recombination to phonons. The statistical fluctuation of the number of trapped carriers leads to excess broadening of the energy peaks (*thermalization noise*). A solution to this problem consists in using metallic-superconductive or small band-gap energy absorbers.

2.2 DIRECT SEARCH FOR NEUTRINO MASS

β decay end-point experiments, also known as "direct searches" for neutrino mass, are essentially free of theoretical assumptions about neutrino properties. High precision end-point measurements of beta decay are required together with $0\nu\beta\beta$ decay experiments, in order to fully disentangle the neutrino mass nature. In particular the search for neutrino mass through the study of β decay end-point will play a fundamental role and should be pursued with different techniques, for the reasons below discussed:

- the possible estimation of the neutrino mass is based only on kinematical assumptions and is therefore totally model indipendent, in contrast to the other techniques involved in this topic.
- the achievable sensitivity ($\sim$ 0.2 eV) matches the present sensitivities of other, model dependent methods; in particular the Klapdor-Kleingrothaus (Heidelberg-Moscow) claim for a neutrino Majorana mass of $\sim$ 0.4 eV can be confirmed, if the case, by a pure kinematical approach.
- the proposed single beta decay experiments are quite difficult and dominated by a complicated systematics; this imposes the use of at least two complementary techniques.

2.2.1 Beta decay and neutrino mass

Beta decay is a nuclear transition in which a nucleus $(A, Z-1)$ decays by emitting an electron and an electron antineutrino $\overline{\nu}_e$:

$$(A, Z-1) \longrightarrow (A, Z) + e^- + \overline{\nu}_e \tag{2.7}$$

The energy E_0 available in the final state is given by:

$$E_0 = M(A, Z-1)c^2 - M(A, Z)c^2 \tag{2.8}$$

where M indicates the mass of the atoms in the initial and final state. Single beta decays can be classified according to the selection rules reported in table 2.2, where $L = \Delta J = |J_i - J_f|$ and J_i, J_f, π_i, π_f are respectively the spins and the parities of the initial and final nuclides.

$L = 0, 1$	$\pi_f \pi_i = +1$	Allowed transitions
$L = 0, 1$	$\pi_f \pi_i = -1$	Non unique first forbidden transitions
$L > 1$	$\pi_f \pi_i = (-1)^L$	Non unique L-th forbidden transitions
	$\pi_f \pi_i = (-1)^{L-1}$	Unique (L-1)-th forbidden transitions

Table 2.2: Classification and terminology for beta decays

Neglecting the nucleus recoil, the energy spectrum of the emitted electrons is described by the general form:

$$N_\beta(Z, E_\beta, m_{\nu_e}) = p_\beta E_\beta (E_0 - E_\beta) \sqrt{(E_0 - E_\beta)^2 - m_{\nu_e}^2 c^4} F(Z, E_\beta) S(E_\beta) [1 + \delta_R(Z, E_\beta)] \tag{2.9}$$

where, by indicating with p_β and E_β the momentum and energy of the emitted electron respectively, the following terms do appear:

- $p_\beta E_\beta (E_0 - E_\beta) \sqrt{(E_0 - E_\beta)^2 - m_{\nu_e}^2 c^4}$ is the phase space term in a three-body decay, where the nuclear recoil is neglected;

- $F(Z, E_\beta)$ represents the Coulombian correction (Fermi function) which accounts for the effect of the nuclear charge on the wave function of the emitted electron;

- $S(E_\beta)$ is the form factor of the beta spectrum, which contains the nuclear matrix element of the electroweak interaction;

- $\delta_R(Z, E_\beta)$ is the radiative electromagnetic correction, usually neglected due to its exiguity.

Usually, for experimental analysis purpose, it is convenient to transform the acquired beta spectrum into a quantity which is linear with the energy E_β of the emitted electron:

$$K(E_\beta) \equiv \sqrt{\frac{N_\beta(Z,E_\beta,m_{\nu_e})}{p_\beta E_\beta F(Z,E_\beta)S(E_\beta)[1+\delta_R(Z,E_\beta)]}} = (E_0 - E_\beta)\left(1 - \frac{m_{\nu_e}^2 c^4}{(E_0-E_\beta)^2}\right)^{1/4} \tag{2.10}$$

The corresponding graph is named *Kurie plot.* Assuming infinite energy resolution and massless neutrinos, the Kurie plot is a straight line intersecting the x-axis at the transition energy E_0. On the other hand, the existence of a massive neutrino, would distort the Kurie plot in proximity of the end-point, and the intersection with the x-axis will appear at the energy $E_0 - m_\nu$ (figure 2.2).

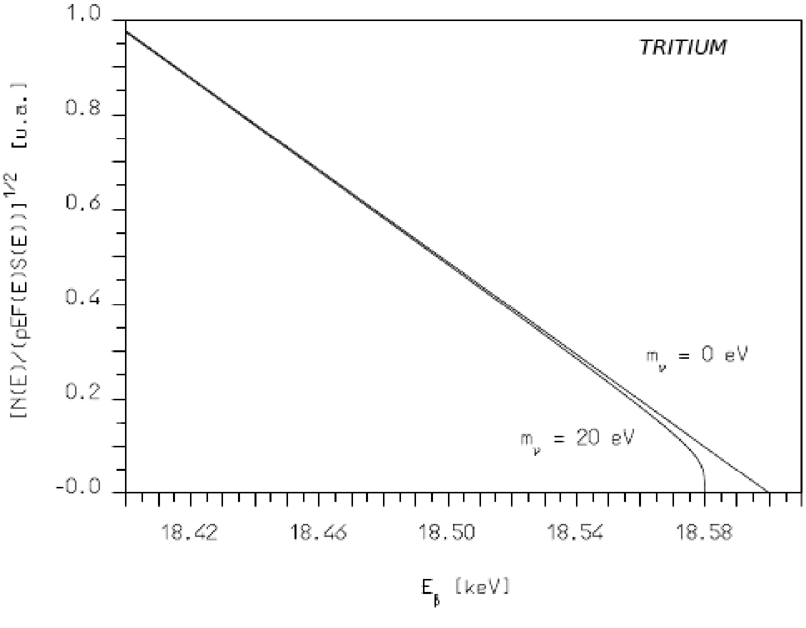

Figure 2.2: Kurie plot in proximity of the tritium end point energy, evaluated considering a neutrino mass of respectively 0 eV and 20 eV

Most informations for the determination of the neutrino mass are therefore contained in an energy interval $\delta E \simeq 3m_{\nu_e}$ close to the final part of the Kurie plot, which is unfortunately the region with the lower counting rate. The fraction of useful events occurring in this region is given by:

$$F(\delta E) = \int_{E_0-\delta E}^{E_0} N_\beta(Z, E_\beta, m_{\nu_e} = 0)dE \simeq 2\left(\frac{\delta E}{E_0}\right)^3 \tag{2.11}$$

The above equation shows clearly that low end-point energy beta becaying isotopes are the ideal candidates to be used in the direct search for neutrino mass, in order to increase as much as possible the statistics in the interesting energy region.

For example in the case of tritium, which have one of the lowest end-point energies available in nature ($E_0 = 18.6$ keV), assuming a neutrino mass equal to 5 eV, the fraction of useful events calculated by means of equation 2.11 corresponds to only 1.5×10^{-9}: this gives an idea of the difficulty of such investigation.

Furthermore other factors do interfere with the evaluation of the neutrino mass from the final part of the Kurie plot. First of all the finite energy resolution of the detector produces a distortion of the Kurie plot in an opposite way with respect to the effect of a finite neutrino mass: for this reason a correct evaluation of the detector response function, which includes the energy resolution but which does not coincides with it, is necessary. As a second point one must take into consideration that the atom or molecule containing the decaying nucleus can be left in an excited state: as a consequence the energy available during the decay is reduced by an amount equal to the excited level itself. Even this effect produces a dangerous distortion in the final part of the Kurie plot. The two above mentioned topics will be treated in details later, since they assume different roles depending on the considered technique.

The third problem one must take into consideration during the analysis of the final part of the Kurie plot deals with the presence of background induced by cosmic rays and environmenal radioactivity, which may affect the neutrino mass determination due to the low beta counting rate in the interesting region. It is possible to show that an uncertainty δB in the radioactive background evaluation modifies the spectrum according to:

$$N_\beta(Z, E_\beta, 0) \simeq p_\beta E_\beta (E_\beta - E_0)^2 \left(1 + \frac{\delta B}{p_\beta E_\beta (E_\beta - E_0) F(Z, E_\beta) S(E_\beta)}\right) F(Z, E_\beta) S(E_\beta) \tag{2.12}$$

thus simulating a negative $m_{\nu_e}^2$ equal to $-2\delta B/(p_\beta E_\beta F S)$. The background rate B and the corresponding uncertainty δB are expressed in counts per time and energy unity.

2.2.2 Measurements with electrostatic spectrometers

Since the Sixties of the last century many experiments were performed for the determination of the neutrino mass using tritium beta decays and magnetic or electrostatic spectrometers. This approach allows to select of only the useful fraction of emitted electrons by means of the effect of a proper magnetic field. The leading technique from the nineties on has become then the one based on electrostatic spectrometers with adiabatic magnetic collimation: in this case the electrons are collimated by means of a magnetic field with a characteristic space profile and selected by an electrostatic potential barrier. The characteristic which mainly differentiates these devices from bolometric detectors is that the source is *external* to the detector. For this reason tritium is the best candidate isotope to be used, thanks to its relatively short half life (12.3 years) which allows to produce high specific activity sources. Furthermore its end-point energy is one of the lowest available in nature. Tritium beta decay:

$$^3H \longrightarrow {}^3He + e^- + \overline{\nu}_e \tag{2.13}$$

is an allowed transition, thus posing no problems for the analytical determination of the electron neutrino energy spectrum.

All the above mentioned characteristics contribute in defining the main advantages and drawbacks of the electrostatic spectrometers in the context of the search for neutrino mass, which can be summarized as follows:

- the fact that it is possible to select only the useful fraction of emitted electrons (with energies close to the end-point region) allows to concentrate the analysis on the relevant part of the Kurie plot, without disturbancies coming from the lower energy electrons: therefore a very high statistics can be accumulated in the ingeresting interval (in contrast to calorimeters for which the pile-up can be one of the main problems to deal with, as discussed in 2.2.3);

- a very high energy resolution can be achieved, of order 1 eV for next generation experiments;

- the fact that the source is external to the detector induces a chain of inconvenient effects: it is necessary to deconvolve the response function of the instrument in order to correctly trace back the pure shape of the electron energy distribution, as below discussed;

- even the effect connected to the role of excited final states is linked to the fact that the source does not correspond to the detector and is one of the points which mainly distinguishes spectrometers from calorimeters.

The experimentally observed beta decay spectrum in the case of spectrometers can be written as:

$$N_{\beta}^{exp}(E) \propto (1+\alpha(E-E_0))S(E)(R\otimes E_L \otimes N_{\beta}(E)) \tag{2.14}$$

where $N_{\beta}^{exp}(E)$ corresponds to the spectrum described by 2.9 and as for the other terms:

- R accounts for the energy resolution which can be determined experimentally by means of a monoenergetic source or through a numerical evaluation: in both cases a systematics is introduced;
- E_L describes the self-absorption in the source, which modifies the energy of the emitted electrons;
- the term $(1+\alpha(E-E_0))$ is present when the source is deposited on a solid substrate and accounts for the effect of electrons emitted towards the support and then reflected backwards into the spectrometer;
- $S(E)$ corresponds to the energy dependent acceptance of the spectrometer, which can be computed analitically.

Two experiments based on electrostatic spectrometers have been carried out in recent years leading to the most sensitive results in the field: the Mainz and Troitsk experiments, which put the neutrino mass limit, obtained within the context of direct searches, down to approximately 2.5 eV [32–34]. At the same time they offered the opportunity to investigate the presence of uneccounted sources of systematics, since some factors, other then those above itemized, did appear after data taking, which were not predicted *a priori*.

The next generation experiment KATRIN is forseen to reduce the neutrino mass limit by another factor of 10 if built successfully [35].

2.2.3 The calorimetric approach

An ideal calorimetric experiment, in which the source is imbedded in the detector, allows to measure the neutrino energy in the form of a missing energy. This is possible since the emitted neutrino is the only form of energy which escapes to detection. In fact even the energy spent for the excitation of atomic or molecular levels is measured through the de-excitation of these states, provided their lifetime being negligible with respect to the detector time response.

The main advantages of calorimeters over spectrometers, which deals with the fact that the source does correspond with the detector, can be summarized as follows:

- there are no problems of self-absorption;
- there is no possibility of backscattering from the detector;
- there is no possibility of reflection on the source substrate;
- even the energy stored in excited states is measured.

All the above mentioned items would represent an added contribution to the systematic uncertainty in the determination of the detector response in the case of an external source, as already pointed out for the case of spectrometers.

The main drawback of calorimeters deals with the fact that the whole beta spectrum is acquired. This forces to keep a low counting rate in order to evoid distortions of the final part of the Kurie plot due to pulse pile-up, with a consequent limitation of the statistics which can be accumulated. This effect is produced by decays which occur within a time interval so short that they can not be resolved by the detector. Therefore a certain fraction of detected events is actually the sum of two or more single events. In particular there will be an amount of pile-up events contributing to the counting rate in the region close to the end-point, thus contaminating the spectral shape. The pile-up effect is even more dangerous in the case of calorimeters, which are intrinsecally slow, in particular if the thermal sensor is a semiconductor thermistor.

Given the above considerations the ideal candidate isotope for the developement of calorimetric detectors for the direct search of neutrino mass is ^{187}Re. A calorimetric study of rhenium beta decay spectrum, with the aim of measuring the neutrino mass, was at first proposed by S. Vitale [36]. ^{187}Re transition energy is 2.47 keV, the lowest known, and its half lifetime is 43.2 Gy. The ^{187}Re beta decay:

$$^{187}Re(5/2^{+})\longrightarrow {}^{187}Os(1/2^{-})+e^{-}+\overline{\nu}_{e} \tag{2.15}$$

is a unique first forbidden transition; therefore the nuclear matrix element is computable, even if not as straight forward as in the case of ^{3}H. The natural isotopic abundance of ^{187}Re (62.8%) allows the fabrication of useful sources with no need of isotopic separation. Furthermore the beta decay rate in natural rhenium is of order $\sim$ 1 Bq/mg, which is ideally suited for the fabrication of calorimetric detectors, as later described.

The optimum parameters which allow to obtain the best performances for a calorimetric rhenium detector can be evaluated by taking into consideration the most important limiting factor in the developement of the considered experiments: the pile-up. Assuming a Poissonian time distribution, the fraction of events suffering with not-identified pile-up is given by:

$$P(\Delta t < \tau_R) = 1 - e^{A\tau_R} \tag{2.16}$$

where τ_R is the pulse-pair resolving time of the detector, which is linked to the rise time, A is the source activity and Δt is the time separation between two events. The consequent beta spectrum is given by the convolution product:

$$N'_\beta(Z,E) = N_\beta(Z,E) + 1 - e^{A\tau_R} \int_0^{E_0} N_\beta(Z,E')N_\beta(Z,E-E')dE' \tag{2.17}$$

The counting rate due to pile-up in the interval δE below the end-point energy is given by:

$$A_{pp}(m_{\nu_e},\Delta E) = A(1-e^{A\tau_R}) \int_{E_0-\Delta E}^{E_0} dE \int_0^{E_0} dE' N_\beta(Z,E')N_\beta(Z,E-E') \tag{2.18}$$

The ratio between spurious events and pure single beta decays in the energy interval ΔE is approximately:

$$\frac{A_{pp}(0,\Delta E)}{A(0,\Delta E)} \simeq 0.25 \frac{\tau_R A E_0^2}{\Delta E^2} \tag{2.19}$$

Imposing this ratio be less than 10%, considering an energy resolution of 10 eV and with $\tau_R \sim 100$ μs, the source decay rate must be less than 0.2 Bq, a value which ideally fit with typical microcalorimeter dimensions and natural rhenium abundance.

An approximate expression for the statistical sensitivity of calorimetric neutrino mass experiments can be evaluated in a simplified approach, in order to illustrate how the characteristics of the detector (energy resolution and rise time *in primis*) and the other factors involved (the measurement time, the source activity and so on) can affect the experimental results. In order to evaluate the effect of a finite neutrino mass m_ν below the end point energy and to rule out such a mass from the Kurie plot distorsion, the experiment must be sensitive to the number of pure beta counts expected in the interesting interval δE in the final part of the spectrum. The fraction of useful events in this region is given by:

$$F_{(\Delta E)}(m_\nu) = \int_{E_0-\Delta E}^{E_0} N_\beta(E, m_\nu)dE \simeq F_{(\Delta E)}(0)\left(1 - \frac{3m_\nu^2}{2\Delta E^2}\right) \tag{2.20}$$

where

$$F_{(\Delta E)}(0) \simeq 2A\left(\frac{\Delta E}{E_0}\right)^3 \tag{2.21}$$

The distorsion effect due to the presence of a finite neutrino mass must be detected in presence of external background and undetected pile-up events: in a first approximation the former of the two contributions can be neglected and the pile-up spectrum can be evaluated by assuming a constant pulse-pair resolving time τ_R, of order of the detector rise time. In this approximation events which occur with a time separation greater than τ_R are detected as being doubles, while those with a lower time separation are accounted as singles. The coincidence rate is than $\tau_R A^2$ and the fraction $F_{\Delta E}^{pp}$ of these events falling within the region ΔE below E_0 is given by:

$$F_{\Delta E}^{pp} \simeq \tau_R A^2 \int_{E_0-\Delta E}^{E_0} N_\beta(E, 0) \otimes N_\beta(E, 0)dE \simeq \frac{9}{5}\tau_R A^2 \frac{\Delta E}{E_0} \tag{2.22}$$

The signal-to-background ratio in the considered energy region ΔE can be evaluated as follows:

$$\frac{signal}{background} = \frac{|F_{\Delta E}(m_\nu) - F_{\Delta E}(0)|t_M}{\sqrt{F_{\Delta E}(0)t_M + F_{\Delta E}^{pp}t_M}} \tag{2.23}$$

where t_M is the measurement time. In order to get a 90% confidence limit the signal-to-backrgound ratio must be ~ 1.7. The effect of the various parameters contained in expression 2.23 can be evaluated considering two limiting situations, in which the square root factor is dominated by one of the two terms.

The pile-up can be considered as negligible when the following condition is valid:

$$\tau_R A << \frac{10}{9}\frac{\Delta E^2}{E_0^2} \tag{2.24}$$

In this situation the 90% confidence limit sensitivity is given by:

$$\Sigma_{90}(m_\nu) \simeq 0.89\sqrt[4]{\frac{E_0^3 \Delta E}{A t_M}} \tag{2.25}$$

Since it is not possible to consider ΔE being less than about $2\Delta E_{FWHM}$, it is evident that an improvement in the energy resolution will inhance the sensitivity. Nevertheless the statistics At_M results to be the most important factor in this approximation.

By diminishing ΔE and increasing A the second limiting situation, where the pile-up dominates, can be reached. In such condition the 90% confidence limit sensitivity can be written as:

$$\Sigma_{90}(m_\nu) \simeq 0.87 \sqrt[4]{\frac{E_0^5 \tau_R}{t_M \Delta E}} \tag{2.26}$$

In the above expression the role of A is substituted by $1/\tau_R$. As a consequence the sensitivity can be improved by acting on the pulse-pair resolving time and once more on the energy resolution.

2.2.4 The MARE experiment & the role of semiconductor thermistors

As already pointed out ^{187}Re is the ideal candidate isotope for the developement of a calorimetric experiment aiming at measuring directly the neutrino mass. Thanks to its transition energy (the lowest available in nature) the fraction of useful events close to the end-point is ~ 350 times higher than the one achievable with tritium. In the previous section other important characteristics of ^{187}Re were discussed, which make this beta decaying nuclide the best choice for the fabrication of microcalirimeters, using rhenium compounds as absorbers.

In particular, ^{187}Re natural abundance and lifetime, combined to the typical microcalorimeter optimum size, allow to produce 1 mg-scale devices with typical activities of order 1 Bq, which match the requests of microcalorimeter technology (including the limitation of the pile-up effect).

Two rhenium compounds are actually available as absorbers: natural metallic rhenium, which contains $\sim 63\%$ of the isotope 187 and dielectric rhenium compounds. Metallic rhenium behave as a superconductor below the critical temperature $T_c = 1.69$ K, where the heat capacity decreases exponentially as already stated in section 2.1.1. Furthermore the expected activity for a 1 mg device is ~ 1 Bq. On the other hand calculations from the BCS theory predict that a large part of the energy released inside the absorber can be trapped in quasi particle states which live for many seconds at temperatures below 100 mK. Despite these theorical considerations, experimental results show that superconductive rhenium performs well as absorber in cryogenic detectors, though no exhaustive explanation has been given for this discrepancy.

The possibility to use a proper dielectric rhenium compound provides a complementary solution, which allows to overcome potential problems with incomplete energy conversion to phonons in superconductive rhenium. Among the several available compounds, silver perrhenate ($AgReO_4$) appears to be the best suitable choice, due to its physical, thermal, practical properties. In this case the possible target for the single crystal mass, resulting from a trade-off between rate, pile-up and energy resolution, is around 250 μg, corresponding to a decay rate of 0.1 Bq.

The considerations so far exposed over microcalorimeter technological requests draw to the conclusion that the most powerful method for the developement of a calorimetric experiment, aiming at the direct search for neutrino mass, will be the realization of a great number of small devices, in order to reach the required statistics while preserving good performances.

At present two italian collaborations have been working on Rhenium based microcalorimeters since the ninties of the previous century: the Genova group, within the project MANU [37] and the Milano-Como group, within the project MIBETA [38].

The MANU group realized a single device based on metallic rhenium (absorber mass 1.6 mg) coupled to a Ge-NTD thermistor (see sections 3.1.1 and 3.1.3). The experiment was run for 0.5 years with energy resolution $\Delta E_{FWHM} = 96$ eV and rise time $\tau_r \sim 200$ μs, resulting in an upper limit on neutrino mass of 19 eV (90% c.l.).

The MIBETA group developed a 10 detecors array which allowed to reach an upper limit on neutrino mass of 15 eV (90% c.l.) with a total live time of 0.6 years. The single elements of the array were based on $AgReO_4$ absorber (0.25 mg) coupled to Si-implanted thermistors (see section 3.1.3), with an average $\Delta E_{FWHM} = 28.5$ eV and $\tau_r = 490$ μs. The MIBETA collaboration has developed a specific know-how on Si-implanted thermistor technologies, which guarantee high reproducibility and possibility of micromachining, useful characteristics for the future expansion of the experiment (see section 3.1.2 and 3.1.3).

These two experiences allowed to set an upper limit on neutrino mass of about 15 eV (90% c.l.). The results obtained by the MANU and MIBETA collaborations have proved the potential of the calorimetric technique applied to the direct search for neutrino mass. Though the achieved sensitivity is about one order of magnitude worse than the present limit set by spectrometric experiments, devoted Montecarlo simulations show the possibility to reach an upper limit of about 2 eV, through present technology detectors, by simply optimizing the single channel performances and scaling up to hundreds devices. This will allow to scrutinize the Mainz and Troitzk experiments, by means of a completely indipendent methodology.

In order to join strenght the MANU and MIBETA collaborations converged giving origin to the next generation experiment MARE [39], with the final goal to reach the same sensitivity as the KATRIN experiment on neutrino mass. In order to pursue this aim the project will be developed in two phases, the first one aiming to increase the sensitivity of about one order of magnitude and serving as a test experience, the second one actually pursuing the main goal.

The first phase, MARE-I, will serve also to improve the understanding about all possible systematic uncertainties and to gather further experience on Rhenium based microcalorimeters. In addition it is crucial to sustain a parallel R&D activity for the second phase of the experiment, aiming at reaching a 0.2 eV sensitivity. This purpose can be attained only by the employment of new technology detectors accompanied by a brute-force expansion of the MARE-I experiment. During the first phase of the project, two experiments, directly discending from the two precursors, will be run separately. A big effort is already put in the optimization of the detector performances, in order to match the requirements in terms of energy resolution and time response. In this context the characterization of the devices being used as thermal sensors and their coupling to the absorbers are of remarkable importance, since they substantially affect the detector performances.

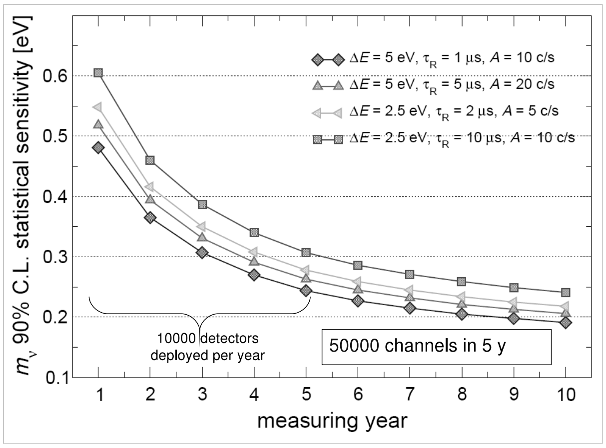

Figure 2.3: Temporal evolution of the sensitivity to neutrino mass in MARE-II, considering four different experimental configurations. The triplet of numbers that labels each curve indicates respectively ΔE_{FWHM} [eV], τ_r [μs] and single channel activity [Bq]

The MANU2 experiment will develop an array of about 300 detection channels, each one composed of a metallic Rhenium single crystal coupled to a TES as thermal sensor [39]. The MIBETA2 experiment will take advantage of the knowledge accumulated during the previous experience as well as of the collaboration with other research groups operating in the field, in order to develop a $\sim$300 detector array based on $AgReO_4$ single crystals (0.45 mg) coupled to Si-implanted thermistors. It is in the context of the MIBETA2 experiment that one of the main subjects of this thesis is developed, dealing with the characterization of Si-implanted thermistors produced by the MEMS group at ITC-irst (see chapter 5). The whole array structure of 300 channels will be deployed through a gradual approach and a total statistics of the order of 10^{10} events will be accumulated during 4 years of running. Two different approaches can be used to evaluate the sensitivity: taking into account the present detector performances, Montecarlo simulations show that a mass limit of about 4 eV can be attained (conservative approach), while considering the possibility that further improvements will lead to $\Delta E_{FWHM} = 15$ eV and $\tau_r \sim 50$ μs, a sensitivity of about 2.5 eV can be reached.

The kick-off of the second phase of the MARE project will be subordinated to the final results of the previous phase. Montecarlo simulations show that in order to reach a 0.2 eV sensitivity substantial improvements over MARE-I are required: a total statistics of about 10^{14} events must be accumulated and an energy resolution of ~ 5 eV and rise time τ_r of ~ 10 μs are needed. New microdetector thecnologies, allowing to match these requirements and suitable to the developement of a 10000 channels array, are already under study and a further R&D activity will be performed in parallel with the MARE-I experiment. MARE-II will consist of a series of modular 10000 pixel arrays, which can be relatively easily installed in any available refrigerator. Figure 2.3 shows the temporal evolution of the sensitivity to neutrino mass, taking into account 4 different experimental configurations and the deployment of one single array per year up to 5 arrays. The final set-up will consist of a spatially distributed array of 50000 elements, 5 years after the data taking start-up, allowing to fulfil the the main purpose of the MARE project.

2.3 DOUBLE BETA DECAY EXPERIMENTS

Neutrinoless double beta decay experiments represent the only available method able to fully disentangle the neutrino mass nature, since they only work if neutrino is a Majorana particle. Next generation double beta decay experiments will be very sensitive, being potentially able to explore at least the inverted hierarchy region, in contrast with beta decay searches, which, given the present available technologies, are in the game in the case of a quasi degenerate neutrino mass scale.

The quantity determined in double beta decay mesurements is the *effective electron neutrino mass*, given by:

$$|\langle m_{\nu_e}\rangle| = \left|\sum_{i=1}^{3} |U_{ei}|^2 m_i e^{i\alpha_i}\right| \tag{2.27}$$

were the sum is over all mass eigenvalues m_i, U_{ei} are the mixing matrix coefficients and α_i are the Majorana phases. The above quantity differs from the value inferred from direct searches, which is given by:

$$m_{\nu_e} = \sqrt{\sum_{i=1}^{3} |U_{ei}|^2 m_i^2} \tag{2.28}$$

In the Standard Model double beta decay processes are allowed transitions, though extremely rare, in which a nucleus (A,Z) transforms into its isobar $(A,Z\pm 2)$ emitting two electrons (positrons) and their corresponding antineutrinos (neutrinos):

$$\begin{aligned} (A,Z) &\longrightarrow (A,Z+2)+2e^- + 2\overline{\nu}_e \\ (A,Z) &\longrightarrow (A,Z-2)+2e^+ + 2\nu_e \end{aligned} \tag{2.29}$$

Double beta decay has been observed for a dozen nuclides and the average half lifetime is of order $10^{18} - 10^{25}$ years. The most direct way to determine if neutrinos are Majorana particles is to explore, in potential nuclear double beta emitters, if they decay without emitting neutrinos, thus violating lepton number conservation. For this non-standard $0\nu\beta\beta$ process to heppen a Majorana neutrino mass is required [40, 41].

Neutrinoless double beta decay is a three body transition, in which the two emitted electrons share the whole available energy Q, in contrast to standard double beta decay process. Experimentally one is looking for a sharp peak in the acquired spectrum, in a position corresponding to the transition energy Q, in the case the whole energy acquired by the two electrons is measured (figure 2.4). On the other hand standard double beta decay spectrum appears as a continuum, since the available energy is even shared by the two neutrinos.

The effective Majorana electron neutrino mass $|\langle m_{\nu_e}\rangle|$ can be inferred from the evaluation of the decay rate of the process, if observed:

$$[T^{0\nu}_{1/2}]^{-1} = \frac{|\langle m_{\nu_e}\rangle|^{2}{}^{2}}{m_e} G^{0\nu}|M^{0\nu}|^2 \tag{2.30}$$

where $[T^{0\nu}_{1/2}]$ is the half lifetime, $G^{0\nu}$ is the two-body phase-space term and $|M^{0\nu}|^2$ is the $0\nu\beta\beta$ nuclear matrix element. On the other hand, if $0\nu\beta\beta$ is not observed, and as

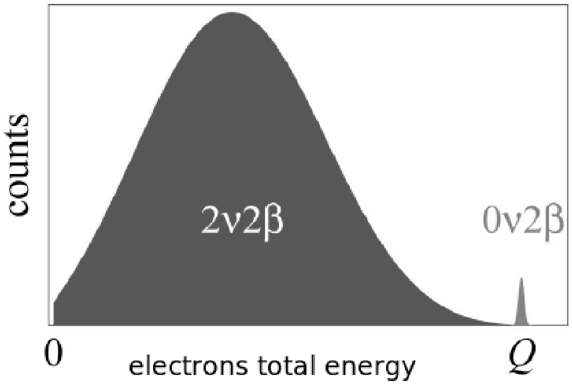

Figure 2.4: Energy spectrum in the case of 2νββ and 0νββ decays

a consequence only a lower limit on the half life is obtained, an upper bound on $|\langle m_{\nu_e} \rangle|$ can be extrapolated.

The experimental investigation of 0νββ decay requires a large amount of potential nuclear double beta emitters in a very low-background environment. Furthermore the detector should have a sharp energy resolution or match other stringent requirements, according to the experimental methodology being used.

The calorimetric technique is a very powerful method for the investigation on 0νββ, due to the high available energy resolution and almost 100% efficiency, when the ββ source corresponds to the detector.

2.3.1 The CUORE experiment & techniques for bolometers stabilization

The CUORE experiment [42] will be devoted to the search for 0νββ decay of the isotope ^{130}Te, one of the known double beta emitters. The set-up will consist of a 988 array of bolometric detectors, each one based on a TeO_2 crystal as absorber, with mass 750 g and 5 cm side, coupled to a Ge-NTD thermistor (see 3.1.1). The bolometers will be arranged in a cubic compact structure, operated at about 10 mK in a low radioactivity dilution refrigerator which will be installed in the Gran Sasso Underground Laboratory (LNGS). Depending on the nuclear matrix element considered in the calculation as well as the detector performances and background configuration, CUORE expected sensitivity on $|\langle m_{\nu_e} \rangle|$ ranges between 27 and 72 meV, for a 5 years data taking.

One of the critical points to deal with when operating an experiment of this kind, for periods of the order of some years, is the necessity to mantain the detectors in conditions as much stable as possible. Unfortunately the complicated cryogenic set-up required for operating the detectors at low temperatures shows intrinsic instabilities, like temperature fluctuations, which can spoil the detector energy resolution, since the small but unavoidable changes in the temperature of the heat sink produce correlated flactuations in the gain.

It is useful to astimate at which level the cryogenic apparatus instabilities can affect the detector performance. This can be roughly done by assuming a naive thermal model, in which the detector is considered as a single element, weakly connected to the heat bath. In this picture the bolometer operation temperature $T_b \sim 10$ mK and the heat sink temperature $T_s \sim 5$ mK are connected by the following relation:

$$P = \frac{g}{\alpha+1}(T_b^{\alpha+1} - T_0^{\alpha+1}) \tag{2.31}$$

where P is the power injected into the detector, due to operating bias current as well as spurious effects like vibrations in the system, and $G = gT^{\alpha}$ is the temperature dependence of the thermal conductance of the detector to the bath. From the above expression one may deduce the relation which links relative variations of the bath temperature to relative variations of the detector operation temperature:

$$\frac{dT_b}{T_b} = \frac{dT_0}{T_0}\left(\frac{T_0}{T_b}\right)^{\alpha+1} \tag{2.32}$$

Fortunately such connection is attenuated by detector/bath thermal decoupling. Since the operation voltage across the bolometer V_b is equal to IR, where I is the applied constant bias current and R the thermistor resistence (see 3.2.1), and since R has a strong temperature dependence, the operation voltage then changes with the bath temperature fluctuations. As a consequence pulse amplitudes also change, thus originating a broadening of the energy resolution.

It is therefore mandatory to develop a specific method for the detector response stabilization, based on mechanisms acting directly on the detector followed by an off-line pulse amplitude correction. The obvious approach to stabilize the response consists in the use of a *pulser*, able to deliver periodically to the detector a fixed and well known amount of energy, generating a pulse as similar as possible to the searched signals. After registering the pulse amplitudes V_p given by the pulser, together with their arrival times, it is possible to reconstruct the detector response as a function of time $V_p(t)$. This function can be used to correct off-line the pulse amplitudes of "real" events, given their arrival times are known. However this method is not the most relyable one, since $V_p(t)$ is sampled with a relatively low rate in order to evoid problems with excessive dead time. As a consequence fast variations in the response are not registered and hence pulses occuring in these time interval are erroneously corrected.

A much more powerful approach to solve the response correction is discussed in the following. The amplitudes V_p can be correlated to the baseline level V_c preceding immediately the pulse developement, which can be inferred for each pulse by registering a baseline segment for a given time interval ($\sim$ 100 ms) before the signal onset. V_c is linked to the operation voltage V_b across the detector by the relationship:

$$V_c = \Gamma(-V_b + V_{off}) \tag{2.33}$$

where Γ is the total gain and V_{off} is the offset added to null the DC output. As a consequence a fast decrease of V_b, corresponding to a pulse, produces a fast increase of the baseline level, while a decrease of the operation temperature leads to an increase of V_b and a decrease of V_c. In the absence of any temperature fluctuation the ratio between V_p and V_c would be a constant, since the signals produced by the pulser correspond to a constant delivered energy. In real cases, where instabilities are present, a plot of V_p versus V_c will be a monolitically decreasing function, which can be in most cases approximated with a negative slope straight line (see figure 2.5).

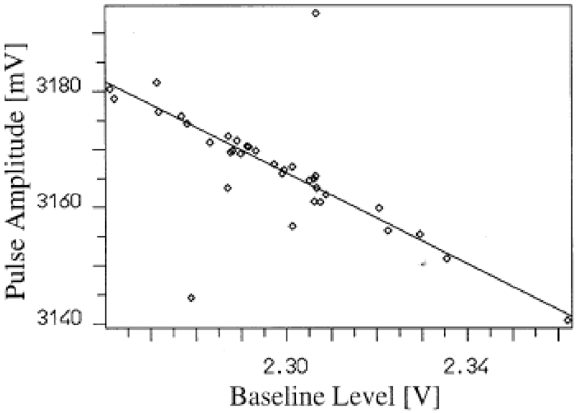

Figure 2.5: Example of pulse amplitude as a function of baseline level

Once the function $V_p(V_c)$ is known the following multiplicative factor can be constructed:

$$\alpha(V_c) \equiv \frac{V_{P_{ref}}}{V_p(V_c)} \tag{2.34}$$

with $V_{P_{ref}} \equiv V_p(V_{c_{ref}})$, where $V_{c_{ref}}$ is a reference baseline. The factor $\alpha(V_c)$ can be used, during the off-line analysis, in order to take back to the reference level $V_{P_{ref}}$ an amplitude V_p corresponding to a pulse acquired when the baseline value was V_c. The same procedure can be used to correct the amplitude of each pulse acquired, given the corresponding baseline level is known.

It has been observed that during long run measurements even the function $V_p(V_c)$ can change: therefore it is not sufficient to determine this relation by means of a single calibration, but it is necessary to continuously monitor the baseline dipendance of the pulse amplitude. The final results of this stabilization mechanism consist in re-compacting peaks in the energy spectrum that had been completely washed off or broadened by the system instabilities (as shown in figure 2.6).

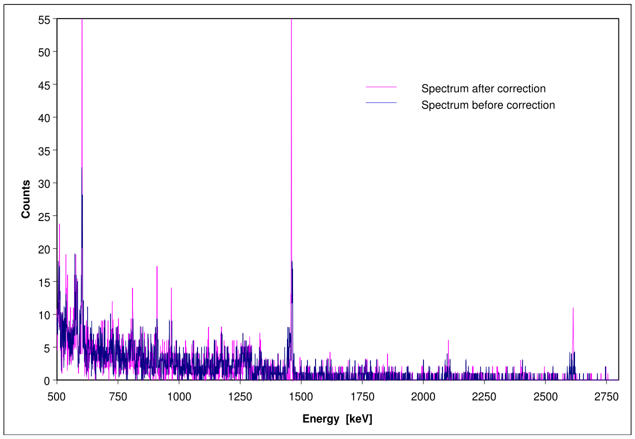

Figure 2.6: Example of energy spectrum acquired by a TeO_2 bolometer before correction ($\Delta E_{FWHM}(2615) = 30$ keV) and after correction ($\Delta E_{FWHM}(2615) = 6$ keV)

Various methods are available to accomplish the tasks of the energy pulser, since the energy injection can occur in the form of:

- energetic partcle absorptions;
- Joule pulses delivered by a proper heating element thermally coupled to the crystal;
- light pulses transmitted through optical fibers.

A discussion and comparison among the above mentioned methods is reported in [43]. In the following a short description is given, while pointing out that the technique based on the use of heating elements has been chosen for the developement of CUORE detectors.

The third method above itemized, based on light pulses, is the most complicated one and the least suitable for the forseen multiplication of channels: so it will not be taken into consideration. Partcle-based stabilization has the advantage that the detector response to the pulser is almost identical to the response to the events of interest. However there are many disadvantages:

- if a gamma source is used, a fully contained gamma event of energy a few MeV (as required for a $\beta\beta$ decay experiment) is accompanied by a large number of lower energy events, thus increasing excessively the background rate;
- if an α source is used the difficulty will be its fabrication, since it must be very thin in order to avoid excessive straggling;
- the calibration rate is limited by the Poissonian time distribution of naturally occuring decays;
- the off-line identification of calibration pulses is simply based on their amplitude, since they are not flagged by any characteristics.

The final choice for CUORE was drawn by taking into account the above arguments and the many advantages offered by the solution based in the use of an heating element as energy pulser. The main advantages of this method deals with the possibility to completely control the calibration mechanisms:

- the produced pulses are equally spaced in time;
- the rate and amplitudes could be easily tuned to the experimental requirements;
- the pulser signals are easily identified by software.

The heating element used to deliver the Joule pulses consists in a resistive device, called *heater*, which must satisfy some requirements as discussed in section 3.2.2. As already announced in section 1.5, heaters can be fabricated from a heavily doped semiconductor material, whose characteristics match the main requests for the developement of stabilizing heating elements. Heaters are operated as follows: square voltage pulses (of order 1 V) are injected into the devices with a programmable pulse generator, tuning the amplitude and the time width (of order 1 ms) in order to develop a few

MeV thermal energy in the pulser. As a consequence it is of basic importance that the resistance of the heating device be almost indipendent of temperature and bias voltage applied, so that the same amount of Joul power is injected into the detector during the whole measurement and each pulse produced by the heater can be rifered to a well defined delivered signal.

A further task which may be accomplished by heaters is the determination of the *optimum point* in the $I - V_b$ curve, corresponding to the maximum detector response. In fact, as better decsribed in section 3.2.1, the thermal sensor coupled to the absorbing element of the bolometer is polarized with a constant current I while operated, thus producing a voltage difference V_b across the thermistor. A set of points in the $I - V_b$ curve can be experimentally determined, by biasing the thermistor with different current values and measuring the voltage V_b. Also the condition corresponding to the maximum amplitude of the voltage pulses can be experimentally evaluated by analysing the detector response to the heater pulses for different bias values: the *optimum point* corresponds to the bias for which the heater pulse is maximum (figure 2.7). Even in this case the heater must accomplish some requirements, which almost fully correspond to those accounted in the characterization of heaters as stabilizing elements.

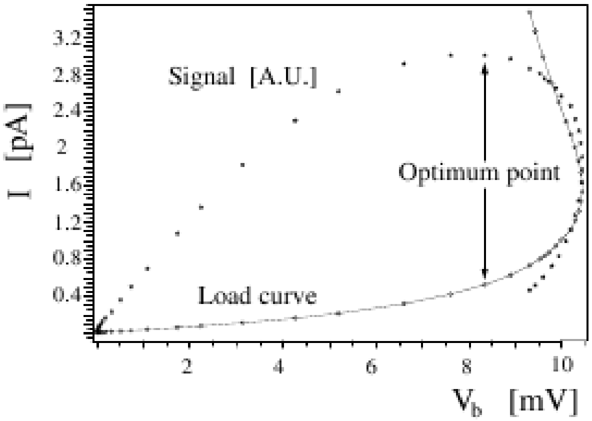

Figure 2.7: Bolometer response as a function of the voltage across the detector V_b superimposed to the detector load curve (I versus V_b) for the evaluation of the *optimum point*

CHAPTER 3

REALIZATION AND LOW TEMPERATURE CHARACTERIZATION OF DOPED SEMICONDUCTOR DEVICES

Semiconductor thermistors operating in VRH regime have been used in thermal detectors of all kinds for more than fifty years. They found at first application for the development of bolometers for infrared astronomy, even before the basic physical principles of the conduction mechanisms taking place in such devices were understood. In the first half of the eighties the application of this technique to microcalorimeters for the detection of low energy photons was proposed in the USA [44]. In the meantime the development of massive thermal detectors (mass of order 1 kg) was started in Europe, finding soon application in the search for rare events, such as double beta decay [45]. Nowadays a lot of research collaborations are involved in the development of thermal detectors to be used in nuclear and subnuclear experiments.

At the same time a better understanding of the behaviour of semiconductor thermistors operating in VRH regime is gradually being obtained, thanks to the modellization of the empirical results coming from performance investigations.

In this frame there is also an increased interest in studying the behaviour of heavily doped semiconductor devices, as they can find an important role for the stabilization of thermal detectors, as discussed in section 2.3.1.

Today, thanks to the improvements in fabrication technologies, semiconductor devices can be designed and produced with predictable characteristics, though a theory of their mode of operation is not yet complete and many aspects involved in their optimization are based on empirical considerations.

In this chapter the basic production processes of semiconductor devices, as well as the main steps towards their characterization and performance optimization, are described, in view of their integration in thermal detectors. For this purpose a specific study is required, capable to disentangle all the problems and factors which could interfer with the realization of good performance bolometers.

The fabrication of semiconductor devices consists of two main steps: production and characterization in conditions very close to the final operating ones, which, in the special case of calorimetric detectors, involves the investigation of their low temperature behaviours.

3.1 PRODUCTION PROCESSES

The first generations of semiconductors could not be properly termed "doped": they were simply very impure, since there was no means to controll the amount of impurities. During the 1950s the success of the new technology of semiconductor electronics provided an increment in experimental studies over pure crystals and a powerful stimulus to the development of the semiconductor theory. However it was during the 1960s that the interest towards impure semiconductors increased, when it became clear that a major role in the fabrication of most semiconductor devices is played precisely by the impurities.

Nowadays the semiconductor electronics industry have solved many of the material fabrication issues. Semiconductors, germanium and silicon in particular, are readily available with more than adequate purity, as well as with controlled impurity levels, at least to a certain extent.

A host of techniques and machines are available which simplify the production processes and large arrays of devices, with integrated electrical interconnections and essentially noise-free, can be quite easily fabricated.

For the purpose of this thesis the specific case of silicon and germanium will be considered in the following sections. The principal doping techniques, used for the production of thermal sensors and heating devices, will be shortly presented, with particular care to the production processes actually involved in the realization of the devices studied in this work.

3.1.1 General description of doping techniques

Controlled impurity levels can be introduced in semiconductors through the following methods:

- addition of elements in the melt during crystal growth;
- addition of elements during epitaxial deposition of a semiconductor film;
- solid-state diffusion of elements from the surface or a suitable interface;
- neutron transmutation doping (NTD);
- ion implantation of elements into the semiconductor at relatively low temperature.

In the early three methods impurity introduction is achieved at a temperature close to or above the melting point of the semiconductor. In the last two methods it may be achieved at any temperature provided the semiconductor is in its solid state, even at or below room temperature, thus avoiding problems associated with high temperature diffusion processes. A uniform doping of the semiconductor results from all techniques, except for solid-state diffusion and ion implantation, which produce an impurity concentration gradient with the highest concentration at the source in the case of diffusion, and within the semiconductor in the case of ion implantation.

The best results in the field of calorimetry have been obtained with neutron transmutation doping and ion implantation. In particular the devices studied in this work (both semiconductor thermistors and heaters) have been realized by ion implantation into silicon.

Neutron transmutation doping is best applied to germanium, expecially for the production of semiconductor thermistors. NTD Ge thermometers are obtained by irradiating an ultrapure Ge crystal by means of a flux of thermal neutrons. Ge nuclei capture the neutrons and form various radioactive Ge isotopes, which subsequentely decay into As, Se and Ga. The natural abundances of two stable Ge isotopes and the corresponding neutron cross sections conspire to produce gallium-doped (p-type) material that is 32% compensated with arsenic. The random distribution of Ge isotopes in the lattice and the moderate neutron cross section, which makes the neutron flux uniform throughout large blocks of Ge, allows the fabrication of a large number of very uniform NTD thermometers.

Ion implantation consists in the introduction of dopants by bombarding the semiconductor with accelerated ions. The penetration depth is a function of the original kinetic energy of the projectile and the properties of the target. It is possible to obtain a quite uniform impurity distribution by implanting ions with energies in a suitable range. Ion bombardment of a crystalline semiconductor results in a crystal damage which degrades the semiconductor characteristics and which can be partially removed in a high-temperature annealing treatment. Ion implantation, which is particularly suited for silicon doping, will be treated in the next section, since it coincides with the technique adopted for the fabrication of the devices studied in this thesis.

3.1.2 Ion implantation

Before entering into the details of the production process, it may be useful to point out that silicon doped devices are usually produced in form of *wafers*, each one composed by a fixed amount of single elements: this layout is useful to speed up the fabrication of a large number of devices with almost the same implant structure. Furthermore one must consider that when ion implantaion is used for the fabrication of thermistors or heating devices, with the aim of developing bolometric detectors, the procedure must even forsee the production of electrical contacts. The details of the ion implantation process used in the specific case of the silicon devices treated in this thesis will be described in the devoted chapters (chapter 4 and 5). In the following the main steps of silicon ion implantation standard technique are summarized.

Oxide and nitride growth SiO_2 or optionally Si_3N_4 are used to protect and partially mask the future devices during the production process. In particular Si_3N_4, being resistent to hydrogen fluoride (HF), is useful when it is necessary to remove the SiO_2 mask only from one side of the devices by using this acid. A Si_3N_4 deposition is obtained by means of LPCVD (Low Pressure Chemical Vapour Deposition) at 795 °C, while the SiO_2 growth can be obtained through the techniques below described.

- Thermal oxidation in dry (O_2 or O_2/N_2) or wet (O_2/H_2) atmosphere at temperatures between 900 and 1000 °C. For each μm of grown SiO_2 a correspondent amount of 0.44 μm of silicon is removed from the substrate. The growth rate in the case of wet atmosphere is larger than in the case of dry atmosphere at a given temperature. When the silicon substrate has been previously doped, the oxide growth may change the dopants concentration at the surface.
- LPCVD at 718 °C in a TEOS atmosphere: this technique is used to increase the thickness of the previously deposited oxides.

- LPCVD at low temperature (LTO): it is used if an Al deposition (for the production of the electrical contacts) is already present, since the previous techniques can not be used in this case, due to the high operating temperatures. However the oxide mechanical and elettrical properties are worse than those obtained with LPCVD-TEOS.

During the whole process the SiO_2 deposition is performed in various occasions and with different aims:

- *Mask oxide* (also called *field oxide*) with thickness of order $500 - 1000$ nm, used as a mask during the definition of the areas to be implanted: in fact a mask of thickness 1 μm is sufficient to completely stop 270 keV B ions and 700 keV P ions; sometimes upon the oxide mask a *photoresist* mask is even deposited.
- *Sacrificial* or *screen oxide* with thickness a few nanometers, grown upon the area to be implanted, in order to protect it in the event of spurious low energy ions emitted by the implanting machine.
- *Thermal oxide* produced during the annealing process in an oxiding atmosphere: its presence influences the dopants diffusion and helps removing crystal damages; furthermore it helps to eliminate the silicon surface layer, which may contain a big amount of impurities.
- *Protective oxide* with thickness about 500 nm, used to cover the devices at the end of the process, in order to protect them from humidity and abrasion.

All the oxides are produced by putting the wafers into devoted quartz ovens and all the important parameters (temperature, time, gas flow) are remotely controlled.

Photolithography This technique allows to define the geometry of the devices: actually a photosensitive varnish called *photoresist* is deposited over the whole wafer, which is then exposed to UV rays only in the areas where the photoresist must be removed. Such areas are subsequently developed and the desired mask is obtained. During the following steps of the process the photoresist can also be used to protect the areas which must not be *etched*.

Metallization This process allows to produce the contact *pads* providing the electrical contacts. It is obtained by the deposition of an Al:Si film, which provides a good adhesion to silicon and becomes superconductive below about 1.1 K (thus introducing a neglegible contribution to the device heat capacity). Such film is deposited upon specific regions of the devices, intentionally highly doped for this purpose.

Etching In order to remove SiO_2 and Si_3N_4 masks chemical etching is used, by means of aqueous solutions (*wet-etch*), also adopted to clean the surfaces before the metal deposition. On the other hand *dry-etching* by means of gas-halogen plasma is used to remove the Al:Si film, or to eliminate the photoresist (*ashing*).

Implantation Uniform dopants concentrations can be obtained by multiple implantations using ions accelerated to the desidered kinetic energy by means of an electric field. The single implant density profile is approximately Gaussian and uniformity can be achieved by a suited combination of subsequent implantations. Thanks to the available techniques it is possible to realize implants with resistivity values whose spread above the whole wafer is whitin 0.5%. Furthermore it is necessary to produce highly doped areas for the realization of the ohmic contacts: this can be done either by diffusion or by ion implantation with suited doses.

Annealing During the implantation process crystal damages may occur. Furthermore there may be a certain fraction of implanted ions not located in substitutional sites, which thus need to be "activated". A thermal treatement (*annealing*) is then necessary in order to provide a redistribution of the dopants through the lattice and to remove the damages. Such thermal treatements are performed at temperatures between 900 and 1000 °C, in an atmosphere which is changed during the process and may be inert (N_2), dry (O_2) or wet (O_2/H_2). The treatement can last from 30 minutes to 2 hours. The high temperatures involved may cause an excessive diffusion of the implanted ions, thus deforming the concentration profile. This is even more dangerous at the beginning of the process, when the crystal appears to be much more damaged. For this reason it may be useful to mantain a higher temperature, thus allowing a faster recombination of the crystal structure. The atmosphere plays an important role too: in the case of dry or wet atmosphere (in presence of oxides) the implant activation is influenced by the stress over the silicon surface due to the oxide growth. The choice of the parameters to be used during the annealing process (temperature, time and atmosphere) plays a major role in determining the final results: for this reason the influence of such parameters must be studied in depth in each specific case.

All the parameters and the procedures must be optimized for each considered case and in particular the implant doses must be suited to accomplish the specific tasks of each device to be produced. For example, in the case of semiconductor thermistors, the implant doses will depend upon the desired T_0 value. The same implantation procedure above described is adopted also when compensation is necessary. In the end the sensitive portion of ion implanted devices usually consist in a kind of resistive meander, whose geometry can be adapted in order to vary the resistance, once the resistivity ρ has been fixed by the doping and compensation levels. One can then act upon the resistance value by varying the *square number* n, corresponding to the ratio between the length l and the width w of the doped region, since the resistance is given by:

$$R = \frac{l}{w}\frac{\rho}{s} = n\frac{\rho}{s} \tag{3.1}$$

where s is the thickness of the doped area.

3.1.3 The case of semiconductor thermistors

As previously announced NTD and ion implantation are the two techniques mainly used for the fabrication of semiconductor thermistors operating in VRH regime. Since in the specific case of this work microcalorimeters using ion implanted silicon thermistors are considered, a comparison between the two methods will be useful to understand the reasons which led to this choice [46].

The NTD process has two main advantages over other techniques: it results in a very homogeneous doping over large portions of material, as already explained, and the doping process may be controlled by changing the integrated flux of neutrons, making it possible to predict the temperature dependence of resistivity. However the penetrating power of the neutrons, which helps in providing uniform doping, also means that it is difficult to dope only selected areas in a crystal, by using masks technologies. For this reason the thermometers must be cut to the optimum dimentions and then individually attached to the detectors. This is not a drawback when the elements are very large as for example in the CUORE project [42].

In the case of silicon it is possible to dope by transmutation, but very large neutron doses are required. Ion implantation is a better suited method in this case and doping by ion beams with kinetic energies from tens of keV to a few MeV is a well-developed technique in the semiconductor electronic industry. Penetration depths of up to $\sim 1\ \mu$m are obtained in this way, with an approximately Gaussian density profile with depth. Uniform densities can be obtained by superimposing implants with several different energies and doses in order to produce a flat-top profile, or by implanting a single dose of each ion beam into a thin silicon piece, masked with SiO_2, and then treating it at high temperature to allow complete diffusion throughout the sample.

The great advantage of this doping method consists in the possibility to apply standard photolithographic techniques to mask silicon pieces. Furthermore the use of micromachining allows the simultaneous fabrication of a large number of thermistors, with almost arbitrarily small dimensions and fully integrated electrical connections. These features are particularly useful in the case of microcalorimeters and allow the production of a large number of homogeneous arrays, with no need of further addition of electrical links, which may act as noise sources. Furthermore silicon also has excellent mechanical and thermal properties, which make it possible to fabricate integrated structures to be used, for instance, for thermal isolation of the individual detector elements or for the realization of integrated heaters, as in the cases presented in chapter 5.

One drawback which has been noticed in ion implanted thermistors is a lack of reproducibility not well understood. Doses and energies can be measured with the adquate precision, but the repeatability from one production run to another is generally so poor that usually a series of wafers with slightly different doses are implanted, and then the one with the resistivity closer to the desired one is chosen. On the other end uniformity across a single wafer is generally good. The above mentioned arguments, dealing with repeatability and uniformity, will be considered again in chapters 4 and 5.

3.2 METHODS OF LOW TEMPERATURE CHARACTERIZATION

For the realization of highly reproducible and good performance calorimeters, each single element should be optimized through a careful characterization in conditions very close to the operating ones. In the following the parameters of interest and the methods to be used for this study will be discussed.

Since the good performance of microcalorimeters is strongly linked to the thermistor behaviours, great care will be given to the methods of characterization of the latter, in the context of a general investigation about the former. In the devoted section (3.2.1) the discussion will focus over ion implanted silicon thermistors, since these devices represent one of the subjects of this thesis.

A discussion about the characterization of heaters will follow (3.2.2). Finally a short description of the cryogenic apparatus available for such investigations will be exposed (3.2.3). The details of the set-up actually used for the purpose of this thesis, will be presented in the devoted chapters (4 and 5).

3.2.1 Microcalorimeters

The role of thermal sensors in microcalorimeters (and bolometers in general) is to convert thermal signals into electrical signals. This is achieved by applying a bias voltage V_{bias} to the circuit in which the thermistor is inserted, thus leading a constant current I to pass through the sensor (figure 3.1). The risultant voltage measured across the thermistor V_b is linked to the lattice temperature thanks to the strong dependence of resistivity over temperature.

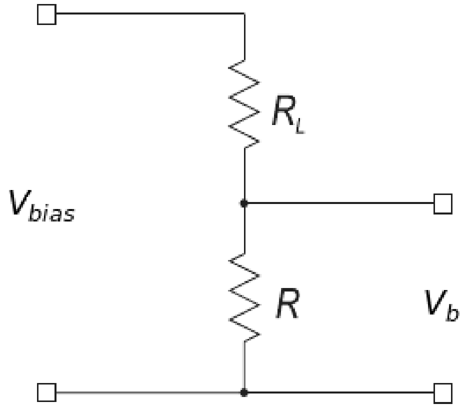

Figure 3.1: Circuit used for the polarization of the thermistors; R_L represents the load resistance of the circuit, through which the polarizing constant current is generated

In the case of a microcalorimeter, in order to precisely measure the temperature signal produced by an energy release into the absorber, a good thermal contact between the latteces of the absorbing element and the thermal sensor must be guaranteed. Due to the resistive nature of this kind of sensors a Joule power is dissipated into the microcalorimeter when it is operated. This modifies the behaviours of the detector in such a manner that it is useful, at first, to study separately the thermal sensor performance, through a *static characterization*.

Static characterization

The static characterization of the thermistor consists in studying its properties in a condition in which it is not operated as a detector. In such a situation it is possible to study the relationship between the static properties and the lattice temperature T_p of the substrate in which the sensor is implanted. For this purpose the thermal coupling between the lattice and the heat sink at temperature T_s, represented by the cryogenic set-up housing the sensor during the measurements, is maximised. This allows to assume T_p as coincident with T_s with no regard to the dissipated power.

VRH conduction regime takes place at temperatures below a few kelvin where the resistivity has an exponential dependence from the lattice temperature. Equation 1.14 takes in this case the form:

$$\rho(T_p) = \rho_0 \exp\left(\frac{T_0}{T_p}\right)^{\gamma} \tag{3.2}$$

where ρ_0, T_0 and γ are the parameters to be experimentally determined. As discussed in section 1.4 the value of the exponent γ can correspond to $1/2$ or $1/4$, depending on the conduction regime involved. The typical operating temperatures of microcalorimeters are of order 100 mK, where the conduction mechanism should be interested by coulombian interactions, thus leading to $\gamma = 1/2$. Nevertheless the Mott behaviour may take place also at lower temperatures then those predicted by theoretical models.

The parameters ρ_0 and T_0 depend on the doping level as shown in equation 1.20. It is possible then to vary the temperature dependence of resistivity by varying the concentration of the majority impurity N or the degree of compensation K. The exact relation between T_0 and N actually depends on the implant process and must be experimentally determined, in order to allow a certain predictability of the thermistor characteristics. An empirical relatioship between ρ_0 and T_0 has also been observed which can be experimentally determined [47, 48].

In view of the characterization of thermal sensors it is useful to introduce the logaritmic sensitivity, defined as:

$$A(T_p) \equiv \frac{d \log R}{d \log T_p} = \frac{T_p dR}{R dT_p} \tag{3.3}$$

which then becomes, by using equation 3.2:

$$A(T_p) = -\gamma \left(\frac{T_0}{T_p}\right)^{\gamma} < 0 \tag{3.4}$$

The voltage pulse ΔV_b produced by a temperature change ΔT_p in the lattice, can then be written as:

$$\frac{\Delta V_b}{\Delta T_p} = \frac{AV_b}{T_p} \tag{3.5}$$

It is then clear how the sensitivity and consequently the signal amplitude are strongly linked to the static parameters of the thermistor.

In section 1.4.2 deviations from VRH theory were discussed, due to non-ohmic behaviours. In presence of such effects the thermistor resistivity may depend on the bias voltage applied, though the lattice temperature remains constant: thus equation 3.2 is valid only for very low values of applied voltage. For this reason a static characterization does not simply consist in the measurement of resistivity at different temperatures. The experimental procedure is more complex and must include the deviations from linearity forseen by theoretical models.

Non-ohmic behaviours can be studied thanks to the characteristic *load curves* of the sensor taken at different temperatures T_p. A *load curve* represents the relationship which links the constant bias current I flowing through the sensor and the voltage V_b measured across the thermistor. A typical load curve is represented in figure 3.2

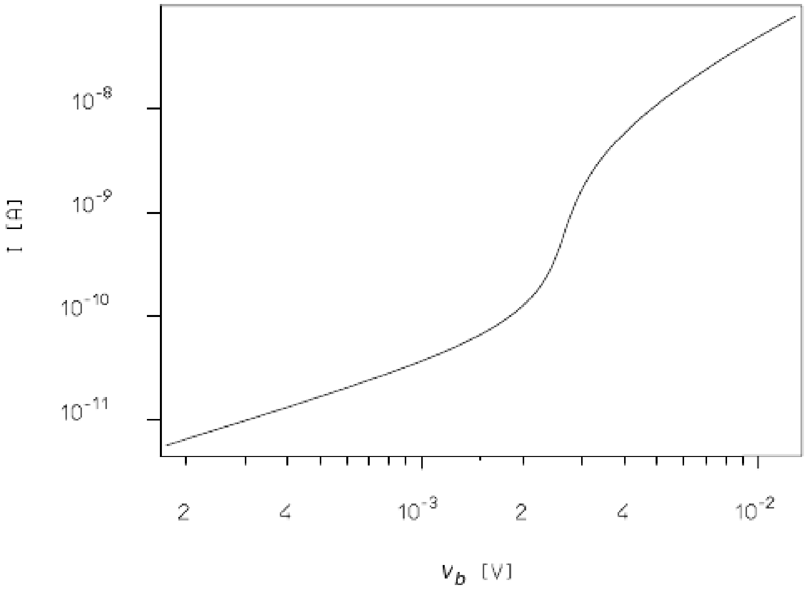

Figure 3.2: Typical load curve in a microcalorimeter simulated using equation 3.22

Each load curve, set up by a given number of $I - V_b$ pairs, corresponds to a certain lattice temperature T_p, assumed equivalent to the heat sink temperature T_s.

As described in section 1.4.2 two models have been proposed in order to explain the non-ohmic behaviours. In the case of thermistors with T_0 lower then 10 K and operating at about 100 mK, as in the case of the devices studied in this work, the effects due to the hot electron model should be predominant over the field effects. This meets with the results obtained in this work and presented in chapter 5.

In the hot electron model the electrons are supposed to form a subsystem with its own temperature T_e, different from the lattice temperature. The sensor resistivity is then linked to T_e (equation 1.22): this produces a lower sensitivity in the evaluation of T_p. Furthermore the value of the sensitivity is reduced as T_e is diminished or as the dissipated power over the electrons P_e is increased. From equations 1.22, 1.23 and 3.3 one gets:

$$A(T_e, P_e) \equiv \frac{d \log R(T_e)}{d \log T_p(T_e)} = -\gamma \left(\frac{T_0}{T_e} \right)^{\gamma} \left(1 - \frac{P_e}{g_{ep} T_e^{\alpha}} \right) \tag{3.6}$$

By assuming the validity of the hot electron model, from the study of the load curves the parameters g_{ep} and α in equation 1.23 can be determined. In a simplified approach the values of R_0, T_0 and γ can be evaluated from the interpolation of the resistivity values obtained in the limit of very low applied voltage, where linearity is still valid.

$P_e - T_e$ pairs can be obtained from $I - V_b$ pairs by using the following equations:

$$P_e = I V_b \tag{3.7}$$

and

$$T_e = T_0 \left[log \left(\frac{V_b / I}{R_0} \right) \right]^{\frac{1}{\gamma}} \tag{3.8}$$

G_{ep} curves as a function of temperature can be extrapolated by numerical differentiation from $P_e - T_e$ curves. Since, in addition to the power due to polarization, the Joule power dissipated into the electrons can be due also to electromagnetic interferences, it could be a problem to find the right values of T_0, R_0 and γ, as in such a situation T_e and T_p do not correspond, also in the absence of any applied bias voltage. This problem can be solved by applying a procedure consisting in the simultaneous interpolation of all the load curves taken at different lattice temperatures and the presence of a Joul power due to electromagnetic interferences can be introduced by adding the term P_e^{bckg}:

$$\begin{cases} R(T_e) = R_0 exp\left[(T_0/T_e)^{\gamma}\right] \\ P_e^{tot} = P_e + P_e^{bckg} = g_{ep}(T_e^{\alpha} - T_p^{\alpha}) \end{cases} \tag{3.9}$$

where $R(T_e) = V_b/I$, $P_e = V_b I$ and R_0, T_0, γ, g_{ep}, α, P_e^{bckg} are free parameters. In presence of the background power term P_e^{bckg} equation 3.6 for the evaluation of the sensitivity is modified by substituting P_e with P_e^{tot}. In [19] it was observed that g_{ep} and α are both determined by the value of T_0 and all the properties of the thermistor can then be predicted on the basis of the doping level. In particular by increasing T_0 the value of $G_{ep}(T_e)$ decreases.

Dynamic characterization

The silicon substrate in which the thermistor is implanted can in principle play the role of the energy absorber in a microcalorimeter: in such case one speaks about a *monolitic microcalorimeter*. Though it results to be completely inadequate in view of the realization of high resolution devices, due to the problems of thermalization in silicon as later discussed, the monolitic configuration is useful in order to get some major informations about the dynamic behaviour of the thermistors.

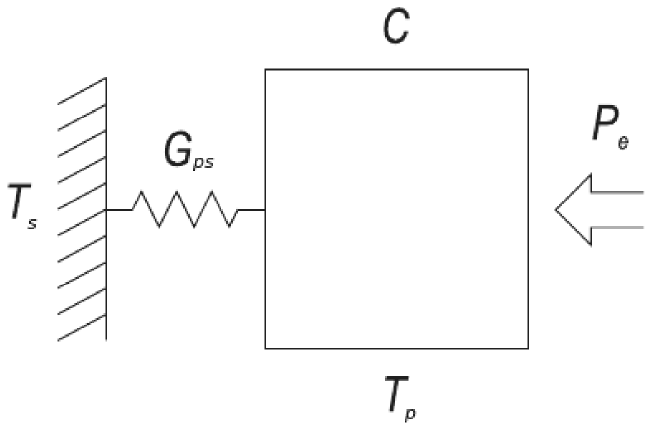

Figure 3.3: Thermal model for a monolitic microcalorimeter

A finite thermal conductance G_{ps} between the heat sink at temperature T_s and the lattice at temperature T_p must be introduced, which allows the production of an observable temperature variation in the latter as a consequence of a finite energy deposition (figure 3.3). In an equilibrium condition, the electrical power P_e dissipated into the thermistor due to the polarization togheter with the background power P^{bckg}, keep the lattice temperature T_p above T_s, following the relation:

$$P_e + P^{bckg} = \frac{V_b^2}{R(T_p)} + P^{bckg} = \int_{T_s}^{T_p} G_{ps}(T')dT' \tag{3.10}$$

The temperature dipendence of G_{ps} can be described by means of the following power law:

$$G_{ps}(T) = \beta g_{ps} T^{\beta-1} \tag{3.11}$$

where β equals 2 in the case of metals and 4 in the case of insulators. When T_p and T_s are very close to each other, equation 3.10 becomes:

$$P_e + P^{bckg} = \frac{V_b^2}{R(T_p)} + P^{bckg} = g_{ps}(T_p^{\beta} - T_s^{\beta}) \simeq G_{ps}(T_p)(T_p - T_s) \tag{3.12}$$

In order to give a complete description of a microcalorimeter it is useful again to study its load curve at the temperature T_s:

$$\begin{cases} V_b/I = R(T_p) = R_0 exp\left[(T_0/T_p)^{\gamma}\right] \\ V_b I + P^{bckg} = g_{ps}(T_p^{\beta} - T_s^{\beta}) \end{cases} \tag{3.13}$$

In this case the difference between T_e and T_p is considered as negligible. Once the characteristic $R(T_p)$ curve, P^{bckg} and the conductance to the heat sink are well known, the *working point* of the microcalorimeter is determined only by its temperature T_p or by the $I - V_b$ pair. If the values T_0, R_0 and γ have been previously determined through the static characterization, the parameters g_{ps}, β, P^{bckg} can be deduced through the interpolation of the load curve 3.13.

When the deposition of an energy ΔE in the lattice breaks the thermodinamic equilibrium, the temporal evolution of the lattice temperature T_p can be described by the equation:

$$C(T_p(t))\frac{dT_p(t)}{dt} + g_{ps}(T_p(t)^{\beta} - T_p^{0\beta}) = P(t) \tag{3.14}$$

where $C(T_p)$ is the total heat capacity of the microcalorimeter, T_p^0 is the solution of equation 3.12 and $P(t)$ is given by:

$$P(t) = \Delta E \delta(t) \tag{3.15}$$

in the case of an instantaneous energy deposition.

Though it is not possible to solve analytically equation 3.14, the heat capacity can be considered as constant and the thermal conductance can be described according to equation 3.12, by assuming the temperature variations being sufficiently small. With these approximations equation 3.14 can be written as:

$$C\frac{dT_p(t)}{dt} + G_{ps}(T_p(t) - T_p^0) = P(t) \tag{3.16}$$

with $T_p^0 = T_p(t=0)$, $C = C(T_p^0)$ and $G_{ps} = G_{ps}(T_p^0)$, values corrisponding to the equilibrium condition (i.e. no energy deposition into the system). The solution of equation 3.16 in the case of an instantaneous energy deposition is then:

$$T_p(t) = \frac{\Delta E}{C}\theta(t)e^{-t/\tau} + T_p^0 \tag{3.17}$$

where $\tau = C/G_{ps}$ represents the characteristic time constant of the system and $\theta(t)$ is the step function ($\theta(t) = 0$ for $t < 0$ and $\theta(t) = 1$ for $t \geq 0$). By using equation 3.5 the voltage pulse produced by an instantaneous energy deposition ΔE can be written as:

$$\frac{\Delta V_b(t)}{\Delta E} = \frac{AV_b}{T_pC}e^{-t/\tau} \tag{3.18}$$

Actually the energy deposition in a microcalorimeter can not always be considered as instantaneous, due to the time required for the complete thermalization of the primary (non thermal) high energy phonons, which in some cases can be of the order of the time constant τ. In such a case an exponential decay of non thermal phonons can be assumed:

$$P(t) = \frac{\Delta E}{\tau_{dec}}e^{-t/\tau_{dec}} \tag{3.19}$$

The solution of equation 3.16 by introducing equation 3.19 is then a combination of two exponentials.

In equation 3.16 the term $P_e = I^2R(T_p)$ due to polarization is considered as constant. This is not completely true, since the resistance decreases as T_p increases, as a consequence of the energy release: this effect is known as the *electrothermal feedback* and contributes a faster return to the equilibrium conditions. It can be shown that, given the above considerations, the response of the microcalorimeter in the frequency domain becomes:

$$S_e(\omega) = \frac{\Delta V}{P(\omega)} = \frac{(Z/R)-1}{2I}\frac{1}{1+j\omega\tau_e} = \frac{AV}{T_p G_{ps}}\frac{1}{1+j\omega\tau_e} = S(0)\frac{1}{1+j\omega\tau_e} \tag{3.20}$$

where R is the resistance of the thermistor, I the constant polarization current, $Z = dV/dI$ the dynamic impedance and the time constant τ_e is given by:

$$\tau_e = \tau\frac{|Z|+R}{2R} < \tau \tag{3.21}$$

All the above considerations are described in details in [49–51], where also the arguments considered in the following are discussed.

As already pointed out non-homic behaviours must be taken into account in order to fully describe how a microcalorimeter actually works. For this reason, also in the simple case of the monolitic detector above described, a further element must be considered, which in the HEM model is represented by the electron subsystem (figure 3.4).

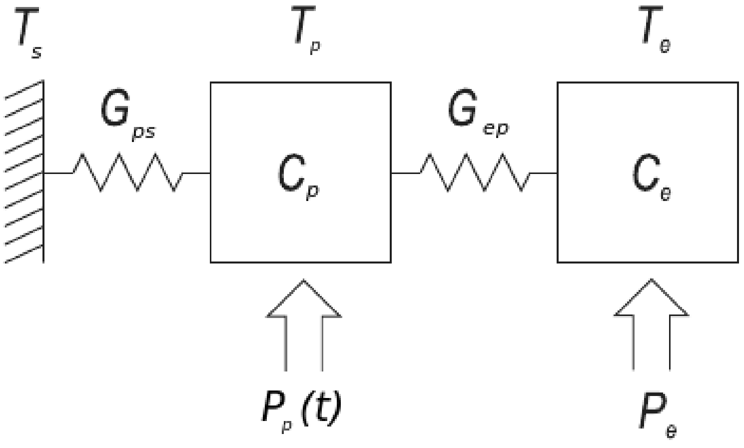

Figure 3.4: Thermal model for a monolitic microcalorimeter considering the HEM

In this configuration only the lattice subsystem is in thermal contact with the heat sink through the conductance G_{ps}. It can then be assumed that a complete thermalization of the primary (non thermal) high energy phonons produced into the absorber takes place before they reach the thermometer. The thermodinamic state of the detector is characterized by the temperatures T_e and T_p of the two subsystems and the load curve assumes the following form:

$$\begin{cases} V_b/I = R(T_e) \\ V_b I + P_e^{bckg} = g_{ep}(T_e^{\alpha} - T_p^{\alpha}) \\ V_b I + P_p^{bckg} + P_e^{bckg} = g_{ps}(T_p^{\beta} - T_s^{\beta}) \end{cases} \tag{3.22}$$

where P_p^{bckg} and P_e^{bckg} are respectively the background power dissipated into the electron and phonon subsystems. Once the values of T_0, R_0, γ, g_{ep} and α have been determined through the static characterization, the values of the parameters g_{ps}, β, P_e^{bckg} and P_p^{bckg} can be deduced through the interpolation of the load curve 3.22.

By means of the same approximations used to derive equation 3.16, the temporal evolution of the temperature signal induced into the microcalorimeter by an energy deposition into the lattice system can be described by the following expression:

$$\begin{cases} C_e \frac{dT_e(t)}{dt} + G_{ep}(T_e - T_p) = 0 \\ C_p \frac{dT_p(t)}{dt} + G_{ps}(T_p - T_p^0) + G_{ep}(T_p - T_e) = P_p(t) \end{cases} \tag{3.23}$$

with $T_p(t=0) = T_p^0$ and $T_e(t=0) = T_e^0$ corresponding to the equilibrium conditions which can be evaluated from equation 3.22; C_e and C_p represent respectively the heat capacity of the electron and the lattice subsystems. In the case of an instantaneous energy deposition of the form 3.15, the general solution of the system 3.23 is given by:

$$T_e(t) = \frac{\Delta E\, G_{ep}}{C_p C_e (1/\tau_2 - 1/\tau_1)} (e^{-t/\tau_1} - e^{-t/\tau_2}) + T_e^0 \tag{3.24}$$

where

$$\tau_1, \tau_2 = 2\left[\frac{G_{ep} + G_{ps}}{C_p} + \frac{G_{ep}}{C_e} \pm \sqrt{\left(\frac{G_{ep} + G_{ps}}{C_p} + \frac{G_{ep}}{C_e}\right)^2 - 4\frac{G_{ep} G_{ps}}{C_p C_e}}\right]^{-1} \tag{3.25}$$

Actually it is convenient to realize microcalorimeters in which $G_{ps} \ll G_{ep}$, otherwise the power dissipated by an impinging particle would flow more rapidly to the heat sink, with fateful consequences on the thermistor performances. With this approximation and in the resulting hypotesis $\tau_2 \ll \tau_1$, equation 3.24 becomes:

$$T_e(t) \simeq \frac{\Delta E}{C_e + C_p} (e^{-t/\tau_1} - e^{-t/\tau_2}) + T_e^0 \tag{3.26}$$

with

$$\tau_1 \simeq \frac{C_e + C_p}{G_{ps}} \tag{3.27}$$

$$\tau_2 \simeq \frac{C_e C_p}{(C_e + C_p) G_{ep}} \tag{3.28}$$

Equation 3.26 was derived by applying the approximation given in 3.12: as a consequence the reduction of sensitivity contained in equation 3.6 is not considered here and must be introduced by hand. Furthermore again the electrothermal feedback is not taken into account. Since the above described effects actually contribute in the formation of real pulses, the resulting signal shape usually differs from the theoretical one given by 3.26, being better described by a somehow different combination of exponential terms.

As previously announced the silicon substrate is completely inadequate in view of the realization of high resolution devices: in fact the signal pulses produced by irradiating the monolitic detector with a monoenergetic source show an excessive broadening of their FWHM. This effect can be ascribed to the presence of metastable states in silicon in which part of the energy deposited is trapped for a time interval longer than the time of formation of the signal. As a consequence the trapped energy is actually lost and the resulting statistical fluctuation of the mesured energy produces a degradation in the energy resolution. A further effect responsible for the broadening of the resolution is due to the partial thermalization of the primary high energy phonons directly into the thermistor: as a consequence the detector response may depend on the interaction point.

In order to get rid of all the above mentioned effects, it is necessary to couple the silicon thermistor to an appropriate absorber. The thermal coupling G_{ap} between the thermistor lattice and the absorber lattice should allow the complete thermalization of the deposited energy into the latter. Figure 3.5 shows the thermal model in the case of such a detector. In a thermodinamic equilibrium condition the following equations describe the considered system:

$$\begin{cases} V_b/I = R(T_e) \\ V_b I + P_e^{bckg} = g_{ep}(T_e^{\alpha} - T_p^{\alpha}) \\ P_a^{bckg} = g_{ap}(T_a^{\eta} - T_p^{\eta}) \\ V_b I + P_p^{bckg} + P_e^{bckg} = g_{ps}(T_p^{\beta} - T_s^{\beta}) \end{cases} \tag{3.29}$$

where T_a is the absorber temperature, P_a^{bckg} is the background power in the absorber and the thermal conductance is assumed to follow the power law 3.11 with parameters

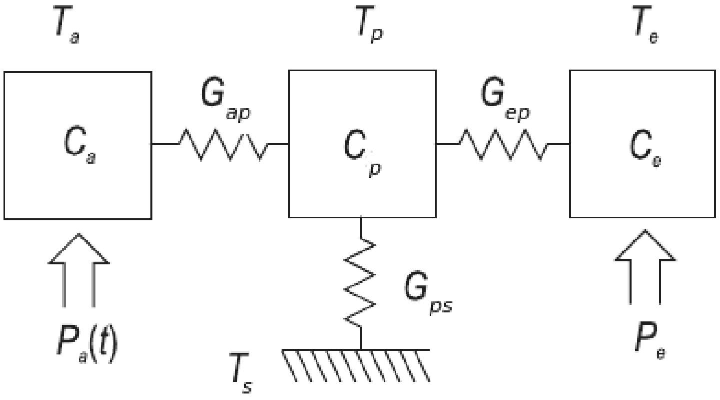

Figure 3.5: Thermal model for a microcalorimeter with absorber considering the HEM

g_{ap} and η. In this case it is not possible to determine all the parameters from a simple static analysis. The following group of equations discribes the dynamic of the considered system in the case of low temperature variations:

$$\begin{cases} C_e\frac{dT_e(t)}{dt}+G_{ep}(T_e-T_p)=0 \\ C_p\frac{dT_p(t)}{dt}+G_{ps}(T_p-T_p^0)+G_{ap}(T_p-T_a)+G_{ep}(T_p-T_e)=0 \\ C_a\frac{dT_a(t)}{dt}+G_{ap}(T_a-T_p)=P_a(t) \end{cases} \tag{3.30}$$

with C_a the heat capacity of the absorber. In the usual approximation of an instantaneous energy deposition, the solution of 3.30 is given by a combination of three exponential functions. Nevertheless, in order to allow the evaluation of all the parameters involved, it is useful to make some approximations. In particular, since in real microcalorimeters the condition $G_{ps} \ll G_{ap} \ll G_{ep}$ is usually valid, the electron-phonon decoupling in the thermistor can be neglected. As a consequence the thermal pulse can be described by the following expression:

$$T_e(t) \simeq \frac{\Delta E}{C_a+C}(e^{-t/\tau_1}-e^{-t/\tau_2})+T_e^0 \tag{3.31}$$

provided that $\tau_2 \ll \tau_1$. Here C represents the total thermistor heat capacity and the time constants are given by:

$$\tau_1 \simeq \frac{C_a+C}{G_{ps}} \tag{3.32}$$

$$\tau_2 \simeq \frac{C_a C}{(C_a + C) G_{ap}} \tag{3.33}$$

The condition $\tau_2 \ll \tau_1$ is verified when $C \ll C_a$. In this case the two time constants can be further approximated by $\tau_1 \simeq C/G_{ap}$ and $\tau_2 \simeq C_a/G_{ps}$.

Optimization

Once the static and dynamic characterizations of microcalorimeters are completed and all the required informations have been collected, a study of the so called *signal to noise ratio* (S/N) must be carried out in order to actually optimize the detector performances. The signal to noise ratio corresponds to the ratio between the maximum pulse amplitude and the noise of the system (calculated as the root mean square noise). This ratio must be maximized in order to achieve the optimum operational conditions of the detectors.

The first step consists in the maximization of the signal, since a complete understanding of the noise of the system is very complex and requires a deep analysis, being linked to many different parameters.

The practical realization of the microcalorimeter must be performed in a way which allows to obtain the best possible performances. Furthermore all the characteristics of the thermistor (studied by means of the static and dynamic characterization) must converge for the fulfilment of such a goal. In particular, as already pointed out, it is usually convinient to realize microcalorimeters in a configuration which assures the condition $G_{ps} \ll G_{ap} \ll G_{ep}$ is met. Given the previous assumption and thanks to some more expedients it is possible to produce a situation in which the time constant $\tau = C/G_{ps}$ dominates over all the other ones described in the previous section. In such a conditin the thermal signal can be approximated by equation 3.17 and the status of the detector can be descibed by an average temperature value T.

Nevertheless the distinction between the temperature T_e of the electron system and the temperature T must be considered in order to taken into account the effects of the hot electron model. Given the above conditions, the signal amplitude in terms of voltage pulse across the thermistor is given by:

$$\Delta V_b = \frac{\Delta E A(T_e(T), P_e^{tot}) \sqrt{P_e R(T_e(T))}}{T C(T)} \tag{3.34}$$

The parameters contained in equation 3.34 where defined in 3.6, 3.8 and 3.9. The term $C(T)$ represents the heat capacity of the detector and is given by the sum of all the contributing elements:

$$C(T) = C_0 + C_1 T + C_3 T^3 \tag{3.35}$$

where C_0 is a constant coefficient which accounts for the localized electrons in the thermistor; the linear term in T is linked to the delocalized electrons in the thermistor; the cubic term in T represents the contribution of the lattice.

In view of the optimization of the detector performances by means of a maximization of the signal to noise ratio and taking into account equation 3.34, the following considerations arise:

- the heat capacity $C(T)$ must be minimized;
- there exists an optimum value for the dissipated power P_e, since equation 3.34 suggests that P_e should be increased in order to produce an enlarged pulse amplitude but at the same time an excessive P_e induces a reduction of the sensitivity (equation 3.6);
- the background power P^{bckg} must be minimized since it contributes to the reduction of the sensitivity (equation 3.6);
- once G_{ps} is fixed as the lowest of the conductances of the system, the temperature of the detector depends only on the applied power: as a consequence the optimum value of P_e defines a precise point in the $I - V_b$ curve and a temperature T which assures the maximization of ΔV_b (*optimum point*);
- also for the parameter G_{ps} there exists an optimum value, since it should be the lowest of all the conductances of the system, but at the same time it must be high enough to evoid an excessive warming-up of the detector due to polarization;
- equations 3.2 and 3.6 suggest the parameter T_0 should be as high as possible in order to increase the signal amplitude, but in this way the decoupling between the electron and the phonon systems get worse as discussed at the beginning of this section (see paragraph "Static characterization"): as a consequence also for T_0 there exists an optimum value;
- also the geometry of the thermistor can be optimized, avoiding to modify the implant structure (which is linked to T_0): this allows to inhance R_0 ($\Delta V_b \propto \sqrt{R_0}$) according to equation 3.1 and as will be described in section 5.3;
- the volume of the thermistor should be increased in order to inhance G_{ep} (see 1.4.2) taking into consideration the consequent increase of the heat capacity;

- at a first sight also the resistance should be increased, but this could lead to an excess of spurious noise sources, as later discussed.

The considerations exposed in this paragraph are based on equation 3.34 which assumes an instantaneous temperature rise. Nevertheless they will be useful to carry on the optimization procedure in an easy way. On the other hand a model taking into account the dynamic behaviour of the detectors and based on equations 3.23 and 3.30 will be useful for a postponed interpretation of the results (see also [52, 53]).

In order to carry on a complete optimization, all the possible sources of noise should be identified and characterized. Some of these sources are intrinsic, and thus fix an unbreakable limit to the energy resolution of the detector. On the other hand the noise introduced by the polarization circuit and, more in general, by the whole acquisition system, can be reduced to a minimum.

Noise sources

The intrinsic noise in a thermal detector is contributed by two main sources: the characteristic Johnson noise of the thermistor and the thermodinamical noise, due to the stocastic nature of the energy transfer through G_{ps}.

Any resistive element (with resistance R) operating at a temperature T generates a white noise with power spectrum given by:

$$e_R = \sqrt{4k_BRT} \tag{3.36}$$

This represents the Johnson noise across the thermistor. In the special case of a weak thermal link to the heat bath (as it happens in the case of microcalorimeters), the effect of the electrothermal feedback can induce a reduction of the low frequency component of the Johnson noise.

Furthermore, any device with a heat capacity C in contact with a heat sink by means of a thermal conductance G is characterized by a thermodinamic noise, due to the statistical fluctuation of the internal energy U of the system, which is linked to the transport of energy through G. The average internal energy fluctuation is given by:

$$\langle \Delta U^2 \rangle = k_BT^2C \tag{3.37}$$

which, using the relation $\Delta U = C\Delta T$, can be written as:

$$\langle \Delta T^2 \rangle = \frac{k_BT^2}{C} \tag{3.38}$$

The power spectrum of these fluctuations is given by:

$$P(\omega) = \sqrt{4k_B T^2 G} \tag{3.39}$$

It can be shown that these fluctuations produce a noise power spectrum which, in terms of voltage across the thermistor, can be written as:

$$e_{th}(\omega) = P(\omega)S(\omega) \simeq \sqrt{4k_B T^2 G}\frac{S(0)}{1 + j\omega\tau_e} \tag{3.40}$$

According to equations 3.40 and 3.20 the thermodinamic noise and the signal are characterized by the same dependence in the frequency domain. As a consequence the S/N ratio should be inhanced by simply extending the adopted frequency band in the absence of any other source of noise. Actually this is not possible due to the presence of the Johnson noise.

As already pointed out in section 2.1.1 the energy resolution of a microcalorimeter can be very close to the thermodynamical limit, for which an analytical expression can be deduced by taking into account uniquely the intrinsic noise sources ([44,54]). Once the temperature of the heat sink T_s and the characteristic parameters of the thermistor are fixed, the intrinsic limit to the energy resolution is given by:

$$\Delta E_{FWHM} = 2.35\xi\sqrt{k_B T_s^2 C(T_s)} \tag{3.41}$$

where ξ is a numerical coefficient which depends on the logaritmic sensitivity A. The resolution given by equation 3.41 is obtained in practice by applying an optimum bias current to the thermistor, which corresponds to the optimum point in the $I - V_b$ curve (and to an optimum working temperature of the device).

Obviously there are other potentially dengerous sources of noise, external to the device itself, which can induce a worsening of the energy resolution and which must be reduced as more as possible.

3.2.2 Heaters

The role of heaters in bolometric detectors has been already discussed in section 2.3.1. Heaters consist in resistive elements capable to inject calibrated amounts of energy through Joul heating into the detector. Since their main task is linked to the stabilization of detector response, as well as to the determination of the *optimum point* in the $I - V_b$ curve, such devices must satisfy the following requirements, which cover both static and dynamic behaviours:

- their resistance must be reasonably indipendent of temperature and applied voltage in order to inject the same amount of Joul power into the detector during the whole measurement, so that each pulse produced by the heater can be refered to a well defined delivered signal;
- their heat capacity must be negligible with respect to the detector one;
- the heater resistance must be much higher than that of connection wires, in order to behave as the main point of power dissipation, but at the same time must not be so high to require excessive voltage pulses to develop the desidered calibration energy.
- the relaxation time of the heat pulse delivered into the crystal τ_h must be much shorter than all the other typical thermal constants, in order to produce an almost instantaneous energy release;
- the signal formation due to Joul heating must simulate as much as possible a particle interaction in order to assure that the pulse amplitude dipendences on time, baseline level and other operation conditions are the same for the two processes;

Reasonable resistance values in the specific case of CUORE experimental configuration range from ~ 1 kΩ to ~ 10 MΩ. Steady resistances with the required values can be realized by means of heavily doped semiconductors, i.e. semiconductor materials doped well above the MIT (see section 1.5). Furthermore the resistive structure, which usually consists in a long, narrow, thin meander necessary to achieve reasonably high resistances, must be integrated in a small, easy to handle chip and finally thermally connected to the detector.

The heat capacity C_h of the heater is a further crucial parameter, not only for its contribution to the total heat capacity of the detector C_d (the heater mass is actually so small that its heat capacity is dominated by that of the crystal), but rather for the role played in the determination of the thermal coupling time τ_h, which is given by:

$$\tau_h = \frac{C_h C_d}{C_h + C_d} \frac{1}{G_h} \simeq \frac{C_h}{G_h} \tag{3.42}$$

where G_h is the thermal conductance between the heater and the detector and τ_h represents the typical time necessary to achieve thermal equilibrium between the two. The above relation shows that, in order to minimize τ_h, it is necessary to reduce as much as possible the heater heat capacity and maximize the heater-detector thermal conductamce.

The first part of chapter 4 is dedicated to a discussion above the explored solutions for the fabrication of heaters and the early results obtained with their application to stabilization processes in TeO_2 bolometric detectors. The following sections of the same chapter are devoted to describe the fabrication process of the heating devices to be used in the CUORE experiment and to their characterization at low temperatures from a static point of view, being this one of the topics covered by this thesis.

To be specific the required tests, concerning the static behaviour, consist in:

- checking the stability of resistance with temperature variations in conditions close to the operating ones (i.e. close to the working temperature of the considered bolometers);
- check the behaviour of resistance, at the operating temperature, with bias voltage variations;
- check that the resistance values of the realized devices match the requests previously discussed at the working temperature;
- check the homogeneity of resistance values among the fabricated devices, since required for the implementation of the electronic system and the connected software used to operate them.

Given the number of devices necessary for the realization of the CUORE experiment, corresponding to the total number of detectors (~ 1000), the amount of elements which actually must be tested is of order 2000, since unavoidably there will be a certain fraction of elements not matching the requests. Furthermore some of the tested devices will be used during the R&D program and it would be convenient to have an amount of heaters exceeding the indispensable number, in case of any problem during the bolometer assembly.

The above arguments show the difficulties involved in the characterization of heaters, since an enormous amount of time would be required in order to test, with the needed accuracy, the whole number of necessary devices, in particular if the tests should be performed at the bolometers operating temperatures (~ 10 mK). For this reason it would be advantageous to perform the static characterization at higher temperatures, once a statistically significant sample has served to test the dynamic and static behaviour of heaters in conditions very close to the operating ones. This requires that a good correlation between very low (< 1 K) and low (down to ~ 1 K) temperature behaviour must be estabilished by means of previous tests. Furthermore, a study of the homogeneity and distribution of resistance values among the produced devices would be very useful in order to speed up the characterization, as better explaned in section 4.2.1: this is possible thanks to the configuration in which the devices are produced.

As will be discussed in 4.2.1, the analysis of the results obtained during the characterization down to ~ 1 K allowed to extrapolate further useful correlations between room temperature, nitrogen temperature (77 K) and $T \leq 1$ K behaviours. By taking advantage of all these results it is possible to save money and time in the selection of heaters to be used in CUORE.

3.2.3 Cryogenic apparatus

In both cases of thermistors and heaters characterization, it is necessary to work in conditions as close as possible to the operating ones, which means first of all that temperatures of order 1 K or less must be reached. In order to achieve these conditions the devices under test are placed, after a suitable preparation, in a devoted refrigerator (or cryostat).

Cryostats of different kinds and suited for various temperature ranges are presently available and commercialized, though they often need to be adapted to the purpose for which they are intended to be used. Examples of activities devoted to this task, to which a great deal of this thesis has been dedicated, are described in 4.2.1. The present section describes the cryogenic technologies used for the fulfilments of this thesis.

As already pointed out in 3.2.2, though the typical operating temperatures of bolometric detectors are below 1 K, it is sometimes useful to work at higher temperatures (> 1 K) since they are easier to reach. In principle, temperatures as low as 1.2 K can be achieved by using a ^{4}He pumped cryostat. This kind of refrigerator consists in a system composed by a volume devoted to house the devices to be tested, and a liquid He bath. The volume housing the samples must be in good thermal contact with the bath and both should be vacuum insulated from outside, in order to reduce the heat load due to conduction and convection. At see-level pressure the boiling temperature of ^{4}He is 4.2 K. By reducing vapour pressure above the He bath, temperatures down to 1.2 K may be attained, as shown in figure 3.6. Obviously a large amount of He is being consumed during the cooling down: as a result, when the whole He initially contained in the bath is evaporated, the refrigerator gradually returns to room temperature.

The helium reservoir must be shielded from room temperature radiation heat load. This task can be accomplished by surrounding the He bath with a liquid nitrogen bath (77 K). In fact, according to Stefan's Law, the amount of heat radiated from a warm body to a cold body varies with the difference between the fourth power of their temperatures. Therefore a 300 K surface radiates 230 times more heat to a 4.2 K surface

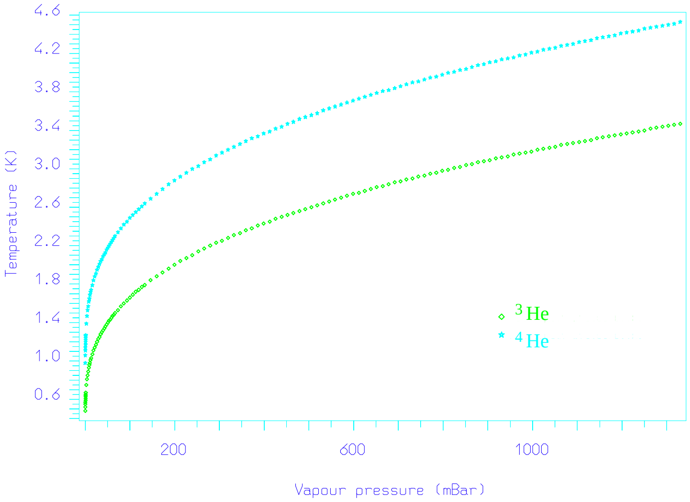

Figure 3.6: Temperature of an He bath as a function of ^{4}He and ^{3}He vapour pressure

than a 77 K surface would do. Furthermore any refrigerator is usually gradually cooled down from room temperature to the operating one, for example by pre-cooling with liquid nitrogen. This expedient allows to limit liquid He consumption and in the mean time is useful to study the behaviour of the devices under test at intermediate temperatures (as discussed in section 4.2.1 and 5.3).

In order to reach temperatures below 1 K the use of different techniques is required. In the context of this thesis three different dilution refrigerators have been used, located in the cryogenic laboratories at Insubria University and Milano Bicocca University. They are all based on the same principles of operation, using a ^{3}He/^{4}He mixture, which is a continuous refrigeration method, in contrast with ^{4}He pumped cryostats. When a mixture of the two stable isotopes of helium is cooled down below a critical temperature equal to 0.87 K it separates into two phases for a well defined range of ^{3}He concentration, as shown in figure 3.7 (where the λ-line represents the superfluid phase transition). The lighter concentrated phase is rich in ^{3}He, while the heavier dilute phase is reach in ^{4}He. ^{3}He concentration in each phase depends upon the temperature. Since the enthalpy of the ^{3}He in the two phases is different, it is possible to obtain cooling by evaporating the ^{3}He from the concentrated phase into the dilute phase (in analogy with the results obtained by forcing evaporation above a ^{4}He bath).

This process has an efficient cooling power even at temperatures close to absolute zero, since ^{3}He concentration does not vanish.

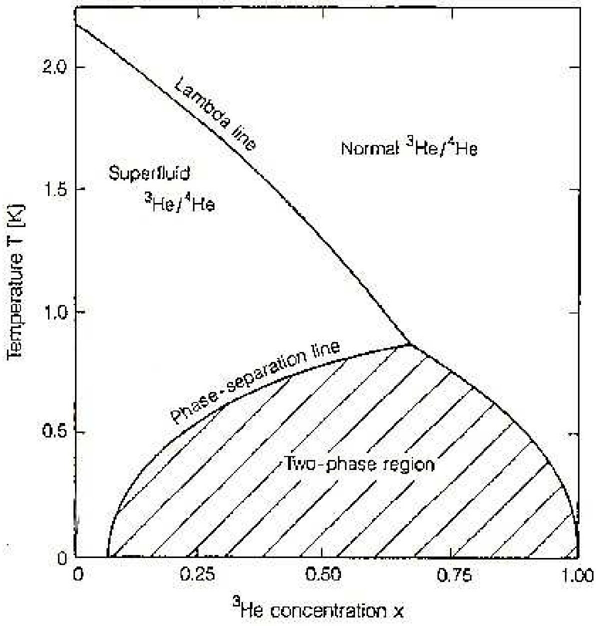

Figure 3.7: Phase diagram for the ^{3}He/^{4}He mixture at saturated vapour pressure. The diagram shows the λ-line for the superfluid transition of ^{4}He and the phase separation line of the mixtures below which they separate into a ^{4}He reach and a ^{3}He reach phase

In a dilution refrigerator the ^{3}He/^{4}He mixture is continously circulated by means of devoted pumpes and compressors. In order to cool down the mixture to the phase separation temperature, two different methods are available. The first one is called the "1K-Pot" method, while the second one is based on the Joule-Thompson effect. In both cases the cooling down is obtained through a series of steps. First of all the mixture, as well as the whole cryostat, must be cooled to the liquid ^{4}He temperature. This can be done by putting the refrigerator into an ^{4}He bath (main bath) and by thermalizing properly with the help of the bath vapours. However other techniques are available to accomplish this purpose (i.e. by using a pulse-tube). The second step consists in further cooling down the mixture to about 1.5 K by means of the 1K-pot or through the Joule-Tompson effect. The 1K-pot is a reservoir continously filled from the main bath with liquid helium, mantained at 1.2 K by a forced evaporation. On the other hand, if the Joule-Thompson effect is used, the liquid helium is compressed by means of a flux impedance and, thanks to the consequent expansion, it cools down to about 2.5 K.

When a proper temperature is reached, the ^{3}He/^{4}He mixture starts to condense, thus filling the two main elements which compose the cryostat: the *mixing chamber* and the *still*. In the still ^{3}He is continously evaporated from the liquid mixture surface, by mantaining the still temperature at $600-700$ mK, corresponding to a ^{3}He vapour pressure about three orders of magnitude greater than the ^{4}He vapour pressure. Due to the evaporation, the ^{3}He concentration in the dilute phase of the mixture located in the still results to be less than the concentration in the mixing chamber. As a consequence of this concentration gradient, there is a flow of ^{3}He from the mixing chamber to the still, resulting in a cooling down of the former. The mixing chamber actually corresponds to the colder element of the cryostat: for this reason the volume housing the devices to be tested is always thermally connected to it. Dilution refrigerators have a very high cooling power and temperatures as low as $\sim 5-10$ mK can be reached. A more detailed description of the operating principles of dilution refrigerators is given in [55, 56].

In order to properly cool down the devices under test it is necessary to realize good thermal links between the samples and the colder part of the considered refrigerator. Great care is then required in the preparation of the holder housing the samples and in the methods used for the thermal connections, which depends on the type of measurement to be realized. Usually the tested devices are glued onto devoted packages then placed into the holder connected to the colder part of the cryostat. The electrical connections are realized, at this level, by means of very thin gold wires ($25-50$ μm diameter), which assure the required thermal conductance is obtained. The gold wires are *ball bonded* using a devoted instrument. The preparation of the samples, in the specific cases treated, will be further described in the dedicated sections (4.2 and 5.3).

Obviously it is necessary to monitor the temperature conditions during the measurements: thermometers of various kind, suited for the different temperature ranges of interest, are commercially available and must be put in proper locations in the cryostat structure. Furthermore electrical connections (wires and connectors) must be added to read the signals from both the samples and the thermometers: the wiring of the cryostat may induce a reduction of the cooling power, due to the addition of a remarkable amount of material to be cooled.

Finally it is worth to notice that since any refrigerator is composed by a series of elements, each one mantained at a typical operating temperature, it is necessary to protect colder elements from the blackbody radiation of warmer elements; this is especially valid for the samples themselves.

CHAPTER 4

HEATERS: LOW TEMPERATURE CHARACTERIZATION AND EXPERIMENTAL RESULTS

This chapter deals with the characterization at low temperatures of the heating devices to be used for the stabilization of CUORE bolometers. The role of such devices and their mode of operation have been previously described in section 2.3.1, while the properties which must be satisfied by heaters are discussed in 3.2.2. In the previous chapters it was also shown that heavily doped semiconductors may satisfy many of the requests for the realization of heaters: steady resistences, exhibiting a low-mobility metallic behaviour, can in fact be produced by using a semiconductor doped well above the MIT. In the present chapter, the actual production processes used in the fabrication of heaters are presented, starting from an overview of the early attempts and the related test performed to verify the fulfilment of the static and dynamic requests. A discussion about the characterization of heaters to be used in the developement of CUORE detectors, performed in the Cryogenic Laboratory at University of Insubria, will follow. For the purpose of such characterization a devoted cryogenic set-up has been developed and tested and will be described, together with the results obtained during the performed measurements. It will be shown how to use such results in order to speed up the selection and to save money during the characterization in view of CUORE.

4.1 PRODUCTION PROCESS

4.1.1 Early results

The early attempts to develop heating devices to be coupled to TeO_2 crystals, based on the use of a heavily doped semiconductor materials, were performed using the Si:As system (silicon doped by arsenic). The details of the production process and the results obtained are reported in [43]. As a first test, a by-product of the R&D program for the fabrication of implanted silicon thermistors, in the context of the developement of the microbolometers also treated in this thesis, was used. Thus the production of heaters to be used in the CUORE experiment actually took origin in the context of the implementation of the microcalorimeters discussed in chapter 5. Both silicon thermistors and heaters have been fabricated by the Istituto per la Ricerca Scientifica e Tecnologica (ITC-irst).

According to standard procedures silicon thermistors fabricated by means of micromachining technologies, as in the considered case, are usually realized in form of wafers, each containing a fixed number of thermistors. This layout includes also suitable test structures, grouped in a so called "test strip", besides the devices of interest. Such test devices allow to control the fabrication process and to measure room-temperature electrical parameters. The ITC-irst test strip contains in particular a resistive structure, used for the contact diffusion, consisting in a narrow doped line with variable width and five contacts: it is this one which has been used as a heating element. The whole wafer, as well as the contact diffusion structure, is fabricated by applying the standard ion implantation technique, described in 3.1.2. In particular, the considered contact diffusion was obtained by opening the corresponding area in a 800 nm thick thermal oxide by lithography and etching, doping by ion implantation with 5.00×10^{15} ions/cm^2 of arsenic at 110 keV and subsequent activation by annealing at $975\,^\circ$C for 1 hour in dry oxygen and 30 minutes in dry nitrogen. As a result a heavily doped diode was obtained, with junction depth of 0.5 μm and a surface concentration of 2.0×10^{20} atoms/cm^3 (the critical concentration for the Si:As system is 8.7×10^{18} atoms/cm^3).

A silicon dice, with dimensions $1.5 \times 1.5 \times 0.5\,\mathrm{mm}^3$, was cut around the test strip. The electrical contacts were provided by contacting the interesting portion, to be used as a heating element, with two 25 μm diameter, 10 mm long, gold wires. The static behaviour, in terms of voltage and temperature stability of the devices, was checked down to 50 mK in a preliminary measurement and was found not excellent, especially in correspondence of low injected powers (see figure 4.1). This test was performed by applying a range of constant bias voltages to the heater, measuring the resultant voltage across it and thus extrapolating the corresponding power injected and the heater resistance. The same procedure, which will be better described later (see 4.2.3), was repeated at different temperatures. At the typical operating temperatures of bolometers (10 – 15 mK) the heating device showed a resistance of about 10 KΩ.

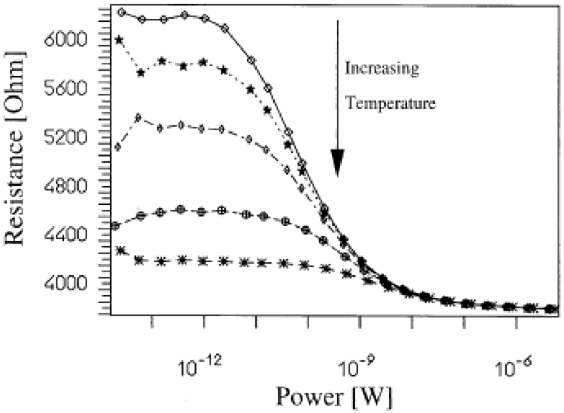

Figure 4.1: Resistance as a function of injected power for the strip heater; the various curves correspond to different temperatures, from 50 to 800 mK

The silicon dice was then glued with an epoxy resin to a 73 g TeO_2 detector and operated at cryogenic temperatures. With the help of a pulse generator, square voltage pulses were injected into the heater in order to develop thermal signals of energy a few MeV. A discussion about the results is given below.

- As shown in figure 4.2, the pulses generated by the heater and those generated by a particle in a TeO_2 bolometer produced signals with the same shape once normalized; this is a consequence of the obtained thermal coupling time ($\tau_h \simeq$ 1 ms) much shorter than the thermal rise time of the detector (50 ms). The value of τ_h can be calculated from equation 3.42, where the heat capacity of the heating device and the thermal conductance can be easily evaluated or previously measured. In particular the heat capacity of the silicon strip is of order 10^{-13} J/K, calculated by assuming that the heavily doped region can be described as an ideal Fermi gas, with a dominating term of metallic type $C_e \propto T$ (see section 1.6); while the thermal conductance of the glue spot is of order 10^{-10} W/K.
- The energy pulses induced by the heater in the bolometer showed an amplitude

E_h which can be written as:

$$E_h \propto \frac{V^2}{R_h}\Delta t \tag{4.1}$$

where V and Δt are respectively the amplitude and the time width of the voltage square pulses applied to the heating element and R_h is the heater resistance; the above equation imposes a stability for the pulse generator at least at the 0.1% level in time and amplitude, since one gets: $dE_h/E_h = 2dV/V$ and $dE_h/E_h = d\Delta t/\Delta t$.

- The signals generated in the detector by the heater pulses showed the same time and baseline dependence as the particle signals, thus allowing to perform an effective stabilization by using heaters.
- The stabilization performed with particle energy-pulser and heaters produced the same effects as shown in figures 4.3 and 4.4, with the advantage that heater pulses could be easily identified by software.

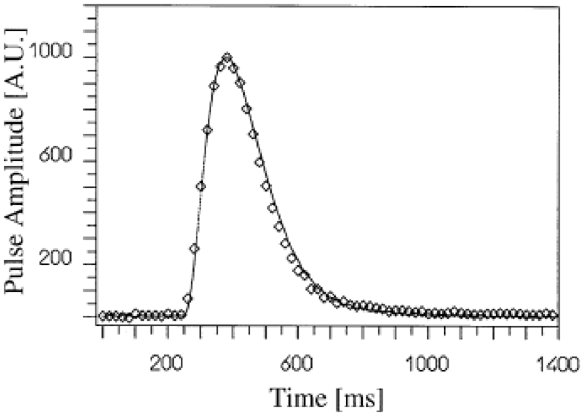

Figure 4.2: Comparison between pulses generated by a particle (points) and the strip heater (solid line) in a TeO_2 crystal

The above discussed results confirmed the advantages of using an heater-based stabilization procedure and showed that the heavily doped silicon device here considered matched the main requests exposed in section 3.2.2, concerning the static and dynamic behaviours necessary to accomplish the tasks of a stabilizing heating element.

For these reasons a devoted production run was started at ITC-irst, with the aim of studying and optimizing the performances of such heating devices, in order to standard-

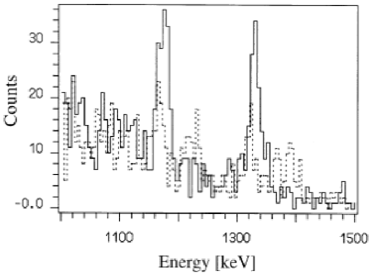

Figure 4.3: Calibration spectrum acquired by a TeO_2 bolometer before correction (dotted line) and after correction (solid line) where the stabilization procedure was performed with $\alpha-$particles

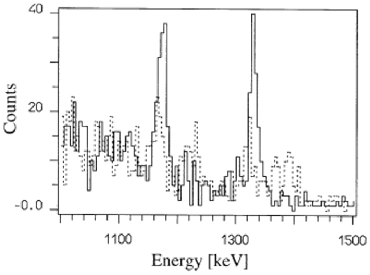

Figure 4.4: Calibration spectrum acquired by a TeO_2 bolometer before correction (dotted line) and after correction (solid line) where the stabilization procedure was performed with heater pulses

ize the fabrication process. For the realization a resistance value of order 100 kΩ at the operating temperature was chosen, to better accomplish to the task of behaving as the main point of power dissipation while operated. The basic layout consisted in a 6 μm wide and about 120000 μm long resistive meander, occuping an area of 1938×1917 μm^2 and with geometrical resistance of 20000 squares (see equation 3.1). In order to obtain larger resistors, with the aim of getting an higher total resistance, more than one of such single modules were printed side by side during the masking process. Furthermore the production process allowed to attach the contact pads almost freely, in various locations through-out the device: as a result the resistance value can still be varied by bonding the suitable pads. During this run different doping elements and levels were tested, as well as various annealing configurations. The final single chip dimensions were chosen in order to be well suited for the bolometer construction and not to exceed the detector heat capacity: therefore the produced wafers were cut in order to obtain $3 \times 3 \times 0.5\,\mathrm{mm}^3$ dices. In figure 4.5 the best obtained performances are reported, showing a very good resistance stability (within 1% between 50 and 800 mK) if compared to the earlier results (figure 4.1). Furthermore the above described devices have been successfully used for long run measurements with bolometric detectors.

4.1.2 Present status

The early test performed were useful to draw the basic procedure for the fabrication of heaters, which was identified taking into account the main requirements already exposed in previous sections. In view of the developement of the CUORE detectors a

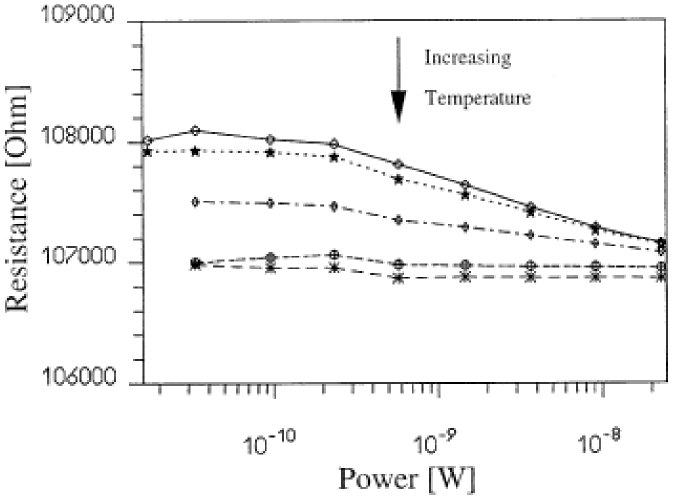

Figure 4.5: Resistance as a function of injected power for the meander heater; the various curves correspond to different temperatures, from 50 to 800 mK

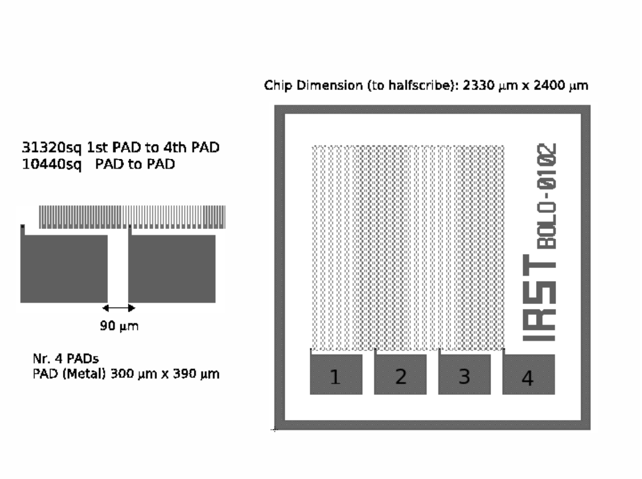

Figure 4.6: Structure of the single heater: chip total dimensions, geometrical resistance (squares) and pads dimensions are shown

devoted production run (named LTR4) was than carried out, in which a total number of 15 wafers, each one with 36×36 single elements, have been produced. Still, taking into account previously obtained results, the Si:P system was chosen in this case, where the starting material is a p-type Si $\langle 100 \rangle$ CZ (monocrystallin silicon grown with the Czochralski method), with a 16 Ω·cm resistivity. The single device structure is shown in figure 4.6: the resistive meander is visible and the dimensions and geometrical resistance *n* (squares number) are reported. Each heater (picture 4.7) is provided with 4 pads: therefore it is possible to use the resistance value better suited (though in the range 100 kΩ) by choosing which of the pads to contact. Since in fact the whole meander structure has been realized with the same implantation procedure, it is expected to exhibit a low temperature uniform resistance. As a result the *pad-to-pad* resistance should equal $1/3$ of the total value, measured between the two pads placed at the extremities of the device. In the context of the characterization at both room and low temperatures, it will be useful to conventionally name the various pads of each heater with 4 subsequent numbers, in order to be able to identify the resistance between them as R_{ij} with $i, j = 1, 2, 3, 4$ (as also shown in figure 4.6). Consequently the pads-to-pads resistances must show, at low temperatures, the following relationships, given the uniformity of the implant process has been fulfilled:

- $R_{12} = R_{23} = R_{34}$ (resistance between two adjacent pads)
- $R_{13} = R_{24} = 2 \cdot R_{12}$
- $R_{14} = 3 \cdot R_{12}$

During the low temperature characterization also the above resistance relashionships were proved: the results are reported in section 4.2.2, thus actually showing that a uniform distribution of the implanted region was achieved.

The scheme of the complete fabrication process is reported in table 4.1 and it is valid for all the 15 wafers, since the optimum procedures identified during the previous test were used (see also for reference 3.1.2). The only still varying parameter is the implant dose, according to which the wafers are splitted into three groups, as shown in table 4.2. As a consequence it is still possible to choose which wafers to use among the three groups, according to the best suited resistance value.

At the end of the production run, room temperature test were performed, in order to check out that the process had been successfully carried out. In particular a screening of each whole wafer allowed to quantify the spread of the resistance values. The pad-to-pad resistances R_{ij} were measured at room temperature by injecting a bias voltage into

Substrate material
p-type Si ⟨100⟩, 16 Ωcm, CZ

Step #	Type	Description		
1. Isolation				
1.1	Oxide growth	Grow screen oxide 43 nm		
		T (°C)	Time (min)	Gas
		975	70	Dry O_2
		975	10	N_2
1.2	Implant (1)	p-substrate adjustment implant (compensation)		
		Implant element	Energy (keV)	Dose (ions/cm^2)
		B	120	4.0×10^{11}
1.3	Oxide growth	Grow mask oxide 300 nm		
		T (°C)	Time (min)	Gas
		975	60	Wet O_2
		975	30	O_2
		975	30	N_2
2. Diode definition				
2.1	Lithography (1)	Define diodes		
2.2	Dry etching (plasma)	Open diodes		
2.3	Implant (2)	n-diodes doping		
		Implant element	Energy (keV)	Dose (ions/cm^2)
		P	130	$\sim 5.0 \times 10^{15}$
2.4	Ashing (plasma)	Remove photoresist		
2.5	Coating	Coating frontside with photoresist		
2.6	Wet etching	Remove backside oxide with HF (10:1)		
2.7	Implant (3)	Implant backside contacts		
		Implant element	Energy (keV)	Dose (ions/cm^2)
		BF_2	120	1.0×10^{15}
2.8	Ashing (plasma)	Remove photoresist		
2.9	Thermal activation *(Annealing)*	Reoxidation and junction drive		
		T (°C)	Time (min)	Gas
		975	60	N_2

Step #	Type	Description
3. Contacts		
3.1	Oxide growth	LPCVD-TEOS deposition (SiO_2 500 nm) Temperature 718 °C
3.2	Lithography (2)	Define contacts
3.3	Dry etching (plasma)	Etch contact holes
3.4	Ashing (plasma)	Remove photoresist
4. Metal		
4.1	Wet etching	Pre-metal deposition cleaning with HF (50:1) for 30 s
4.2	Metallization	Sputter Al:Si deposition (1200 nm) Temperature 225 °C
4.3	Lithography (3)	Define metal
4.4	Dry etching (plasma)	Etch metal
4.5	Wet etching	Post-metal definition cleaning with TI for 10 s
4.6	Ashing (plasma)	Remove photoresist
5. Over-glass		
5.1	Oxide growth	LPCVD-LTO deposition (SiO_2 200 nm) Temperature 430 °C
5.2	Lithography (4)	Define protective over-glass
5.3	Dry etching (plasma)	Etch over-glass
5.4	Ashing (plasma)	Remove photoresist
6. Backside contacts		
6.1	Coating	Coating frontside with photoresist
6.2	Wet etching	Remove backside oxide with HF (10:1)
6.3	Ashing (plasma)	Remove photoresist
6.4	Metallization	Sputter Al:Si deposition (500 nm) Temperature 225 °C
6.5	Al:Si thermal treatment	Sinter contacts T (°C) Time (min) Gas 400 5 Forming gas

Table 4.1: LTR4 production process: the meaning and role of the various steps are described in section 3.1.2

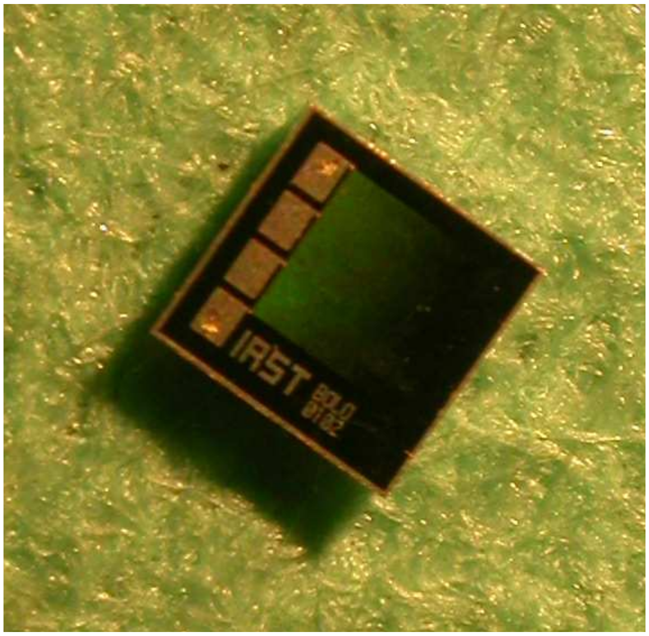

Figure 4.7: The single LTR4 chip

Name	Dose (ions/cm^2)	wafers
Implant P 1/3	5×10^{15}	1,2,3,4,5,6,7
Implant P 2/3	6×10^{15}	8,9,10,11
Implant P 3/3	4×10^{15}	12,13,14,15

Table 4.2: Splitting of the 15 LTR4 wafers according to the implant dose

the single devices forming the wafers, by contacting two of the 4 pads each time. The measurements were performed with two different bias voltages: 100 mV and 1 V. The results were used to produce three different kinds of wafer maps, for each performed test. In figure 4.8 the case of wafer 2 is reported as an example:

- the first map simply allows to select those devices which show a value of resistance so high to result as not measurable: such devices are signed in black and cannot be used;
- the second map is more precise than the first one: it was realized by assigning to each device a particular shade of colour corresponding to the measured resistance, according to the scale reported sideways and fitting the colours throughout the wafer;
- the third map was realized with a similar procedure as the second one; however, thanks to the use of different colours instead of using shades of the same colour, different areas, corresponding to various room temperature behaviours, can be easily identified.

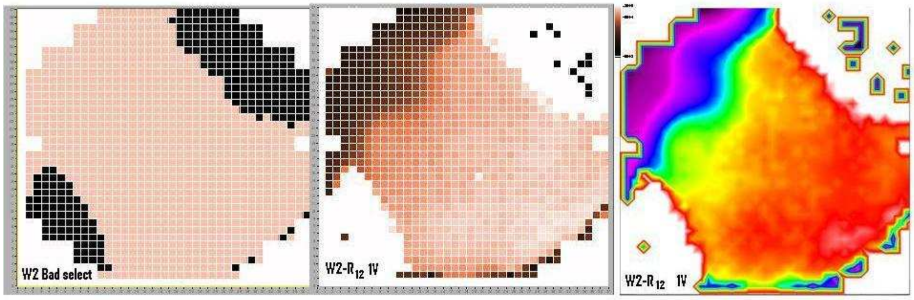

Figure 4.8: Example of the three kind of maps realized using the results of room temperature measurements: "bad-select" map, "shades" map and coloured map (wafer 2, R_{12}, applied bias voltage 1 V)

A study of the correlations between room and low temperature behaviours was carried out, in the context of the low temperature characterization, as will be discussed in the following sections. The results obtained, together with the use of the three kinds of maps realized at room temperature, has been and will be useful to speed-up the selection of the devices to be tested in view of CUORE.

4.2 LOW TEMPERATURE CHARACTERIZATION

The first part of this chapter was devoted to describe the early results obtained with the heating devices developed at ITC-irst, based on heavily doped semiconductor materials, in terms of both dynamic and static behaviours. Such devices represent the precursors of the heaters to be used in CUORE, whose fabrication process was described in the previous section. The good results obtained with such precursor devices show that they match the main requests pointed out in section 3.2.2. Furthermore they have been successfully used for the stabilization of bolometers during long run measurements. Since the LTR4 heaters to be used for CUORE are realized basically with the same procedure and given the big number of devices which in principle should be tested (see section 2.3.1), it was decided to perform a selection simply based on the static characterization of each single device, down to the easiest attainable temperature. A complete characterization of both dynamic and static properties of the whole number of heaters (~ 2000) whould in fact require an enormous expense in terms of time and money.

Next sections are devoted to describe this static characterization performed down to ~ 1 K, easily achievable with respect to lower temperatures (see section 3.2.3) and allowing to realize simple and quick measurements. Furtheremore it is worth to notice that the usage of some LTR4 heaters as stabilizing elements during the R&D phase of CUORE, still provided evidence for their reliability and good performances. Finally one test at temperatures close to the operating ones has been performed (see section 4.2.3), whose results allowed to make a comparison with older measurements performed with precursor devices, still showing the reliability of higher temperature test.

4.2.1 Set-up for the characterization down to ~ 1.5 K

Given the previous considerations, in view of the static characterization of the heaters to be used in CUORE, a devoted set-up has been realized and tested in the Cryogenic Laboratory at Insubria University, as below discussed.

The cryogenic set-up

The cryogenic set-up is based on a ^{4}He pumped refrigerator (see section 3.2.3) produced by INFRARED. In figure 4.9 the schematic structure of the cryostat is reported, where the following elements are shown:

- the two dewars housing the cryogenic liquids: the main bath, for liquid helium and the secondary bath, for liquid nitrogen; the secondary bath serves as a shielding from room temperature radiation heat load and it is useful to limit the He consumption;
- the copper holder housing the samples, in good thermal contact with the colder part of the cryostat (in this specific case the ^{4}He bath);
- the 77 K shielding, connected to the liquid nitrogen reservoir, useful to protect the copper holder from 300 K blackbody radiation;
- the vacuum insulation, useful to reduce the heat load due to conduction and convection.

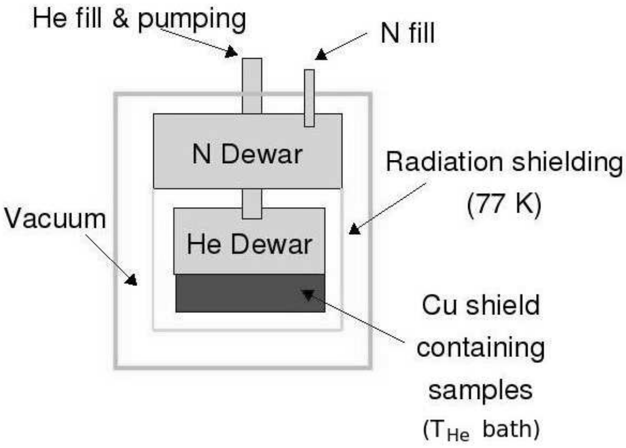

Figure 4.9: Schematic structure of the INFRARED ^{4}He pumped refrigerator

The copper holder was specially realized and added to the INFRARED cryostat: it is made up of a copper plate, screwed to the ^{4}He dewar, upon which the holders for the samples were then placed (figure 4.10). After the samples have been put onto the holders and are ready for the measurement, the plate is covered with a copper lid, in order to protect the samples from 77 K blackbody radiation. Copper is the material usually adopted for the realization of many cryogenic accessories, because of its physical properties. *In primis* its high thermal conductance allows to realize very good thermal contacts between different parts of the refrigerator (in the considered specific case between the samples and the main bath). The sample holders are screwed to the copper plate and are provided with 40 pins (20 on each side) for the electrical connections, realized so that the packeges to which the samples are glued (as later described) perfectly fit into them.

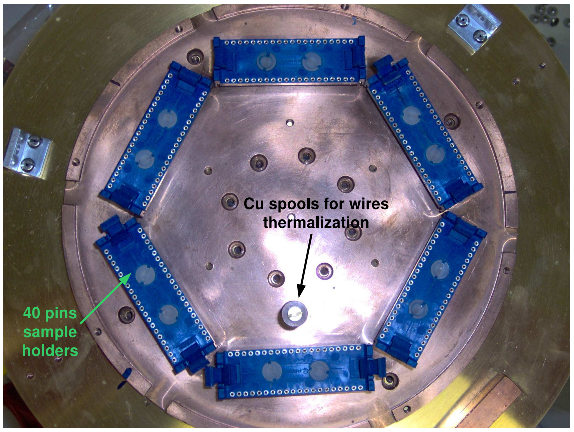

Figure 4.10: Copper plate screwed to the ^{4}He dewar, with the sample holders placed and screwed upon it. One of the spools used for the thermalization of the reading wires is also shown

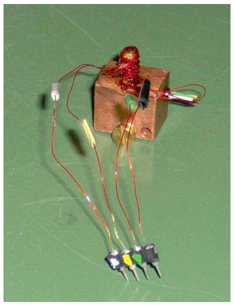

Figure 4.11: Copper box housing the LakeShore thermometer: the four reading wires, wrapped around the copper spool, are visible

In view of the forseen measurements a proper "wiring" of the cryostat was carried out, in order to provide the necessary electrical connections; furthermore a calibrated thermometer was added; finally a system for filling the cryogenic liquids and for pumping ^{4}He was provided. Concerning the wiring a complete project was realized, taking into account the nature of the forseen characterization, which substantially consists in the extrapolation of the resistance of the devices under test by applying a square excitation voltage and measuring the risultant current flow.

Thermometer

In order to monitor the temperature during the measurements, a LakeShore germanium resistor was placed inside the copper sample holder. The resistor consists itself in a lightly doped germanium sensor, operating in VRH regim. It is provided with four wires, so that the resistance value is read by a "four-lead measurement" ($I^{\pm}$ and $V^{\pm}$ are read), which is more accurate than a simpler "two-lead measurement". The location of the thermometer was chosen so that the thermometer operating conditions were as similar as possible to the samples measuring conditions: for this reason the germanium resistor was placed inside a devoted copper box, provided with a hole with proper dimensions (see figure 4.11), then screwed to the center of the copper plate. A thermal grease was used in order to inhance the thermal coupling between the thermometer and the copper box. Furthermore the four wires provided to read the signals were wrapped around a copper spool for a good thermalization.

A calibration of the thermometer is provided by LakeShore, with the experimental data and the derived expression for the resistance-temperature conversion. The calibration is valid in the temperature range 500 mK to 100 K. Furthermore the resistance values corresponding to room temperature, liquid nitrogen temperature and liquid helium temperature are provided. Since a simple expression for the resistance-temperature conversion is necessary for an immediate interpretation of the mesurement results, the experimental data provided were fitted by means of the following equation (by analogy with expression 1.14), valid in the temperature range $0.5-5$ K:

$$R(T) = R_0 \exp\left(\frac{T_0}{T}\right)^p \tag{4.2}$$

were $R(T)$ is the measured resistance, T the correspondent temperature value (data provided by LakeShore) and T_0, R_0, p are the free parameters. It is interesting to notice that the value of the exponent p resulting from the fitting procedure is ~ 0.5 in the considered temperature range, thus in agreement with equation 1.18.

In order to provide the electrical connections between the thermometer and the room temperature electronics, the four thermometer wires were soldered to four phosphor bronze[1] wires, leading the signals outside from the cryostat.

Wiring

The sample holders were realized so that each one can house ten samples; not all the fourty pins are used, in fact: usually one is left unused between two used pins, thus providing a connection to ground. As a result twenty pins are actually available for each holder. Also in this case (as for the thermometer) the resistance is read by a "four-lead measurement". A pair of twisted (to minimize noise pickup) wires was soldered to each of the ten available pins located on one side of the holder and used to read the I^+ and V^+ signals. All the twenty pins located on the opposite side of the holder were connected together and to two pairs of twisted wires by means of tin soldering. They are used for the I^- and V^- signals, which are thus read in common and act as the

---

[1] Phosphor bronze (together with constantan) is one of the materials typically used for the realization of cryogenic wires, due to its low thermal conductivity and high electrical resistivity

reference potential. The scheme of the wiring at the level of the holders is shown in figure 4.12.

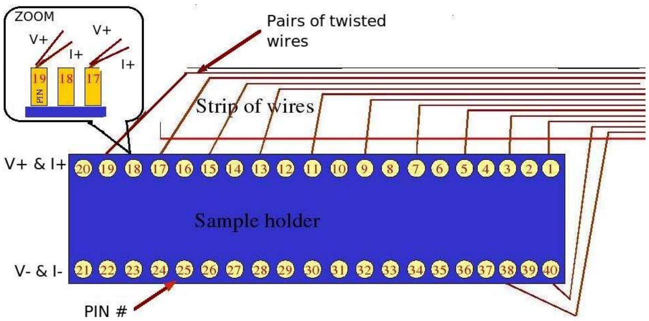

Figure 4.12: Scheme of the wiring at the level of the sample holders

The connections were realized using strips of twelve pairs of twisted constantan wires and soldering one extremity of each wire to the corresponding pin. An important task which should be pursued consisted in providing a good thermalization to all the elements used for the electrical connections. Since the signals must undertake a long way from the colder part of the cryostat to room temperature, it was necessary to evoid an excessive heat load by thermalizing the wires at several temperature stages.

First of all the strips coming from the sample holders were wrapped and glued around the devoted copper spools, previously screwd to the copper plate, by using VGE-7031 varnish. The varnish serves two purposes: it physically holds the leads in place and it increases the contact surface area between wires and surroundings. A layer of cigarette paper was varnished and put around the spools before wrapping the wires, in order to assure electrical insulation. A similar technique was used also for the thermometer reading wires. Then both the wire strips and the thermometer wires were thermalized to the outer part of the ^{4}He dewar, where they were soldered to twelve pins connectors providing a first decoupling between liquid ^{4}He temperature and nitrogen temperature. A second twelve wires strip was then soldered to each connector and well thermalized to the 77 K shielding, by using the same method as before: a layer of cigarette paper was varnished to the thermal anchor and the wires then wound over the paper and varnished down. A couple of complete turns around the whole shielding were enough to obtain a good thermalization. Figure 4.13 shows the inner volume of the refrigerator and the copper plate after the wiring was completed.

Each wire strip was finally connected to a 24 pins Fischer connector placed on the

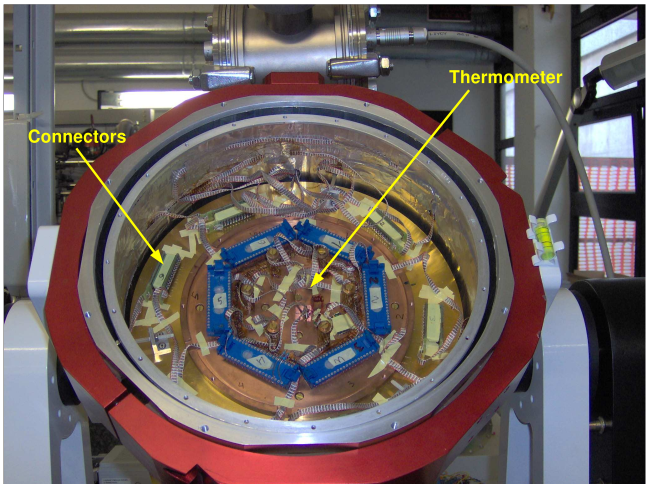

Figure 4.13: The inner volume of the cryostat with the completed wiring

flanges located outside the cryostat, at room temperature, as shown in figure 4.14. Each pin corresponds to one of the 24 wires coming from the sample holders. On the other hand the four phosphor bronze reading wires of the thermometer were connected to four corresponding BNC connectors, located on the outer flanges as well. Such flanges and connectors should obviously assure a good vacuum tight.

Data acquisition system

Both the resistances of the thermometer and of the samples are read with a "four-lead measurement" by means of an AVS-47 bridge, produced by RV-Elektroniikka. This instrument consists in an automatic AC resistance bridge, which measures the AC current flowing in the device after injecting a square excitation voltage of order 10 Hz. The AVS-47 bridge can then extrapolate the resistance value with a *lock-in* technique: the maximum measurable resistance is ~ 2 MΩ, with a dissipated power into the device which can be minimized to $\sim 10^{-5}$ pW (for resistances of order 1 MΩ). One can select among different excitation voltages, from a minimum of 3 μV to a maximum of 3 mV.

The AVS-47 bridge can read eight channels per time, each channel being composed by the four reading wires ($I^{\pm}$ and $V^{\pm}$) and corresponding to one specific resistor. One of the eight channels was then definitively assigned to the thermometer, while the others were left available for the samples. As a consequence only seven samples per time can be read. Since each holder can house ten samples, the cryogenic section of the wiring

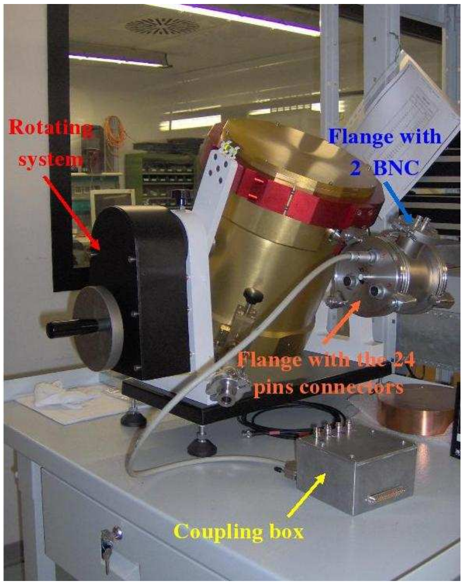

Figure 4.14: The cryostat ready for a measurement: the connectors located on the vacuum tight flanges are visible, as well as the rotating system, used as a support for the cryostat, and the box for the coupling between the cryogenic section of the wiring and the AVS-47 bridge

and the AVS-47 bridge needed to be properly coupled. To this purpose a coupling box was realized (shown in figure 4.14), which allows to change which channels to connect to the AVS-47, thus making it possible to measure all the ten channels in two different steps.

The AVS-47 bridge can be coupled to a PC where a devoted acquisition system for the automatic control of the electronics (realized by C. Rusconi) is installed. Through this automatic program it is possible to record the measured resistance values of the devices and the correspondent acquisition time, as well as the temperature, during a long run measurement. After selecting the devices to be measured and setting the required parameters (excitation voltage to be injected, duration of the run, number of measurements for each device over which calculate the average resistance value) the program makes the run start and the measurement is performed over a number of cycles, corresponding to the pre-selected duration of the run. During each cycle the resistances of the selected devices and of the thermometer are read one by one, according to the number of selected measurements for each channel. The average resistance is then calculated and registered for each cycle, together with the corresponding standard deviation. For each device then an overall text file is produced, with the registered resistance values, standard deviations, applied excitation voltage and time.

Since the resistance of the devices is not measured exactely at the same time as the temperature during a single cycle, a devoted software in C language was developed, in order to solve this problem. This software processes the input files produced by the acquisition program by fitting the temperature values versus time with a linear function and assigning to each resistance value of the devices under test the temperature corresponding to their acquisition time. The output files contains then three main parameters: the resistance value of the tested device, its acquisition time, the corresponding temperature calculated by the software.

Test of the set-up

When the whole wiring of the cryostat was completed, a series of test were performed before starting the measurements, as below described:

- test of the vacuum tight;
- test of the wiring at room temperature, to assure no shorts were produced while soldering and attaching the wires and to check the status of the realized connections;
- test of the whole cooling down procedure: this served in order to check how both the cryogenic system and the wiring system were working at cryogenic temperatures.

The first test was performed by closing the cryostat, thus simulating the measuring conditions (apart from the temperature) and by pumping vacuum inside the refrigerator volume by means of a devoted rotary pump. The system reached a minimum vacuum of order 10^{-3} mBar, sufficient to the purposes of the set-up, thus showing the good vacuum tight of the whole system (including flanges and connectors).

A further room temperature test was performed by putting into the sample holders a set of known resistances, thus simulating the samples to be measured, in order to check if the whole wires and electronic systems did measure the expected values and to verify no shorts had been produced during the wiring. Also this test gave successful results.

The early low temperature runs carried out were useful to estabilish the standard cooling down procedure (a practical manual was also realized) and to check the performances of the set-up as a whole. The cool down procedure can be summarized as follows:

1. after placing the samples inside the holders, the cryostat must be closed and well tightened; the rotating system shown in figure 4.14 is then used to turn upside down the refrigerator, since the filling holes for the cryogenic liquids are located on the opposit side with respect to the volume housing the samples;
2. vacuum pump the volume of the cryostat down to $\sim 10^{-3}$ mBar;
3. pre-cool the main bath by filling liquid nitrogen and let it thermalize at 77 K for about one hour;
4. fill liquid nitrogen in the secondary bath;
5. empty the main bath and fill it with liquid helium; though the capacity of the main bath is about 4 liters, the helium consumption is about 30 liters, since a big fraction is used to thermalize the set-up in contact with the main bath;
6. pump with a devoted set-up the volume inside the main dewar to reduce the vapour pressure above the He bath, till the lowest attainable temperature is achieved; the so obtained condition can be mantained for about 1-2 days, till the whole helium initially contained is consumed;
7. usually the lowest attained temperature is kept for the minimum time required for the measurements; the set-up is then left to come back to room temperature by stopping to pump.

The conditions attained during the cooling down may differ from run to run, depending upon various factors, as for example the time left for the thermalization at nitrogen temperature or the amount of He contained in the main bath before starting to pump it. Thus also the lowest temperature reached is not the same from run to run. During a single run the measurements can be manually performed (without the help of the automatic acquisition system) at the various temperature stages: room temperature, liquid nitrogen temperature, liquid helium temperature and finally pumped liquid helium temperature. Then it is useful to run a long measurement by means of the automatic acquisition system while the set-up comes back to liquid helium temperature, since this process may take about 10 hours. During this last step of the procedure it is also possible to keep under control the vapour pressure above the helium bath, by means of a pressure sensor properly connected to the pumping system.

During the early runs, old samples characterized in the past at cryogenic temperatures were used in order to test if a good thermalization was attained. By comparing presently obtained data, old data, the temperature recorded by the thermometer and the helium vapour pressure (at least during the warming up process) it was possible to make a complete check of the performances of the set-up.

The old samples used for the test consist in a series of silicon thermistors produced by ITC-irst, called BL10 (from the number of the production run), operating in VRH regime, which will be further discussed in chapter 5. Such samples have a temperature dependent resistance, which in the range considered here ($\sim$ 1 K - 4.2 K) is given by equation 1.11. Data from old measurements performed with a similar cryogenic set-up and with a well calibrated thermometer, concerning the resistance versus temperature behaviour of such devices, were compared to the presently attained data.

During the first and second runs a minimum temperature of about 1.8 K was reached, as measured by the thermometer, thus larger than the minimum potentially attainable, corresponding to 1.2 K. On the other hand the He vapour pressure measured in the same condition corresponded to a temperature of about 1.3 K (as evaluated from the plot shown in figure 3.6). This first contrasting result induced to suppose that the thermometer was not sufficiently thermalized to the copper plate.

Furthermore, the resistance of the BL10 sensors measured at various temperatures did not exactly correspond to that of the old data, still confirming a not complete thermalization, in this case of the samples. Figure 4.15 shows the results of the present measurements (data acquired with the automatic acquisition system during the warming up) compared to the old results as an example. As shown, the old data clearly follow the linear relation:

$$\ln R = \ln R_0 + \left(\frac{T_0}{T}\right)^{1/4} \tag{4.3}$$

derived from equation 1.11. On the other hand, the data resulting from the new measurements, besides investigating a reduced range of temperatures, show a different slope: their resistance seems to grow up more slowly than in the case of old data, which means their temperature is higher than expected.

By fitting the old data according to relation 4.3, the parameters T_0 and R_0 for the BL10 sensors were extrapolated and used to evaluate the real temperature of the samples during the new measurements. Such temperature resulted to be even higher ($\sim 2-3$ K) than the one read by the thermometer.

Given the previous results some expedients were used in order to solve the problems of thermalization found: first of all the wires inside the volume of the cryostat were better fixed to the walls of the refrigerator, in order to evoid direct contacts between elements placed at different temperature stages; secondly the samples were better coupled to the copper plate by means of a piece of adhesive copper strip. During

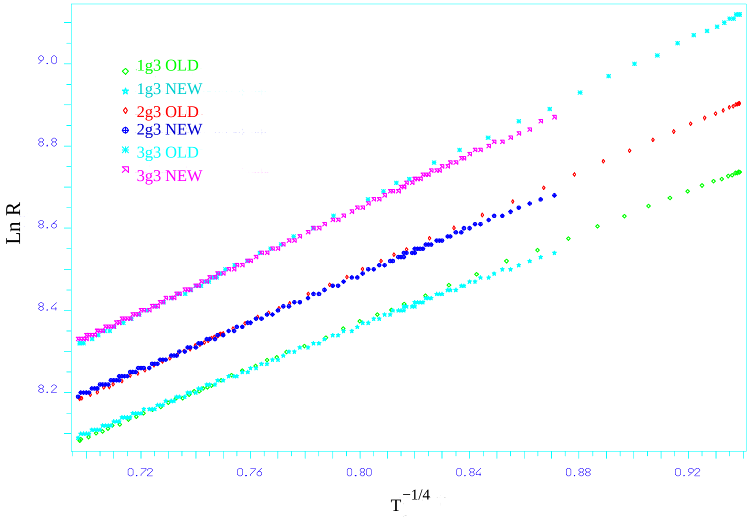

Figure 4.15: Comparison between old and new data of resistance versus temperature for the BL10 sensors, plotted according to relation 4.3

Temperature (K)	$\Delta R(\%) = (R_{new} - R_{old})/R_{old}$					
2^{nd} **run**	1 g3	2 g3	3 g3	5 g3	6 g3	7 g3
300	0.29	0.43	0.22	0.26	0.11	0.58
77	0.86	0.23	0.08	−0.01	0.71	1.1
4.2	−6.86	−7.33	−7.98	−8.64	−7.36	−7.23
∼ 1.8	−25.21	−27.88	−30.96	−32.0	−27.1	−27.55
4^{th} **run**	1 g3	2 g3	3 g3	5 g3	6 g3	7 g3
300	0.07	0.23	0	0.03	−0.07	0.38
77	1.24	0.58	0.4	0.25	0.13	1.42
4.2	0.18	0.19	0.22	0.16	0.19	0.32
∼ 1.6	−3.17	−1.57	−2.4	−3.91	−2.68	−2.49

Table 4.3: Discrepancy (%) between old and new values of resistance at various temperatures, evaluated during the second and the fourth cool down runs for some of the BL10 sensors (here identified by two numbers and one letter, the meaning of which will be discussed in chapter 5)

the subsiquent runs, temperatures as low as $\sim 1.5-1.8$ K were reached, as measured by the thermometer and further confirmed by the measured resistance of the BL10 sensors. The discrepancy between old and new resistance values of the BL10 sensors resulted to be strongly suppressed. This is shown in table 4.3, where the quantity $\Delta R = (R_{new} - R_{old})/R_{old}$ is reported for various temperature stages, for the second and the fourth cooling down runs. The preceding analysis moreover shows that the precision of the measurements is of order $\sim 1\%$ at the lower attainable temperature.

The fact that it was not possible to cool down the set-up to 1.2 K, could be explained by considering the amount of material added inside the refrigerator (wires, connectors, copper holder for the samples), which during the cool down certainly inhances the helium consumption, as well as the heat load.

4.2.2 Measurements down to ~ 1.5 K

Preparation of the samples

After the test of the set-up had been successfully carried out, the characterization of LTR4 heaters was started. In view of the measurements the devices were glued upon devoted packages by using VGE-7031 varnish, which besides providing the necessary contact surface area between samples and holders (to assure a good thermalization), can be easily removed with ethanol. The electrical connections were provided by means of 50 μm diameter gold wires, *ball bonded* to the contact pads using a devoted bonding machine. The packages were realized using fiberglass (a material often adopted for cryogenic purposes) and their structure was studied so that they could properly fit into the holders located inside the cryostat (see figure 4.16).

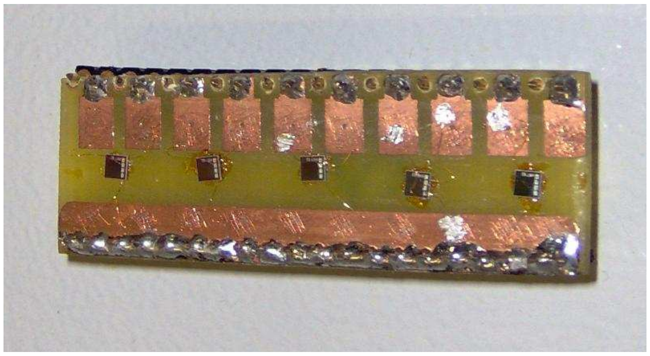

Figure 4.16: Package in fiberglass with glued and bonded heaters, ready for the measurements

As shown in figures 4.10 and 4.13 the experimental volume was sufficient to place six sample holders, each one capable to house no more then ten samples. As a consequence a total number of 60 heaters can be measured during a single cool down run. This fact is really advantageous, since taking into account that a single complete run can last about one week, a total number of 2000 heaters can be potentially tested in less than one year.

Measurements and Results

The static characterization performed down to 1.5 K was carried out taking into account the good results obtained during the early test on the precursor devices and can be summarized through the following items:

- measurement of the resistance trend during the cooling down, by injecting a fixed excitation voltage, which allowed to:
    1. estabilish useful correlations among resistance values at various temperature stages;
    2. extrapolate interesting informations about the behaviour of heavily doped semiconductor materials while cooled down to cryogenic temperatures;
    3. evaluate the stability of resistance with temperature variations below 4.2 K.
- measurement of the resistance at a given temperature stage, by injecting different excitation voltages by means of the AVS-47 bridge: this kind of test was performed at 4.2 K (the lowest and at the same time more stable temperature attainable) over a significant sample of devices;
- check of the validity of the relationships discussed in section 4.1.2, which link the resistance between different pads of each divice; this task was carried out by connecting simultaneously three different pads of the same heater, thus measuring two different resistances R_{ij}; also this kind of measurement was not performed for all the heaters, but only over a significant sample of devices.
- check of the homogeneity of the resistance measured at and below 4.2 K throughout each single wafer and evaluation of the spread of values among all the characterized devices: to this purpose the use of the wafer maps has been very helpful.

During the early runs the devices were taken from various wafers and various areas, in order to make a kind of screening of the available heaters. The room temperature "bad-select" map was useful to discarde the devices signed in black. From the obtained results some useful relations between low temperature values of resistance and room temperature maps were identified, as well as the global status of the available devices. During the subsequent runs the attention focused mainly upon two wafers, chosen because of their homogeneity and since their average resistance tunes the requests for the developement of CUORE bolometers.

The characterization was carried out by injecting a standard excitation voltage of 1 mV at the various temperature stages. This value produces very stable readings if compared to lower excitations ($< 0.001\%$ uncertainty compared to $\sim 1\%$ obtained with 300 μV) without warming up the samples. For the purposes of the characterization, "puntual" measurements undertaken at various temperature stages are sufficient and can be carried out by operating manually the AVS-47 bridge, without the help of the automatic acquisition software. In figure 4.17 the resistance versus temperature trend is shown for some of the tested heaters. The single devices are identified with the name of the wafer (i.e. w1 refers to wafer 1) and with two numbers referring to the position of the device inside the wafer: the first number refers to the line, while the second refers to the column.

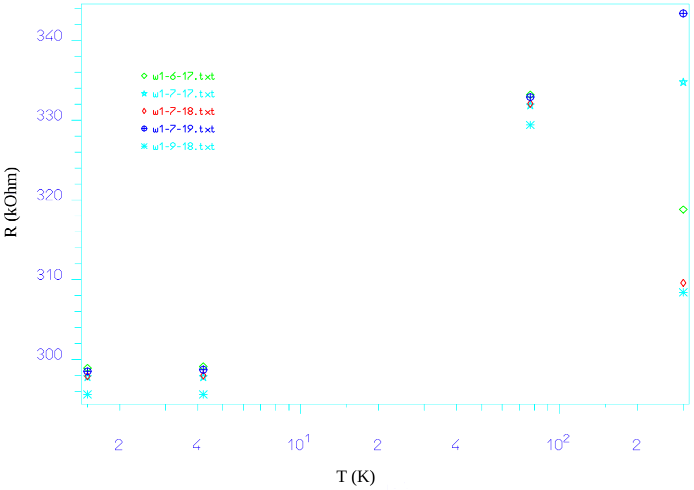

Figure 4.17: Trend of resistance (R_{14}) as a function of temperature for some of the tested heaters

The trend shown in figure 4.17 concords quite well with the theoretical prediction discussed in section 1.5 about the behaviour of HDS. The resistance in fact decreases with decreasing temperature, at least between 77 K and 4.2 K, due to the reduction of phonons and lattice vibrations. This reduction is of order $\sim 15\%$, thus in accordance to the theory of conduction in metals, in which the electrical conductivity weakly depends upon temperature variations. Furthermore the resistance remains constant below 4.2 K, still confirming the theoretical predictions: in this range of temperatures the presence of impurity ions prevails, thus contrasting the global decreasing trend. The only open question concerns the behaviour between room temperature and nitrogen temperature: in this specific range not all the devices show the same trend. In some cases the resistance slowly decreases with decreasing temperature, in accordance with the expected behaviour, while in many other cases it slowly increases. This fact lacks a complete theoretical explanation, but can be interpreted in terms of a partial recombination of carriers taking place at the beginning of the cooling down process.

Still, figure 4.17 shows that the value of resistance below 4.2 K is of order ~ 300 kΩ, thus matching the requests in the context of the CUORE experiment, as already pointed out. The spread of resistance values at 4.2 K, evaluated after a statistically significant number of devices was tested, is shown in figure 4.18.

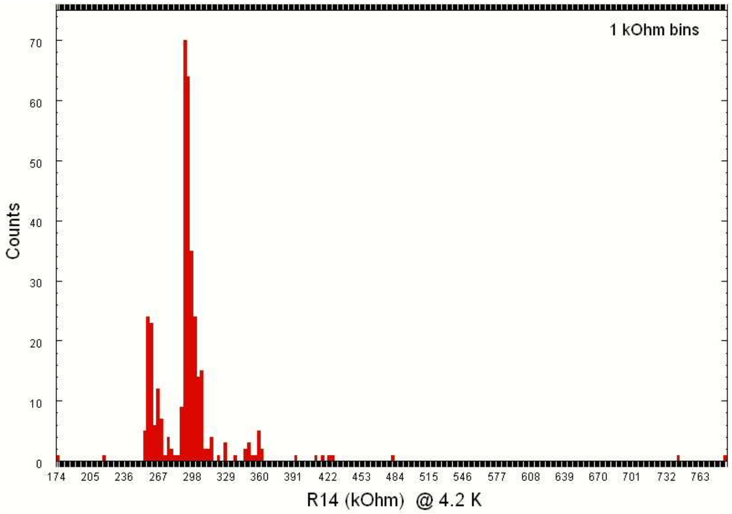

Figure 4.18: Values of resistance (R_{14}) measured at 4.2 K (coinciding with the values measured at 1.5 K) for a total number of 354 heaters, belonging to different wafers

The main peak is centred at $\sim 300 \pm 12$ KΩ, and accounts for devices coming from central areas of wafers 1, 2, 3, 5, 6. An other sharp peak is visible centred at about 265 KΩ, which accounts for wafers 8 and 9. Finally the tested heaters, taken from wafers

4 and 12, show a value of resistance slowly higher then that of the others. There are also some devices which show a very high resistance (~ 700 KΩ) if compared to the majority, which can be easily identified as coming from the edge of the wafers. A more accurate analysis of the relations between the measured resistences and the wafers, also making reference to the room temperature maps, will be discussed later.

The histogram in figure 4.18 was useful to give a global idea of the available resistances, in order to choose which wafers to test in view of the realization of CUORE. Since the most part of the wafers showed resistances which can be placed in the main peak, the subsequent characterization was carried out choosing devices mostly belonging to such wafers, in order to obtain the lowest possible spread.

The validity of the relationships linking the resistances R_{ij} between the various pads was checked for a total number of 85 samples, belonging to all the wafers. In this case both the resistances R_{14} and R_{24}, or R_{13} and R_{23}, were mesured for each considered device. In order to evaluate the actual homogeneity of the resistive meander structure, the values R_{24} or R_{23} were respectively calculated according to the expected relashionships, from the measured value of R_{14}. Then, the difference between the actual (R_m) and the expected (R_e) values of R_{24} and R_{23} was estimated according to the following expression:

$$\Delta R_{me} = \frac{R_m - R_e}{R_e} \tag{4.4}$$

As a result ΔR_{me} was found to vary between 0.02% and 1% for all the wafers, except for the number 8, thus showing that a good homogeneity through-out the resistive meander had been generally achieved. Wafer 8 showed a larger value of ΔR_{me}, varying between $\sim 2\%$ and $\sim 30\%$ among the tested devices (actually a small fraction mostly taken from areas close to the edges). This fact, together with some other results later discussed, induced to discard this wafer during the heaters selection in view of CUORE.

Measurements performed at 4.2 K by injecting various excitation voltages (30 μV, 300 μV, 1 mV and 3 mV) proved the stability of resistance as the devices are operated with different bias. At least a hundred of samples, belonging to different wafers, undertook this test. As a result a variation of resistance lower than 0.5% was determined in all cases.

From the measurements performed at 4.2 and $1.5 - 1.8$ K it turned out that the resistance of the devices is very stable below liquid helium temperature. The maximum measured variation ΔR_{14} is of about 0.1%, lower than the 5% requested by the electronic set-up to be used in CUORE.

wafer	# of devices	average R_{14} (kΩ)	σ_R (kΩ)	σ_R %
w1	185	295	4	1
w2	64	298	5	2
w3	49	297	5	2
w4	7	319	8	2
w5	45	293	2	1
w6	59	299	4	1
w8	10	272	7	3
w9	69	261	4	1
w12	30	360	51	14

Table 4.4: Average resistances R_{14} and standard deviations σ_R at 4.2 K for the tested wafers; the number of tested devices is also reported

Table 4.4 shows the average resistance R_{14} at 4.2 K for each tested wafer, together with the number of tested devices and the standard deviation. These data, in accordance to the histogram displayed in figure 4.18, show a good homogeneity through-out each single wafer, since the standard deviation is always lower than 3%, apart from wafer 12. In principle all the wafers turned out to be useful, once discarded those devices showing an anomalous behaviour, mainly coming from areas located at the edges of the wafers. Nevertheless wafers 4, 8, 9 and 12 were discarded from the subsequent selections, due to the following reasons:

- their resistance greatly differs in the average from that of the others, which on the other hand give origine to one single peak of half width 4% in the histogram of figure 4.18;
- they generally show a larger spread of resistances with respect to the others, as proved by the calculated standard deviation;
- they sometimes show anomalous behaviours concerning the stability of resistance below 4.2 K or the relationships linking the resistances R_{ij} between different pads, as already pointed out in the case of wafer 8.

A more interesting analysis can be carried out by comparing the obtained results with the room temperature maps. In fact the values of resistance tend to increase in correspondence to the areas signed in red in the coloured map, though within the evaluated standard deviation. Furthermore, anomalous behaviours, such as unusually high values of resistance at 4.2 K or contacts which open at low temperature, usually turns out in correspondence to the dark areas in the "shades" maps, mostly located at the edges. The devices showing such strange behaviours were discarded during the selection. Furthermore this analysis helped to speed up the selection, by evoiding to choose for the test the devices located at the edges. By this expedient the efficiency of the characterization was greatly inhanced: while initially it was of order 70%, it was then improved to $\sim$ 90%.

The low disuniformities revealed through-out each single wafer can be explained in terms of the doping level. In fact the devices show a metallic behaviour in a very narrow range of dopants concentration, as experimentally observed during the early production runs. Since the precision of the implanting machine is about 1%, the spread of the doping level is more likly due to a non perfectly uniform annealing process (which serves to completely diffuse the implant). The ovens used for the annealing can control the temperature within 0.5°C, but it is possible that very small differences of temperature ($\sim 1-2^\circ$C) take place at different positions inside the oven, being sufficient to influence the doping level.

The above described results were used in order to carry out a faster selection of the heaters in view of CUORE. In particular the subsequent characterization focused on wafers 1, 2, 3, 5, 6, which showed a quite similar average resistance with a low enough spread. In view of the first phase of CUORE, named CUORE-0, which forsee the realization of a 58 bolometers experiment, the selection was focused on one single wafer (actually w1), also for more practical reasons. In fact an automatic gluing system is being developed for the assembly of the detectors: for this reason the variations in the dimensions of the chips must be reduced as much as possible. The typical thickness of the wafers is 525 μm, with a variation through-out a single wafer of $\sim 1-2$ μm; while taking into account different wafers the variation is $\sim 3-4$ μm. Since CUORE-0 will consist of "only" 58 bolometers, the necessary heaters can be easily chosen from one single wafer, thus assuring both the required homogeneity of resistance and uniform thickness.

During the characterization down to pumped helium temperature, a strong correlation between the resistance measured at liquid nitrogen temperature and that measured at 4.2 K turned out. The average resistance R_{14} measured at 77 K and the corresponding standard deviation for the tested wafers are reported in table 4.5. On the other hand room temperature resistances showed a wider spread which, though to some extent consistent with the implant structure and with low temperature results, made them not completely reliable in view of the selection.

wafer	# of devices	average R_{14} (kΩ)	σ_R (kΩ)
w1	185	328.4	7
w2	64	333.5	7
w3	49	331	5
w4	7	354	8
w5	45	234	9
w6	59	328	4
w8	10	302	7
w9	69	296	6
w12	30	418	30

Table 4.5: Average resistances R_{14} and standard deviations σ_R at 77 K for the tested wafers; the number of tested devices is also reported

A deep analysis of the correlation between liquid nitrogen and liquid helium temperature results allowed to determin a selection procedure simply based upon measurements performed at 77 K. Such procedure was derived through a sort of "blind analysis": one of the wafers was chosen as reference, in order to extrapolate some well defined rules of selection, which were then applied to the other wafers and the obtained results compared to those actually attained through the measurements. While performing this analysis the following considerations arose:

- the devices showing at 77 K a value of resistance compatible, within the standard deviation, with the average values reported in 4.5, show a similar behaviour at lower temperatures: such devices, which luckly represent the majority, can be considered as the "good" ones in view of CUORE;
- the devices showing an unusually high resistance value at 77 K generally show an even higher value at lower temperatures, thus resulting unuseful in view of CUORE; this behaviour is more often exhibited by the heaters located at the edges of the wafers, within the dark area in the "shades" map;
- some devices, though showing a finite resistance value at room temperature, turned out to exhibit an infinite resistance at lower temperature, thus needing

to be discarded; the interesting and useful matter consists in the fact that this anomalous behaviour always turns out at 77 K.

- a small fraction of heaters showed a resistance value substantially lower than the average at liquid nitrogen temperature, while resulting to behave like the majority at lower temperatures.

The above considered points drove to the formulation of a well defined selection procedure to be applied at 77 K. Such procedure, which turned out to be effective when tested upon the heaters already characterized, can be summarized as follows:

- select the devices to be tested among those not belonging to the edges of the wafers, in order to maximize efficiency, by evoiding heaters which are more likly to behave in an anomalous way;
- discard the heaters which exhibit an infinite resistance at liquid nitrogen temperature;
- discard the heaters which show at nitrogen temperature a value of resistance higher than a precise value, calculated for each single wafer as:

  $$R_{off} = R_{ave} + 4 \cdot \sigma_R \tag{4.5}$$

  where R_{ave} is the average resistance and σ_R the standard deviation evaluated taking into account only the heaters considered "good" during the previous measurements;
- discard the devices showing at 77 K a resistance value lower than the average, well besides the calculated standard deviation; though this last expedient was not really necessary, it was used only for safe.

Such rules of selection were applied to all the already tested wafers, in order to check their reliability. In figure 4.19 the results obtained by applying this method to wafer 2 are shown as an example. The two plots show the value of resistance measured at 4.2 K and $\sim$ 1.5 K versus the value measured at 77 K. For practical purposes infinite resistances are assigned a fixed value of 1000 KΩ. In both cases it is possible to appreciate the linearity of the relationship linking the values measured at 77 K and at lower temperatures. In the first plot the "good" heaters can be identified since they form a spot precisely located in this bidimensional plane. Heaters showing anomalous behaviours are also visible and can be easily distinguished from the others since they are spread through-out the plane. The second plot shows the heaters selected by applying the previously discussed procedure: the obtained results prove the effectiveness and the reliability of such a procedure.

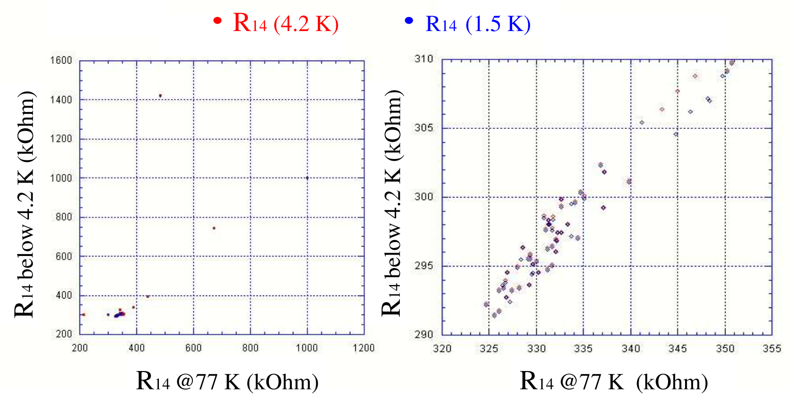

Figure 4.19: Bidimensional plots showing the resistance R_{14} measured at 4.2 K and $\sim$ 1.5 K versus the resistance measured at 77 K for wafer 2. In the first plot the values measured for all the tested devices are reported, while in the second plot only the "good" selected heaters are considered. For practical purposes infinite resistances are assigned a fixed value of 1000 KΩ

Consequently the subsequent characterization could be carried out in a very simple manner, by testing the devices down to 77 K (and no more to below 4.2 K) and using the derived rules of selection. Furthermore, as previously pointed out, the positive results obtained for a significant sample of devices in terms of stability of resistance with varying excitation voltage and in terms of homogeneity through-out the resistive meander, induced to evoid to still take such test for all the devices. As a consequence this new method of action allowed to save a lot of time and money.

By considering all the tested wafers, further interesting considerations arise, concerning the correlation between the low temperature behaviour and the implant splittings reported in table 4.2. Figure 4.20 shows a bidimensional plot of the resistance measured at 4.2 K and $\sim$ 1.5 K versus the resistance measured at 77 K for all the wafers, considering only the "good" selected heaters. The different spots, which can be identified in the bidimentional plane, are easily associated to the corresponding wafers, by using the data (in terms of average resistance and spread) reported in tables 4.5 and 4.4. Globally the resistance measured at 4.2 K and at $\sim$ 1.5 K versus that measured at 77 K shows a linear trend, which can be ascribed to the implant splitting. In particular, the wider spot centered at about 300 KΩ in terms of R_{14} at 4.2 K and $\sim$ 1.5 K, cor-

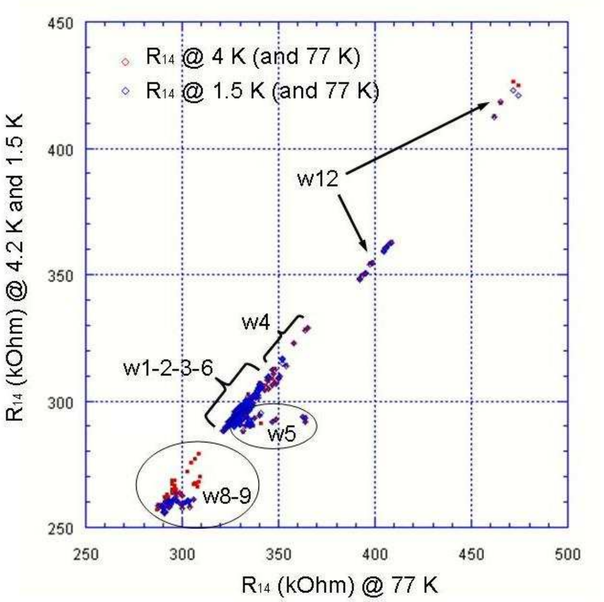

Figure 4.20: Bidimensional plot showing the resistance R_{14} measured at 4.2 K and $\sim$ 1.5 K versus the resistance measured at 77 K for all the wafers; only the "good" selected heaters are considered in this case

responds to wafers 1, 2, 3, 5, 6, which are produced with the same doping level (the intermediate one). These results are also in accordance with the hystogram reported in figure 4.18, where the above mentioned wafers give origin to the main peak. Wafer 5 shows a quite anomalous behaviour, since it does not lay on the straight line formed by the others: actually it shows the same resistance value as the others at 4.2 K and $\sim$ 1.5 K, but an higher resistance at 77 K. Also wafer 4, though belonging to the intermediate doping level, appears in the plot as located in a region corresponding to higher resistence values. The total spread of resistance measured at 4.2 K and $\sim$ 1.5 K, taking into account all the wafers belonging to the intermediate splitting (wafers 1-6), is of about 40 kΩ.

The location of wafers 8 and 9 in the bidimentional plot is actually ascribed to their higher doping level (20% higher than the first splitting). The distance between the center of the spot ascribed to wafers 8-9 and that ascribed to wafers 1, 2, 3, 4, 5, 6 is $\sim$ 50 kΩ, of the same order of the spread shown by the devices belonging to the intermediate doping level. As a consequence, the anomalies showed by wafers

5 and 4 with respect to the others belonging to the same splitting, can be ascribed to disuniformities in the annealing process, as already pointed out (even taking into account that the precision of the implanting machine is about 1%).

Finally the devices belonging to wafer 12 correspond to higher values of resistance with respect to the others, in accordance to the lower dopant concentration (20% less then the intermediate splitting). The resistance values in this case are spread over a quite wide range, in agreement with the data reported in tables 4.5 and 4.4.

The results above discussed concord with the theoretical interpretation of the physical processes taking place in HDS. Furthermore they allowed to inhance the efficiency of the selection process, still proving that the realized heaters match the main requirements in view of CUORE, from a static point of view. Still, the dynamic performances are continously tested, since samples of LTR4 heaters are often used as stabilizing elements during R&D runs. Finally, in order to validate the reliability of such devices at temperatures very close to the operating one, a characterization run below 1 K was carried out, as described in the next section.

4.2.3 Characterization below 1 K

The reliability of LTR4 devices is assured by the static behaviour shown during the characterization down to ~ 1.5 K, together with the good performances shown while operated as stabilizing elements. Nevertheless a characterization similar to the one described in section 4.1.1, performed in the case of the early realized heating devices, was carried out in order to check the stability of resistance at the operating temperature (~ 20 mK) also in the case of LTR4 devices.

The cryogenic set-up

The measurements below 1 K were carried out using a dilution refrigerator (see section 3.2.3) produced by a french company named TBT (Air Liquid group), still located in the Cryogenic Laboratory at Insubria University. Such refrigerator will be better described in section 5.3. In view of the measurements the samples were glued onto a copper holder (see figure 4.21) provided with a calibrated thermometer, already tested and successfully used in the past, then coupled to the mixing chamber of the cryostat. The holder is also provided with a heating element of fixed resistance even at cryogenic temperatures, useful to warm up the whole set-up housing the samples through Joule power dissipation. The devices were ball bonded as usual with 50 μm diameter gold wires in order to provide the electrical contacts.

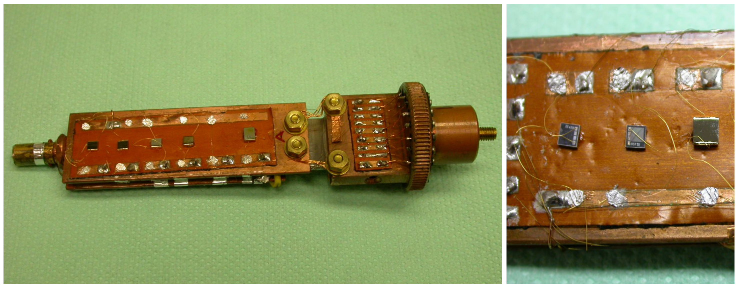

Figure 4.21: Copper holder for the characterization below 1 K with the heaters glued and bonded; other samples (NTD sensors) cheracterized during the same cool down run are also visible

For practical reasons, related to lack of space and electronic connections, only two heaters were prepared for the characterization. Unfortunately one of them got lost during the cooling down, so that only one device, belonging to wafer 1, was actually tested.

The two following measurements were performed:

- load curves similar to those traditionally realized during the characterization of semiconductor thermistors, in the temperature range between 15 and 100 mK, by injecting into the tested device a bias current corresponding to a voltage across the heater in the range $3 - 50$ mV (of the same order of the voltage across the heaters while operated as stabilizing elements);

- static measurements of the resistance at a fixed temperature, by applying a wide range of bias voltages through a circuit similar to the one shown in figure 3.1, but provided with two symmetric load resistances instead of one; voltages across the heater as high as ~ 5 V were obtained in this case; although these conditions does not correspond to the operating ones, the results allowed to appreciate the good match between the two investigated voltage ranges.

The first measurement was performed by means of an automatic acquisition system, able to remotely control the electronic apparatus devoted to the realization of the load curves. This set-up, which will be better described in section 5.3, includes a polarization circuit more complex than the one of figure 3.1, which allows to select the best suited load resistance among a defined range. It is also provided with a preamplifier for the measurement of the voltage produced across the device. A digital multimeter measures both the applied and the produced voltages, which are then recorded by the automatic acquisition program, together with other useful informations (i.e. load resistance, calculated Joule power dissipated, calculated bias current and calculated resistance). The automatic acquisition system is able to control the sequence of operations necessary to determin the whole load curve, by implementing the bias voltage applied step by step.

The temperature of the holder, and thus of the tested devices, can be varied by dissipating a proper Joule power into the heating resistor using a TS-530A temperature controller (by Picowatt), which cooperates with the the AVS-47 bridge (as better described in 5.3).

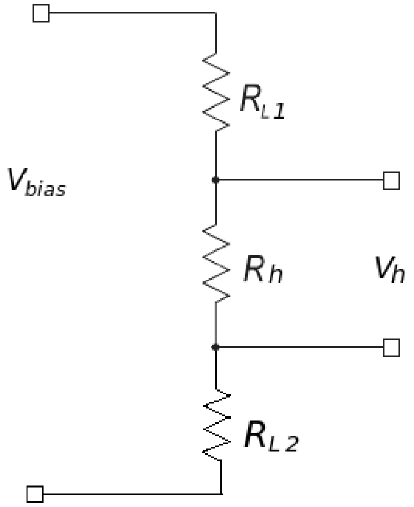

Figure 4.22: Polarization circuit used to measure the heater resistance; R_{L1} and R_{L2} represent the load resistances of the circuit, through which the polarizing constant current flow across the device is generated

The second measurement was performed manually at a fixed temperature (in the range $15-100$ mK) attained by dissipating into the heating resistor a Joule power less than 1 μW. A series of bias voltages V_{bias} in the range 50 mV and 10.5 V was injected into the tested heater, through a circuit provided with two symmetric load resistances R_{L1} and R_{L2} (see figure 4.22), each of order $1/2$ the expected resistance of the device under test (from the results obtained at 4.2 K). The value of the two load resistances was chosen in order to be able to produce the desired voltage across the heater. Both the bias voltage and the one produced across the device were measured by means of a digital multimeter. The resistance of the heater can be evaluated using the following expression:

$$V_h = R_h \cdot I = R_h \cdot \frac{V_{bias}}{R_{L1} + R_{L2} + R_h} \tag{4.6}$$

where R_h is the resistance R_{14} of the heater under test, V_h and I the voltage and current flow generated across the device by the injected bias voltage.

With the condition $R_{L1} \sim R_{L2} \sim R_h/2$, and assuming $R_L = R_{L1} + R_{L2}$, from equation 4.6 one gets:

$$R_h = \frac{R_L \cdot V_h}{V_{bias} - V_h} \tag{4.7}$$

The Joule power dissipated into the device due to the measurement can be evaluated as:

$$P = \frac{V_h^2}{R_h} \tag{4.8}$$

which provides an estimate of the heating power due to the measuring procedure and can be compared to the Joule power dissipated into the heating resistor.

Results

Figures 4.23 and 4.24 show respectively the trend of the heater resistance measured using the automatic load curves acquisition system as a function of the voltage produced across the device and of the dissipated Joule power. The load curves were determined at various temperature stages (in the range 15 – 100 mK) by injecting a Joule power varying between $10^{-7} - 10^{-6}$ W into the heating resistor. In both figures are reported the results related to five temperature stages: four obtained in correspondence to the lower temperature stages, one in correspondence to the highest.

The trend of resistance versus injected power reproduce the same observed in the case of the precursor devices, shown in figures 4.1 and 4.5. The plot tends to reach a plateaux corresponding to the value of resistance previously measured at 4.2 K ($\sim$ 295 kΩ). Furthermore the device shows a very good stability of resistance with changing temperature, still higher than the one observed in the past.

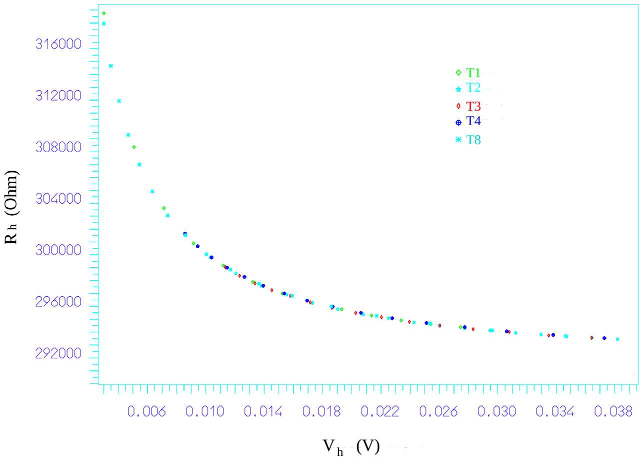

Figure 4.23: Resistance R_h as a function of the voltage V_h measured, at various temperatures, by means of the automatic acquisition system for the determination of the load curves

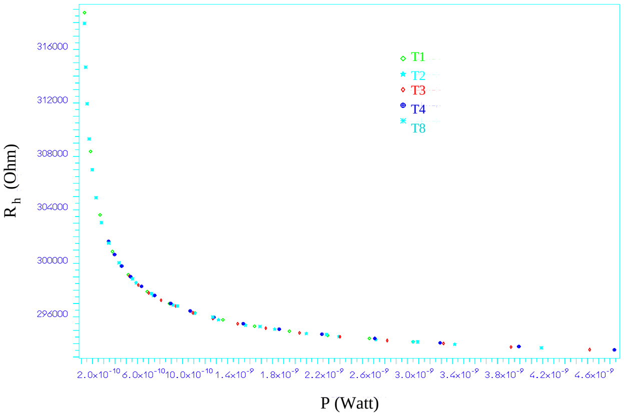

Figure 4.24: Resistance R_h as a function of the dissipated Joule power measured, at various temperatures, by means of the automatic acquisition system for the determination of the load curves

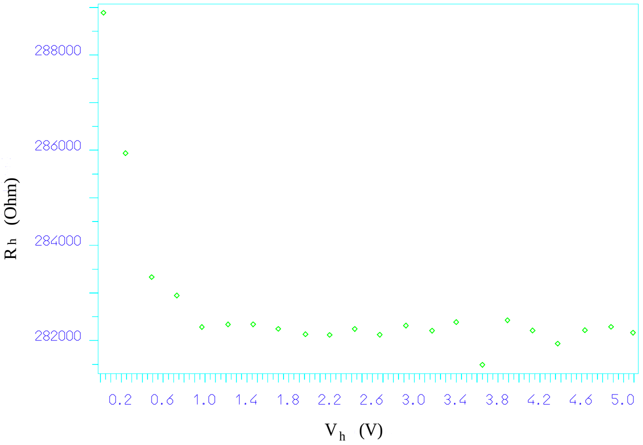

Figure 4.25: Resistance R_h evaluated using equation 4.7 as a function of the voltage V_h measured across the device for a fixed temperature of the holder

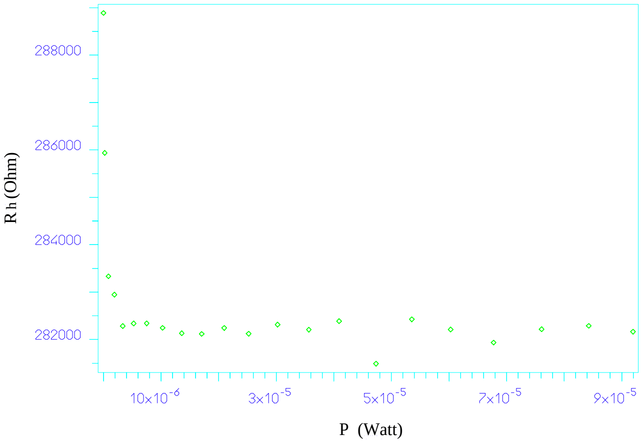

Figure 4.26: Resistance R_h evaluated using equation 4.7 as a function of the dissipated Joule power P evaluated from equation 4.8 for a fixed temperature of the holder

Figures 4.25 and 4.26 refers to the second measurement performed. They show respectively the trend of the heater resistance evaluated using equation 4.7 as a function of the voltage measured across the device and of the dissipated Joule power. Such measurement was performed at a fixed temperature of the holder, corresponding to a Joule power dissipated into the heating resistor of ~ 1 μW and was carried-out in 22 steps, by varying the bias voltage injected into the tested heater. The corresponding Joule power dissipated into the device, as a consequence of the measuring procedure, is in the range $10^{-9} - 10^{-5}$ W. The measuring procedure is likly to warm-up the sample at least when the dissipated power is of the same order or exceeds the power injected into the heating resistor.

The obtained results show a very good stability of resistance ($\sim$ 2%) with changing injected power. Furthermore the difference between the asymptotic value, equal to 282 kΩ, and the resistance measured at 4.2 K ($\sim$ 295 kΩ), can be ascribed to the heating effect of the Joule power dissipated in the former case.

4.3 EXAMPLES OF BOLOMETERS STABILIZATION

In the present section a practical example of the stabilization procedure performed with an LTR4 heater is described. The considered detector was realized in the context of CUORE R&D activities, more precisely in view of the run named CCVR (Chines Crystal Validation Run), carried-out in a devoted cryostat in hall C at LNGS. The set-up consists in a group of four TeO_2 crystals, each provided with two NTD thermistors and one heater (see figure 4.27). For the purpose of this thesis one single bolometer will be considered, and in particular the data acquired by one of its two thermistors.

The configuration of the set-up was developed in order to operate in parallel two heaters coupled to two different crystals, which means that the same electronic channel is used for them. Consequently they are injected the same bias voltage: this fact implies that the two heaters should show a quite similar resistance value, in order to produce an energy pulse with similar amplitude (remember equation 4.1). It is for the same reason that a good homogeneity of resistance among the heaters is required in view of CUORE: in that case in fact 13 heaters will be operated in parallel.

In view of the CCVR run the pulse generator was programmed in order to inject into the considered heater a square voltage pulse of amplitude 2.05 V and time width 1 ms every 5 minutes. From equation 4.1, taking into account the attenuation factor on the bias voltage provided by the electronic set-up (thus producing a voltage across the heater of order 10 mV) and the heater resistance ($\sim$ 300 kΩ), the energy of the pulse

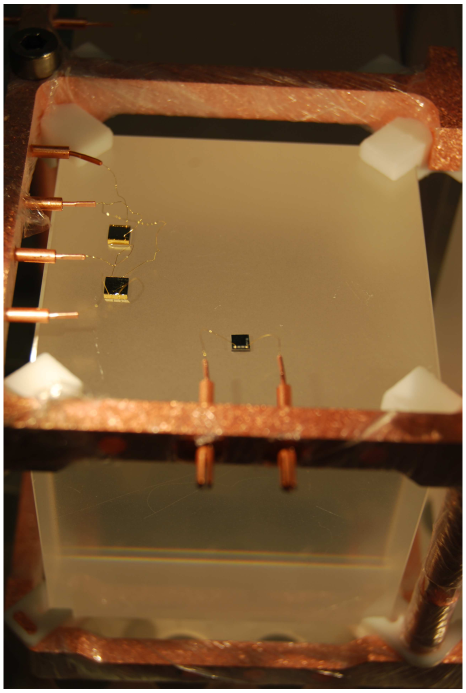

Figure 4.27: TeO_2 bolometer provided with two NTD thermistors and one heater

can be evaluated by the following expression:

$$E_h[\text{Joule}] = \frac{(2.05/200)^2}{300 \times 10^3} \times 0.001 \tag{4.9}$$

corresponding to a developed pulse energy of 1287 keV.

Figure 4.28 shows the trend of the pulse energy of the heater as a function of the baseline level and the peak which, in the energy spectrum, accounts for the heater pulses. The obtained results concord with the expectations, as discussed in section 2.3.1. In the left plot the heater pulse energy appears as a monolitically decreasing function of the baseline. In the right plot the efficiency of the stabilization procedure is put into evidence, by comparing the peak produced by the heater pulses before and after applying the corrections.

Figure 4.29 still shows the results obtained by applying the stabilization procedure to two background peaks: ^{40}K γ line at 1460 keV and ^{208}Tl γ line at 2615 keV. In both cases the energy resolution was implemented by $\sim$ 20%.

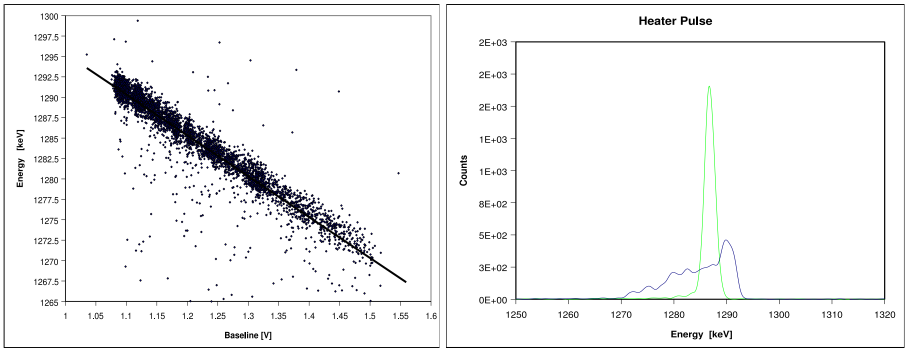

Figure 4.28: Left plot: pulse energy of the heater as a function of the baseline level; right plot: peak produced by the heater pulses before (blue line) and after (green line) applying the corrections

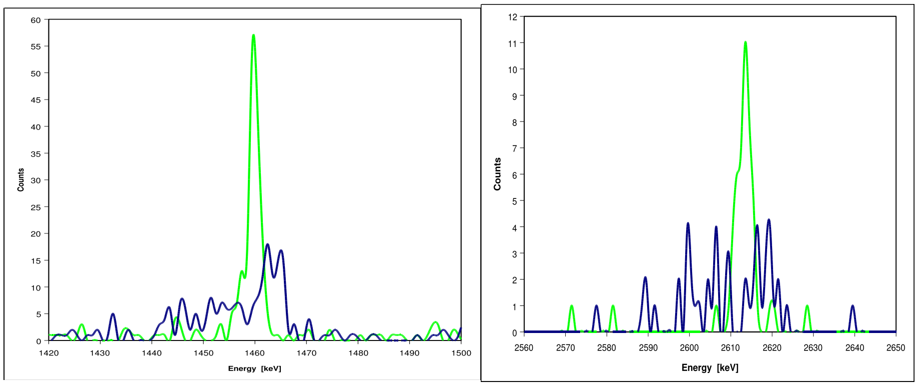

Figure 4.29: Two background peaks before (blue line) and after (green line) applying the stabilization procedure; left plot: ^{40}K γ line at 1460 keV; right plot: ^{208}Tl γ line at 2615 keV

CHAPTER 5

THERMISTORS: LOW TEMPERATURE CHARACTERIZATION AND EXPERIMENTAL RESULTS

This chapter deals with the characterization of silicon implanted thermistors, operating in VRH regime, in view of their application for the developement of microcalorimetric detectors, in the context of the MIBETA2 experiment (see 2.2.4). The motivations which led to realize an experiment based on a large array of microbolometers were discussed in the devoted sections (see 2.1 and 2.2). On the other hand, sections 3.1 and 3.2 investigate more in depth the required characteristics of semiconductor thermistors, still in the context of their application for the developement of microcalorimetric detectors.

In the first part of this chapter the status of the art, concerning the silicon thermistors to be implemented in microcalorimetric detectors, is discussed. The aim of sections 5.1, 5.2 and 5.3.1 is to put into a clear context the experimental results and prospects drawn during this thesis work.

The various attempts performed in the context of the MIBETA experiment, together with the experimental results so far obtained, concerning the realization of silicon implanted thermistors coupled to microbolometers, are described in 5.1. The subsequent sections deal with the techniques presently adopted or under study for the realization of the silicon thermistors to be used in the context of MIBETA2, by describing their characterization and the results obtained by the MIBETA collaboration. To be specific section 5.2 deals with the silicon implanted thermistor array fabricated by NASA, which is being presently used for the first part of the MIBETA2 experiment.

Finally, the real subject of this thesis, besides the characterization of the CUORE heaters (presented in chapter 4), is treated in details in the last part of section 5.3, which deals with the fabrication, characterization and performance study of the array of ten silicon thermistors produced by ITC-irst.

5.1 MIBETA DETECTORS

In the context of the MIBETA experience, before setting-up the final experiment, several attempts were performed in order to find the most suited detector configuration. To fulfil this task, several metallic rhenium absorbers were initially tested, coupled to both Ge-NTD and Si:P thermistors, with different forms and using several types of glues (Stycast, Araldit, Silver Epoxy[1]). Since all these experiments gave no satisfactory results (it was never possible to get energy resolutions better than 70 eV FWHM at 6 keV) the MIBETA group decided to move to dielectric absorbers, to be specific to $AgReO_4$.

Silicon thermistors doped by ion implantation were adopted as thermometric elements for the developement of the MIBETA experiment, due to their proved extreme sensitivity and to their high reproducibility, obtained by means of the microelectronics technology. Nevertheless detectors using different thermal sensors were tested. In particular very interesting results were obtained with a Ge-NTD flat-pack sensor, fabricated by J. W. Beeman at the Lawrence Berkeley Laboratory, coupled to an $AgReO_4$ crystal. The principle of operation of both Si implanted and Ge-NTD sensors has been already explained in chapter 3, where also the methods for their characterization were described.

Figure 5.1 shows the single detector configuration used in MIBETA: in the left picture the top of the silicon thermistor is visible, while in the right picture the bottom with the glued $AgReO_4$ crystal is shown. The 4 bonded Al wires (2 mm long and with 17 μm diameter), used for the thermal and electrical coupling, are also visible. The mass of each single crystal was of about 300 μg, ideally suited for the experimental conditions. The silicon implanted thermistors were fabricated by the MEMS group at

---

[1] All these glues share characteristics which make them useful for cryogenic purposes, providing in primis a good thermal link; they differ in some other aspects, such as their coefficient of thermal expansion or their adhesive properties

ITC-irst. Figure 5.2 shows the structure of the sensor, which consists of a sensitive volume doped just below the MIT (which represents the true thermistor), two smaller volumes doped well above the MIT, providing a low resistance electrical contact, and two superconducting metal pads, which allow to bond the connection wires. These thermistors show the steep temperature dipendence of resistance typical of the VRH regime, given by equation 1.18, at the bolometers operating temperature. They have a T_0 of about 3.3 K and an implant area of 600×600 μm^2 or 800×800 μm^2. Such characteristics were carefully selected among large available ranges, in order to optimize the detector performances, according to the procedure described in section 3.2.1.

The fabrication process developed at ITC-irst for the realization of the MIBETA thermistors, as well as their properties, will be discussed in details in section 5.3, since they represent the precursors of the thermistor arrays produced in view of MIBETA2.

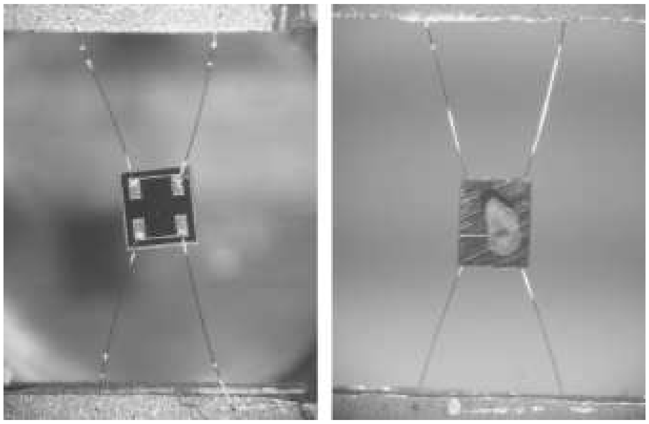

Figure 5.1: Left picture: top of the silicon thermistor, used for MIBETA; right picture: bottom of the silicon thermistor with the glued $AgReO_4$ crystal, used for MIBETA

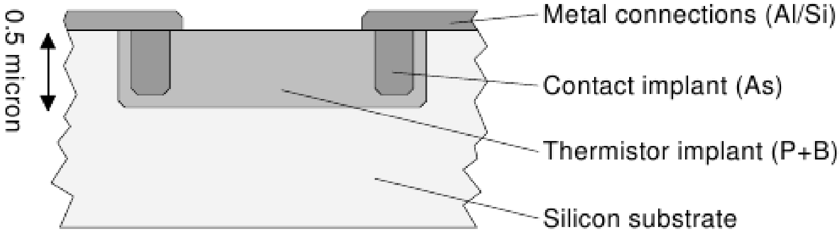

Figure 5.2: Cross section of the silicon implanted thermistor fabricated by ITC-irst

Taking into account the MIBETA results, an R&D work has been carried out in order to develop large silicon implanted thermistor arrays in the context of the first phase of the MARE project, by using micromachining techniques. The aim of this R&D work has been the improvement of the properties of such devices, in order to make them well suited for the realization of a large number of similar detectors: thus homogeneity represents one of the main requirements. Furthermore the devices should be suited to be coupled to crystals of larger mass (0.45 mg) and easy to be handled, since a great number of detectors is going to be prepared. The use of micromachining allowed to realize arrays of sensors, with integrated structures to be used as thermal and electrical links, so that no further additional connections are needed (see section 3.1.3). In the next sections the two techniques adopted for the developement of silicon thermistors, in the context of MIBETA2, will be discussed.

5.2 NASA THERMISTORS

The silicon implanted array presently being used for the first phase of the MIBETA2 experiment has been produced by NASA/GSFC. It was originally developed for the XRS2 (X-Ray Spectrometer) to be flown on Astro-E2 in the year 2005. The XRS2 array was developed using three innovative technologies applied for the first time to silicon implanted microcalorimeters:

- deep reactive-ion etching (DRIE) together with silicon-on-insulator (SOI) wafers to produce 1.5 μm thick free standing pixels with complex shapes without mechanical stress;
- uniform sensor doping throughout the pixel 1.5 μm thickness;
- SU8 structural polymer photolithographically shaped for the absorber mounting points.

By combining the above mentioned technologies a great improvement in the detector performances has been obtained, in particular a substantial increase of the electron-phonon coupling, the elimination of any low frequency excess noise and a greater reproducibility. As a result a remarkable performance of the XRS2 instrument was obtained, as shown in figure 5.3.

The NASA silicon array consists of a grid of 36 suspended pixels (see figure 5.4), each 1.5 μm thick, with an ion-implanted 300×300 μm^2 sensor. Figure 5.5 shows the

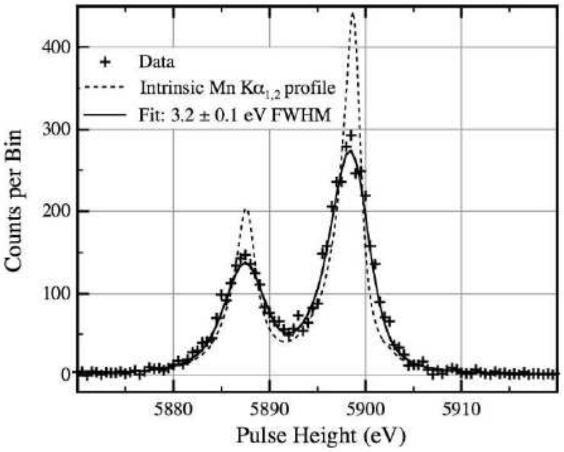

Figure 5.3: Separation of the MnK$_\alpha$ line in its two components in a spectrum collected with a XRS2 array element

single element, with its four thin silicon beams providing the thermal links to the heat-sink and the respective ion-implanted traces for the electrical connections. The four absorber support tabs, with the SU8 polymer absorber spacers, are also visible. The array design is very strong in the axial direction.

The measured thermal conductance of the silicon beams is of about 7×10^{-11} W/K at 100 mK (the typical operating temperature of the considered microcalorimeters). The thermistors show a temperature dependence of resistance given by equation:

$$R(T) = R_0 \exp\left(\frac{T_0}{T}\right)^{\gamma} \tag{5.1}$$

with $T_0 = 1.035$ K, $R_0 = 2737.12\ \Omega$ and $\gamma = 0.7954$. The resulting value of γ thus differs from the expected one for a sensor operating in VRH regime, which considering the Coulomb gap behaviour should equal $1/2$. This fact has been observed also in other cases and different theoretical interpretations were suggested [46], without driving to a definite conclusion. Since for thermometric purposes it is convenient to have an analytic expression, properly fitting the data, the following empirical function was derived:

$$R(T) = R_0 exp\left(\frac{T_0}{T}\right)^{1/2} + R_0' exp\left(\frac{T_0'}{T}\right)^{1/2} \tag{5.2}$$

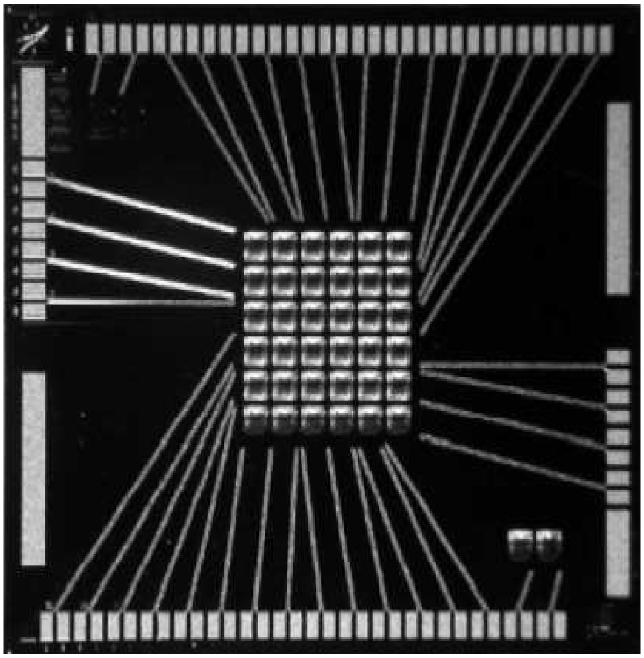

Figure 5.4: 6×6 NASA XRS2 array

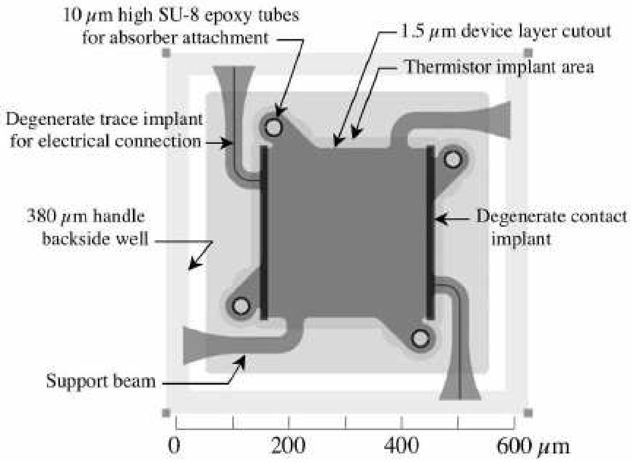

Figure 5.5: The single pixel of the NASA XRS2 array

where the parameters extrapolated in the case of the XRS2 array are:
$R_0 = 270\ \Omega$
$T_0 = 7.2$ K
$R_0' = R_0 exp(2.522 T_0^{-0.25} - 8.733)\ \Omega$
$T_0' = 2.715 T_0 + 1.233$ K.

Some preliminary test performed in Milan, with the aim of studying the best suited thermistor-absorber coupling technique, showed that the crystals can not be fit on all four the SU8 supports simultaneusly, neither in the space between them, because of their irregular shapes. In order to solve this problem two different approaches were tested (see picture 5.6):

- the first one consisted in gluing 0.5×0.5 mm^2 wide and 18 μm thick silicon chips on all four SU8 supports using epoxy resin ST1266; the $AgReO_4$ crystals were then glued upon these platforms using different kind of epoxy resins;
- the second one consisted in gluing 0.3×0.3 mm^2 wide and 10 μm thick silicon chips directly to the thermistors, thus acting as a kind of spacers fitted between the four SU8 supports; in this case different kind of glues were used for both the thermistor-spacer and the spacer-absorber coupling.

For the test, $AgReO_4$ crystals of mass ~ 0.45 mg were used. Measurements at several working temperatures, between 60 and 110 mK, were performed in the Cryogenic Laboratory at Milano Bicocca University, the aim of which consisted in the optimization of the operating conditions, based on the considerations discussed in section 3.2.1. The detectors were operated with a voltage across the thermistors of about 1.7 mV (corresponding to a temperature of about 85 mK). The performed measurements can be divided into two main runs: one refers to the year 2006, the other one to the year 2008. During the devoted cool down runs the following general results arose:

- the detectors maden with the platforms glued on the four SU8 supports showed very slow and small pulses due to the weak thermal link provided by the SU8 themselves;
- the detectors realized using the second technique above described showed much better performances;
- the best trade off operating temperature is around 100 mK, with target resistance of order 1 MΩ;

- the best and most homogeneous results were obtained by gluing spacers on thermistors using araldit and crystals on spacers using Stycast 2850.

The most interesting results, in terms of rise time, energy resolution and operating temperature, are reported in table 5.1. The data referring to the year 2008 do not reproduce "in toto" the results obtained in the year 2006: in particular the rise time when considering 2008 data is generally higher if compared to 2006 data, referring to the same detector configuration. Furthermore figure 5.7 shows the energy spectrum obtained with one of the best tested detectors operated at 85 mK.

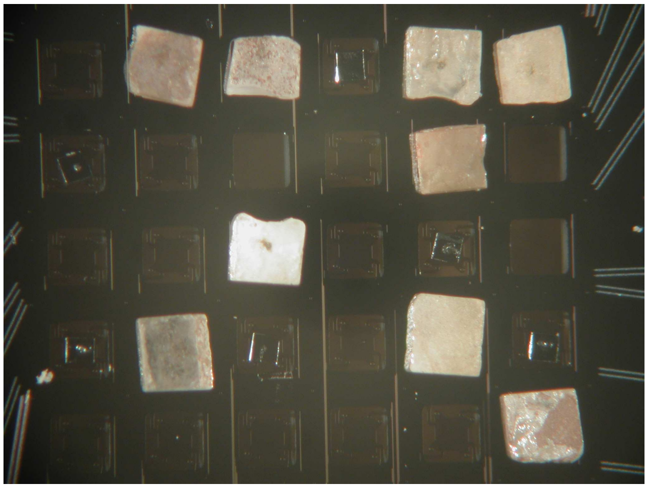

Figure 5.6: NASA XRS2 array with glued $AgReO_4$ crystals over some pixels

Considering the good results obtained with the NASA XRS2 array, the first part of the MIBETA2 experiment is being developed using these thermistors. Nevertheless, in parallel with the characterization of the NASA thermistor array performed in Milan, an alternative production process has been carried out at ITC-irst, based on the implementation of the thermal sensors used for the MIBETA experiment. The importance of such parallel activity lays in the opportunity to develop a complitely indipendent methodology, which is, furthermore, "home-maden" and specially devoted. In the next section the ITC arrays are discussed, starting from a description of the precursor devices. A discussion about the characterizations performed in the Cryogenic Laboratory at Insubria University, representing one of the two subjects of this thesis, will follow.

Det # & year	AgReO$_4$ mass (μg)	glue	T_{op} (mK)	R_{op} (MΩ)	τ_r (μs)	baseline (eV)	ΔE @1.5keV (eV)	ΔE @2.6keV (eV)
1 ’06	402	A/A	79	6.5	410	11	19	24
			85	4.2	310	14	21	28
			94	2.3	230	21	28	31
2 ’08	402	A/A	85	3.3	280	27	29	31
3 ’08	388	A/A	85	4.2	410	47	–	50
4 ’06	456	A/S1	77	7.2	450	17	27	35
			84	4.4	350	21	30	37
			93	2.5	260	30	37	44
5 ’08	497	A/S1	85	4.6	500	33	37	31
6 ’08	381	A/S1	85	4.0	500	18	25	33
7 ’08	421	A/S1	85	–	560	27	29	32
8 ’06	406	S2/S1	79	6.5	410	16	28	37
			85	4.0	320	22	33	38
			94	2.3	240	31	41	48
9 ’08	384	S2/S1	85	3.3	370	27	33	45
10 ’06	430	S1/S1	80	5.8	700	132	30	39
			86	3.7	600	132	35	41
11 ’06	390	SU8/S2	84	4.2	750	113	30	39
			91	2.7	650	113	35	41

Table 5.1: Results in terms of rise time (τ_r), energy resolution (ΔE) at 1.5 keV and 2.6 keV, operating temperature (T_{op}) and operating resistance (R_{op}) for the most interesting cases of the tested detectors; the following conventions are used for the glues: the first letter stands for the glue used between sensor and spacer, while the second stands for the glue used between spacer and crystal; A stands for Araldit, S1 stands for Stycast 2850, S2 stands for Stycast 1266; the tested detectors are identified with a number and the year (’06 or ’08) of the measurement

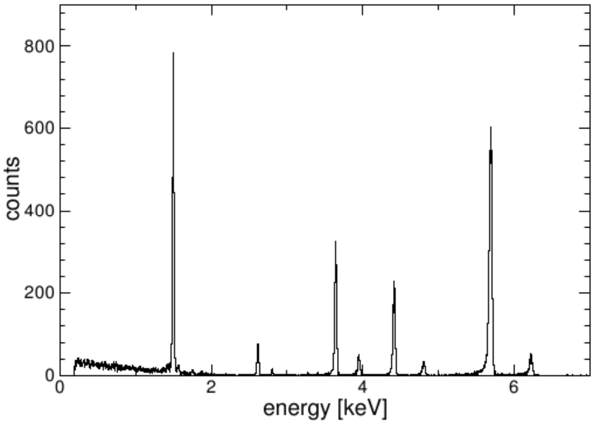

Figure 5.7: Energy spectrum obtained with the best tested detector operated at 85 mK

5.3 ITC-IRST THERMISTORS

The collaboration between the MIBETA group and ITC-irst started in the year 1992, aiming at the realization of highly sensitive thermal sensors to be used for the developement of large microcalorimeter arrays. Several production runs have been carried out at ITC in order to define the best suited process, assuring that the realized devices match the experimental requirements (see section 3.2.1). From now on the production runs will be referred to as BL (which stands for BoLometer) followed by a number, assigned by following the order of fabrication. The early runs were devoted to define the implant doses and the annealing procedures, and to identify the optimum combination of R_0 and T_0, by properly adjusting the doses and the implant geometries. During these early production processes, only single chip thermistors, similar to those reported in figures 5.1 and 5.2, were realized. Once obtained the desired optimum performances, by testing the fabricated devices at low temperatures, the chosen thermistors were used for the developement of the MIBETA experiment. In the meantime, further production runs were carried out, aiming at the fabrication of arrays of thermal sensors by means of micromachining techniques, in view of the MIBETA2 experiment.

The first part of this section is devoted to summarize the early production processes and the related results obtained through the characterization of the early fabricated devices, which represent the precursors of the thermal sensors studied in this thesis. The description of the thermistors actually characterized during this thesis work will follow, together with the results of their characterization at low temperatures. Finally the performances of such devices, while operated as detectors, will be discussed.

Before entering into the details of the specific devices produced and tested, it will be useful to remind which are the main requests the studied devices should match:

- homogeneity and reproducibility among the various sensors, with the same characteristics in terms of doping level and geometry, must be proved: this can be easily tested down to ~ 1.5 K (instead of more difficult measurements below 1 K);
- they must show the temperature dependence of resistance typical of the VRH regime, without excessive deviations from the theoretical expectations: this is linked to the shape of the impurity profile of the single sensors, which must be uniform and approximate the so called *box profile* (see 5.3.1);
- the characteristic parameters, determined through a static characterization carried out below 1 K (as discussed in section 3.2.1), should conform to the requirements for the optimization of the detector performances.

Finally, the results obtained from the above discussed measurements, should be used for a correct interpretation of the dynamic behaviour of the thermistors, while operated as detectors.

5.3.1 Precursor devices

Technological characterization of precursor devices

The early attempts to realize silicon implanted thermistors in view of their application to microcalorimeters, in the context of the MIBETA-ITC collaboration, are reported in [57, 58]. The first important request which such devices must accomplish deals with the steep temperature dependence of resistance, typical of VRH regime, they must show at cryogenic temperatures. In order to exploit this, well known and controlled amounts of impurities should be introduced in the initial semiconductor material, in order to provide a concentration close to the critical one, signing the metal-to-insulator transition. In most cases it is also useful to introduce compensating elements, which favour the activation of the VRH regime and which influence the values of R_0 and T_0. In the considered case the thermistors are based on the Si:P system, with boron used as compensating element.

While defining the production process it is of crucial importance to consider that the doped volume must be highly uniform and as deep as possible: local fluctuations of the concentration of dopants could otherwise produce alternative paths for the charge transport, thus causing significant deviations from the theoretical $R(T)$ curve. It is furthermore important to maximize the electrons-lattice coupling, parametrized by the thermal conductance G_{ep}, which is proportional to the implant volume (coinciding with the sensitive region of the thermistor).

The above mentioned characteristics depend exclusively on the instruments used for the implant fabrication and from the implantation and annealing parameters. In order to provide a deep and uniform implantation, it is important that the concentration of dopants through the sensor volume approximates the so called *box profile*, with a large and flat maximum, then quickly decreasing at the bottom of the implanted region. The tails of the profile should be reduced since they do not contribute to the electrical conduction, but only to the heat capacity.

The most suited technique for the realization of the *box profile* of dopants concentration consists in the multiple ion-implantation. Once fixed the thermistor thickness to 0.5 μm, the number of single implants to 5, and the overall implant concentration and compensation value, the necessary doses and energies for each implant can be determined with the help of a simulation tool (SUPREM3). In figure 5.8 the simulated profiles are shown, both for phosphor (for a concentration of 3.5×10^{18} ions/cm^3) and boron (for a 30% compensation) implants. The energy and doses for each implant, referring to the same case, are reported in table 5.2. Furthermore highly doped regions must be produced to provide the ohmic contacts: this is accomplished by one single arsenic implantation.

For all the considered production runs performed at ITC, the silicon substrate consists of a wafer of p-type Si $\langle 100 \rangle$ CZ, with a 20 Ω·cm resistivity. The nominal bulk boron concentration is 8×10^{14} ions/cm^3. The wafers have a diameter of 10 cm and thickness 525 μm. Upon each wafer a fixed number of devices is realized, together with a certain number of test structures, used to control the various steps of the process. During each production run a series of wafers is realized, each corresponding to a well defined implant dose and value of compensation, linked to the resistivity and to T_0. The various single thermistors belonging to each wafer can still differ for their geometry, which is linked to the value of the resistance (see section 3.1.2) and to G_{ep}. In order to allow the fabrication of a large number of squares upon a limited area, the sensitive region of the devices is devided into a certain number of strips by the presence of interposed metallized tracks, as shown in figure 5.9. This structure determines the ratio between the fixed length (TL) and the width (TW multiplied by the number of strips) of the doped region, equal to the square number.

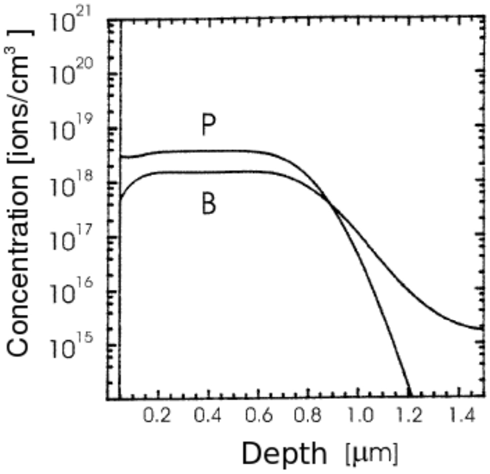

Figure 5.8: Simulated profiles for the phosphor and boron implantation, obtained with SUPREM3, for an overall P implant concentration of 3.5×10^{18} ions/cm^3 and a B compensation of 30%

P implant concentration: 3.5×10^{18} ions/cm^3		
Dopant	Energy (keV)	Dose ($\times 10^{13}$ ions/cm^2)
P	400	11.2
P	250	5.43
P	160	3.46
P	105	2.15
P	60	1.68
B compensation: 30%		
Dopant	Energy (keV)	Dose ($\times 10^{13}$ ions/cm^2)
B	270	2.74
B	170	1.75
B	85	1.61
B	50	1.12
B	20	1.19

Table 5.2: Implant doses and energies used for the production runs BL1, BL2, BL3 to obtain an overall P implant concentration of 3.5×10^{18} ions/cm^3 and a B compensation of 30%

The aim of the first two production processes, BL1 and BL2, was to define a calibration of the implant doses and annealing procedures. For this reason various implant concentrations, compensation values and annealing conditions have been tested. The geometry of BL1 and BL2 sensors consisted of an implanted area of $2500 \times 2220\ \mu\text{m}^2$, with square number n equal to 0.008 (see figure 5.10).

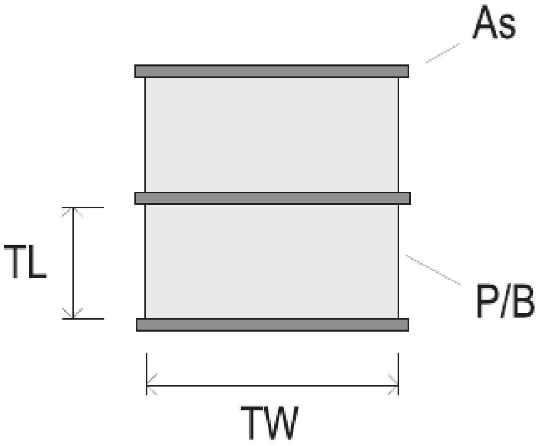

Figure 5.9: Definition of the dimensions and structure of the BL thermistors

Measurements performed at room temperature, taking advantage of the presence of the test structures, allowed to estabilish the best suited annealing parameters (temperature and atmosphere) producing a complete activation of the implant and a concentration profile as similar as possible to the one of figure 5.8. During the low temperature characterization some further considerations arose, such as the presence of side conduction channels and a not well defined geometry. Consequently some options of the fabrication procedure have been modified, in order to get rid of these defects. The complete production process, defined through these early test and applied to the subsequent runs, is described in table 5.3. Still various annealing options have been tested, as shown in table 5.4, as well as various implant energies and doses (both for P and B).

The results obtained during the subsequent production runs induced to take the final decision to choose option 2 of table 5.4, which forsee an annealing step in wet atmosphere at 1000 °C. This choice assures an initial diffusion of the dopants, thanks to the strongly oxidant atmosphere, which provides a larger extension of the implant profile if compared to the other options. However, during the more recent production runs (BL9 and BL10), still two different possibilities have been tested, distinguished

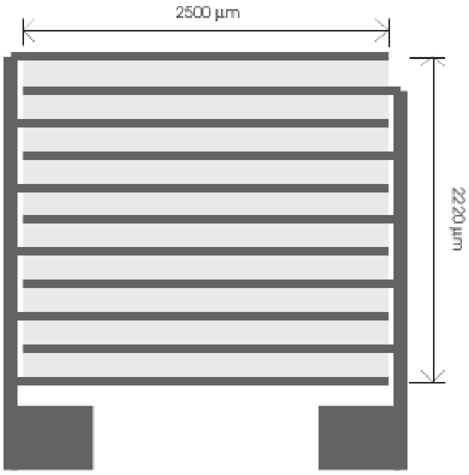

Figure 5.10: Classical geometry for the devices produced during the first two runs (BL1 and BL2)

only by the duration of the annealing step in O_2/H_2 atmosphere. To this purpose option 2 has been applyed to all the wafers, but with an annealing time for the step in O_2/H_2 varying, from wafer to wafer, between two values: $4'15$" and $2'15$". Furthermore, the post-annealing step (1000 °C in N_2 atmosphere) has been applyed only to a certain fraction of wafers.

The early measurements performed at low temperatures, induced also to limit the range of the implant doses and compensations, thus allowing to perform a more refined and detailed screening among the interesting values. The shape of the single thermistors has been modified as well, by varying their volume and their geometries. Figures 5.11 and 5.12 show the geometries defined for the devices produced respectively during the early and the more recent runs. Each thermistor is identified by a group of three characters: the first one refers to the wafer, the second one refers to the volume, the third one refers to the square number. The meaning of the second and the third characters are shown in table 5.5 and 5.6. Concerning the wafers, the specific characteristics change from run to run. The experimental results, obtained with the thermistors produced during the early runs, showed that the performances of the detectors are optimized by the devices with larger volumes and square number (as later explained). For this reason the production of the smaller thermistors was abandoned, while new and larger dimensions began to be realized.

Finally, the overall P implant concentration has been defined and fixed to $\sim 3.5 \times$

Step #	Description
1	Screen oxide growth: SiO_2, 43 nm
2	Implant: channel stop (B); this technique is used to prevent the formation of conductive channels, and consists in implanting, above the whole wafer, a small amount of boron with low energy (see [47] for details)
3	Mask oxide growth: SiO_2, 1000 nm
4	Photolithography: diods definition (1)
5	Wet etch to remove SiO_2 with HF (7:1)
6	Plasma ashing to remove photoresist
7	Sacrificial oxide growth: SiO_2, 23 nm
8	Photolithography: degenerate contact region definition
9	Contact implant: As ions, energy 110 keV, dose = 5×10^{15} ions/cm^2
10	Plasma ashing to remove photoresist
11	Thermal activation of the implant
12	Photolithography: diods definition (2)
13	Wet etch to remove SiO_2 (sacrificial oxide) with HF (7:1)
14	Thermistors multiple implant (P)
15	Plasma ashing to remove photoresist
16	Photolithography: compensated region definition
17	Wet etch to remove SiO_2 with HF (7:1)
18	Compensation multiple implant (B)
19	Plasma ashing to remove photoresist
20	Wet etch to remove SiO_2 (mask oxide) with HF (7:1)
21	Thermal activation of the implant
22	LPCVD-TEOS 718 °C deposition: SiO_2, 500 nm
23	Photolithography: contact areas definition
24	Wet etch to remove SiO_2 with HF (7:1)
25	Plasma ashing to remove photoresist
26	Pre-metal deposition cleaning: wet etch with HF (50:1) for 30 s
27	Al:Si deposition (1200 or 600 nm): sputtering at 225 °C
28	Photolithography: metal definition
29	Dry etch with plasma of Al:Si
30	Freckle etch of Al:Si
31	Wet etch with HF (10:1) for 10 s (cleaning)
32	Plasma ashing to remove photoresist
33	LPCVD-LTO 430 °C deposition: SiO_2, 500 nm

Step #	Description
34	Photolithography: contact areas definition
35	Wet etch to remove SiO_2 with HF (7:1) and TI (1:1:1)
36	Plasma ashing to remove photoresist
37	Coating frontside with photoresist
38	Wet etch with HF (7:1) to remove backside oxide (SiO_2)
39	Plasma ashing to remove photoresist
40	Al:Si Thermal treatment

Table 5.3: Complete production process for BL thermistors, as defined from the early fabrication runs

Option #	Temperature (°C)	Duration (min)	Atmosphere
1	920	15	N_2/O_2
	920	15	O_2/H_2
2	1000	15	N_2/O_2
	1000	5	O_2/H_2
	1000	10	N_2
3	900	15	N_2/O_2
	900	20	O_2/H_2
	900	30	N_2

Table 5.4: Annealing options for thermistor implant activation (both P and B); step number 14 and 18 of table 5.3

10^{18} ions/cm^3, thus varying only the degree of compensation from wafer to wafer. This allowed to perform a more pricise screening of T_0.

Low temperature characterization of precursor devices

The aim of this paragraph is to summarize the results (reported in [48]) obtained with the more recently realized thermistors (BL9 and BL10), which to a certain extent represent the starting point for the BL12 sensors, real subject of this thesis. The production process adopted for BL9 and BL10 has been already described in the previous paragraph. The aim of these runs was to definitively estabilish the standard procedure to be used for the annealing step and to refine the screening of the T_0 values, by varying

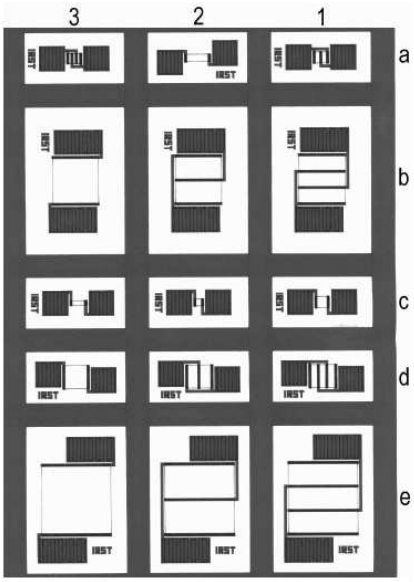

Figure 5.11: Geometries for the devices produced during the early runs (BL3 and BL4)

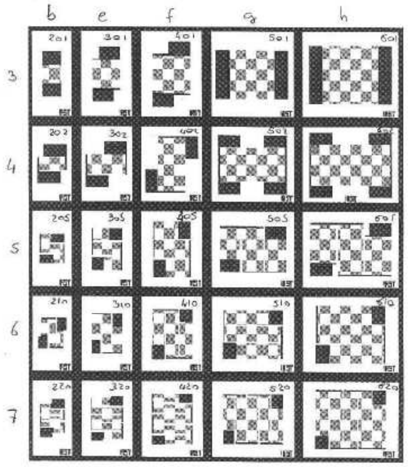

Figure 5.12: Geometries for the devices produced during the more recent runs (BL9 and BL10)

Geometry	n (sq)	Volume (μm^3)	Width (TW) (μm)	Length (TL) (μm)
a1	0.25	1250	50	25
a2	3	1633.5	33	99
a3	0.11	1012.5	45	15
b1	0.11	20100	200	67
b2	0.25	20000	200	100
b3	1	20000	200	200
c1	1	1250	50	50
c2	1	450	30	30
c3	3	600	20	60

Table 5.5: Geometrical characteristics for some of the BL3 thermistors, with reference to figure 5.11; the thickness is fixed to 0.5 μm

Geometry	Area (μm^2)	Number	n (sq)
d	200×200	3	1
e	300×300	4	2
f	400×400	5	5
g	500×500	6	10
h	600×600	7	20

Table 5.6: Geometrical characteristics of the BL9 and BL10 thermistors, with reference to figure 5.12; the thickness is fixed to 0.5 μm

the degree of compensation. For this reason, in the case of BL9, various wafers were produced, with three different compensation degrees: 20%, 30% and 40%. As will be pointed out the value of T_0 increases as the degree of compensation is inhanced. It will be also shown that the main parameters, determined during the static characterization and which mostly influence the performances of the thermistors, are linked to T_0, and hence to the degree of compensation, through an empirical relation.

The results obtained with the BL9 showed that, in order to optimize the performances, the electron-phonon thermal conductance G_{ep} should be further increased, while preserving the resistance value, in accordance with the results arisen from the preceding experiences. To accomplish this task the attention was then focused on realizing devices with lower T_0 values, larger volumes (to increase G_{ep}) and an increased square number (to mantain a large enough resistance). In the case of BL10 different wafers were produced, with compensation varying between 15% and 35%, in steps of 5%.

The first characteristic which should be tested is the reproducibility of the devices. This can be done by measuring the $R(T)$ curves at temperatures in the range $4.2 - 1.2$ K. To be specific two kinds of reproducibility should be checked: one depends on the implant homogeneity all over the wafer, the other one is linked to the geometrical precision of the photolitographic process. In order to evaluate the former, the $R(T)$ curves of the devices with the same shape coming from different regions of a wafer are compared. While in the second case the homogeneity is evaluated by calculating the sheet resistance, for devices with different geometries, as:

$$R_{sq}(T) = R(T)/n \tag{5.3}$$

where n is the square number. For BL9 and BL10 both analyisis showed an average dispersion[2] of about 2.5%.

The $R(T)$ curves in the range $4.2-1.2$ K can be interpolated by equation 5.1, in order to get an evaluation of the parameters R_0, T_0 and γ in this temperature region. The results obtained in the considered case, by leaving all the parameters free, showed that the value of γ is around $1/4$, as expected from Mott theory. Nevertheless, a slight dependence of the exponent γ on the degree of compensation has been oserved, also at lower temperatures, though not heavily affecting the overall results.

The good definition of the geometries can be further investigated by studying R_0, determined by the above described analysis, as a function of the square number: these two parameters should in fact be linked through a linear relation ($R_0 = n \cdot R_{0sq}$). The results obtained for BL9 and BL10 thermistors actually confirmed the expectations.

Apart from these useful considerations, a correct evaluation of the significant parameters can be accomplished only by measuring the $R(T)$ and $I-V_b$ curves at lower temperatures, meaning in the range $0.05-1$ K. In this case, the static characterization described in 3.2.1, is carried out. The load curves can be simultaneously interpolated according to equation 3.9, with a code using the MINUIT CERN library. In most cases the value of γ well approximates $1/2$, in accordance with the suggestion of the VRH Coulomb gap regime. Thus the exponent γ could be fixed, in order to make significant comparisons among the parameters extrapolated for different sensors.

From the obtained data the following empirical relations could be extrapolated:

$$\ln(\rho_0) = 8.170 - 0.2202 \cdot (T_0)^{0.5} \tag{5.5}$$

$$\alpha = 5.350 + 0.0095 \cdot T_0 \tag{5.6}$$

$$\ln(G_{ep}(100\ \mathrm{mK})) = 8.662 - 0.0388 \cdot T_0 \tag{5.7}$$

where $G_{ep}(100\ \mathrm{mK})$ represents the electron-phonon thermal conductance, at 100 mK, normalized with respect to the volume and the other parameters were defined in equations 1.22 and 1.23. Such relations show then how all the relevant parameters of the hot electron model can be determined simply by the value of T_0, and thus from the degree of compensation. The above relations were evaluated taking into account

---

[2] The dispersion σ_R of the $R(T)$ curves for N devices with M points $R-T$ is defined as:

$$\sigma_R = \sum_{i=1}^{M} \frac{1}{M\langle R(T_i)\rangle} \left[\frac{1}{N-1} \sum_{j=1}^{N} (R_j^2(T_j) - \langle R(T_i)\rangle^2) \right]^{1/2} \tag{5.4}$$

only 1 square geometries and fixing $\gamma = 1/2$. These results appeared to be in good agreement with similar relationships derived for the BL3 and BL4 thermistors. The accordance was even higher by considering only the devices with the same volume: for this reason the derived phenomenological relations were supposed to slightly depend upon the volume.

It's interesting to notice how the $R(T)$ curve, measured below ~ 1.2 K, well matches the curve measured between $4.2-1.2$ K: this is shown in figure 5.13, where the case of one of the thermistors characterized is reported. The figure also shows the difficulty of taking data at very low temperatures, since the density of the $R(T)$ points is clearly less below 1.2 K.

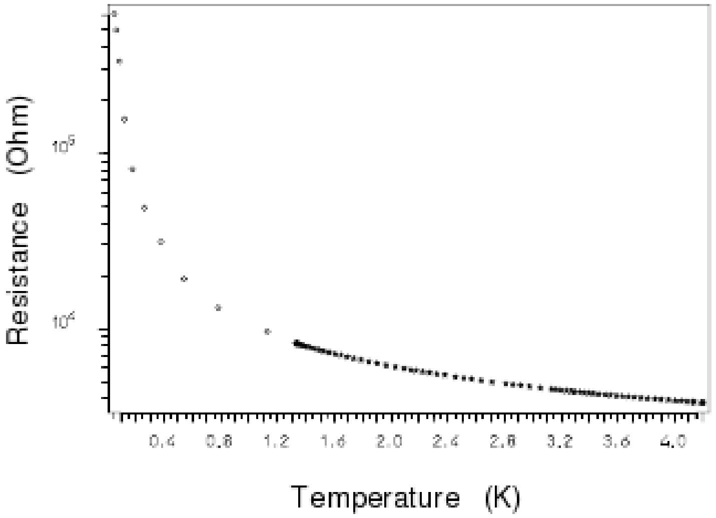

Figure 5.13: R(T) curve measured in the range $0.05-4.2$ K for one of the BL10 thermistors

An interesting and useful analysis consists in studying the relation between T_0 and the degree of compensation, since it is this parameter which, in the end, allows to determine all the other foundamental characteristics in the game concerning the optimization of the detectors. Figure 5.14 shows the trend of T_0 as a function of compensation for the BL10 thermistors. The three lines refer to the four possible combinations of the various annealing options available (discussed in the previous paragraph): to be specific the letters l and b identify, respectively, the long and brief annealing time in O_2/H_2, while y and n distinguish between the processes including the post-annealing or not.

Once determined all the useful parameters by means of the static characterization,

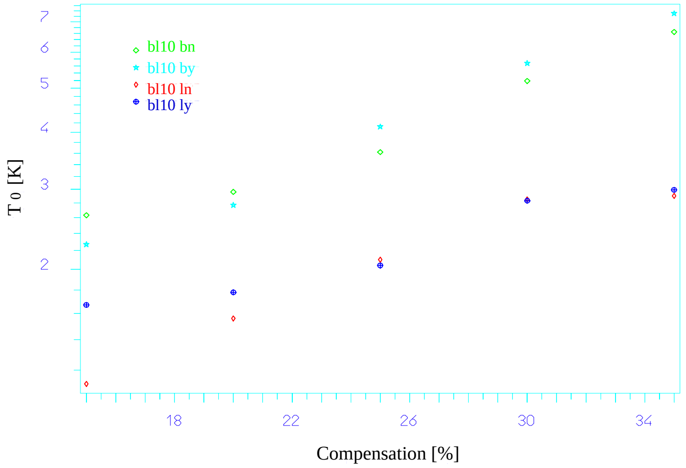

Figure 5.14: T_0 as a function of the degree of compensation for the four combinations of the various annealing options used during the production of BL10; ln: $4'15$” annealing time in O_2/H_2, without post-annealing; ly: $4'15$” annealing time in O_2/H_2, with post-annealing; bn: $2'15$” annealing time in O_2/H_2, without post-annealing; by: $2'15$” annealing time in O_2/H_2, with post-annealing

some detectors were realized coupling the BL thermistors to suited crystals, acting as the absorbing element of the microbolometers. The assemblying procedure should always assure the accomplishement of the requests concerning the values of the thermal conductances in the game. To be specific, as pointed out in chapter 3, while discussing the optimization procedures, G_{ps} should be the lowest, while G_{ep} the highest. Actually the absorbers were coupled to the thermistors using a suitable amount of Stycast 2850. The connection to the heat sink was obtained by means of four Al wires, bonded to the sensor pads, thus also providing the electrical connections. The configuration of the detectors was in the end the one shown in figure 5.1 (since these detectors were actually adopted in the MIBETA experiment).

Using about four Al wires ~ 2 mm long and with 17 μm diameter, a global thermal conductance to the heat sink of order 10 pW/K was obtained, thus lower of about 1 order of magnitude with respect to the electron-phonon conductance, resulting from the static characterization.

The results obtained in terms of pulse shape, energy resolution and rise time, suggested that the detector performances are optimized by larger volumes and using sensors with $T_0 \sim 3$ K. For these reasons, in view of the subsequent production runs, the attention was focused on the realization of large volume thermistors and with compensation varying in a narrow range. Furthermore, taking into account the results shown in figure 5.14, the production process was definitively standardized choosing the option with $2'15''$ annealing time in O_2/H_2 and including the post-annealing step.

5.3.2 BL12: production run

During the last production run carried out at ITC, named BL12, arrays of ten thermistors have been realized, conceived as an alternative to the NASA array in the context of MIBETA2. A significant fraction of this thesis work has been devoted to their characterization and to study their performances while operated as detectors.

The technique used for the fabrication of the thermistor arrays is based on silicon anisotropic wet etching using TMAH chemical reagent. Each array consists of a series of ten sensors, held together by means of a kind of silicon frame, upon which the metal pads are realized. The single thermistor and the array structures are shown in figures 5.15, 5.16 and 5.17, where examples of various sensor geometries are reported. Each thermistor is provided with three silicon legs, 2 mm long, which link the sensor to the silicon frame, or more precisely to the metal pads, through devoted metal tracks (see figure 5.18). The three legs provide also the thermal coupling to the heat sink G_{ps}, the value of which should be measured in order to check its suitability. For a better control of the absorber gluing, the production process forsee also the fabrication of SU8 supports on a silicon structure, with limited coupling G_{ap} to the thermistor. However some problems arose concerning this topic during the fabrication, since the supports seemed to break off at least in some cases. Furthermore each thermistor is provided with an integrated heating resistor, anchored to the crystal support and based on a highly doped implant structure. Two of the three silicon legs, about 20 μm wide, are devoted to provide the electrical connections between the heater and its metal pads, located on the silicon frame. The third leg, about 50 μm wide, provides the electrical connections to the thermistor.

The fabrication of the sensors is based on the multiple implant technique. The standard procedure described in table 5.3 has been applied to the BL12 thermistors, integrated with the option using $2'15''$ annealing time in O_2/H_2 and including the post-annealing step, due to the good results obtained during the preceding runs. The nominal phosphorus concentration of the implanted thermistors is of 3.5×10^{18} ions/cm^3, obtained with the single implant doses and energies reported in table 5.2. Various com-

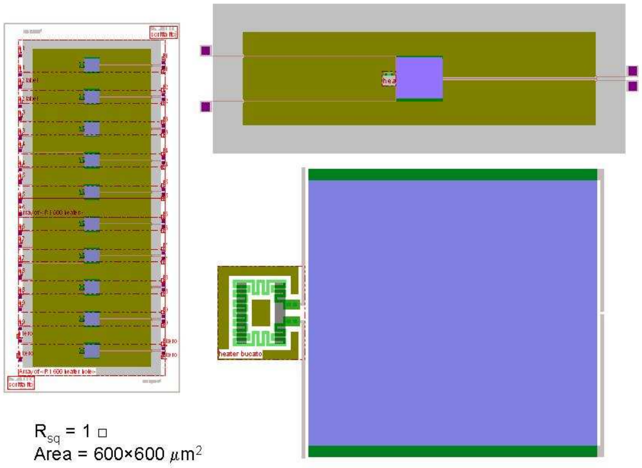

Figure 5.15: BL12: single thermistor and array structures for geometry 1 sq and area 600 × 600 μm^2

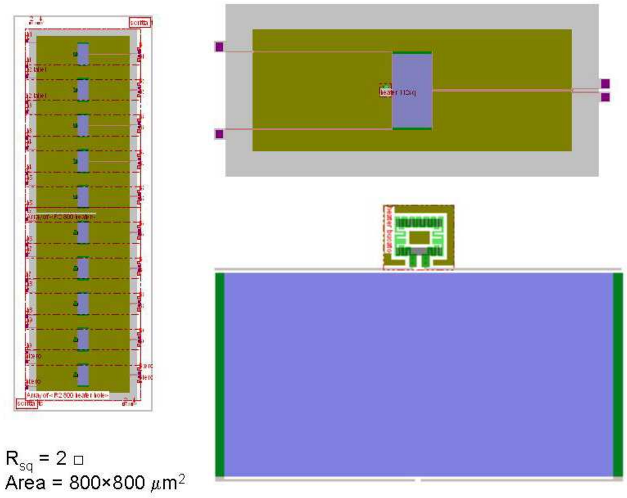

Figure 5.16: BL12: single thermistor and array structures for geometry 2 sq and area 800 × 800 μm^2

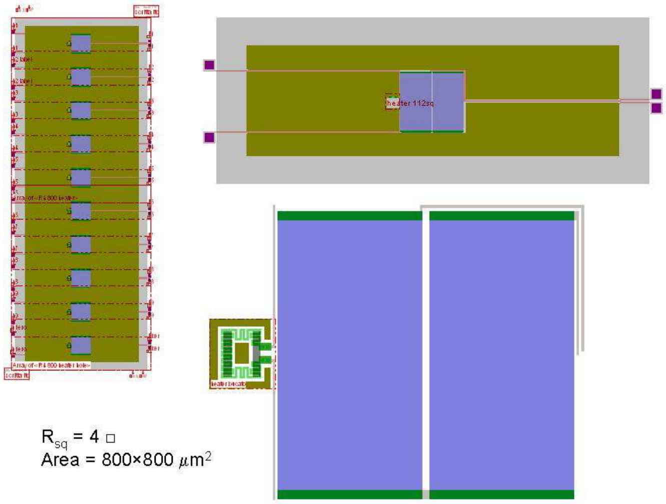

Figure 5.17: BL12: single thermistor and array structures for geometry 4 sq and area 800 $\times$ 800 μm^2

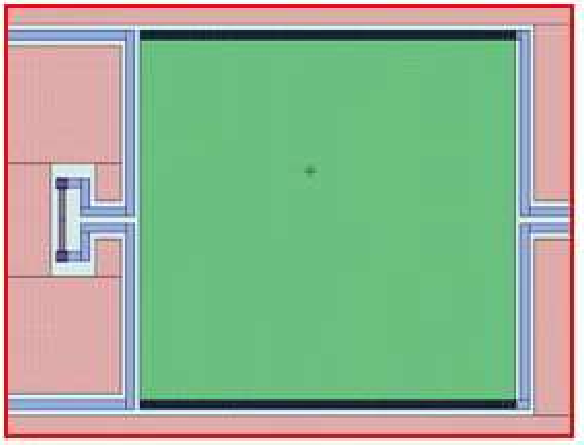

Figure 5.18: BL12 single element layout: zoom on the thermistor, where the metal tracks are visible

pensation splittings have been realized, using different boron energies and doses. The implant depth and profile is almost equal to the one of the preceding production runs.

A total of 20 wafers have been produced, each of them including three arrays of ten theristors for each of the following geometries:

- 1 squares, 600×600 μm^2
- 1 squares, 800×800 μm^2
- 2 squares, 600×600 μm^2
- 2 squares, 800×800 μm^2
- 4 squares, 600×600 μm^2
- 4 squares, 800×800 μm^2

The wafers further include one test array for each geometry. The values of compensation are reported in table 5.7, while figure 5.19 shows the sigle wafer layout. Unfortunately, during the fabrication some arrays were completely destroyed, due to their fragility and to the use of too aggressive techniques. In particular none of the 36% compensation wafers survived.

Due to the results obtained with precursor devices, as pointed out in the previous section, only large volume thermistors have been produced, with implant areas of 600×600 μm^2 or 800×800 μm^2, and square number varying between 1 and 4. The implant thickness is fixed to 0.5 μm, while the final total thickness of the detectors and of the silicon legs is ~ 40 μm.

Wafer	Compensation (%)
W1, W2, W3	28
from W4 to W7	30
from W8 to W13	32
from W14 to W17	34
W18, W19, W20	36

Table 5.7: Compensation splitting of BL12 wafers

After the standard fabrication procedure, the single arrays appear as shown in picture 5.20: a kind of silicon membrane, of 40 ± 10 μm thickness (the same as the detectors), still links the ten themistors together and to the silicon frame. This configuration

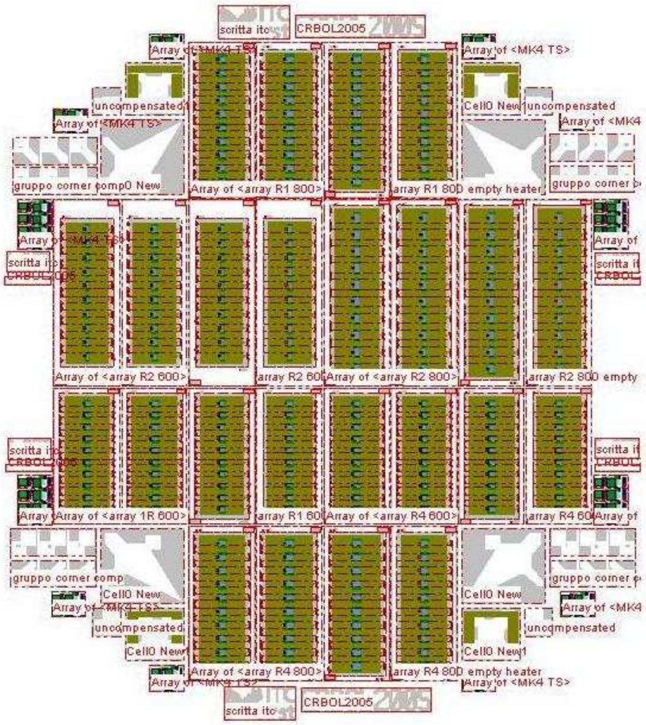

Figure 5.19: Wafer layout for the BL12 production run

is still suited in view of the static characterization, since it assures a more stable and solid structure to the devices, while providing the required thermal conductance to the heat sink. Nevertheless the silicon membrane must be removed in view of the realization of the microbolometric detectors, by means of a final step in the production process, based on the TMAH anisotropic wet etching (figure 5.21).

Unfortunately this final step produced non uniform results throughout each single array, due to the non perfect planarity of the wafer surfaces, so that in many cases a further etching procedure was necessary. As a consequence some of the thermistors resulted to be damaged and only one array finally survived the TMAH etching process, though many variants to the procedure have been tested. The single useful array realized has been operated as a detector in the Cryogenic Laboratory of Insubria University, as discussed in section 5.3.4.

In order to solve the problems arisen during the production of the BL12 thermistors,

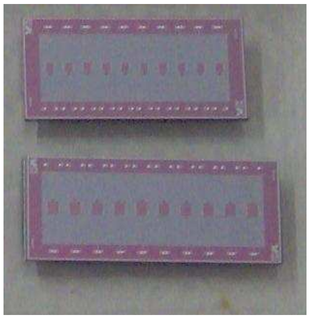

Figure 5.20: BL12 arrays with the silicon membrane

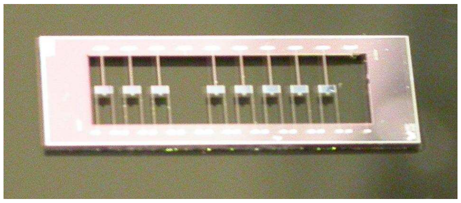

Figure 5.21: BL12 array in the final configuration (after the final TMAH etching); only eight of the ten thermistors did survive

a completely different technique has been suggested, very similar to the one used by NASA, based on the use of SOI wafers and DRIE to remove the silicon membrane. It was not possible to apply the DRIE method to the presently available devices, since the wafers had already been cut: it was not possible then to mask the single arrays, as needed in order to carry out the DRIE techinique. Nevertheless the use of the new proposed methods should be taken into account in view of a new complete production run.

In order to have an immediate evaluation of the quality of the production process, in terms of homogeneity and good geometrical definition, room temperature measurements are performed at ITC using a *probe-station*. This allows to determine the spread of the sheet resistance (in Ω/sq) among different thermistors belonging to the same wafer. During the preceding production runs it was observed that the measured values of sheet resistance resulted to be precise within 1% for each considered wafer: this fact also give a useful information about the precision of the implanting machine being used. Furthermore the run-to-run stability was proved as well. In the case of BL12 the measured values at room temperature appeared to be consistent with the results of the precursor devices (395 ± 25 Ω/sq for 32% compensation in BL12, compared to 351 ± 2.3 Ω/sq for 30% compensation in the case of the precursors). The measurements performed at room temperature also allowed to estimate a contribution due to the metal tracks of about 25 Ω.

5.3.3 BL12: characterization at low temperatures

The static characterization of BL12 was performed using the arrays still provided with the membrane, in order to evaluate the quality of the production run, before completing the whole process. The test were performed following the schedule below reported, which is similar to the case of the precursors, but includes some more measurements, since required by the different structure of the devices.

- Measurements between 4.2 K and $\sim$ 1.5 K in order to:

  1. check the uniformity of devices with similar construction parameters;
  2. compare the T_0 values with those of the precursors realized using similar fabrication parameters (i.e. compensation) to check the run-to-run stability of the implanting machine;
  3. use such comparisons to get a preliminary evaluation of R_0, T_0 and γ.

  The measurements in this temperature range were performed using the ^{4}He pumped refrigerator and the related acquisition system described in section 4.2.1, located in the Cryogenic Laboratory of Insubria University.

- Measurements below 1 K in order to evaluate the parameters which determine the behaviour of the thermistors in the hot electon model; this is accomplished by measuring the load curves and interpolating them using the system of equations 3.9.

- Measurements below 1 K to verify the stability of the resistance of the integrated heaters with changing temperature.

- Measurements below 1 K using the integrated heaters to evaluate the thermal conductance to the heat sink provided by the silicon membrane.

Preparation of the samples

The samples to be measured were prepared by gluing them upon devoted packages, similar in the structure to those adopted for the heaters of CUORE. The packages were conceived in order to fit into the holders of the cryostats. During the preparation of the BL12 samples, many problems arose, due to their fragility. The first matter to deal with concerned which gluing method to adopt, in order to provide a good thermal contact with the heat sink, while avoiding excessive mechanical stress due to different coefficients of thermal expansion of the devices and the package. The second matter dealt with the choice of the best suited bonding technique.

For the precursor devices devoted packages were realized, based on a ceramic support (which provides a thermal expansion coefficient similar to the one of silicon), with

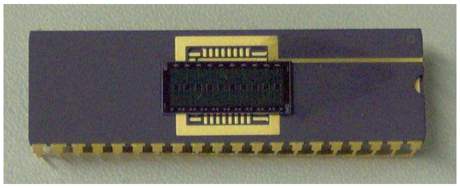

Figure 5.22: BL12 array prepared for the test, glued upon one of the old ceramic packages

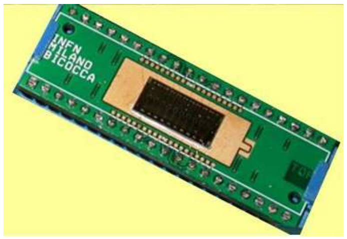

Figure 5.23: BL12 array prepared for the test, glued upon one of the new devoted packages

a hole covered by a gold foil, to provide the necessary thermal contact. The packages have 40 pins, arranged in a similar way with respect to the packages used for the characterization of CUORE heaters, so that ten samples per time can be tested. The BL thermistors were usually prepared in the past by gluing them onto the gold surface, using one spot of silver epoxy resin[3]. The electrical connections were provided by 25 μm diameter gold wires ball bonded to the pads of the thermistors and of the packages.

A few old ceramic packages were still available for the BL12, though the dimensions of the golden hole were not suited to the dimensions of the BL12 arrays. As a consequence, at least for the early measurements, the arrays were glued as shown in figure 5.22, directly onto the ceramic material. Concerning the glue, one spot of Stycast 2850, which assures a strong adhesion, was put between the silicon frame (on the narrower side of the array) and the package. The electrical connections were realized following the past procedures: unfortunately this bonding method resulted to be not well suited for the BL12 case. Ball bonding in fact produces a too much high mechanical stress on the arrays, with the result that a part of the membrane was broken, as well as some of the silicon legs. This was probably due also to the configuration of the set-up (package-sample coupling), since a large part of the array was not directly leaning against the package surface.

Nevertheless two samples prepared as above described were measured in the range 4.2 K and ~ 1.5 K, and one of them also below 1 K. To solve the problems dealing with the preparation of the samples, new packages (made of fiberglass) have been studied and prepared, in collaboration with the Milano Bicocca group, involved in the MIBETA activities. The structure of the package is shown in figure 5.24: it was conceived in order to allow to bond 20 samples at the same time (i.e. both the heaters and the

---

[3] Epotek H 20E, 73% charged with silver

thermistors of the arrays of ten sensors), and measure them during two subsequent cool down runs, if using the ^{4}He pumped refrigerator at Insubria University. By using the new packages it was then possible to glue the arrays directly onto the gold surface, thus assuring a better thermalization of the samples, besides providing a better mechanical stability (see figure 5.23).

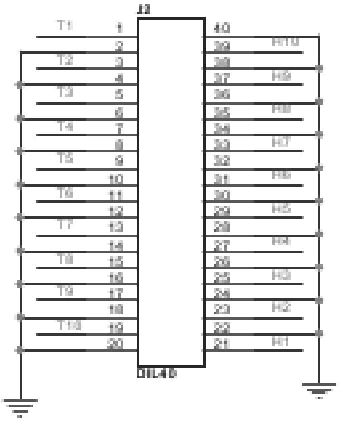

Figure 5.24: Scheme of the structure of the new packages realized for the BL12 characterization

Measurements between 4.2 K and ~ 1.5 K

The three arrays below described have been tested in the range of temperatures between 4.2 K and ~ 1.5 K:

- array from wafer 11, compensation 32%, 4 squares, area 600×600 μm^2; two thermistors tested, named 11b7 and 11b8;
- array from wafer 11, compensation 32%, 4 squares, area 800×800 μm^2; two thermistors tested, named 11b9 and 11b10;
- array from wafer 17, compensation 34%, 1 squares, area 600×600 μm^2; one thermistor tested, named 17b9;

The samples named 11b7, 11b8, 11b9 and 11b10 were glued upon the old packages, while the sample named 17b9 was glued upon one of the new packages.

The measurements were performed using the automatic acquisition program coupled to the AVS-47 bridge, described in 4.2.1. The values of resistance recorded during the warming up from ~ 1.5 K to 4.2 K were fitted using equation 4.3, by means of the Paw-CERN analysis tool, after being processed with the devoted C software (as discussed in 4.2.1). In order to compare data referring to different geometries, the resistance values were normalized to the square number and the exponent γ was fixed to 0.25.

In chapter 4 it was pointed out that the set-up showed some problems of thermalization, which were partially solved. Nevertheless, still from the acquired data for the BL12 thermistors, the samples seemed to be not well thermalized, as can be seen from figures 5.25 and 5.26. The value of resistance in fact appears to flatten as the temperature is as low as ~ 2 K. Consequently the data were then fitted in the range 4.2 K and 2 K. From now on, the parameter which in equation 4.3 is identified as T_0, will be refered to with the symbol T_0* when related to the temperature range between 4.2 K and ~ 1 K, since it does not correspond to the parameter extrapolated from measurements performed below 1 K. For practical purposes then the symbol T_0 will refer only to the parameter determined by measuring the thermistors below 1 K. The values of T_0*, obtained by fitting the data, should be compared to the ones determined in the same range of temperatures for the precursor devices with similar construction parameters.

To this purpose, data regarding the BL10, acquired with the ^{4}He pumped refrigerator in Como, were used. Still, it is worth to notice that the so performed comparison must be considered simply as a first and approximated evaluation of what to expect from lower temperature measurements. Table 5.8 shows the results of this analysis, which seem to suggest a value of T_0 lower than the one expected considering only the degree of compensation. In particular, the expected T_0 for the BL12 thermistors belonging to wafer 11, with compensation 32%, is ~ 5 K (see figure 5.14). In terms of the results obtained by measuring them between 4.2 K and 2 K, they can be compared to BL10 thermistors with compensation in the range $15-20\%$, the corresponding T_0 being thus ~ 3 K. Concerning the BL12 thermistors belonging to wafer 17, with compensation 34%, the expected T_0 from figure 5.14 is ~ 6.5 K. In this case, the results obtained between 4.2 K and 2 K suggest that this sensor can be compared to the BL10 with compensation $\sim 30\%$, thus with $T_0 \sim 5-6$ K. For the 17b9 sensor it must be also pointed out that a better thermalization was obtained, with respect to the other tested BL12, thanks to the good thermal coupling provided by gluing it directly onto the gold foil of the new packages.

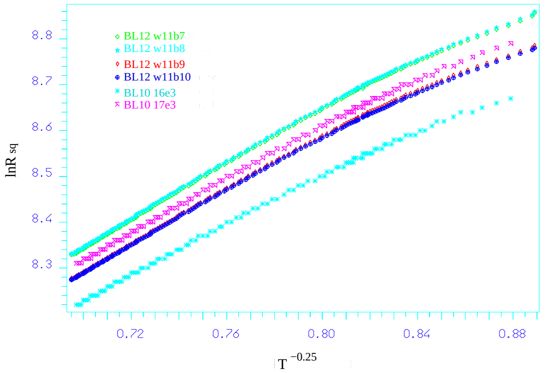

Figure 5.25: Trend of resistance as a function of temperature, in the range 4.2 K and ∼ 1.2 K, plotted according to equation 4.3; the data refers to the BL12 thermistors belonging to wafer 11 and to BL10 thermistors with similar construction parameters, measured with the ^{4}He pumped refrigerator at Insubria University

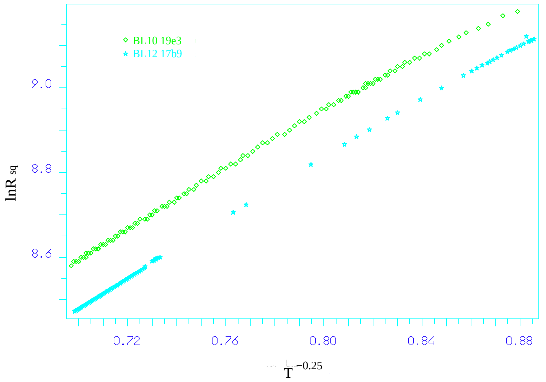

Figure 5.26: Trend of resistance as a function of temperature, in the range 4.2 K and ∼ 1.2 K, plotted according to equation 4.3; the data refers to the BL12 thermistor w17b9 and to BL10 thermistors with similar construction parameters, measured with the ^{4}He pumped refrigerator at Insubria University

The difference between the expected and the determined T_0 values can be explained considering that the BL12 production run was realized quite long time after the preceding runs: therefore it is not to exclude a drift of the implanting machine during this period of time.

BL12 thermistor			R_0* (Ω/sq)	T_0* (K)
11b7			522	79.6
11b8			524	79.4
11b9			531	69.8
11b10			539	67.5
17b9			395	162.5
BL10 thermistor	compensation (%)	T_0 (below 1 K) (K)	R_0* (Ω/sq)	T_0* (K)
16e3	15	2.3	569	53
17e3	20	2.9	544	61
19e3	30	5.8	466	151

Table 5.8: Results obtained by fitting the data in the range 4.2 K and 2 K for the BL12 and the BL10 thermistors, while measured with the ^{4}He pumped refrigerator at Insubria University; for BL10 also the values of T_0 determined below 1 K during past measurements are reported [48]

Nevertheless, from the measured data and as can be seen from the values of R_0* (this symbol still refers to the parameter determined in the range 1 K - 4.2 K) reported in table 5.8, the thermistors belonging to the same wafer show similar behaviours. In particular the sheet resistance spread remains within $\sim$ 2%, thus confirming the precision of the implanting process. The spread is even lower when considering thermistors belonging to the same array. Furthermore, as expected, T_0 grows with increasing degree of compensation.

Measurements below 1 K @ Milano Bicocca

The two BL12 thermistors above named 11b7 and 11b8 have been characterized below 1 K, from a static point of view, in the Cryogenic Laboratory at Milano Bicocca University, where a set-up devoted to this task and used for the characterization of precursor devices is located.

In chapter 3 the steps toward the static characterization of thermistors were described. The measurements actually consist in determining the resistance of the devices at various temperatures by means of the polarization circuit of figure 3.1. A constant bias voltage V_{bias} is delivered to the sensor, thus generating a constant current flow I: the resistance can then be determined by the following equation:

$$R = R_L \frac{V_b}{V_{bias} - V_b} \tag{5.8}$$

where R_L is the load resistance of the circuit and V_b the voltage produced across the thermistor. The current flow generated by the injected bias voltage can be approximated to a constant ($I \approx V_{bias}/R_L$) given the condition $R_L \gg R$. The load curves are determined by mesuring the resistance R of the thermistor with changing bias voltage, at various temperature stages.

The bias voltage is produced by means of a battery, it is delivered to the polarization circuit through a resistive partition and it is then measured by a multimeter. Concerning the voltage across the sensor, taking into account the various noise sources (due to the preamplifier located at room temperature, the Johnson noise of the resistance, the microphonic noise), it should usually be of order at least a few μV, needing still to be preamplified by a factor ~ 200 in order to be measured.

The cryostat used for the measurements is a ^{3}He/^{4}He dilution refrigerator (see section 3.2.3) produced by the english company Oxford Instruments, with a refrigeration power of 200 μW at 100 mK and able to reach a temperature of about 5 mK. In view of the measurements the same package described in the preceding paragraph, upon which the samples were glued, was mounted in a copper holder, housing also a calibrated thermometer (a LakeShore germanium resistor) and a heating resistor of ~ 1 KΩ. The thermometer resistance was read by a four lead measurement, using an AVS-47 bridge (as described in section 4.2.1). The copper holder was coupled to the mixing chamber of the cryostat through a low enough thermal conductance, which allowed to warm up the experimental set-up to about 1 K, without affecting the cryostat functioning. The temperature of the holder housing the samples was changed by delivering a known Joule power, between 10^{-7} and 10^{-4} W, into the devoted heating resistor, corresponding to a range of temperatures (as measured by the LakeShore termometer) between ~ 50 mK and ~ 1 K. This was accomplished using a remotely controlled programmable power supply.

The above described set-up was tested in the past and used for the characterization of some of the early BL devices. Nevertheless, since some years were passed, a calibration of the heater was performed, concerning the correspondence between injected power and holder temperature.

An automatic program remotely controlled by a pc and realized for the character-

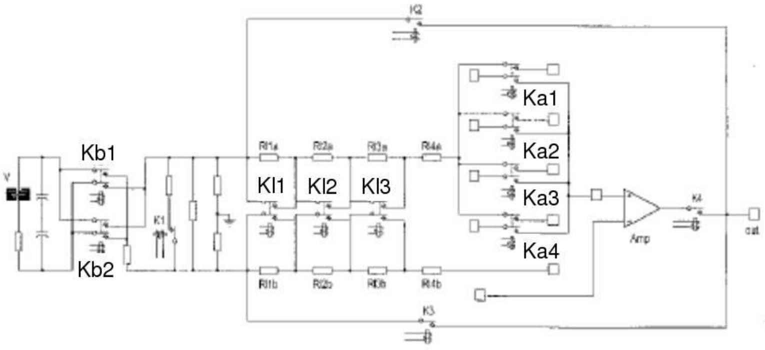

Figure 5.27: Polarization circuit provided with the 15 relé, for the automatic static characterization of thermistors below 1 K, located in the Cryogenic Laboratory of Milano Bicocca Unversity

ization of the precursor devices (as described in [47]), allowed to perform a cycle of detailed load curve measurements at various temperature stages, in a limited amount of time (about 24 hours). The polarization circuit used in this case is modified, with respect to the one of figure 3.1, by the presence of 15 relé, as shown in figure 5.27. This kind of circuit allows to measure four devices by a four lead reading (relé Ka1, Ka2, Ka3, Ka4) and to choose among four load resistances (relé Kl1, Kl2, Kl3). It also includes the preamplification stage for the measure of V_b. The bias voltage is applied to the partition circuit by a programmable power supply through the relé Kb1 and Kb2 and a digital multimeter measures both V_{bias} and V_b, amplified by selecting the most suited gain among the available ones. A pc is coupled to the polarization circuit by means of a devoted board (8255) and to the other instruments by a GPIB connection.

The automatic acquisition program controls the sequence of operations necessary for both the determination of the load curves and the complete cycle of measurements at various temperature stages. For this reason the pc is also coupled to the AVS-47 bridge, in order to control the stability of the temperature by adjusting the power dissipated into the heating resistor. The results of the calibration performed to determine the correspondence between the power injected into the heater and the holder temperature are inserted into the acquisition program. Once estabilished the number and the values of the temperature stages, as well as the number of points for each load curve to be measured (corresponding to a number of injected V_{bias}), the program makes the cycle start: the characterization is performed for increasing temperature stages and for each stage all the thermistors are measured.

In the case of the two BL12 thermistors 11b7 and 11b8 the load curves were measured for a total of about 20 temperature stages, between 50 mK and 1 K. For the simultaneous interpolation of the measured load curves, by means of equation 3.9, a tool based on the MINUIT-CERN library was used. This tool converts the $I-V_b$ pairs recorded by the acquisition program into $R-P_e$ pairs, which are then interpolated in order to get the hot electron model parameters. Figures 5.28 and 5.29 show the $R-P_e$ curves for the two BL12 thermistors characterized. The fit, obtained by fixing $\gamma = 1/2$, is shown only in the case of the thermistor 11b7, because it was not possible to record the plot for thermistor 11b8, due to some problems with the analysis tool. The resistance of the thermistor at a given temperature, in the ohmic region, can be extrapolated by averaging over the points in the load curves which coincide with the lower values of V_b (i.e. the flat portion of the $R-P_e$ curves). Figures 5.30 and 5.31 show the so calculated resistance, for the various temperature stages, as a function of temperature and the fit obtained by interpolating the data, using equation 5.1, with $\gamma = 1/2$ fixed.

The experimental data appear to be well interpreted by the hot electron model theory, over all the considered temperature range, both considering the resistance trend as a function of temperature and the $R-P_e$ curves. Considering the obtained results, there is no evidence of the existence of side conduction channels in the tested devices. Concerning this topic, figures 5.32 and 5.33 show the effect produced by the presence of such alternative conduction paths in some precursor devices (BL3 thermistors): in this case the $R-P_e$ curves are not well fitted by the hot electron model below about 200 mK and the value of resistance appears to flatten below the same temperature.

In table 5.9 the values of the parameters of the hot electron model are reported, as extrapolated from the simultaneous interpolation of the load curves with $\gamma = 0.5$. The values of the same parameters, determined in the case of the BL10 thermistors with similar construction characteristics, are also reported for comparison purposes. Concerning the thermal conductance G_{ep} and the coefficient g_{ep}, they are normalized to the volume of the sensors, still for comparison purposes. To be specific, for the BL12 thermistors, they were calculated considering a total volume given by $600 \times 600 \times 0.5$ $\mu\mathrm{m}^3$. Concerning G_{ep}(100 mK) it was calculated according to equation 1.23, using the values of the parameters determined from the interpolation and reported in table 5.9 as well. From the analysis of the obtained results the following considerations arise:

- the value of T_0 extrapolated by the interpolation of the load curves below 1 K coincides with the value derived from the analysis performed at higher temperatures (in the range between 1.5 K and 4.2 K);
- the parameters α and g_{ep} appear to be quiet less with respect to the values deter-

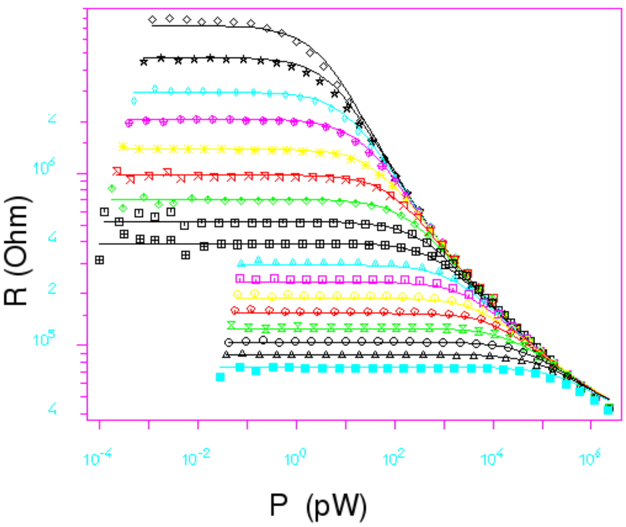

Figure 5.28: $R-P_e$ curves for the BL12 thermistor 11b7, interpolated with the hot electron model, in the temperature range between 50 mK and 1 K

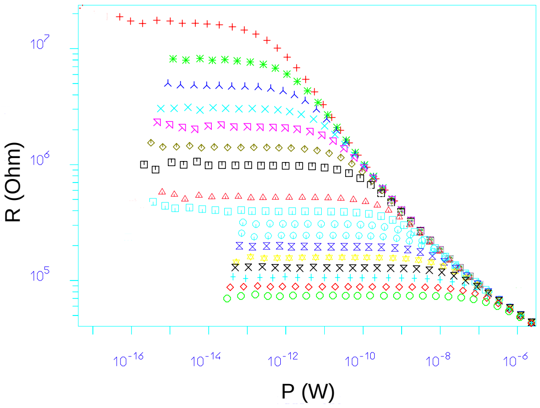

Figure 5.29: $R-P_e$ curves for the BL12 thermistor 11b8, in the temperature range between 50 mK and 1 K

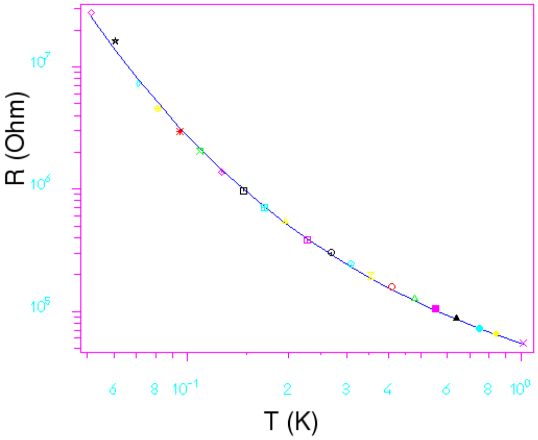

Figure 5.30: $R-T$ curve for the BL12 thermistor 11b7, interpolated with the hot electron model, in the temperature range between 50 mK and 1 K

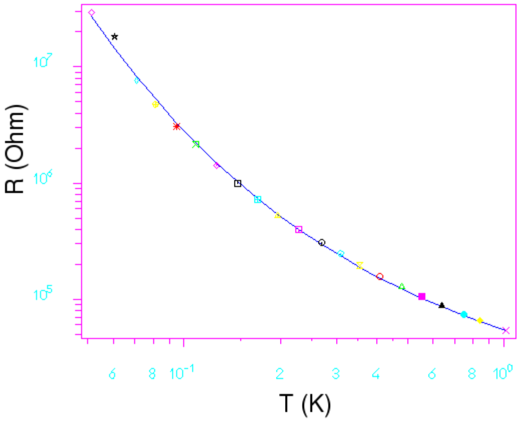

Figure 5.31: $R-T$ curve for the BL12 thermistor 11b8, interpolated with the hot electron model, in the temperature range between 50 mK and 1 K

mined for the precursors, though they are consistent;

- the electron-phonon thermal conductance G_{ep}(100 mK) results to be consistent with the value calculated for the precursors, though quite lower; this can be explained taking into account that a dependence of this parameter on the volume was observed in the case of the precursor devices;
- the background power extrapolated by the interpolation results to be of order 0.15 pW, in accordance to the value measured during past characterizations and reported in [47]

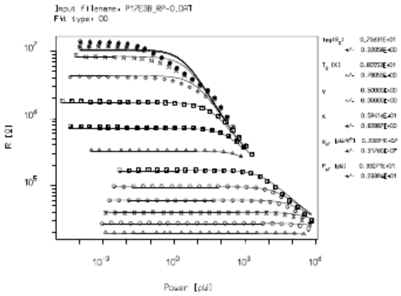

Figure 5.32: $R-P_e$ curves for a BL3 thermistor, interpolated with the hot electron model, in the temperature range between 50 mK and 1 K [47]

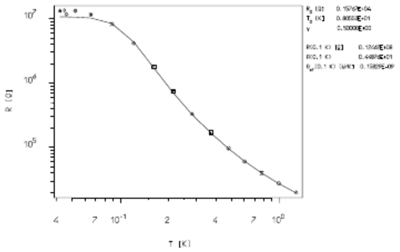

Figure 5.33: $R-T$ curves for a BL3 thermistor, interpolated with the hot electron model, in the temperature range between 50 mK and 1 K [47]

Thermistor	R_0 (Ω/sq)	T_0 (K)	α	g_{ep} (W/K$^{\alpha}$·m^3)	G_{ep}(100 mK) (W/K·m^3)
11b7	2259	3.3	4.94	6.8×10^6	3817
11b8	2217	3.3	4.97	7.4×10^6	3919
16e3	2316	2.3	5.5	2.9×10^7	4600
17e3	2272	2.9	5.5	2.8×10^7	4933

Table 5.9: Parameters of the hot electron model, as extrapolated from the simultaneous interpolation of the load curves with $\gamma = 0.5$, for the two BL12 thermistors and the BL10 thermistors with similar construction characteristics [48]; the degree of compensation of the two considered BL10 sensors is repoted in table 5.8

Altogether the obtained results are consistent with the expectations (apart from the relation between T_0 and degree of compensation), both drawn from measurements performed at higher temperatures as well as from the results concernig the precursor devices, and even taking into account the hot electron model theory. Concerning the values of α and g_{ep}, the difference with respect to the precursors can be ascribed to the different geometry and somehow different production process (i.e. the BL12 thermistors are realized in form of arrays, instead of being single sensors). Also the sensitive volumes are generally larger: in the case of the precursors the various parameters showed a slight dependence from the volume, even when normalized.

Some further interesting considerations arise taking into account the plot shown in figure 5.34. The data there reported refers to the values of $G_{ep}(T)$ as calculated by the numerical differentiation of the curves P_e versus T_e, previously dtermined with the sinoultaneous interpolation of the load curves. The plot also shows the values $G_{ep}(T)$ calculated according to the theorical expression given by equation 1.23, using the experimentally determined parameters of table 5.9. A comparison between this plot with the one of figure 5.35, which refers to one of the BL3 thermistors, still proves the absence of side conduction channels, which produced in the precursors a clear deviation from the theorical behaviour below about 150 mK. Still, the $G_{ep}(T)$ values calculated by numerical differentiation for the BL12 thermistors, generally follow the theorical trend, apart from the cases of low power dissipation, as already noticed in the case of the precursors (BL4 and BL10), as reported in [47] and [48].

Measurements below 1 K @ Insubria

In view of future measurements it was then decided to realize a completely indipendent set-up in the Cryogenic Laboratory at Insubria University, similar to the one located in Milano Bicocca University and above described. This was possible taking advantage of an automatic program for the measurement of the load curves (the same used for the characterization of heaters below 1 K, as described in 4.2.3), realized by S. Sangiorgio, which needed some adjustments in order to be useful for the purpose of this thesis work. The software in this case remotely controls the measure of the complete load curve, but it is not suited to perform an entire cycle of mesurements at different temperature stages. For this reason the stabilization of the samples at the desired temperature must be performed manually: thus the complete characterization requires a longer time with respect to the case of the Milano Bicocca set-up (about one week, for about twenty temperature steps, for 2-3 samples).

A description of the set-up located at Insubria University is given below, together with the needed adjustments realized.

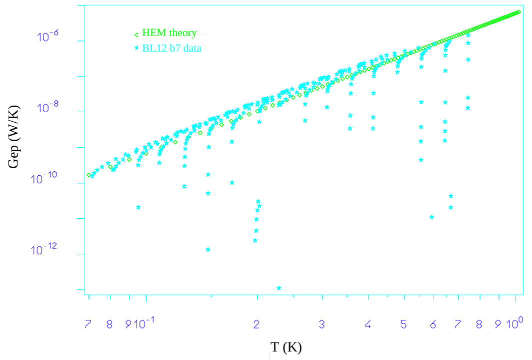

Figure 5.34: $G_{ep} - T$ curves for the BL12 thermistor 11b7, as determined by the numerical differentiation, superimposed to the theorical $G_{ep} - T$ trend (identified as HEM theory), determined according to equation 1.23, in the temperature range between 50 mK and 1 K

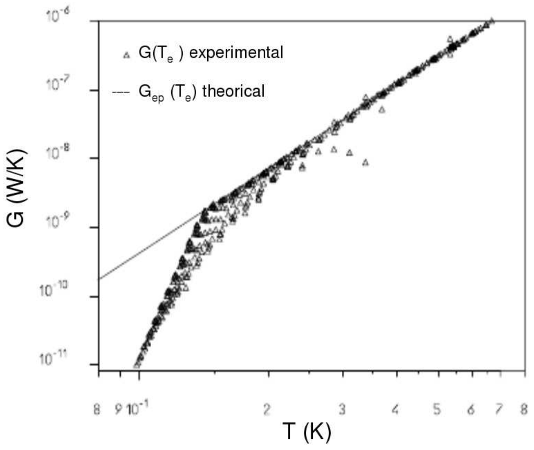

Figure 5.35: $G_{ep} - T$ curves for one of the BL3 thermistors, as determined by numerical differentiation, superimposed to the theorical $G_{ep} - T$ trend, determined according to equation 1.23, in the temperature range between 70 mK and 1 K [47]

Figure 5.36: TBT dilution unit, in the Cryogenic Laboratory at Insubria University

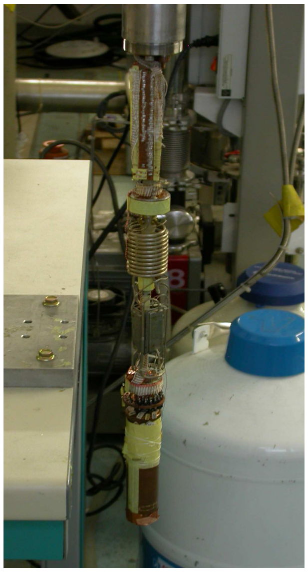

Figure 5.37: Copper holder for the samples coupled to the mixing chamber of the TBT cryostat

- Concerning the cryostat the TBT dilution refrigerator was used. The dimensions of the dilution unit can be appreciated from figure 5.36. The reduced size makes this refrigerator quite easy to handle, and the cool down lasts in principle a couple of days. The working principles of dilution refrigerators were discussed in section 3.2.3. In the specific case of the TBT cryostat the mixture is condensed by means of the Joule-Thompson effect. A liquid helium reservoir serves as the main bath, for the pre-cooling of the refrigerator. The volume housing the samples, which are coupled to the mixing chamber, as shown in figure 5.37, is shielded against the ^{4}He bath by means of the 4K stainless steel IVC (inner vacuum chamber) shielding. The bottom part of it must be screwed on the top, after the samples have been prepared. Inside the IVC a very high vacuum condition is reached by using a series of suited pumps (rotary and diffusive pumps). The TBT cryostat has a refrigeration power of 20 μW at 100 mK and temperatures as low as 13 mK can be attained. A Faraday cage, with acoustic absorption panels, surrounds the liquid helium dewar, where the refrigerator is inserted during the measurements, as shown in figures 5.38 and 5.39. The big problem with this refrigerator deals with the IVC sealing: in order to obtain the needed vacuum tight, it is not sufficient to screw the bottom part of the IVC on the top. A special material must be wrapped around the point of connection to assure the required leak tightness. Nevertheless, the effects of this sealing method are not completely repeatable from run-to-run, so that in some cases many subsequent cool down attempts are necessary. Finally, the available experimental volume below the mixing chamber is very limited: about 25 cm lenght, with a diameter of 5 cm.

- The sample holder should be suited to the limited experimental space offered by the TBT cryostat and should provide an adequate shielding of the samples, operated at the mixing chamber temperature, from the 4.2 K blackbody radiation of the IVC. For the purpose of the static characterization of the thermistors, through the measurement of the load curves, a copper holder (shown in figure 5.40), already used in the past to characterize precursor BL sensors, was used. The holder is very similar to the one of the Milano Bicocca set-up: also in this case it provides a low enough thermal coupling to the mixing chamber, which allows to warm up the experimental set-up to about 1 K, without affecting the cryostat functioning. The holder is also provided with a heating resistor of about 1 KΩ.

- The holder was not yet provided with a thermometer. To this purpose an old LakeShore germanium resistor was added and calibrated, using the available resistance versus temperature data (in analogy to what done in the case of the ^{4}He pumped refrigerator).

- For the temperature monitoring the AVS-47 bridge was used. A TS-530A temperature controller (by PICOWATT) was coupled to the AVS-47, in order to control the stability of the temperature by adjusting the dissipated Joule power into the heating resistor. The TS module can be manually operated or faced to a pc to be remotely controlled. For the purpose of this thesis the temperature stabilization was performed by hand, since the automatic acquisition program was not suited for the temperature monitoring. However an upgrade of the software is at present under developement, in order to make it able to completely control the whole cycle of measurements, at various temperature stages.

- The electronic set-up for the load curves measurements is quite similar to the one of Milano Bicocca. The structure of the polarization circuit resembles the one of figure 5.27, being provided with a series of relé and including the preamplification stage for the measurement of V_b. The bias voltage is applied to the partition circuit by the programmable power supply Agilent 34401A. In this case two different digital multimeters Agilent 6623A measure V_{bias} and V_b, amplified by selecting the most suited gain among the available ones. A pc is coupled to the polarization circuit by means of a devoted board and to the other instruments by a GPIB connection. The electronic set-up is suited for the simultaneous measurement of a total of eleven thermistors.

- The automatic acquisition program allows to select the channel (i.e. the thermistor) and the number of $I - V_b$ pairs to be measured, the range of values for V_{bias} and the load resistance to be used. The output files contain all the parameters useful in view of the data analysis.

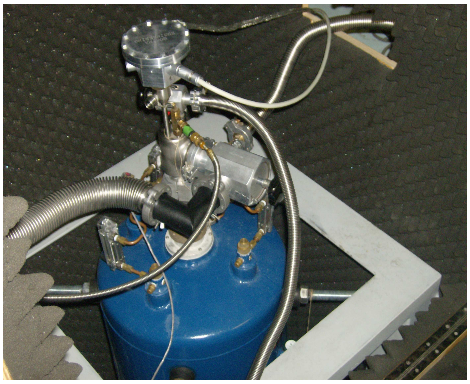

Figure 5.38: TBT inserted into the liquid helium dewar, surrounded by the Faraday cage with acoustic absorption panels

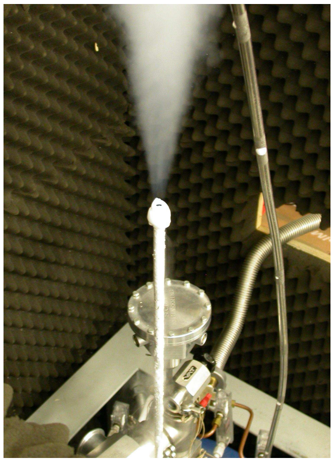

Figure 5.39: The liquid helium dewar during ^{4}He refilling

Due to the adjustments carried out in order to make the set-up useful for the purpose of this thesis work, a test cool down run was performed in order to check the reliability of the measurements, with particular regard to the thermometric system. To this purpose the same array, previously characterized in the Cryogenic Laboratory of Milano Bicocca, was put into the copper holder, placed in the TBT cryostat, and a complete characterization, based on the measurement of the load curves, was performed. The results were then compared to the ones obtained during the characterization performed using the Milano Bicocca cryogenic set-up.

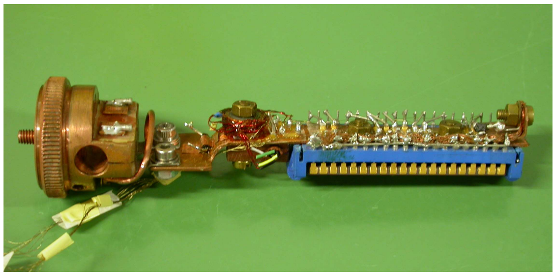

Figure 5.40: Holder used for the characterization of the BL12 sensors below 1 K at Insubria University

Figure 5.41 shows the results of this comparison: the values of resistance, determined in the homic region, as a function of temperature, are plotted for the two thermistors characterized, using the two cryogenic set-up located in Milano Bicocca and at Insubria University. The plot allows to appreciate the good agreement between the data determined in the two cases, which resulted to differ for less than 1%. The lack of points in the lower temperature range, in the case of the measurements performed in the TBT cryostat, is due to the difficulties encountered during the manual stabilization of the temperature in this range.

In table 5.10 the results obtained with the simultaneous interpolation of the load curves are reported in the two cases. As can be seen, the agreement among the extrapolated values for the parameters of the hot electron model is not perfect, though the value of T_0 is consistent. The difference can be ascribed to a problem with the modality of operation of the automatic program, which is now going to be solved. To be specific, the step width, used to deliver the bias voltage in the selected range, produced a lack of points in the measured $I-V_b$ curves, which probably affected the results of the interpolation. Furthermore, the points in the $R-P_e$ curves, corresponding to the higher values of delivered Joule power, were not useful due to a saturation of the preamplifier, which affected the resulting value of resistance. Finally, in the case of the TBT cryostat, the background power determined by the interpolation resulted to be of about 0.1 pW.

After testing the set-up, a new cool down run was performed, in order to characterize below 1 K a BL12 array with degree of compensation 34%. Three thermistors belonging to the same array of wafer 17 have been tested, with geometry 4 squares and area $800 \times 800\ \mu\text{m}^2$. They will be identified in the following as: 17bol1, 17bol2, 17bol9. The array was glued upon one of the new devoted packages and bonded as usual with 25 μm diameter gold wires.

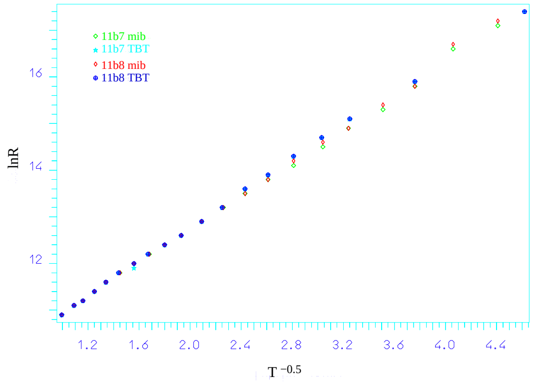

Figure 5.41: Trend of the resistance as a function of temperature, for the BL12 thermistors 11b7 and 11b8, as determined with the two cryogenic set-up located at Milano Bicocca (mib) and Insubria University (TBT)

Thermistor	R_0 (Ω/sq)	T_0 (K)	α	g_{ep} $(\mathrm{W/K^{\alpha} \cdot m^3})$	G_{ep}(100 mK) $(\mathrm{W/K \cdot m^3})$
11b7 MiB	2259	3.3	4.94	6.8×10^6	3817
11b8 MiB	2217	3.3	4.97	7.4×10^6	3919
11b7 TBT	2276	3.4	5.1	5.3×10^6	3686
11b8 TBT	2234	3.4	5.2	5.9×10^6	3721

Table 5.10: Parameters of the hot electron model, as extrapolated from the simultaneous interpolation of the load curves with $\gamma = 0.5$, for the two BL12 thermistors, measured using the two cryogenic set-up located in Milano Bicocca (MiB) and at Insubria University (TBT)

The results determined for the hot electron model parameters, by the simultaneous interpolation of the load curves performed with $\gamma = 0.5$ fixed, are reported in table 5.11. Figures from 5.42 to 5.47 show the $R - P_e$ and $R - T$ curves, for the three thermistors. The results can be summarized as follows:

- the determined value of T_0 is quite consistent with the value extrapolated from higher temperature measurements (see table 5.8); furthermore, its spread among the three thermistors is below 1%, which, even taking into account the systematic uncertainties of the measuring procedure, confirms the uniformity of the implanting process;
- the value of α results to be less than in the case of the precursors, as already pointed out for the BL12 previously characterized; the same consideration is valid for g_{ep}, though in this case the values related to the BL12 and to the precursors appear to be more consistent;
- the value of $G_{ep}(100\ \mathrm{mK})$ is quite consistent with the case of the precursors, taking into account the geometrical dependence;
- the background power seems to be higher than that determined during the preceding measurements performed in the Oxford cryostat in Milano Bicocca: this fact can also justify the problems with the thermistor 17bol1, which shows a quite different behaviour with respect to the others;
- the $R - P_e$ curves are well interpolated by the hot electron model equations in the whole range of temperatures considered (40 mK - 1 K) and no evidence for the existence of side conduction channels was noticed; the lack of points for some of the measured $R - P_e$ curves is still due to the modality of operation of the automatic program and to the saturation of the preamplifier, as previously pointed out;
- also the $R - T$ curves are well interpolated using the hot electron model; the slight flattening of the curves below 50 mK can be ascribed to the relatively high background power.

Given the above results, the values obtained for T_0 can be plotted as a function of the degree of compensation and compared to the results related to the BL10 thermistors. Figure 5.48 shows such plot, which still confirms an apparent shift of the relation between T_0 and the degree of compensation (the BL12 thermistors were fabricated using the same annealing procedure as the one used for BL10, identified with "by" in

Thermistor	R_0 (Ω/sq)	T_0 (K)	α	g_{ep} (W/K$^\alpha\cdot$m^3)	G_{ep}(100 mK) (W/K$\cdot$m^3)	P_e^{bckg} (pW)
17bol1	2275	4.1	4.9	7.8×10^6	4660	1.6
17bol2	2100	4.2	5.2	1.3×10^7	3995	0.5
17bol9	2010	4.2	5.2	1.3×10^7	3864	0.3
19e3	1888	5.8	5.5	2.3×10^7	4306	0.15

Table 5.11: Parameters of the hot electron model, as extrapolated from the simultaneous interpolation of the load curves with $\gamma = 0.5$, for the three BL12 thermistors with degree of compensation 34%, measured in the TBT cryostat; for comparison purposes, the values of the same parameters for a BL10 thermistor, with similar construction characteristics, are reported (the corresponding degree of compensation is shown in table 5.8)

the plot). As pointed out at the beginning of this section, this result is likely to be a consequence of a drift in the calibration of the implanting machine.

Table 5.12 shows the values of the parameters ρ_0, α and G_{ep}(100 mK) for all the BL12 characterized, calculated using the empirical relations 5.5, 5.6 and 5.7, linking such parameters to T_0. A comparison between these results with those of tables 5.11 and 5.10, still confirms the consideration pointed out concerning the BL10 sensors, dealing with the hypothesis of a dependence of such relations on the geometry. Nevertheless it is interesting to notice that the value of α, determined by interpolating the load curves, appears to be consistent to the value calculated using the empirical relations.

Thermistor	R_0 (Ω/sq)	α	G_{ep}(100 mK) (W/K$\cdot$m^3)
11b7 MiB	2376	5.4	5094
11b8 MiB	2366	5.4	5081
17bol1	2266	5.4	4935
17bol2	2244	5.4	4901
17bol9	2245	5.4	4906

Table 5.12: Parameters of the hot electron model, calculated using the empirical relations 5.5, 5.6 and 5.7, for all the BL12 thermistors characterized below 1 K; for the calculation the value of T_0 determined by the interpolation of the load curves was used

Finally, figure 5.49 shows the trend of the total electron-phonon thermal conductance (not normalized by the volume) at 100 mK, extrapolated from the interpolation

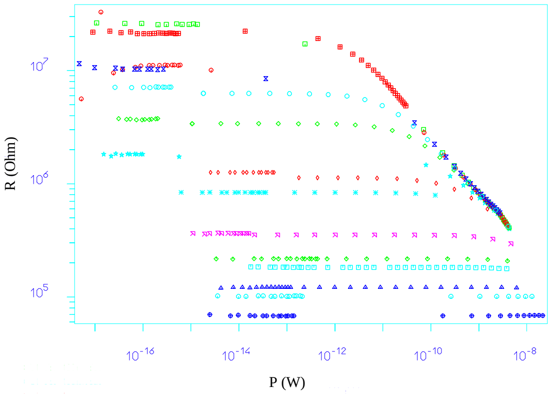

Figure 5.42: $R-P_e$ curves for the BL12 thermistor 17bol1, interpolated with the hot electron model, in the temperature range between 40 mK and 1 K

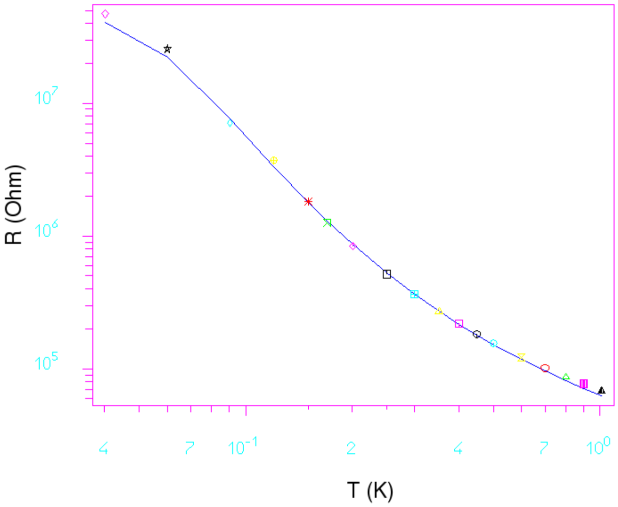

Figure 5.43: $R-T$ curve for the BL12 thermistor 17bol1, interpolated with the hot electron model, in the temperature range between 40 mK and 1 K

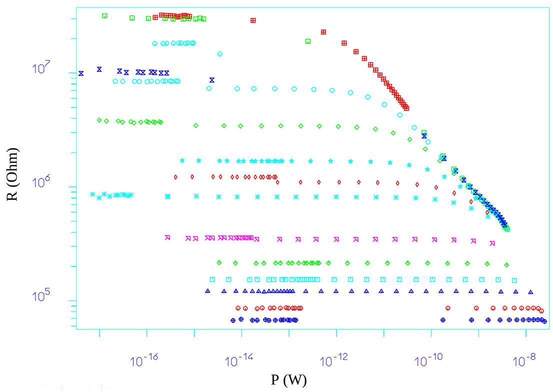

Figure 5.44: $R - P_e$ curves for the BL12 thermistor 17bol2, interpolated with the hot electron model, in the temperature range between 40 mK and 1 K

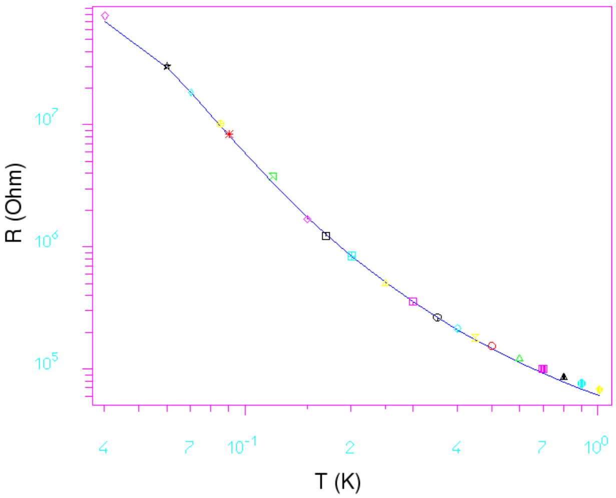

Figure 5.45: $R - T$ curve for the BL12 thermistor 17bol2, interpolated with the hot electron model, in the temperature range between 40 mK and 1 K

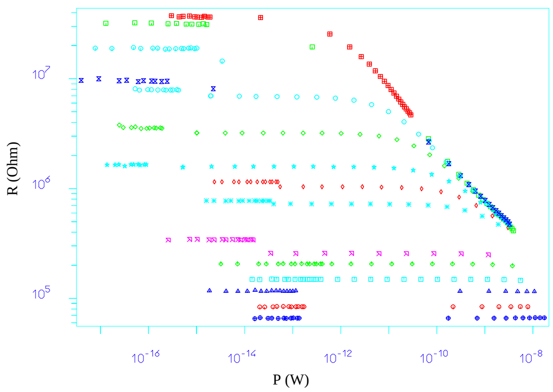

Figure 5.46: $R-P_e$ curves for the BL12 thermistor 17bol9, interpolated with the hot electron model, in the temperature range between 40 mK and 1 K

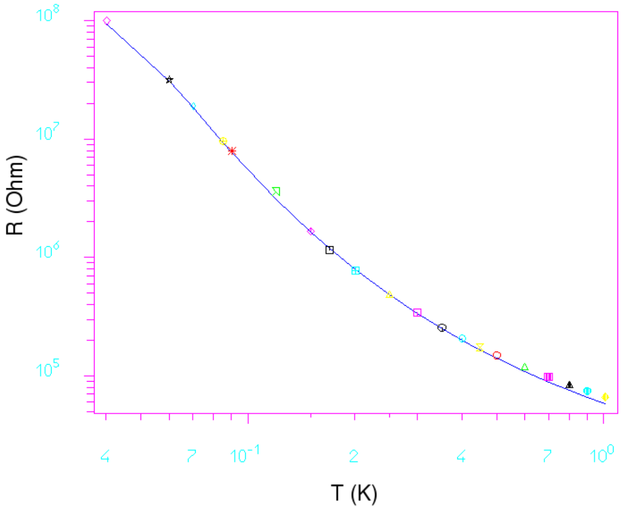

Figure 5.47: $R-T$ curve for the BL12 thermistor 17bol9, interpolated with the hot electron model, in the temperature range between 40 mK and 1 K

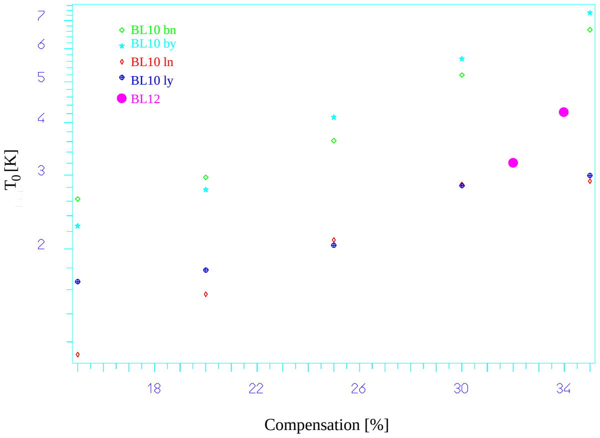

Figure 5.48: T_0 as a function of the degree of compensation for the two BL12 arrays measured below 1 K, superimposed to the trend determined in the case of the four combinations of annealing options used during the production of BL10 (see figure 5.14 for reference)

of the load curves, as a function of volume. The data represent the value averaged over sensors with the same dimensions and refers respectively to BL12, BL10 and BL4 thermistors. This plot put into evidence the proportionality to the volume of the parameter G_{ep}(100 mK), measured in W/K.

During the last cool down run performed in the TBT cryostat, also two of the integrated heaters have been chacterized, named h1 and h4. The measurements were performed using the automatic load curve acquisition system, as done in the case of the LTR4 sample while measured below 1 K. The resistance value resulted to be stable within 0.2%, with the voltage across the heater varying between 100 μV and 5 mV. Figure 5.50 allows to appreciate the good stability (less than 1%) of the resistance of the heaters (calculated by averaging over the measured values at different bias voltages, for a given temperature stage) as a function of temperature, in the range 40 mK - 1 K.

Using the integrated heaters, interesting informations can be drawn about the thermal conductance to the heat sink G_{ps}. In the case of the arrays so far considered, the coupling to the heat sink is provided by the silicon membrane, while in the case of the thermistors which have undertaken the last step of the production process, and which are ready to be used as detectors, it is provided by the silicon legs. During the cool down run performed in the TBT cryostat, during which the array belonging to wafer 17

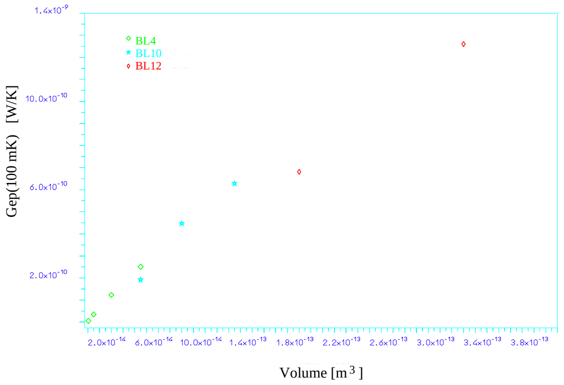

Figure 5.49: Trend of the total electron-phonon thermal conductance at 100 mK, extrapolated from the interpolation of the load curves, as a function of volume

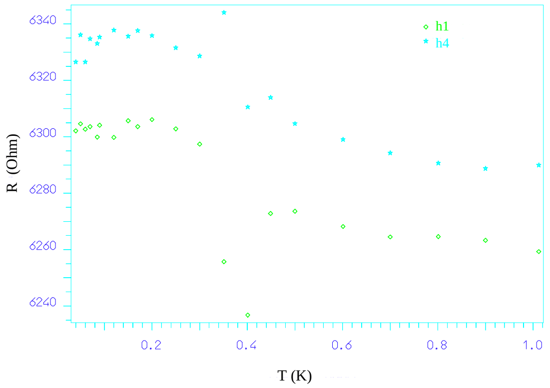

Figure 5.50: Trend of resistance as a function of temperature, measured in the range 40 mK - 1 K, for the two integrated heaters h1 and h4

has been characterized, an attempt to measure the thermal conductance G_{ps} provided by the silicon membrane was also performed. To be specific, the measurement was carried out for the thermistor 17bol1, using the corresponding heater h1.

Before describing the results, it is better to remember the conditions assumed for the static and dynamic characterization of the thermistors, presented in chapter 3. In the following, the parameter G will always refer to the total thermal conductance, measured in W/K. First of all the system of equations 3.9, used for the interpolation of the experimentally determined load curves, is valid assuming that the thermal coupling between the phonons and the heat sink is maximized. In this condition the temperature of the lattice can be considered equal to the temperature of the heat bath, with no regard to the power dissipated into the system, and the only thermal conductance in the game is G_{ep}. On the other hand, when a definite amount of power is dissipated directly into the phonon system by an interacting particle or, as in the considered case, by an heating resistor, the temperature of the phonon system is changed, being no more coincident with that of the heat bath. The evaluation of the thermal conductance G_{ps} can be performed by measuring a series of $P_h - T_p$ pairs, with P_h corresponding to the power dissipated into the phonon system. The temperature of the phonons should be determined by avoiding to warm up the electron system, so that the temperature of the electrons and of the lattice can be considered equivalent. By interpolating the $P_h - T_p$ pairs using a polinomial fit, the value of G_{ps} as a function of the temperature T_p can finally be calculated as $\frac{dP_h}{dT_p}$, by a numerical differentiation.

The procedure actually adopted in the considered case can be described as follows:

- a complete "traditional" load curve of the thermistor has been measured as a first step; this allowed to calculate the temperature of the electron system, once determined the parameters T_0 and R_0, using equation 5.1 with $\gamma = 0.5$;

- different Joule powers (of order nW) were delivered into the thermistor lattice by biasing the heater through a circuit provided with a suited load resistance (in the specific case $R_L = 20$ MΩ); the power injected was calculated as $P_h = (V_{bias}/R_L)^2/R_h$, where R_h is the heater resistance (previously measured);

- the consequent temperature increase of the lattice was measured by dissipating into the electron system a Joule power lower than that delivered to the phonon system (in the specific case of order 10^{-5} pW); to be more precise, the measured quantity was as usual the resistance, from which the temperature of the phonon system was extrapolated still using equation 5.1.

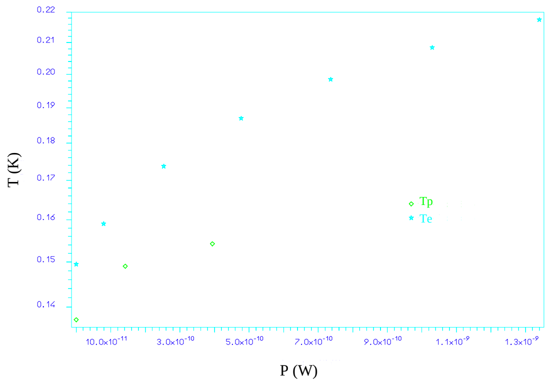

Figure 5.51: T_p and T_e as functions of the Joule power dissipated into the thermistor; from the plot the decoupling between the phonon and the electron system can be appreciated

The measurement was performed at a temperature of the heat sink of about 140 mK. Actually only three points in the $P_h - T_p$ curve were measured, due to external problems dealing with the cryogenic set-up. However the decoupling between the phonon and the electron system can be appreciated in figure 5.51, where the trend of T_p and T_e as functions of the Joule power dissipated are shown. The value of G_{ps}, extrapolated by the numerical procedure above described, is of order 20 nW/K at 100 mK. This value should be compared to the total electron-phonon thermal conductance of the considered thermistor, which, using the data of table 5.11, resulted to be of order $1 - 0.1$ nW/K. In chapter 3 it was pointed out that in the optimum detector configuration the electron-phonon coupling constant should be the highest of the conductances in the game: this is clearly not the case for the arrays still provided with the silicon membrane, which thus can not be used as detectors.

5.3.4 BL12 as detectors

As previously announced only one array, useful to be operated as a detector, did survive to the last production step. Furthermore only eight of the ten thermistors were available (the others got broken during the fabrication), provided with their integrated heaters. The survived array has the following characteristics: it belongs to wafer 16, with compensation 34%, 2 squares, area 600×600 μm^2.

Preparation of the sample and holder for the dynamic characterization

Considering the fragility of the sample, and also taking into account the problems encountered during the preparation (gluing and bonding of connection wires), a number of test was carried out in order to identify the safer gluing and bonding techniques. The test were performed using some samples provided with the membrane, which were glued upon the new devoted packages using different kinds of glues and bonded using various techniques, as below described. The so prepared test samples were cooled down to nitrogen temperature, using the ^{4}He pumped refrigerator, in order to check the gluing system strength, as well as that of the bonding.

- Concerning the glues silver epoxy, stycast and conductive thermal grease were tested. Silver epoxy was used in the case of the precursors, but in the case of BL12 arrays it proved not to be suitable, since the samples always came off, after a cool down run. The problem with silver epoxy in the case of BL12 probably deals with the dimensions of the arrays: this glue resulted to have a poor strength when used for so large devices, also considering that it was necessary to put it over a small fraction of the sample, in order to avoid dangerous thermal contractions. Stycast 2850 showed a quite higher strength, even when put in the form of few close spots. In this case, the contact surface area between the array and the package was inhanced by putting some thermal grease upon the gold foil on the package, just in correspondence to the position of the frame of the sample. Thermal grease is particularly suited to this task, since it leaves the needed freedom of motion required by the thermal contractions.

- Concerning the bonding thechnique, ball bonding using ligther parameters of the machine was tested at first, in order to decrease the stress upon the sample. Since any effort in this direction did not provide good and reliable results, wedge bonding was tested in the end. This thecnique is in fact generally less intrusive with respect to ball bonding. The bonding machine located in the cryogenic laboratory of Insubria University is in fact provided with interchangeable tools, both for ball and wedge bonding. Many test were necessary before the most suited wedge bonding parameters were found.

In view of the dynamic characterization of the BL12 thermistors, a new devoted holder was realized. Figure 5.52 shows the project for the realization of this copper holder, which should fulfill the following requests:

- a series of pins for the electrical connections should be provided, being suited to

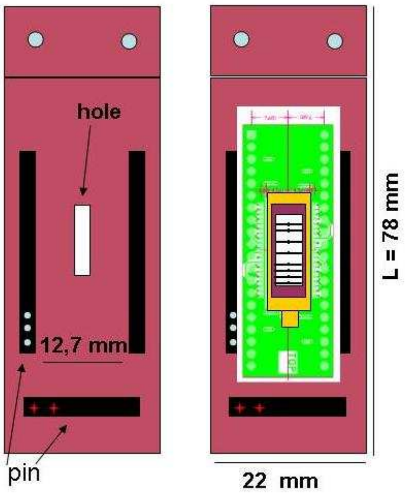

Figure 5.52: Project and structure of the copper holder realized in view of the measurement of the BL12 thermistors, operated as detectors

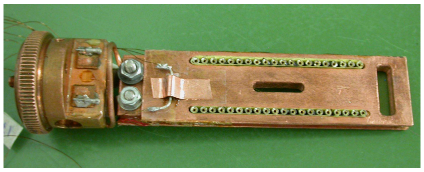

Figure 5.53: Picture of the realized copper holder: the pins, glued and isolated from the copper using mylar, are visible

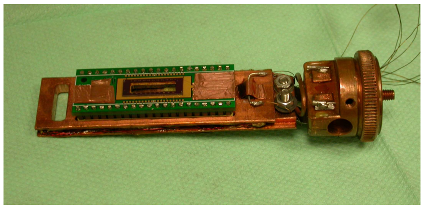

Figure 5.54: Picture of the realized copper holder, with the BL12 array glued upon the devoted package, inserted in its place

the structure of the packages; thus two holes of the required dimensions and in the right position were produced in the copper holder, and two lines of twenty pins each have been inserted and glued (using Stycast 2850); great care was put in order to avoid direct contacts between the pins and the copper, which could produce electrical grounds;

- for the wiring the required connections were provided by soldering constantan wires to the related pins; since in this case each detector should be measured by means of a "two wires reading", being completely indipendent from the other devices, all the pins were left indipendent from each other, not being connected (differently from the case of the static characterization, in which one line of pins was read in common);
- the project also forsaw a further line of pins to be added to the holder, in order to provide the possibility to read in common the devices, if needed;
- in the case considered here, the operating temperature of the thermistors (which is typically around 100 mK) is in principle changed by simply delivering a corresponding bias voltage, since the sensors are coupled to the heat sink through the silicon legs, which should provide a low enough thermal conductance G_{sp}; as a consequence it should not be necessary to use an heating resistor to inhance the temperature of the whole holder; nevertheless a 10 kΩ heater was added to the set-up, in case of any need;
- concerning the thermometer a LakeShore germanium resistor was put in good contact with the holder, by inserting it into a devoted hole and using thermal conductive grease; the wiring was carried out using constantan wires, thermalized to the holder using a varnished layer of cigarette paper; however, in this case the holder temperature simply provides a useful information about the conditions of the experimental set-up, while the important parameters are directly provided by the sensors themselves;
- finally, the holder was provided with a central hole in correspondence to the position of the detectors, in order to allow to face them to a suited radioactive source; to this purpose also the package was provided with a similar central hole, before gluing the array.

Figures 5.53 and 5.54 show some pictures of the holder realized and above described.

Calibration source

In order to characterize the dynamic properties of the BL12 array, a point like ^{55}Fe source was used [59]. ^{55}Fe dacays by EC to ^{55}Mn, which subsequently emits two X-ray lines at 5.90 keV (K_α) and 6.49 keV (K_β): these two X lines are used for the evaluation of the energy resolution of the detector. Taking into account the desidered activity induced in the detectors ($\sim$ 0.1 Bq), the geometrical configuration of the experimental set-up, and the attenuation coefficient of the considered X-rays in silicon (shown in figure 5.55), a ^{55}Fe source of total activity $\sim$ 75 Bq was chosen. The rate produced in the detectors, directly facing the source, was evaluated considering the distance separating them. The result obtained, considering the source placed on the opposite side of the holder, with respect to the location of the package, showed that a too high total activity was required. For this reason the source was attached to the package, on the opposite side with respect to the location of the array, so that a distance just equal to the package thickness separates the two. In this configuration the expected rate induced in the detectors is of about 0.3 Bq.

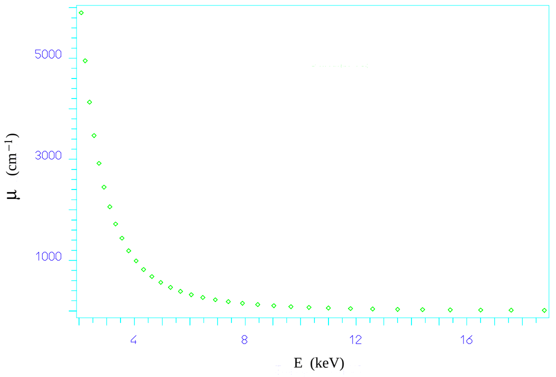

Figure 5.55: Linear attenuation coefficient of X-rays, as a function of energy, in silicon

The used source was produced some years ago, by putting a suited spot of aqueous solution containing ^{55}Fe on to a piece of mylar and drying. Since it was not possible to find reliable informations regarding the precise location of the spot on the mylar support, a devoted measure was carried out in order to solve this problem. The source was measured using a silicon pixel detector, with 17 μm spacial resolution, located in the Laboratory of Silicon Detectors at Insubria University. The source was faced to the silicon detector, able to detect the X-rays coming from it (figure 5.56). At the same time a laser beam was used to lighten the source: the silicon detector is also able to detect this light, where not stopped by the presence of an interposed element. This procedure allowed to take a kind of picture of the shape of the mylar support, superimposed to the picture of the source spot, producing the X-rays. The result is shown in figure 5.57, where the shadow of the mylar support and the location of the ^{55}Fe spot, as suggested by the arrow, are visible. Figures 5.58 and 5.59 show some pictures taken at the microscope of the detectors faced to the ^{55}Fe source.

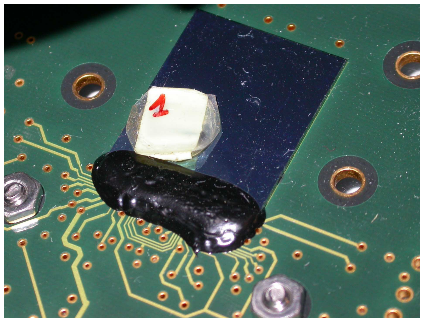

Figure 5.56: Picture of the ^{55}Fe source during the measurement performed with the silicon pixel detector

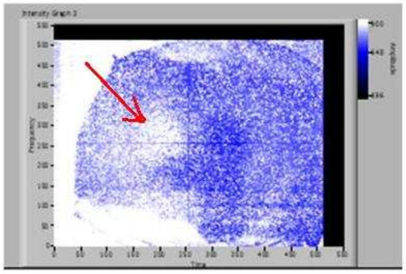

Figure 5.57: Shadow produced by the mylar support superimposed to the "picture" of the ^{55}Fe spot, as detected by the silicon pixel detector

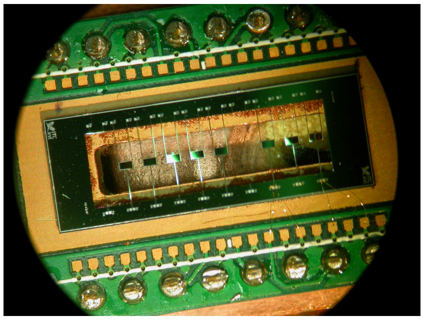

Figure 5.58: Picture of the BL12 detectors faced to the ^{55}Fe source, taken at the microscope

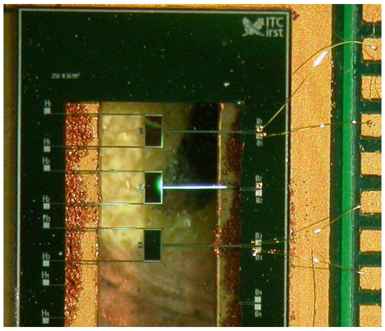

Figure 5.59: Picture of the BL12 detectors faced to the ^{55}Fe source, taken at the microscope; the wedge bonding are also visible

Dynamic characterization

Various cool down runs have been carried out, since during the early ones no useful results, in terms of the dynamic characterization, were drawn, due to problems dealing with excessive noise or with the electronic set-up. Unfortunately, during this series of attempts, a further problem occured with the BL12 array: the stycast did not withstand the sequence of cooling down and consequently some of the silicon legs went broken. In the end two thermistors, only provided with the silicon leg linking the thermistor to the heat sink (see figure 5.60), were characterized from a dynamical point of view. Furthermore the measurements were performed without any absorber coupled to the sensors: in this case the thermistors operate as calorimeters themeselves, the silicon substrate acting as the absorbing element.

Nevertheless, the early runs carried out in the TBT cryostat were useful to evaluate the thermal conductance of the three silicon legs (before they went broken), by means of an indirect approach, as described in the next paragraph.

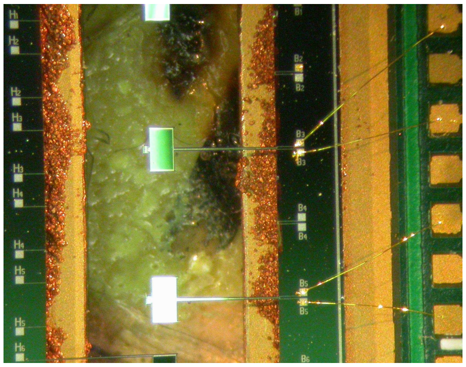

Figure 5.60: Picture (taken at the microscope) of the two thermistors provided with one silicon leg, characterized from a dynamical point of view

The measurements descussed in the following, concerning two sensors provided with only one silicon leg, were performed in a different dilution refrigerator, still located in the Cryogenic Laboratory at Insubria University. This cryostat arrived in Como directly from the Air Liquide Laboratories of Grenoble: for this reason it will be refered to as AL cryostat. It is quite different from the TBT, since it has been designed to work without the liquide ^{4}He bath. The condensation of the mixture is in fact achieved by means of a cryocooler, namely a Pulse Tube (PT), and the Joule-Thompson effect [60, 61]. The AL cryostat is provided with both an IVC shielding and an OVC (outer vacuum chamber), isolating the inner volume from room temperature blackbody radiation. Temperatures as low as $10-15$ mK can be reached in principle. A quite large space is available below the mixing chamber in this case (20 cm height × 18 cm diameter). The cryostat is equipped with a set of thermometers and two Jaeger connectors, with 12 pins each. The wiring, provided by Air Liquide, is thermalized at various temperature stages. The choice to use this refrigerator instead of the TBT, in view of the dynamic characterization of the BL12 thermistors, was due to the more stable conditions attainable using the PT cooling system, with respect to the use of an ^{4}He bath. In figure 5.61 some pictures of the dilution unit of the AL cryostat are shown.

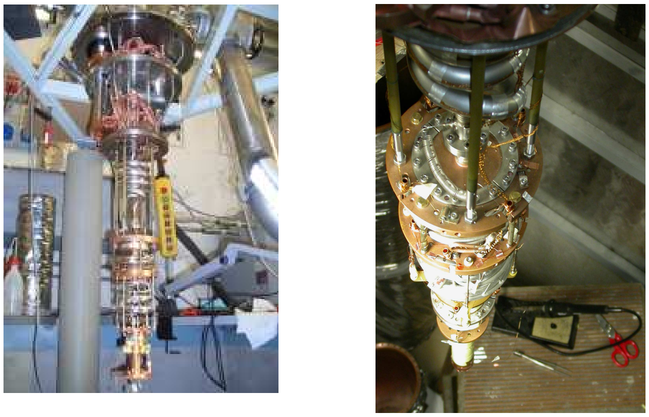

Figure 5.61: The left picture shows the complete dilution unit of the AL cryostat; the right picture shows the bottom part of the dilution unit, with the holder for the dynamic characterization of BL12 thermistors coupled to the mixing chamber

The general measurement procedure, adopted for the dynamic characterization of microcalorimeters, can be summarized as follows:

- measurement of a complete load curve in order to find the optimum working point, as explained at the end of section 2.3.1; this is accomplished by leaving the holder housing the detectors at a temperature corresponding to the base temperature of the cryostat; the operating temperature of the bolometers is then inhanced as a consequence of the polarization;

- setup the devoted electronics;

- acquire pulses induced by the source, and baselines (which correspond to the voltage level before the developement of a pulse), and finally analyze them to deduce the properties of the detectors and to evaluate the signal to noise ratio.

Figure 5.62 shows the electrical read-out configuration used for the measurement, which can be devided into four main parts (see also [62]):

Biasing system The thermistor is symmetrically biased by means of two load resistors R_L. In this way a differential signal is read, thus avoiding common mode noise. At the working temperature the condition $R_L \gg R$ should be assured, in order to produce a constant bias current into the bolometer. Since the silicon thermistors behave like a resistance of order $1 - 100$ MΩ at the typical operating temperatures (~ 100 mK), R_L is chosen with values of order GΩ. These high load resistance values allow to reduce the Johnson noise contribution, due to the high bolometer resistance.

First differential stage It consists of a differential preamplifier with gain $G = 218$, which contributes to the reduction of the common mode noise (as the microphonic noise). In fact it cancels all the noise pulses of this kind, since they reach the differential stage with the same phase.

Bessel filter A low pass Bessel filter is used in order to cut as much as possible the spurious frequences, which could otherwise worsen the signal to noise ratio. It is possible to set the value above which all the frequences are cut by choosing among a limited available range (maximum 70 Hz). In order not to affect the signal amplitude, the cut frequency should be higher then the maximum frequency contained in the signal. This is a crucial point, especially in the considered case: the electronic set-up used is in fact optimized for macrobolometric measurements, where the signals are usually slow and thus not affected by the presence of a low frequency Bessel filter. Microcalorimeters, on the other hand, usually produce faster signals. As a consequence, the use of a relatively too low Bessel filter (the effect of which consists in an integration of the pulse) might change even dramatically the signal shape. As will be discussed, the results obtained concerning the detector performances actually suffered from this non optimized operating condition.

Second stage An additional amplifier stage, with adjustable gain, is set before the signal is transmitted to the ADC.

A further crucial point, concerning the electronic set-up of our laboratory, deals with the fact that it operates at room temperature. Great improvements of the signal to noise ratio can be achieved by using a cold electronic stage. In particular the first differential stage can be set to operate at ~ 120 K: in this case, series and parallel preamplifier noise is reduced by the fact that this noise decreases with temperature. Cold electronics can also help to reduce microphonic noise, which is quite disturbing when observing low energy signals. Concerning this point, the parasit capacitance of the signal wires from the mixing chamber to room temperature electronics is estimated to be around 100 – 1000 pF. The combination of this capacitance with the typical bolometer impedance (several MΩs) produces a pole which integrates the signal with a time constant of about several ms. This prevents the observation of the fast component of the signal and surely leads to a substantial underestimation of the pulse amplitude.

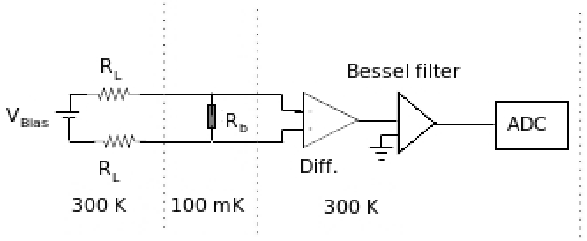

Figure 5.62: Scheme of the electrical read-out set-up

After being processed by the electronic set-up, which is placed inside a devoted Faraday cage, the signals are sent simultaneously to the Analog to Digital Converter (ADC) and to the trigger that commands the ADC. If the pulse amplitude is higher than the trigger threshold (which is independently set for each detector) the signal is digitalized and transmitted to a PC. The acquisition hardware is composed by CAMAC boards and the custom acquisition software was written by L. Foggetta, in the context of the CUORE R&D activities carried out in our Laboratory [63]. The ADC parameters can be adjusted on pulse characteristic, but usually a voltage range of 0 – 10 V is used. The sampling rate is usually set to 1 – 5 kHz and for each pulse 1024 points are acquired.

The data analysis is completely performed off-line, using software tools devoted to the Cuoricino data analysis. The main goals of the analysis procedure consist in the extraction of the useful informations concerning the pulse shape (amplitude, rise and decay time) and the noise sources, in order to evaluate the detector performances in terms of signal to noise ratio. The analysis procedure adopted for the two BL12 thermistors characterized can be summarized as follows:

- at a first level the single pulses recorded are studied, in order to estimate their shape, in terms of amplitude and rise time, and to produce an average pulse;

this stage is also useful for the rejection of spurious events, triggered by the acquisition system and recognizable by means of pulse shape analysis; the signal to noise ratio can be estimated by a parallel analysis of the acquired baselines, which carry the informations regarding the noise spectrum;

- the final aim of the first level analysis consists in the production of reliable ntuples, which contain the parameters needed for the construction of the energy spectra; this second level analysis allow then to evaluate the actual energy resolution, which should be compared to that expected by the signal to noise ratio previously determined.

The software tool used for the first level analysis, calculates the important parameters contained in the ntuples by processing the single pulses using the optimum filter (OF) technique. This allows to evaluate the best estimate of the pulse amplitude, in presence of superimposed noise. Once the noise spectrum $N(\omega)$ is determined by studying the baselines, the optimum filter defines a trensfer function $H(j\omega)$ given by [64]:

$$H(j\omega) \propto \frac{S_j^*(\omega)}{N^{1/2}(\omega)} \tag{5.9}$$

where $S_j(\omega)$ (defined in equation 3.20) is the pulse shape determined as the average over a significant number of recorded pulses. The noise spectrum $N(\omega)$ is calculated as the average of the Fourier transforms of the acquired baselines. The other parameters evaluated and recorded in the ntuples, besides the optimum filtered amplitude in both time and frequency domain, are: the absolute time at which each pulse occurred, the baseline level (a small portion of which is registered before each triggered pulse) which is linked to the temperature of the system, the baseline root mean square for the noise trend analysis, the signal rise (10-90%) and decay times (90-30%), the pulse shape parameters which contain the informations regarding the difference between the recorded signal and the calculated average pulse.

Concerning the baseline level, it is in principle useful to correct off-line the temperature instabilities, which consequently produce voltage and thus sensitivity variations. This correction can be performed with the aid of heater pulses, as explained in 2.3.1. Since in the case considered here it was not possible to carry out such analysis, the baseline instabilities should be considered as a further contribution to the broadening of the energy resolution.

The two thermistors characterized will be named in the following b3 and b5. First of all a complete load curve was measured for both thermistors, using the electronic set-up above described, without activate the bessel filter and the second stage. The load curves were determined manually and the working point found empirically (without the aid of heater pulses).

The electronic set-up allows to deliver a series of bias voltages V_{bias} and to measure the corresponding voltage produced across the thermistor V_b; the constant current flow I can be calculated since the load resistance is also known (in the usual approximation $R_L \gg R$); finally the resistance of the sensor R can be extrapolated, from which the corresponding temperature of the electron system T_e can be derived, using the hot electron model equation 5.1, with $\gamma = 0.5$. Concerning the parameters T_0 and R_0, the values previously determined by the static characterization can be used[4].

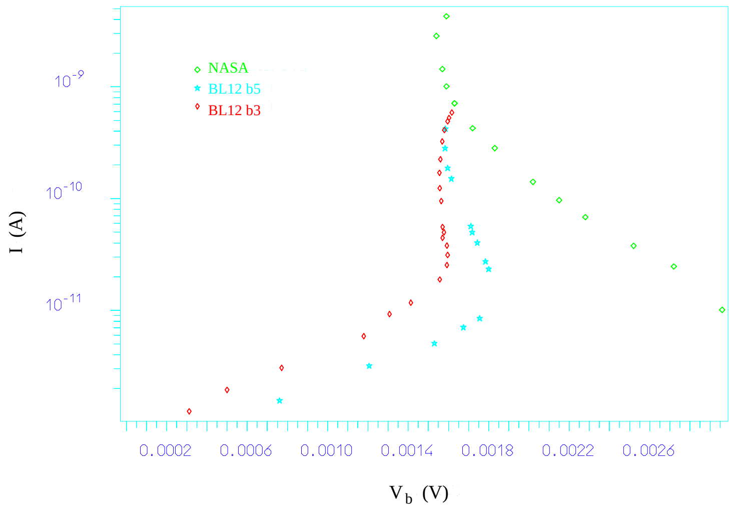

Figure 5.63: Load curves determined for the two BL12 thermistors b3 and b5, and for detector 6 of table 5.1

Figure 5.63 shows the load curves, measured for the two BL12 thermistors, compared to the load curve of detector number 6 of table 5.1, composed by one pixel of the NASA array coupled to a $AgReO_4$ crystal. The NASA thermistor shows a higher resistance, with respect to the two BL12 sensors, at least in the lower temperature range (below $\sim$ 75 mK), as can be appreciated in figure 5.64, where the ratio between the two

---

[4] Since the array considered here was not characterized from a static point of view, the values of T_0 and R_0, determined for the BL12 thermistors with degree of compensation 34%, previously characterized in the TBT cryostat, were used; concerning R_0 it was normalized considering the different square number

resistances is plotted as a function of temperature. This explains the different slopes in the initial part of the load curves and the higher voltage inversion point for the NASA thermistor.

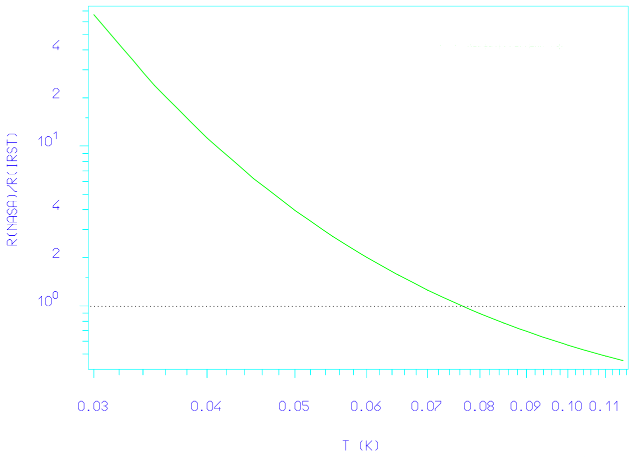

Figure 5.64: Ratio between the resistance of the NASA thermistor and that of the BL12 thermistors, as a function of temperature (green line); the dotted line indicates a value of the ratio equal to unit

Furthermore, the two BL12 thermistors characterized show a similar, though not identical, behaviour: in particular the resistance of b5 appears to be slightly higher with respect to b3. This fact can be explained using various hypothesis, though it was not possible to draw a definitive conclusion:

- the temperature of thermistor b3 may be inhanced by the presence of a higher background power, as a consequence its resistance is reduced with respect to b5;
- there may be a slight temperature gradient along the copper holder and consequently through the sample;
- there may be a slight dishomogeneity of the implant through the array.

Microcalorimeters, unlike macrobolometers, are often operated beyond the inversion point of the load curve, since in that region the electrothermal feedback can be exploited in order to produce very fast pulses. In particular, detector 6 from the NASA array was operated with $V_b \sim 1.7$ mV, corresponding to a temperature of 85 mK.

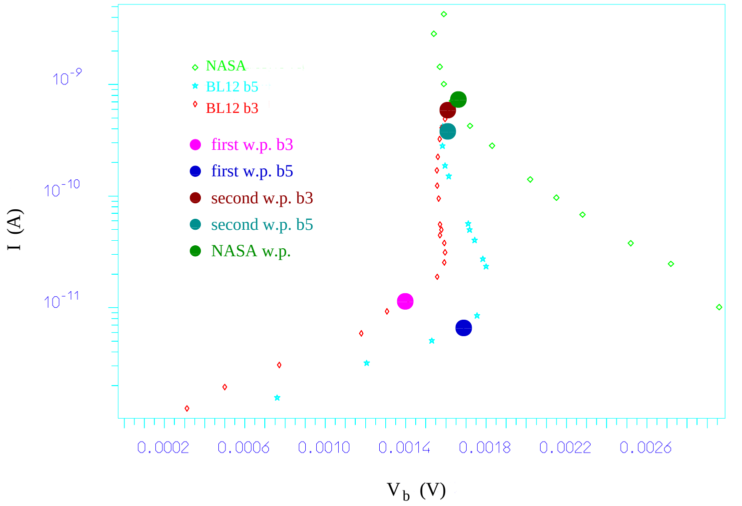

Figure 5.65: Working points for the two BL12 thermistors and the NASA thermistor

In the case of the BL12 thermistors the dynamic measurements were performed in correspondence of two different working points, in order to study the different behaviour below and beyond the inversion point of the load curves. To be specific, the two detectors were characterized in correspondence of the following working points, as shown in figure 5.65:

- for b3, first working point: $V_b \sim 1.4$ mV, $I \sim 12$ pA, corresponding to a temperature of ~ 40 mK;
- for b5, first working point: $V_b \sim 1.7$ mV, $I \sim 7$ pA, corresponding to a temperature of ~ 37 mK.
- for b3, second working point: $V_b \sim 1.6$ mV, $I \sim 588$ pA, corresponding to a temperature of ~ 100 mK;
- for b5, second working point: $V_b \sim 1.6$ mV, $I \sim 300$ pA, corresponding to a temperature of ~ 85 mK.

Before entering into the details of the measurements performed, it would be useful to remind again and summarize the experimental conditions, which, since not optimized, surely induced a limitation to the detector performances:

- the absence of a cold stage of the electronic set-up surely leads to an underestimation of the pulse amplitude, due to the combination of the parasit capacitance of the signal wires with the typical bolometer impedance;
- similarly, the impossibility to set-up the electronics in a configuration optimized for microcalorimetric measurements, leads to an underestimation of the signal amplitude, due to the presence of a low frequency Bessel filter, even more in the case of very fast signals;
- the presence of ground loops in the actual configuration of the set-up would have required a stronger effort, in order to reduce all the noise frequencies introduced, like the 50 Hz component;
- the holder housing the samples is not optimized in order to evoid microphonic contributions to the noise spectrum;
- the absence of a proper absorbing element coupled to the thermistors and the not suited properties of silicon, to act as the energy absorber, surely limit the energy resolution;
- the relatively low counting rate of the source used, makes the background counts to compete with the rate of events from the source;
- the absence of heater pulses, to be used for the correction of the baseline instabilities, further contributes to the broadening of the energy resolution.

However, the discussion which follows, concerning the analysis of the measurements performed, shows that the results so far obtained are very promising and that great improvements could be obtained by simply optimizing the experimental set-up.

Taking into account the considerations above discussed, the dynamic measurements were performed using the maximum available total gain and the maximum available bessel filter, equal to 70 Hz. Figures from 5.66 to 5.69 show the typical pulses recorded for thermistor b3 and b5 respectively, in correspondence of the two different working points, superimposed to the related average pulse. The signals for the two detectors, at a given working point, are similar, but not identical: in particular, pulses from thermistor b3 show faster rise and decay times. This can be justified taking into consideration the different behaviour shown also during the measurement of the load curves. Furthermore the signals appear to be quite faster in correspondence to the second working point, as expected due to the position located beyond the inversion point of the load

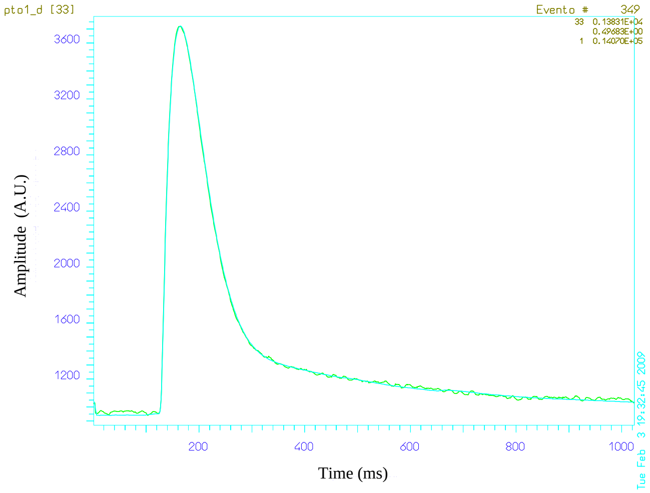

Figure 5.66: Pulse recorded for thermistor b3, in the configuration corresponding to the first working point described in the text, superimposed to the calculated average pulse

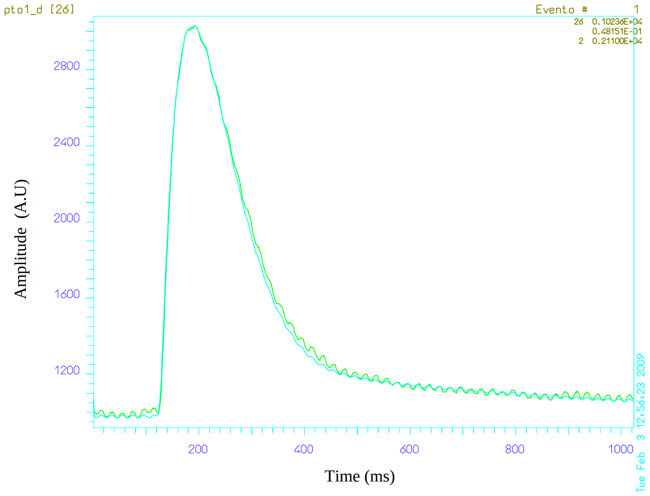

Figure 5.67: Pulse recorded for thermistor b5, in the configuration corresponding to the first working point described in the text, superimposed to the calculated average pulse

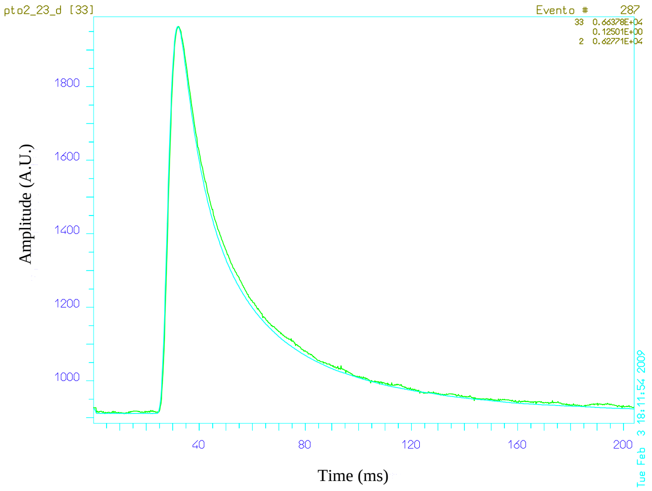

Figure 5.68: Pulse recorded for thermistor b3, in the configuration corresponding to the second working point described in the text, superimposed to the calculated average pulse

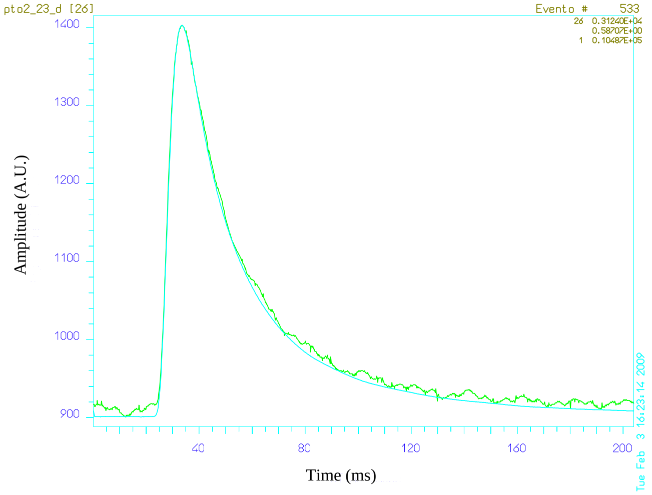

Figure 5.69: Pulse recorded for thermistor b5, in the configuration corresponding to the second working point described in the text, superimposed to the calculated average pulse

curves. Of course, by observing the pulses, a characteristic noise component of frequency ~ 50 Hz appears, which is especially visible in the case of the first working point: this is surely due to a ground loop which was not eliminated.

Figures from 5.70 to 5.73 show the noise spectra, obtained from the analysis of the acquired baselines, for the two thermistors, in correspondence of the two working points, superimposed to the signal spectra, in the frequency domain. Two elements arise by observing the plots:

- the 50 Hz frequency peak is visible, as already noticed by observing the pulses; other components are also present, mainly due to microphonism;
- the signal spectrum gets below the noise spectrum in correspondence of a frequency of about 5 Hz for the first working point and 20 Hz for the second working point: the useful frequency bands appear to be abnormally low for microbolometers. This may be explained through the artificial slowness of the pulses (because of the bessel cut-off and the parasitic capacitance) and the not optimized noise level.

The noise spectra were integrated between $1 - 500$ Hz, in order to evaluate the root mean square noise (Vrms): the results are reported in table 5.13.

The energy spectra from figure 5.74 to 5.77 show clearly the presence of one main peak, which can be ascribed to the superimposition of the two X-ray lines, coming from the ^{55}Fe source: the energy resolution appears to be not sufficient to separate between the two lines. However, in order to perform a correct evaluation of the FWHM, a deeper analysis was carried out as later described. A second, lower peak is also visible, located at lower energy: its origin is probably due to fluorescence X-rays, coming from calcium contained in the fiberglass package[5] and corresponding to an energy of about 3.7 keV. The typical signal amplitude, for events corresponding to a 5.90 keV X-ray, can be extrapolated from the energy spectra, since it corresponds to the position of the peak centroid, normalized by the gain of the electronic set-up. The amplitude values so determined are reported in table 5.13.

The mean rate measured in all cases is of order $0.01 - 0.03$ Hz, thus slightly lower then the 0.3 Hz rate evaluated during the preparation of the sample: however the difference can be justified considering the approximations and imprecisions in the evaluation of the source-detector distance.

---

[5] Fiberglass contains 58 to 60 percent SiO_2, 11 to 13 percent Al_2O_3, 21 to 23 percent CaO, 2 to 4 percent MgO and 1 to 5 percent TiO_2

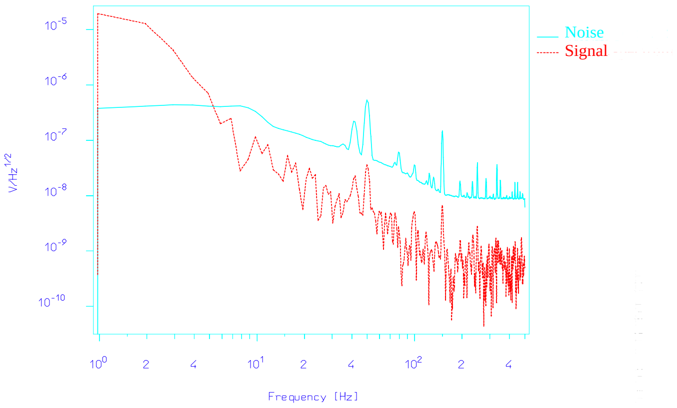

Figure 5.70: Noise spectrum for thermistor b3 superimposed to the signal spectrum, in the frequency domain, recorded in the measurement configuration corresponding to the first working point described in the text

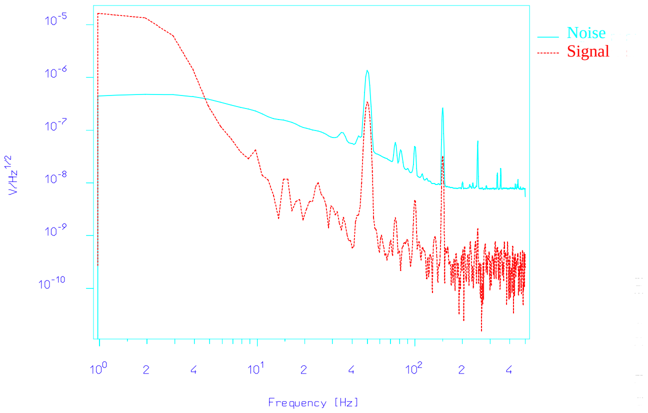

Figure 5.71: Noise spectrum for thermistor b5 superimposed to the signal spectrum, in the frequency domain, recorded in the measurement configuration corresponding to the first working point described in the text

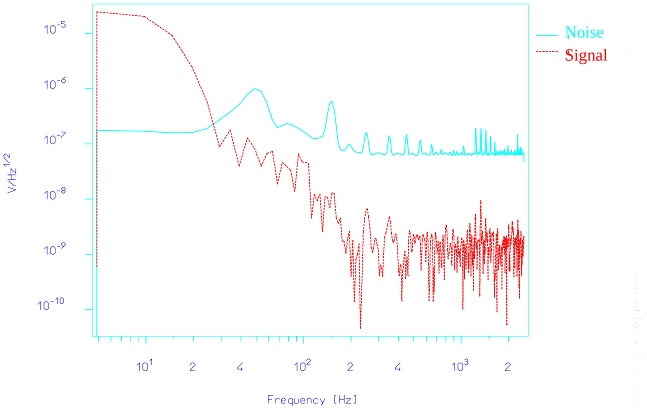

Figure 5.72: Noise spectrum for thermistor b3 superimposed to the signal spectrum, in the frequency domain, recorded in the measurement configuration corresponding to the second working point described in the text

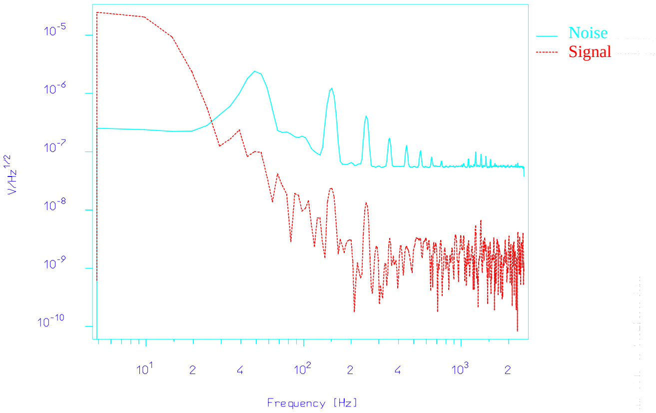

Figure 5.73: Noise spectrum for thermistor b5 superimposed to the signal spectrum, in the frequency domain, recorded in the measurement configuration corresponding to the second working point described in the text

The signal to noise ratio was evaluated using a devoted analysis tool (the same used to calculate the noise spectrum integral). The corresponding expected FWHM value, measured in Volt, was also determined. The expected energy resolution in eV was then calculated by using the proportionality:

$$\Delta E_{FWHM}[\text{eV}] = \frac{\text{FWHM}[\text{Volt}] \times 5900}{\text{Amplitude @5.9keV}[\text{Volt}]} \tag{5.10}$$

were 5900 corresponds to the energy in eV of the K_α line of the ^{55}Fe source, and the Amplitude @5.9 keV in Volt corresponds to the peak centroid determined from the energy spectrum (normalized by the gain).

In table 5.13 all the results of this analysis are reported, together with the typical values of rise (τ_r) and decay time (τ_d), also shown in figures from 5.78 to 5.83.

Thermistor & working point	Amplitude @5.9 keV (μV)	Vrms (μV)	ΔE_{FWHM} @5.9 keV (eV)	τ_r (ms)	τ_d (ms)
b3 w.p. 1	143	1.7	964	20 – 25	63 – 80
b5 w.p. 1	178	2.6	424	33 – 44	113 – 127
b3 w.p. 2	19	0.4	288	2 – 6	17 – 25
b5 w.p. 2	31	0.8	198	3 – 7	26 – 28

Table 5.13: Results in terms of signal amplitude @5.9 keV, root mean square noise (Vrms) calculated by integrating the noise spectrum between $1-500$ Hz, typical range of rise and decay time of the pulses, and expected energy resolution ΔE_{FWHM} @5.9 keV obtained through the analysis described in the text

Concerning the root mean square noise, the resulting values are quite high, confirming that the whole set-up requires to be further optimized, as already pointed out. The expected energy resolution is consequently affected by a not optimized signal to noise ratio. The values of ΔE_{FWHM} @5.9 keV, obtained from the analysis, confirm in fact that it is not possible to separate between the two ^{55}Fe X-ray lines.

Nevertheless, in correspondence to the second working point (located beyond the inversion point) the energy resolution appears to be improved, as well as the rise and decay times, which result to be shorter (faster pulses). On the other hand, the signal amplitude is quite lower at the second working point, as expected due to the lower resistance value (higher temperature). However, it is worth to notice that the low frequency of the Bessel filter may affect even more the pulse shape in correspondence of

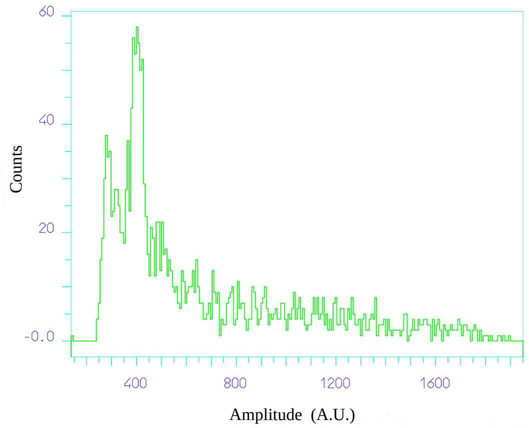

Figure 5.74: Energy spectrum for thermistor b3 (amplitude in arbitrary units), recorded in the measurement configuration corresponding to the first working point described in the text

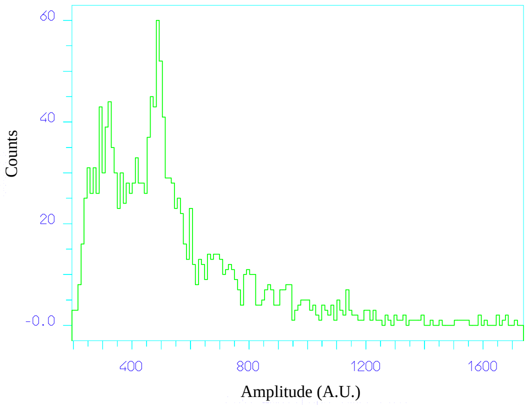

Figure 5.75: Energy spectrum for thermistor b5 (amplitude in arbitrary units), recorded in the measurement configuration corresponding to the first working point described in the text

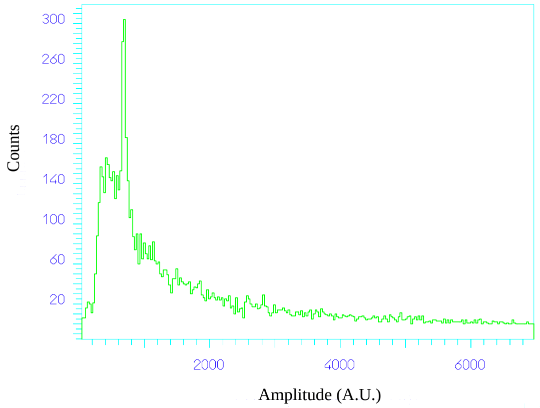

Figure 5.76: Energy spectrum for thermistor b3 (amplitude in arbitrary units), recorded in the measurement configuration corresponding to the second working point described in the text

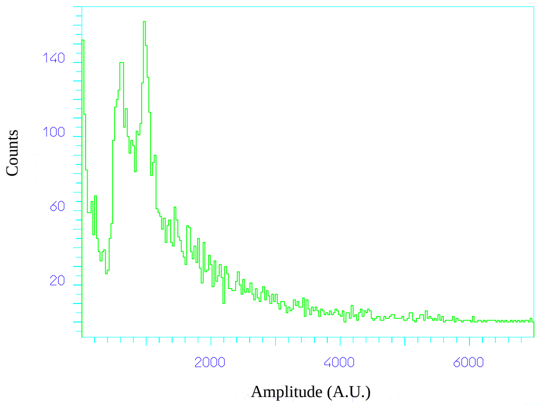

Figure 5.77: Energy spectrum for thermistor b5 (amplitude in arbitrary units), recorded in the measurement configuration corresponding to the second working point described in the text

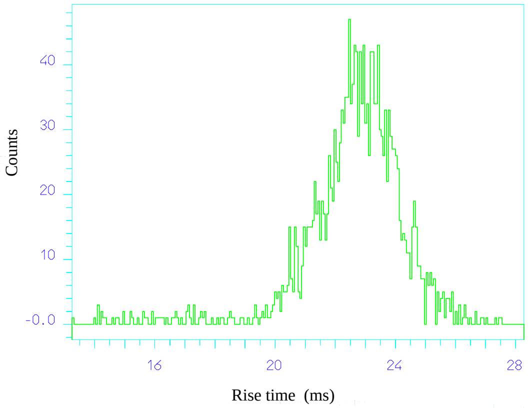

Figure 5.78: Rise time spectrum for thermistor b3, recorded in the measurement configuration corresponding to the first working point described in the text

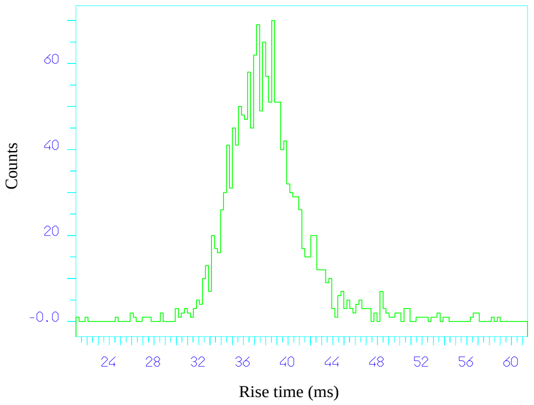

Figure 5.79: Rise time spectrum for thermistor b5, recorded in the measurement configuration corresponding to the first working point described in the text

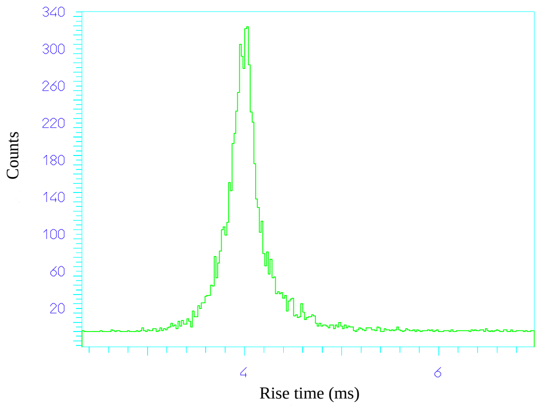

Figure 5.80: Rise time spectrum for thermistor b3, recorded in the measurement configuration corresponding to the second working point described in the text

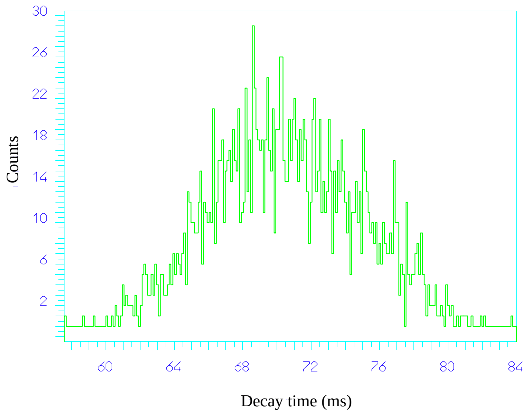

Figure 5.81: Decay time spectrum for thermistor b3, recorded in the measurement configuration corresponding to the first working point described in the text

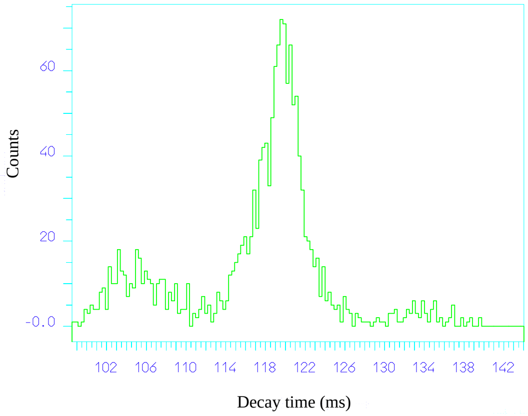

Figure 5.82: Decay time spectrum for thermistor b5, recorded in the measurement configuration corresponding to the first working point described in the text

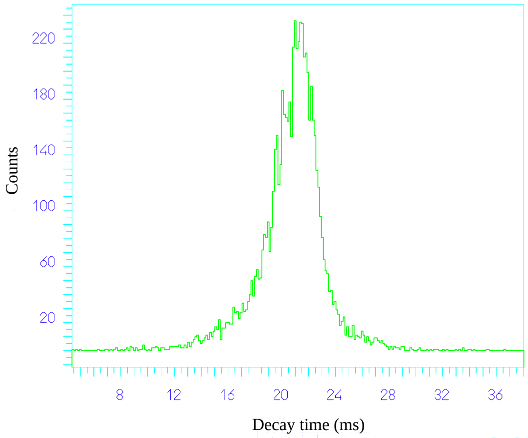

Figure 5.83: Decay time spectrum for thermistor b3, recorded in the measurement configuration corresponding to the second working point described in the text

the second working point, were the signals show faster rise and decay times. By observing the energy spectra reported in the related figures, the actual energy resolution appears to be in accordance with the expected value, or even slightly worse.

Besides the considerations so far pointed out, concerning the not optimized operating conditions, the asymmetric shape of the main peak, as well as the broadened energy resolution, can be also ascribed to the absence of a proper energy absorber. Concerning this topic, the following considerations about the use of silicon as energy absorber were pointed out in chapter 3:

- the detector response may depend on the interaction point, due to the partial thermalization of the primary high energy phonons directly into the thermistor;
- the silicon substrate is not well suited to act as the energy absorber, due to the presence of metastable states, in which part of the deposited energy can be trapped for a time interval longer than the time of formation of the signal.

For the same reason, a comparison with the detector performances obtained with the NASA array will not be meaningful, since in the latter case the thermistors are coupled to proper absorbing elements.

A further contribution to the broadening of the energy resolution must be considered to complete the analysis. Figures from 5.84 to 5.87 show the trend of the baseline level with time, which is clearly unstable in all the considered cases, thus surely affecting the results in terms of energy resolution.

Finally, the best spectrum acquired, corresponding to the second working point for thermistor b5, was calibrated using the two X-ray peaks recognized: the 3.7 keV K_α line from Ca and the 5.9 keV K_α line from Mn. The calibration gave as a result the following linear relation, between energy (E) and ADC channel (ch):

$$E(\mathrm{keV}) = 0.1812\frac{\mathrm{keV}}{\mathrm{ch}} \cdot \mathrm{ch\ number} + 0.22 \tag{5.11}$$

Figure 5.88 shows the spectrum calibrated according to the above relation.

Evaluation of the phonon-bath thermal conductance

As previously announced, the measurements performed during the early cool down runs carried out in the TBT cryostat were useful to determine the phonon-bath thermal conductance, in the case of the sensor linked to the heat sink by the three silicon legs. It was then possible to make interesting comparisons between the results obtained in this case and in the case of the thermistors provided with one single silicon leg, measured

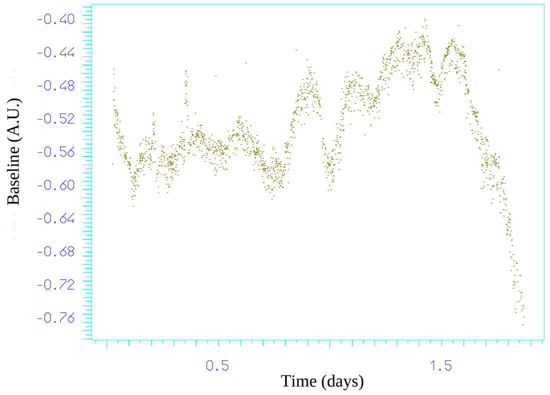

Figure 5.84: Baseline trend as a function of time for thermistor b3, recorded in the measurement configuration corresponding to the first working point described in the text

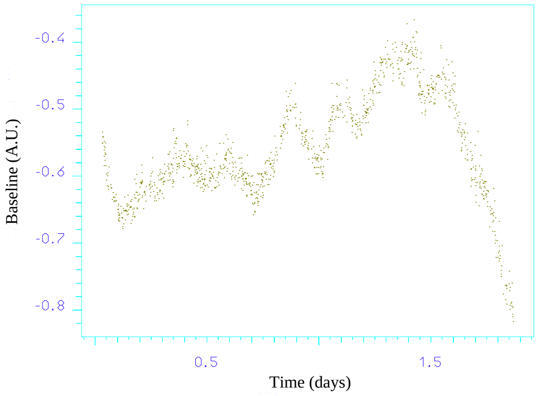

Figure 5.85: Baseline trend as a function of time for thermistor b5, recorded in the measurement configuration corresponding to the first working point described in the text

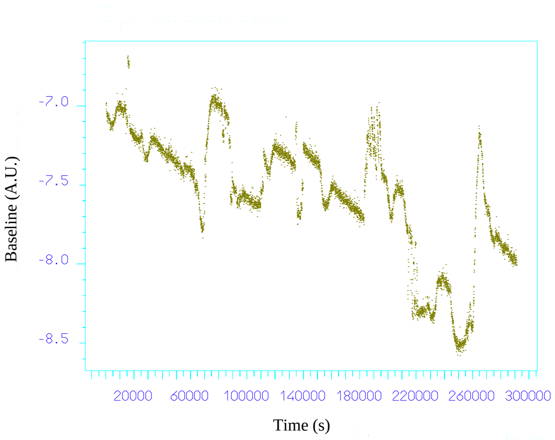

Figure 5.86: Baseline trend as a function of time for thermistor b3, recorded in the measurement configuration corresponding to the second working point described in the text

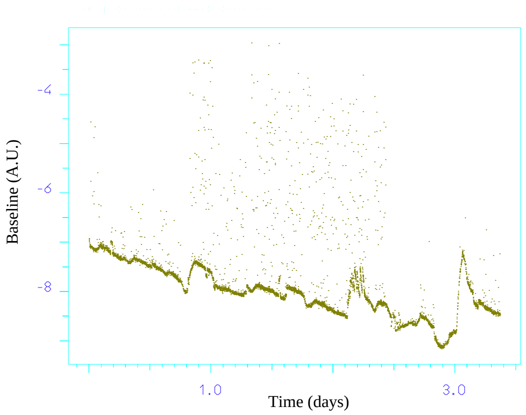

Figure 5.87: Baseline trend as a function of time for thermistor b5, recorded in the measurement configuration corresponding to the second working point described in the text

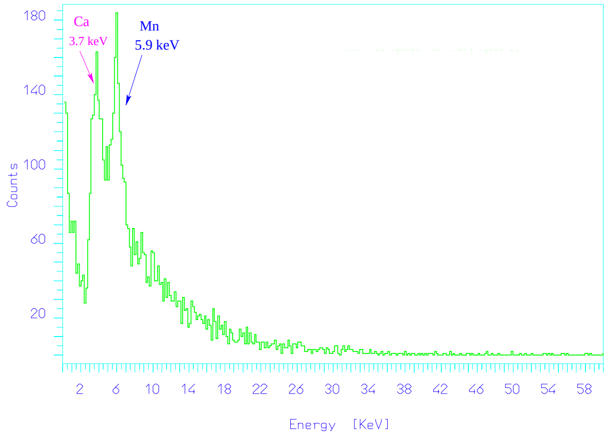

Figure 5.88: Spectrum for thermistor b5, recorded in the measurement configuration corresponding to the second working point, calibrated according to the relation 5.11

in the AL cryostat. Furthermore the results were compared to the theorical expected value, calculated using the kinetic gas model.

Before entering into the details of the performed measurements, it will be better to remind the conditions assumed for the dynamic characterization of the calorimeters and the relation occurring between the thermal conductances in the game. Still in the present case the symbol G will identify the total thermal conductance, mesured in W/K. As discussed in chapter 3, in order to optimize the detector performances, the thermal conductance to the heat bath should be minimized. In the considered case the thermal model includes two thermal conductances, operating in series (since the absorber actually coincides with the phonon system): the electron-phonon thermal conductance G_{ep} and the phonon-bath thermal conductance G_{ps}. The measurable parameter corresponds to the total thermal conductance, which is given by:

$$G_{tot} = \frac{G_{ep} \cdot G_{ps}}{G_{ep} + G_{ps}} \tag{5.12}$$

G_{tot} corresponds to the parameter determined from the interpolation of the load curves, or from the numerical differentiation of the corresponding $P_e - T_e$ curve. In the case of a high phonon-bath thermal conductance, so that $G_{ep} \sim G_{ps}$ (as in the case of the thermistors provided with the silicon membrane) G_{tot} can be approximated to the electron-phonon thermal conductance. In the case treated here the thermistor is coupled to the heat sink throught the silicon legs, so the validity of the previous approximation should in principle break down. Given the above considerations, if one determines G_{tot} by using a measured load curve, it should be possible to evaluate G_{ps} by means of equation 5.12, by inserting the value of G_{ep} previously determined through the static characterization.

The procedure actually adopted for the evaluation of G_{ps} can be described as follows:

- A complete load curve was measured by hand, using the same electronic set-up adopted for the dynamic characterization of the detectors and described in the previous paragraph. The load curve was measured in order to estabilish the optimum point of the considered detector, at the base temperature of the heat bath (about 30 mK in the case of the TBT, and 20 mK in the case of the AL cryostat). As already discussed, the resistance of the sensor R can be extrapolated from the measured load curve, and the corresponding temperature of the electron system T_e can be derived using the hot electron model equation. Finally, also the Joule power P_e dissipated into the thermistor can be calculated. By interpolating the $P_e - T_e$ curve so determined using a polinomial fit, the total thermal conductance G_{tot} as a function of temperature can be evaluated as $\frac{dP_e}{dT_e}$.
- Since the considered array was not previously characterized from a static point of view, the value of G_{ep} as a function of temperature can be determined by using the results obtained for the BL12 thermistors with degree of compensation 34%, previously measured in the TBT cryostat. To be specific, the electron-phonon thermal conductance of the considered thermistor was evaluated using equation 1.23, where the value of g_{ep} (in W/K$^{\alpha}$) was calculated taking into account the different volume of the presently measured thermistor, starting from the results obtained during the static characterization of the others.
- The so determined values of G_{ep} and G_{tot} can be inserted into equation 5.12 in order to evaluate G_{ps} as a function of temperature, corresponding to the thermal conductance provided by the silicon legs. Furthermore the results obtained concerning $G_{ps}(T)$ can be interpolated using a power law function, in order to check the consistency of the observed trend with the theorical model, given by equation 3.11.

The measurement was carried out for only one thermistor in the case of three silicon legs (identified by G^3_{ps}), and for both the thermistors (b3 and b5) in the case of one silicon leg (identified as $G^1_{ps}(b3)$ and $G^1_{ps}(b5)$).

The obtained results are very promising, since the thermal conductance to the heat sink provided by the silicon legs (in both cases of three or one) resulted to be less than the electron-phonon thermal conductance, by more then one order of magnitude, around 100 mK (the typical operating temperature of microcalorimeters). Some data are reported in table 5.14.

Temperature (K)	G_{ep} (W/K)	$G^1_{ps}(b3)$ (W/K)	$G^1_{ps}(b5)$ (W/K)	G^3_{ps} (W/K)
0.086	3.6×10^{-10}	2.35×10^{-11}	2.22×10^{-11}	3.3×10^{-11}
0.091	4.6×10^{-10}	2.73×10^{-11}	2.53×10^{-11}	3.8×10^{-11}
0.104	8.3×10^{-10}	3.84×10^{-11}	3.46×10^{-11}	5.8×10^{-11}
0.116	1.3×10^{-9}	5.07×10^{-11}	4.46×10^{-11}	7.9×10^{-11}
0.123	1.7×10^{-9}	5.86×10^{-11}	5.11×10^{-11}	9.5×10^{-11}

Table 5.14: Results obtained for the value of the thermal conductance to the heat sink in the case of three silicon legs (G^3_{ps}) and one silicon leg ($G^1_{ps}(b3)$ and $G^1_{ps}(b5)$) compared to the values of G_{ep}, at various temperatures around 100 mK

The expected value of G_{ps} can be calculated using the kinetic gas model (considering a gas of phonons) and taking into account the dimensions of the silicon legs reported in section 5.3.2. According to the kinetic theory of gases, the thermal conductivity of a gas of phonons is given by:

$$g[\mathrm{W/K\cdot cm}] = \frac{n\langle v\rangle\lambda c_v}{3N_A} \tag{5.13}$$

with:

$n =$ particles per unit volume, calculated as $(\rho_{Si}/A_{Si})\cdot N_A$

$N_A =$ Avogadro number

$\lambda =$ mean free path (the minimum possible path was considered, corresponding to the thickness of the silicon legs $= 4\times10^{-3}$ cm)

$\langle v\rangle =$ mean velocity of acoustic phonons in silicon (sound speed $= 220\times10^3$ cm/s)

$c_v = \frac{12}{5}\cdot\pi^4 R(\frac{T}{\Theta_D})^3$ is the molar heat capacity of silicon ($R = 8.314$ J/K·mol).

The thermal conductance can then be determined as:

$$G_{ps}[\mathrm{W/K}] = g\cdot\frac{S}{L} \tag{5.14}$$

where S is the cross-section area and L the length of the considered silicon leg. Considering the dimensions of the larger silicon leg (the one linking the thermistor to the heat sink) the theorical calculation gives: $G^1_{ps}(100\text{ mK}) = 1.8 \pm 0.45 \times 10^{-11}$ W/K, thus in good agreement with the measured values (the uncertainty takes into account the imprecision on the evaluation of the thickness). An inverse approach can be used in order to estimate the actual mean free path of phonons, which is expected to be slightly higher with respect to the value used in the previous calculation. The phonons can in fact move through the silicon leg in all directions, and the mean free path should correspond to an average value over all the possible paths. Starting from the value G^1_{ps} experimentally determined at ~ 100 mK ($\sim 3.5 \times 10^{-11}$ W/K) the corresponding mean free path results to be 8×10^{-3} cm.

Furthermore, the values obtained by the measurements for $G^1_{ps}(b3)$ and $G^1_{ps}(b5)$, in the cases of thermistors provided with only one leg, coincide with $\sim \frac{5}{9} G^3_{ps}$, determined in the case of three silicon legs, as expected taking into account the relative dimensions of the three legs.

Figure 5.89 shows the comparison among G_{ep}, the values of G_{ps} determined in the two cases of one (G_{ps} b3 1leg and G_{ps} b5 1leg) and three legs (G_{ps} 3legs) and the calculated value $G^1_{ps} = \frac{5}{9} \cdot G^3_{ps}$.

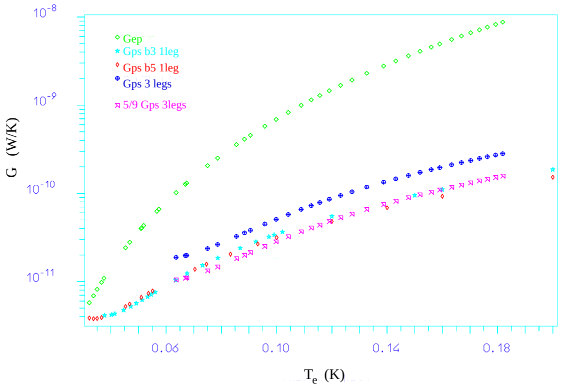

Figure 5.89: Comparison among G_{ep}, the values of G_{ps} determined in the two cases of one (G_{ps} b3 1leg and G_{ps} b5 1leg) and three silicon legs (G_{ps} 3legs) and the calculated value (5/9 G_{ps} 3legs); the data cover different temperature ranges, depending upon the region considered during the measurements

Finally figures 5.90, 5.91 and 5.92 show the results of the interpolation of the determined G_{ps} values as a function of temperature, for the three cases considered: three silicon legs, one silicon leg thermistor b3 and one silicon leg thermistor b5. The data

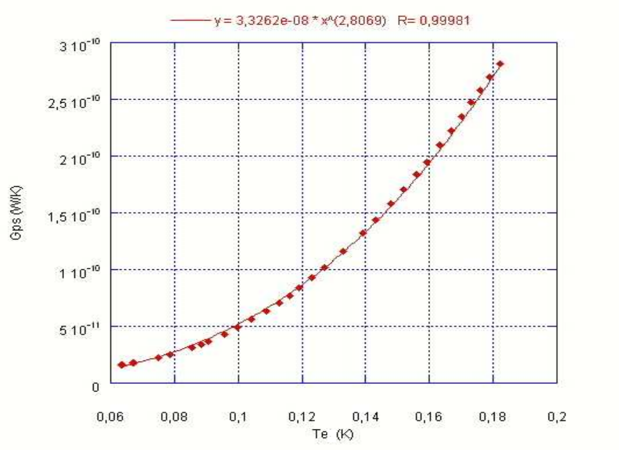

Figure 5.90: Result of the interpolation of the determined G^3_{ps} values, for the case of three silicon legs, as a function of temperature, according to a power law function; the exponent determined by fitting the data is ~ 2.8

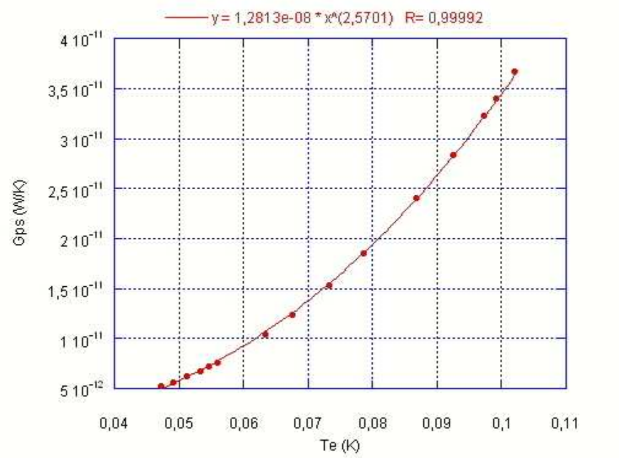

Figure 5.91: Result of the interpolation of the determined $G^1_{ps}(b3)$ values, for the case of one silicon leg, thermistor b3, as a function of temperature, according to a power law function; the exponent determined by fitting the data is ~ 2.6

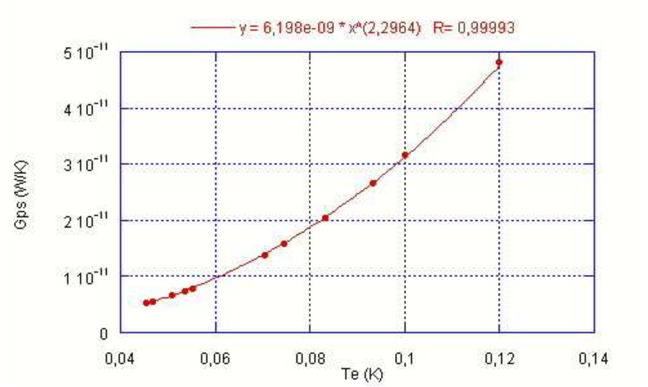

Figure 5.92: Result of the interpolation of the determined $G^1_{ps}(b5)$ values, for the case of one silicon leg, thermistor b5, as a function of temperature, according to a power law function; the exponent determined by fitting the data is ~ 2.3

appear to be well interpolated by a power law function, with exponent $\sim 2.3 - 2.8$, thus in good agreement with the theorical value in the case of dielectric materials (see equation 3.11). The rather low value in the two cases of one silicon leg can be ascribed to the fact that a narrow range of temperatures was considered during the measurements.

CONCLUSIONS

In this thesis work, the fundamental mechanisms which are at the basis of the low temperature transport properties of doped semiconductor devices have been studied, as applied to the developement of bolometric detectors of particles.

The first part was devoted to the study of the low temperature behaviour of resistive elements, realized using silicon doped well above the MIT, to be used for the sabilization of CUORE bolometers. Concerning this topic, interesting and useful results have been obtained. The characterizations performed allowed, not only to test and select the devices to be actually used for the developement of the CUORE detectors, but also to better understand the physical properties of such devices and to determine further useful informations about their low temperature behaviour. In particular, interesting correlations were found, linking the properties shown at or below liquid helium temperature and at nitrogen temperature. The measurements performed below 1 K, in the typical range of temperatures at which bolometers are operated, gave positive results as well, in terms of stability of resistance of the studied devices, which thus appear to be well suited to accomplish their main tasks. The performances actually shown, while operating them as stabilizing elements in the context of the CUORE R&D activities, performed in hall C at LNGS, further confirmed the reliability of the tested devices.

In conlusion, the heating elements characterized during this thesis work will be used for the construction of CUORE detectors. Furthermore, the informations meanwhile gathered will be used to speed up and save money during their selection, which is still in progress.

Finally, a set-up based on a ^{4}He pumped refrigerator, realized in view of the characterization of CUORE heaters, is at present available in the Cryogenic Laboratory at Insubria University, useful for any kind of measurement for which temperatures as low as ~ 1.5 K are required.

The second part of this thesis work was devoted to characterize the static and dynamic properites of silicon based thermistors, operating in the variable range hopping regime. Such sensors were realized mainly following the techniques drawn from the results already obtained with precursor devices. However, new technologies, based on the use of micromachining, have been included, in order to fabricate arrays of thermistors, relatively easy to handle, in view of their integration in large microcalorimeter arrays (in the context of the MARE experiment).

Concerning this topic, the results obtained showed that, though many problems arose dealing with the production process, the main parameters which actually control the thermistor performances appear to be well suited for their foreseen aims. In particular, the value of T_0, the geometry and dimensions, the electron-phonon thermal conductance and the phonon-bath thermal conductance (provided by the integrated silicon legs) appear to be optimized for the desired detector performances. Considering the results obtained during the dynamic characterization, it is worth to notice that further investigations should be accomplished, in order to build a complete understanding of the behaviours of the thermistors studied. Nevertheless, even taking into account that the operating conditions were not optimized, the results are very promizing.

Thanks to the characterization performed, still some problems arose, mainly dealing with the fragility of the samples and with the production process. Given the positive results obtained concerning the detector performances, a new fabrication run can be performed, adopting the new methodology suggested, based on the use of SOI wafers and DRIE, to safely complete the production process.

BIBLIOGRAPHY

[1] N.W. Ashcroft and N.D. Mermin. *Solid state physics*. Saunders College, 1976.

[2] S.M. Sze and K.Ng. Kwok. *Physics of semiconductor devices*. John Wiley and Sons, 2007.

[3] C. Kittel. *Introduction to solid state physics*. John Wiley and Sons, 1986.

[4] B.I. Shklovskii and A.L. Efros. *Electronic properties of doped semiconductors*. Springer-Verlag, 1984.

[5] N.F. Mott and J.H. Davies. Metal-insulator transition in doped semiconductors. *Phil. Mag. B*, 42:845, 1980.

[6] H. Fritzsche. Effect of compensation on conduction near the metal non-metal transition. *Phil. Mag. B*, 42:835, 1980.

[7] B.I. Shklovskii and A.L. Efros. Impurity band and conductivity of compensated semiconductors. *Sov. Phys.- JETP*, 33:468, 1971.

[8] C. Yamanouchi. Hall coefficient and resistivity in the intermediate impurity conduction of n-type germanium. *J. Phys. Soc. Japan*, 20:1029, 1965.

[9] H. Nishimura. Impurity conduction in the intermediate concentration range. *Phys. Rev. A*, 138:815, 1965.

[10] A. Miller and E. Abrahams. Impurity conduction at low concentrations. *Phys. Rev.*, 120:745, 1960.

[11] M. Pollak. A percolation treatment of d.c. hopping conduction. *J. Non-Crystal. Solids*, 11:1, 1972.

[12] N.F. Mott. Conduction in glasses containing transition metal ions. *J. Non-Crystal. Solids*, 1:1, 1968.

[13] V. Ambegaokar et al. Hopping conductivity in disordered systems. *Phys. Rev. B*, 4:2612, 1971.

[14] E.M. Hamilton. Variable range hopping in a nonuniform density of states. *Phil. Mag.*, 26:1043, 1972.

[15] M. Pollak. Effect of carrier-carrier interactions on some transport properties in disordered semiconductors. *Disc. Farady Soc.*, 50:13, 1970.

[16] M.L. Knotek and M. Pollak. Correlation effects in hopping conduction: Hopping as multielectron transition. *J. Non-Crystal. Solids*, 8-10, 1972.

[17] R.M. Hill. Hopping conduction in amorphous solids. *Phil. Mag.*, 24:1307, 1971.

[18] N. Wang et al. Electrical and thermal properties of neutron-transmutation-doped Ge at 20 mk. *Phys. Rev. B*, 41:3761, 1990.

[19] J. Zhang et al. Non-ohmic effects in hopping conduction in doped silicon and germanium between 0.05 and 1 kelvin. *Phys. Rev. B*, 57:4472, 1998.

[20] A.C. Anderson and R.E. Peterson. Thermal resistance between electrons and phonons in copper. *Phys. Lett.*, 38:519, 1972.

[21] K.S. Hirata et al. Kamiokande-II: Experimental study of the atmospheric neutrino flux. *Phys. Lett. B*, 205:416, 1988.

[22] Y. Fukuda et al. Tau neutrinos favored over sterile neutrinos in atmospheric muon neutrino oscillations. *Phys. Rev. Lett.*, 85:3999, 2000.

[23] M. Ambrosio et al. Atmospheric neutrino oscillations from upward throughgoing muon multiple scattering in MACRO. *Phys. Lett. B*, 566:35, 2003.

[24] Q.R. Ahmad et al. Direct evidence for neutrino flavor transformation from neutral-current interactions in the Sudbury Neutrino Observatory. *Phys. Rev. Lett.*, 89:011301, 2002.

[25] Q.R. Ahmad et al. First results from KamLAND: evidence for reactor antineutrino disappearance. *Phys. Rev. Lett.*, 90:021802, 2003.

[26] Z. Maki, M. Nakagawa, and S. Sakata. Remarks on the unified model of elementary particles. *Prog. Theor. Phys.*, 28:870, 1962.

[27] S. Pascoli and S.T. Petcov. The SNO solar neutrino data, neutrinoless double beta decay and neutrino mass spectrum. *Phys. Lett. B*, 544:239, 2002.

[28] F. Feruglio, A. Strumia, and F. Vissani. Neutrino oscillations and signals in β and $0\nu2\beta$ experiments. *Nucl. Phys. B*, 637:345, 2002.

[29] G. Steigman. Neutrinos, cosmology and dark matters. *Nucl. Phys. (Proc. Suppl.)*, 31:343, 1993.

[30] H.V. Klapdor-Kleingrothaus et al. Evidence for neutrinoless double beta decay. *Mod. Phys. Lett. A*, 16:2409, 2001.

[31] G.F. Knoll. *Radiation detection and measurement*. John Wiley and Sons, Inc., 1989, 2nd edition.

[32] C. Kraus et al. The Mainz neutrino mass experiment investigates the end point region of the tritium β decay spectrum. *Eur. Phys. J. C*, 33:805, 2004.

[33] V.M. Lobashev et al. Direct search for neutrino mass and anomaly in the tritium beta-spectrum: status of Troitsk neutrino mass experiment. *Nucl. Phys. B*, 91:280, 2001.

[34] V.M. Lobashev. The search for the neutrino mass by direct method in the tritium beta-decay and perspectives of study it in the project katrin. *Nucl. Phys. A*, 719:153, 2003.

[35] Katrin: A next generation tritium beta decay experiment with sub-eV sensitivity for the electron neutrino mass. The KATRIN Collaboration, 2001. hep-ex/0109033.

[36] S. Vitale et al. INFN Internal Report: A new determination of the mass limits of the anti-neutrino, 1985. INFN/BE-85/2.

[37] F. Gatti et al. A second generation experiment for direct neutrino mass measurement via ^{187}Re β-decay. *Nucl. Phys. B*, 143:541, 2005.

[38] M. Sisti et al. New limits from the Milano neutrino mass experiment with thermal microcalorimeters. *Nucl. Instr. Meth. A*, 520:125, 2004.

[39] Mare: Microcalorimeter arrays for a rhenium experiment. The MARE Collaboration, 2006. http://mare.dfm.uninsubria.it/frontend/exec.php.

[40] J. Schechter and J.W.F. Valle. Neutrinoless double-β decay in SU(2)×U(1) theories. *Phys. Rev. D*, 25:2951, 1982.

[41] B. Kayser et al. New and exotic phenomena. In *Edition Frontiers*. Ed. O. Facker, 1987.

[42] Cuore: A cryogenic underground observatory for rare events. The CUORE Collaboration, 2005. crio.mib.infn.it/wig/Cuorepage/CUORE-proposal.pdf.

[43] A. Alessandrello et al. Methods for response stabilization in bolometers for rare decays. *Nucl. Instr. and Meth. Phys. Res. A*, 412:454, 1998.

[44] S.H. Moseley, J.C. Mather, and D. McCammon. Thermal detectors as X-ray spectrometers. *J. Appl. Phys.*, 56:1257, 1984.

[45] E. Fiorini and T.O. Niinikoski. Low-temperature calorimetry for rare decays. *Nucl. Instr. and Meth.*, 224:83, 1984.

[46] D. McCammon. Semiconductor thermistors. In *Cryogenic Particle Detection, Topics Appl. Phys.* Springer-Verlag, 2005.

[47] A. Nucciotti. *Sviluppo di microcalorimetri a bassa temperatura da utilizzare in un esperimento per la determinazione della massa del neutrino*. PhD thesis, University of Milano, 1996.

[48] M. Pedretti. *Sviluppo di array di rivelatori a basse temperature per la misura della massa dell'antineutrino elettronico*. University of Milano, Master thesis, 2000.

[49] J.E. Vaillancourt. Complex impedance as a diagnostic tool for characterizing thermal detectors. *Rev. Sci. Instrum.*, 76:043107, 2005.

[50] M. Galeazzi and D. McCammon. Microcalorimeter and bolometer model. *J. Appl. Phys.*, 93:4856, 2003.

[51] R.C. Jones. The general theory of bolometer performance. *J. Opt. Soc. Am.*, 43:1, 1952.

[52] A. Alessandrello et al. Heat capacity of P-doped Si thermistors at low and very low temperature measured by alpha-particles and X-rays. *Europhys. Lett.*, 7:69, 1988.

[53] A. Alessandrello et al. Heat capacity of low temperature Ge- and Si-calorimeters and optimization of As-implanted silicon thermistors. *Nucl. Instr. and Meth. Phys. Res. A*, 263:233, 1988.

[54] J.C. Mather. Bolometers: ultimate sensitivity, optimization and amplifier coupling. *Appl. Opt.*, 23(4):584, 1984.

[55] G.K. White and P.J. Meeson. *Experimental Techniques in Low-Temperature Physics*. Oxford University Press, 4th edition, 2002.

[56] F. Pobell. *Matter and methods at Low Temperatures*. Springer-Verlag, 2nd edition, 1996.

[57] A. Alessandrello et al. Construction and characterization of Si thermistors for high resolution X-ray detectors. *Czech. J. Phys.*, 46:2893, 1996.

[58] A. Alessandrello et al. Fabrication and low-temperature characterization of Si-implanted thermistors. *J. Phys. D: Appl. Phys.*, 32:3099, 1999.

[59] A. Alessandrello et al. High energy resolution bolometers for nuclear physics and X-ray spectroscopy. *Phys. Rev. Lett.*, 82:513, 1999.

[60] K. Uhlig. ^{3}He/^{4}He dilution refrigerator with pulse tube refrigerator precooling. *Cryogenics*, 42:73, 2002.

[61] K. Uhlig. Dry dilution refrigerator with pulse tube precooling. *Cryogenics*, 44:53, 2004.

[62] S. Sangiorgio. *Advanced detector technologies for the CUORE experiment*. PhD thesis, University of Insubria, 2006.

[63] L.G. Foggetta. *Sviluppo di un sistema di acquisizione per rivelatori criogenici innovativi*. University of Insubria, Master thesis, 2004.

[64] F. Gatti and P.F. Manfredi. Processing the signals from solid-state dtectors in elementary-particle physics. *Nuovo Cimento*, 9:1, 1986.

ACKNOWLEDGEMENTS

I would like to acknowledge all the people I met during these three years of intense work. From each of them I came to learn something special, which in a very personal way paved the road I am going to walk on in both the world of research and life. From the many experiences undertaken, I will always consider the period of time just passed as one of the main steps towards my personal and professional growth.

IL PROGETTO

Le attività concernenti questo lavoro di ricerca sono state finanziate dal Ministero dell'Istruzione, dell'Università e della Ricerca, all'interno di un progetto presentato dal Professor Jug e dal Professor Giuliani, del Dipartimento di Fisica e Matematica dell'Università degli Studi dell'Insubria. Il progetto di ricerca, inquadrato nell'ambito di indagine prioritario "Nuovi Materiali Strutturali e Funzionali", ha avuto come obiettivo lo sviluppo di alcune tra una serie di tematiche proposte, nei campi della fisica sperimentale, teorica e della materia.

In particolare, il presente lavoro di dottorato di ricerca è stato incentrato sulle tematiche seguenti:

- studio della conduzione elettrica in regime di Variable Range Hopping di semiconduttori drogati al livello della transizione metallo-isolante, nello specifico dal punto di vista sperimentale, e integrazione di dispositivi basati su questo meccanismo di conduzione in rivelatori di radiazione ionizzante;
- studio delle proprietà di trasporto, di quelle termiche e dielettriche dei materiali interessati.

THE PROJECT

The activities concerning this research work have been funded by the Ministry of Education, University and Research, within a project submitted by Professor Jug and Professor Giuliani, of the Department of Physics and Mathematics at University of Insubria. The main goals of the project, developed in the frame of the priority research area "New Structural and Functional Materials", concerned the study of a selection among a series of themes, proposed in the fields of experimental, theoretical and material physics.

In particular, the PhD work here presented has been centred around the following themes:

- study of the charge transport in the Variable Range Hopping regime, in semiconductors doped just below the metal-to-insulator transition, from an experimental point of view, and integration of devices based upon such conduction mechanism in ionizing radiation detectors;
- study of the thermal, dielectric and transport properties of the considered materials.